

Molecular basis of collybistin conformational activation

Molekulare Prinzipien der konformellen Aktivierung von Collybistin



Thesis for a doctoral degree at the Graduate School of Life Sciences
Julius-Maximilians-Universität-Würzburg

Section:
Biomedicine

Submitted by:
Nasir Imam

From:
Bokaro Steel City, India

Würzburg 2022



Submitted on:

Office Stamp

Members of *Promotionskomitee*:

Chairperson: PD Dr. Frank Döring

Primary Supervisor: Prof. Dr. Hermann Schindelin

Supervisor (Second): Prof. Dr. Carmen Villmann

Supervisor (Third): Prof. Dr. Thomas Müller

Supervisor (Fourth): Prof. Dr. Katrin Heinze

Date of Public Defence:

Date of Receipt of Certificates:

Dedicated to my beloved late parents

Table of Contents

Table of Contents	3
Summary	7
Zusammenfassung	9
Statement of individual author contributions and of legal second publication rights to manuscripts included in the dissertation	12
Statement of individual author contributions to figures/tables of manuscripts	14
1. Introduction	16
1.1. Inhibitory synaptic neurotransmission	19
1.2. Receptors architecture	19
1.3. Gephyrin	22
1.3.1. Gephyrin domain architecture	22
1.3.2. Gephyrin orthologs	24
1.3.3. Gephyrin post-translational modifications	25
1.3.4. Gephyrin-mediated receptors clustering	26
1.4. Collybistin	27
1.4.1. Structure of CB	28
1.4.2. CB intramolecular interactions and relief of autoinhibition	28
1.4.3. CB role in inhibitory postsynapse organization	30
1.4.3a. SH3 domain	30
1.4.3b. DH Domain	32
1.4.3c. PH Domain	34
1.5. Ras GTPases	37
1.5.1. Ras GTPase classification	37
1.5.2. Rho subfamily	39
1.5.3. Rho GTPase structure and mechanism	39
1.5.4. Rho GTPase interaction with CB	41
1.6. Aims and objectives	42
2. Deciphering the conformational dynamics of gephyrin-mediated collybistin activation	43
2.1. Abstract	44

2.1.1. Keywords	44
2.2. Why it matters	44
2.3. Introduction	45
2.4. Methods	49
2.4.1. Cloning and expression	49
2.4.2. Circular-dichroism spectroscopy	49
2.4.3. <i>In vitro</i> FLAsH labeling	50
2.4.4. Time-resolved setup and data acquisition	50
2.4.5. Time-resolved fluorescence decay analysis	51
2.4.6. K_D determination	52
2.4.7. Förster distance calculation	53
2.4.8. Average FRET efficiency calculation	53
2.4.9. FRET distance distribution analysis	53
2.4.10. Uncertainty estimation of distance distribution	54
2.4.11. Model-free distance distribution analysis	55
2.4.12. FRET-restrained Markov-chain Monte-Carlo sampling	55
2.4.13. Statistical analysis	56
2.5. Results	56
2.5.1. Sensor engineering and characterization	56
2.5.2. Gephyrin, NL2 and free SH3 mediate CB activation	59
2.5.3. Two-state dynamics during CB activation	63
2.5.4. The E domain of gephyrin mediates CB binding and activation	64
2.5.5. A monomeric E-domain induces a stronger CB conformational change	66
2.5.6. Active state mutant sensors design and characterization	68
2.5.7. Gephyrin binding elicits differential responses in a series of FRET sensors	73
2.5.8. Markov-chain Monte-Carlo sampling studies reveal CB conformations	75
2.6. Discussion	78
2.7. Acknowledgements	82
2.8. Author contributions	82
3. Differential modulation of collybistin conformational dynamics by the closely related GTPases Cdc42 and TC10	83
3.1. Abstract	83

3.1.1. Keywords	84
3.2. Introduction	84
3.3. Methods	86
3.3.1. Cloning, expression, purification and <i>in vitro</i> FAsH labeling	86
3.3.2. Time-resolved setup and data acquisition	87
3.3.3. Time-resolved fluorescence decay analysis	88
3.3.4. K_D determination	89
3.3.5. Average FRET efficiency calculation	89
3.3.6. Förster distance calculation	89
3.3.7. FRET distance distribution analysis	90
3.3.8. Uncertainty estimation of distance distribution	91
3.3.9. Model Free distance distribution analysis	91
3.4. Results	92
3.4.1. Comparative analysis of TC10 and Cdc42 structures	92
3.4.2. TC10 mediates conformational activation of auto-inhibited CB	94
3.4.3. TC10 stabilizes an open conformation of CB	95
3.4.4. TC10 C-terminal variants efficiently recognize CB	97
3.4.5. Deletion of TC10 C-terminal stretch enhances its affinity for CB	100
3.4.6. Cdc42 and TC10 efficiently interact with active state mutant sensors of CB	100
3.4.7. Active state sensors display differential responses upon GTPase binding	103
3.4.8. Cdc42 and TC10 induce variable responses in additional FRET sensors	106
3.4.9. Cdc42 and TC10 display different electrostatic potentials	108
3.5. Discussion	110
3.6. Acknowledgement	113
3.7. Author contributions	113
4. Cumulative discussion	114
4.1. Gephyrin-mediated Collybistin activation	114
4.2. Differential Rho GTPases recognition by Collybistin and its conformational activation	116
5. Future perspectives	117
5.1. Gephyrin-Collybistin Interaction	117
5.2. Collybistin and Rho GTPase interaction	117

5.3. CB interaction with the GABA _A R α 2 subunit _____	117
5.4. CB interaction with phosphoinositides _____	118
6. References _____	119
7. List of publications _____	139
8. Abbreviations _____	140
9. Plasmid constructs _____	143
10. Affidavit _____	144
11. Acknowledgements _____	145
12. Curriculum Vitae _____	147

Summary

The nervous system relies on an orchestrated assembly of complex cellular entities called neurons, which are specifically committed to information management and transmission. Inter-neuronal communication takes place via synapses, membrane-membrane junctions which ensure efficient signal transfer. Synaptic neurotransmission involves release of presynaptic neurotransmitters and their reception by cognate receptors at postsynaptic terminals. Inhibitory neurotransmission is primarily mediated by the release of neurotransmitters GABA (γ -Aminobutyric acid) and glycine, which are precisely sensed by GABA type-A receptors (GABA_ARs) and glycine receptors (GlyRs), respectively. GABA_AR assembly and maintenance is coordinated by various postsynaptic neuronal factors including the scaffolding protein gephyrin, the neuronal adaptor collybistin (CB) and cell adhesion proteins of the neuroligin (NL) family, specifically NL2 and NL4.

At inhibitory postsynaptic specializations, gephyrin has been hypothesized to form extended structures underneath the plasma membrane, where its interaction with the receptors leads to their stabilization and impedes their lateral movement. Gephyrin mutations have been associated with various brain disorders, including autism, schizophrenia, Alzheimer's disease, and epilepsy. Furthermore, gephyrin loss is lethal and causes mice to die within the first post-natal day. Gephyrin recruitment from intracellular deposits to postsynaptic membranes primarily relies on the adaptor protein CB.

As a moonlighting protein, CB, a guanine nucleotide exchange factor (GEF), also catalyzes a nucleotide exchange reaction, thereby regenerating the GTP-bound state of the small GTPase Cdc42 from its GDP-bound form. The CB gene undergoes alternative splicing with the majority of CB splice variants featuring an N-terminal SH3 domain followed by tandem Dbl-homology (DH) and pleckstrin-homology (PH) domains. Previous studies demonstrated that the most widely expressed, SH3-domain containing splice variant (CB_{2SH3+}) preferentially adopts a closed conformation, in which the N-terminally located SH3 domain forms intra-molecular interaction with the DH-PH domain tandem. Previous cell-based studies indicated that SH3 domain-encoding CB variants remain untargeted and colocalize with intracellular gephyrin deposits and hence require additional factors which interact with the SH3 domain, thus inducing an open or active conformation. The SH3 domain-deficient CB isoform (CB_{2SH3-}), on the contrary, adopts an open

conformation, which possess enhanced postsynaptic gephyrin-clustering and also effectively replenishes the GTP-bound small GTPase-Cdc42 from its GDP-bound state.

Despite the fundamental role of CB as a neuronal adaptor protein maintaining the proper function of inhibitory GABAergic synapses, its interactions with the neuronal scaffolding protein gephyrin and other post synaptic neuronal factors remain poorly understood. Moreover, CB interaction studies with the small GTPase Cdc42 and TC10, a closely related member of Cdc42 subfamily, remains poorly characterized. Most importantly, the roles of the neuronal factors and small GTPases in CB conformational activation have not been elucidated.

This PhD dissertation primarily focuses on delineating the molecular basis of the interactions between CB and postsynaptic neuronal factors. During the course of my PhD dissertation, I engineered a series of CB FRET (Förster Resonance Energy Transfer) sensors to characterize the CB interaction with its binding partners along with outlining their role in CB conformational activation. Through the aid of these CB FRET sensors, I analyzed the gephyrin-CB interaction, which, due to technical limitations remained unaddressed for more than two decades (refer Chapter 2 for more details). Subsequently, I also unraveled the molecular basis of the interactions between CB and the neuronal cell adhesion factor neuroligin 2 (refer chapter 2) and the small GTPases Cdc42 and TC10 (refer chapter 3) and describe how these binding partners induce a conformational activation of CB.

In summary, this PhD dissertation provides strong evidence of a closely knit CB communication network with gephyrin, neuroligin and the small GTPase TC10, wherein CB activation from closed/inactive to open/active states is effectively triggered by these ligands.

Zusammenfassung

Das Nervensystem ist eine komplexe Ansammlung zellulärer Einheiten, darunter sind die Neuronen, die speziell für die Verarbeitung und Übertragung von Informationen zuständig sind. Die Kommunikation zwischen Neuronen erfolgt über Synapsen, spezialisierte Membran-Membran-Kontakte, die eine effiziente Signalübertragung gewährleisten. Die synaptische Neurotransmission umfasst die präsynaptische Freisetzung von Neurotransmitters und deren Empfang durch entsprechende Rezeptoren in den Postsynapsen. Die inhibitorische Neurotransmission wird in erster Linie durch die Freisetzung der Neurotransmitter GABA (γ -Aminobuttersäure-Typ) und Glycin vermittelt, die von GABA-Typ-A-Rezeptor (GABA_AR) bzw. Glycinrezeptoren (GlyR) präzise wahrgenommen werden. Der Aufbau und die Aufrechterhaltung von GABA_AR Clustern wird durch verschiedene postsynaptische neuronale Faktoren koordiniert, darunter das Gerüstprotein Gephyrin, das neuronale Adaptorprotein Collybistin (CB) und Zelladhäsionsproteine der Neuroligin (NL)-Familie, insbesondere NL2 und NL4.

Es wird angenommen, dass Gephyrin an hemmenden postsynaptischen Spezialisierungen ausgedehnte Strukturen unterhalb der Plasmamembran bildet, und durch Interaktion mit den Rezeptoren deren laterale Diffusion verhindert. Gephyrin-Mutationen wurden mit verschiedenen Hirnkrankheiten in Verbindung gebracht, darunter Autismus, Schizophrenie, Alzheimer und Epilepsie. Der Verlust von Gephyrin ist tödlich und führt dazu, dass Mäuse innerhalb des ersten postnatalen Tages sterben. Die Rekrutierung von Gephyrin aus intrazellulären Ablagerungen zu postsynaptischen Membranen hängt in erster Linie von CB ab.

Als Moonlighting-Protein katalysiert CB, ein Guanin-Nukleotid-Austauschfaktor (GEF), auch den Nukleotidaustausch und somit die Reaktivierung der kleinen GTPase Cdc42. Das CB-Gen wird durch alternatives Spleißen modifiziert; die meisten CB-Spleißvarianten weisen eine N-terminale SH3-Domäne auf, gefolgt von Tandem aus einer Dbl-Homologie (DH)- und einer Pleckstrin-Homologie (PH)-Domäne. Frühere Studien zeigten, dass die am häufigsten exprimierte Spleißvariante, die eine SH3-Domäne enthält (CB2SH3+), vorzugsweise eine geschlossene Konformation annimmt, bei der die N-terminal gelegene SH3-Domäne eine intra-molekulare Interaktion mit dem DH-PH-Tandem eingeht. Zellbasierte Studien zeigten, dass CB-Varianten, die für die SH3-Domäne

kodieren, sich innerhalb der Zelle nicht an spezifischen Orten anreichern und stattdessen mit intrazellulären Gephyrin-Ablagerungen kolokalisieren. Zusätzliche Faktoren werden benötigt, die mit der SH3-Domäne interagieren und so eine offene oder aktive Konformation hervorrufen. Die SH3-Domänen-defiziente CB-Isoform (CB2SH3-) hingegen nimmt eine offene Konformation an, die eine verstärkte postsynaptische Gephyrin-Anhäufung aufweist und die GTP-gebundene kleine GTPase Cdc42 aus ihrem GDP-gebundenen Zustand effektiv wieder regeneriert.

Trotz der grundlegenden Rolle von CB als neuronales Adaptorprotein, das die ordnungsgemäße Funktion hemmender GABAerger Synapsen aufrechterhält, ist seine Interaktion mit dem neuronalen Gerüstprotein Gephyrin und anderen post-synaptischen neuronalen Faktoren nach wie vor unzureichend verstanden. Darüber hinaus sind die Interaktionsstudien von CB mit der kleinen GTPase Cdc42 und TC10, einem eng verwandten Mitglied der Cdc42-Unterfamilie, noch immer unzureichend charakterisiert. Somit war die Frage, ob diese neuronalen Faktoren sowie die kleinen GTPasen an der CB-Konformationsaktivierung beteiligt sind.

Diese Dissertation konzentriert sich in erster Linie auf die Beschreibung der molekularen Grundlagen der Interaktion von CB mit postsynaptischen neuronalen Faktoren. Im Rahmen meiner Dissertation habe ich eine Reihe von CB-FRET-Sensoren (Förster-Resonanz-Energie-Transfer) entwickelt, um die CB-Interaktion mit seinen Bindungspartnern zu charakterisieren und ihre Rolle bei der CB-Konformationsaktivierung zu beschreiben. Mit Hilfe der CB-FRET-Sensoren entschlüsselte ich das langjährige Rätsel der Gephyrin-CB-Interaktion, das aufgrund technischer Beschränkungen mehr als zwei Jahrzehnte lang ungelöst blieb (siehe Kapitel 2 für weitere Einzelheiten). In der Folge habe ich auch die molekularen Grundlagen der CB-Wechselwirkung und damit ihre konformelle Aktivierung durch den neuronalen Zelladhäsionsfaktor Neuroligin 2 (siehe Kapitel 2) und die kleinen GTPasen Cdc42 und TC10 (siehe Kapitel 3) analysiert.

Zusammengefasst liefert diese Dissertation starke Beweise für ein engmaschiges CB-Kommunikationsnetzwerk mit Gephyrin, Neuroligin und der kleinen GTPase TC10, in dem der CB-Konformationswechsel vom geschlossenen/inaktiven zum offenen/aktiven Zustand effektiv durch die Liganden ausgelöst wird.

This dissertation is based on the following manuscripts:

1. Imam N^ψ., Choudhury S^ψ., Hemmen K., Katrin G. H.,* Schindelin H.*(2022). Deciphering the conformational dynamics of gephyrin-mediated collybistin activation. *Biophysical Reports*. Volume 2, Issue4. doi: <https://doi.org/10.1016/j.bpr.2022.100079>.

2. Imam N., Choudhury S., Katrin G. H.,* Schindelin H.*(2022). Differential modulation of collybistin conformational dynamics by the closely related GTPases Cdc42 and TC10. *Frontiers in Synaptic Neuroscience*. Volume 14.
<https://doi.org/10.3389/fnsyn.2022.959875>

^ψ Authors contributed equally to this work.

* Corresponding authors.

“Dissertation Based on Several Published Manuscripts“

Statement of individual author contributions and of legal second publication rights to manuscripts included in the dissertation (If required please use more than one sheet).

Manuscript 1 (complete reference): Imam N., Choudhury S., Hemmen K., Katrin G. H., Schindelin H. (2022). Deciphering the conformational dynamics of gephyrin-mediated collybistin activation. <i>Biophysical Reports</i> . Volume 2, Issue 4.					
Participated in	Author Initials, Responsibility decreasing from left to right				
Study Design	NI	SC	KH	HS	KGH
Methods Development	NI	SC	KH	HS	KGH
Data Collection	NI				
Data Analysis and Interpretation	NI	SC	KH		
Manuscript Writing					
Writing of Introduction	NI	HS			
Writing of Materials & Methods	NI	SC			
Writing of Discussion	NI	HS			
Writing of First Draft	NI	HS			

Statement of individual author contributions to figures/tables of manuscripts included in the dissertation.

Manuscript 1 (complete reference): Imam N., Choudhury S., Hemmen K., Katrin G. H., Schindelin H. (2022). Deciphering the conformational dynamics of gephyrin-mediated collybistin activation. <i>Biophysical Reports</i> . Volume 2, Issue 4.					
Figure	Author Initials, Responsibility decreasing from left to right				
1	NI	HS			
2	NI	SC			
3	NI	SC			
4	NI	SC			
5	NI	SC			
6	NI	SC	KH		
7	NI	HS			

Explanations (if applicable):

I also confirm my primary supervisor's acceptance.

Nasir Imam

2022

Würzburg

Doctoral Researcher's Name

Date

Place

Signature

Manuscript 2 (complete reference): Imam N., Choudhury S., Katrin G. H., Schindelin H. (2022). Differential modulation of collybistin conformational dynamics by the closely related GTPases Cdc42 and TC10. *Frontiers in Synaptic Neuroscience*. Volume 14.

Figure	Author Initials, Responsibility decreasing from left to right				
1	NI	HS			
2	NI	SC			
3	NI	SC			
4	NI	SC			
5	NI	SC			
6	NI	HS			
7	NI				
Table	Author Initials, Responsibility decreasing from left to right				
1	NI	SC			

Explanations (if applicable):

I also confirm my primary supervisor's acceptance.

Nasir Imam

2022

Würzburg

Doctoral Researcher's Name

Date

Place

Signature

1. Introduction

The nervous system is an intricate network of cells that are specialized in information processing and its efficient transfer (Ludwig et al., 2022; Sousa et al., 2017). The nervous system detects environmental changes that impact the body and works in coordination with other systems to efficiently respond to such events. In vertebrates, the nervous system can be broadly subdivided into the central nervous system (CNS) and the peripheral nervous system (PNS). The CNS is largely comprised of the brain and spinal cord, whereas the PNS mainly consists of nerves which are enclosed bundles of the long fibers or axons that connect the CNS to every other part of the body.

At the cellular level, the nervous system is defined by the presence of specialized cells called neurons (frequently referred as nerve cells) that represent the principal basic unit of the nervous system (Fig. 1.1). The basic cellular organization of neurons resembles that of other cells; however, they are remarkably distinguished by their abilities for intercellular communication. Although neurons are not intrinsically good conductors of electricity, they have evolved elaborate mechanisms for generating these signals based on the flow of ions across their plasma membranes. Neurons are polarized cellular entities that possess two pronged extensions pointing away from the central cellular body – known as axons and dendrites (Fig. 1.1). Neurons communicate with each other via specialized structures called synapse (Fig. 1.1). Synapses are membrane to membrane junctions that contain molecular components which ensure rapid inter-neuronal signal transmission. The extracellular space between pre- and postsynaptic elements is called the synaptic cleft (Fig. 1.1), which, however, is not simply a space but also harbors a niche for extracellular proteins that influence the diffusion, binding, and degradation of molecules secreted at the presynaptic terminal. On average, the synaptic signals received by each nerve cell in the human nervous system varies from 1 to approximately 100,000 inputs (Herculano-Houzel & Lent, 2005). This clearly reflects a fundamental role of nerve cells in integrating information from neighboring neurons.

Neurotransmitters released from the presynaptic terminal are received by cognate receptors located at postsynaptic sites (Fig. 1.1). The synaptic cleft, the extracellular space between the pre- and postsynaptic neuron, harbors a niche for extracellular

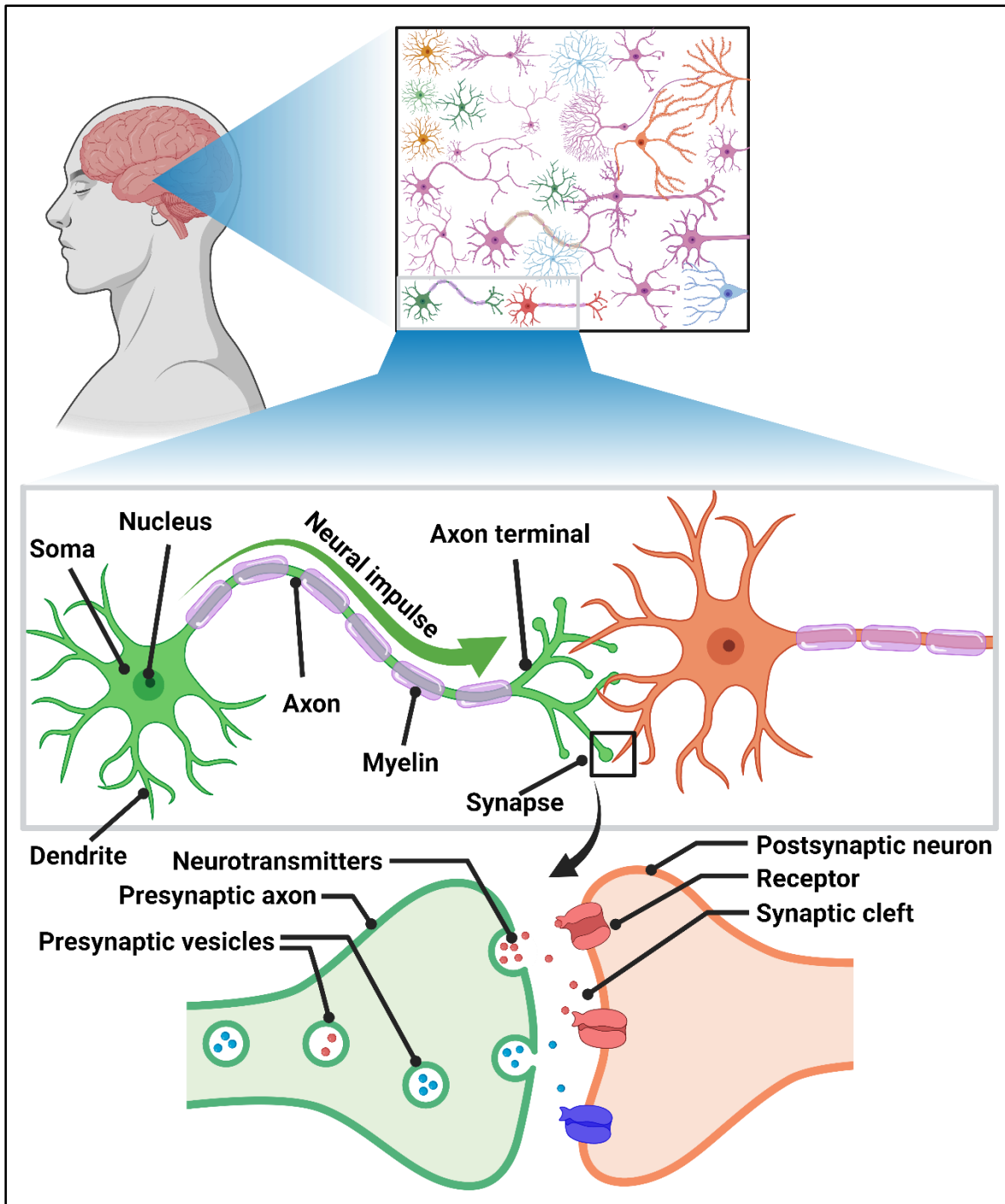


Figure 1.1. Schematic description of nerve cell networking and synaptic transmission. The human brain is predominantly composed of a complex web of neurons. A neuron consists of a cell body, many dendrites, and a single axon. The neuronal cell body encloses the nucleus. Dendrites are forked projections that extend from the cell body and receive signals from neighboring neurons. Neurons serve as specialized conductors that receive from and transmit to adjacent neurons electrochemical impulses through a specialized membrane to membrane junction called the synapse. Synapses ensure rapid and efficient inter-neuronal signal transmission.

neuronal factors that influence the diffusion, binding, and degradation of molecules secreted at the presynaptic site (Fig. 1.1). The chemical or electrical processes through which an information encrypted by action potential is passed on to the adjacent neuron at these synaptic contacts is called synaptic transmission. The presynaptic terminals and their postsynaptic specializations together form chemical synapses, which are the most prevalent type of synapse in the nervous system.

The presynaptic terminals of chemical synapses comprise synaptic vesicles which are filled with neurotransmitter molecules (Fig. 1.1). Vesicle positioning and their fusion with the presynaptic membrane initiates neurotransmitter release, and this process is regulated by a plethora of neuronal factors. Upon release, the neurotransmitters bind to receptors, which are localized at the postsynaptic sites, thereby modifying the electrical properties of the target neuron. Specifically, neurotransmitter binding induces conformational changes in the receptor, which leads to channel opening and triggers ion influx or efflux in response to the respective ion concentrations in the cytosol and the synaptic cleft and the selectivity of the respective neurotransmitter. Ion influx or efflux result in local changes in the membrane potential, consequently eliciting either an inhibitory postsynaptic potential (iPSP) or an excitatory postsynaptic potential (ePSP). Synapses eliciting ePSP and iPSP at the postsynaptic neuronal cell are termed as excitatory and inhibitory synapses, respectively (Bear et al., 2020). Excitatory receptors permit the entry of positively charged ions, which depolarize the neuronal membrane, hence increasing the possibility for neuronal cells to self-initiate electrical responses. Inhibitory receptors, on the other hand, allow the influx of negatively charged ions, hence reducing the target neuron activity by stabilizing, or hyperpolarizing the resting membrane potential and eventually making it more arduous for the target cell to generate an action potential (Bear et al., 2020).

According to a quantitative tool developed by Herculano and Lent (Herculano-Houzel & Lent, 2005), an adult human brain on average contains 86 billion neuronal cells which are interlinked by trillions of synaptic circuits. Through these circuits an individual neuron can target an adjacent single neuronal cell as well as numerous other distantly located neurons. Depending on the development stage, neurons can be targeted predominantly by excitatory synapses at one stage and further by inhibitory synapses at another stage (Bear et al., 2020). To comprehend the neuronal function, it is essential to

decrypt the regulatory mechanisms of these synapses. This thesis aims to gain new molecular insights into the function of inhibitory synapses and hence the subsequent introductory section will focus on inhibitory synapses.

1.1. Inhibitory Synaptic Neurotransmission

The synaptic inhibition in the central nervous system is predominantly initiated by the neurotransmitters glycine, and γ -aminobutyric acid (GABA). The inhibitory activity of glycine and GABA molecules are mediated by the cognate glycine receptors (GlyRs) and the GABA receptors belonging to subtype-A (GABA_ARs), respectively (Fig 1.2 A-B). Both GABA_ARs and the GlyRs belong to the Cys-loop superfamily of receptors which possess a characteristic pentameric structure and act as a ligand-gated ion channels (Fig 1.2 A-B) (Jaiteh et al., 2016). The Cys-loop superfamily furthermore is comprised of the serotonin receptor (5-HT), nicotinic acetylcholine receptor (nAChR), and the zinc-activated receptor (Olsen & Sieghart, 2009). GlyRs consist of two different subunit types (α and β) with five different (four α and one β) subunit classes in total. Compared to the GlyRs, GABA_ARs are more diverse consisting a of combinations of subunit families $\alpha(1-6)$, $\beta(1-3)$, $\gamma(1-3)$, δ , ϵ , θ , π and ρ (Rudolph & Möhler, 2006), hence tallying to numerous distinct classes of subunit. Irrespective of GABA_AR α -subunits being highly homologous, they are known to be specifically localized, with GABA_ARs containing the $\alpha 1$ subunit being enriched at dendritic and somatic synapses, whereas $\alpha 2$ -subunit containing receptors are localized to synapses on the axon initial segment (Klausberger et al., 2002; Nusser et al., 1996; Nyíri et al., 2001). In contrast to GlyRs (Fig. 1.2 B, E), which can form functional homo-pentameric receptors, functional GABA_ARs are hetero-pentamers, which predominantly comprise two α , two β and one γ -subunit (Sigel & Steinmann, 2012; Tyagarajan & Fritschy, 2014).

1.2. Receptor Architecture

Structural studies of GABA_ARs (Kim & Hibbs, 2021; Novello et al., 2022; Zhu et al., 2018) and GlyRs (Du et al., 2015; Kumar et al., 2020; Yu et al., 2021) have revealed that both receptors share a similar architecture (Fig. 1.2 A-B), consisting of an extracellular domain predominantly consisting of β -strands, four transmembrane α -helices and two

intracellular highly unstructured loop regions, which connect the transmembrane

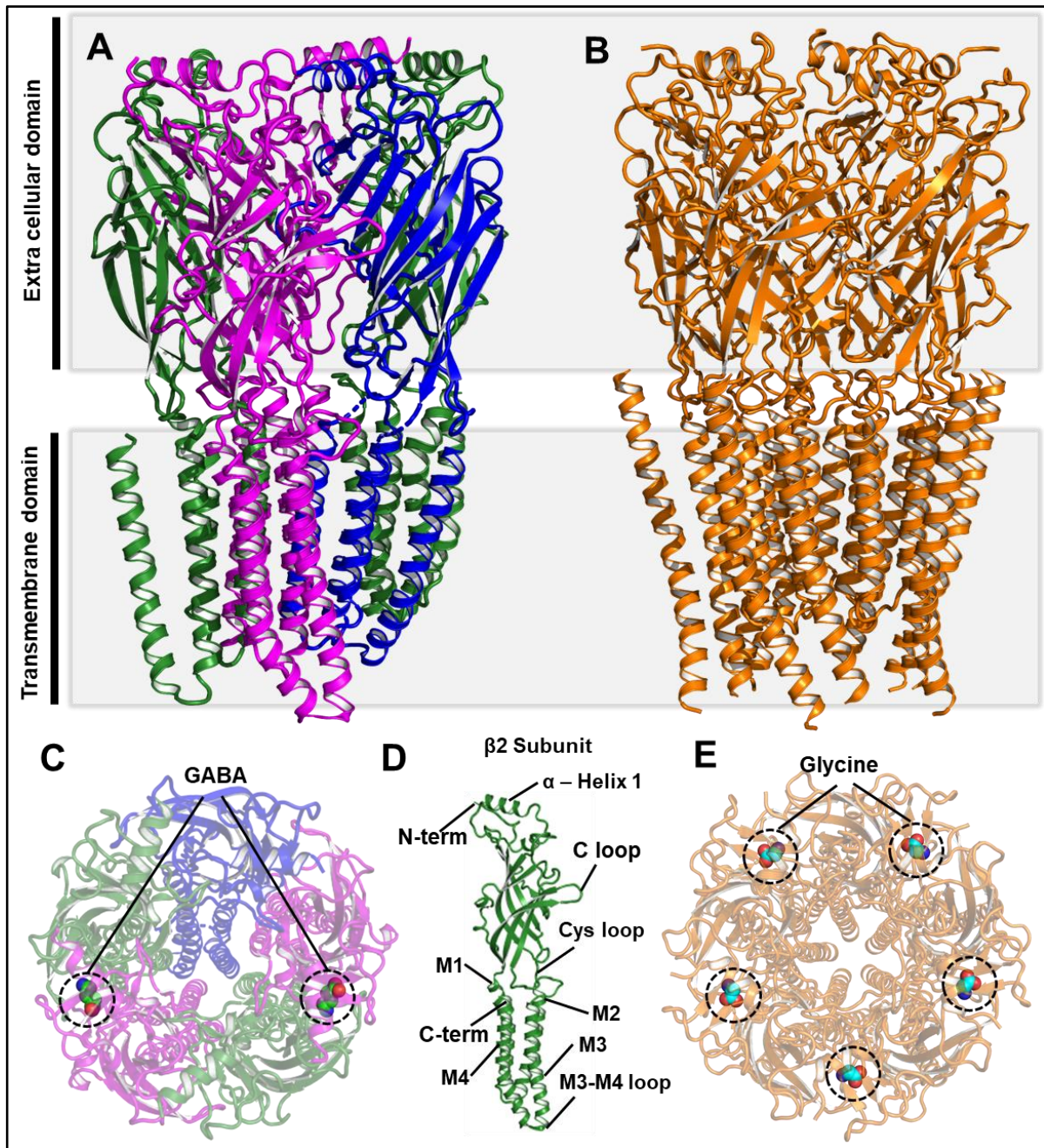


Figure 1.2. Structures of representative GABA_A and glycine receptors. (A) Cartoon depicting the tertiary structure of a GABA_AR (PDB entry 6D6U). Individual $\alpha 1$, $\beta 2$, and $\gamma 2$ subunits are represented in magenta, green and blue, respectively. (B) Cartoon representation of the homopentameric $\alpha 1$ glycine receptor (PDB entry 6UBT). Individual subunits are shown in orange. (C) Top view of the GABA_A receptor in complex with GABA (represented in spheres) molecules bound to the extra cellular domain. (D) Structure of a single $\beta 2$ -subunit of the GABA_A receptor highlighting individual loops. (E) A view of glycine receptor (PDB entry 6UBT) from the extracellular side of the receptor. Bound glycine molecules are depicted in sphere representation.

helices. GABA_ARs are the targets of a remarkably diverse range of drugs. These include the benzodiazepines (Sternbach, 1979), allosteric modulators of GABA_A receptors that are widely used in the treatment of epilepsy, insomnia and anxiety (Sieghart, 2006, 2015; Sigel & Buhr, 1997; Sigel & Steinmann, 2012). In addition to benzodiazepines, other drugs targeting GABA_ARs include barbiturates and neurosteroids, which are pharmacologically well described (Sieghart, 2006; Uusi-Oukari & Korpi, 2010). They act on distinct sites on the GABA_ARs eventually leading to membrane anion (Cl⁻ and bicarbonate) conductance increase thereby inducing hyperpolarization (Vashchinkina et al., 2014). GABA_ARs sensitive to benzodiazepine mainly encompasses α 1-3, and/or α 5 subunits and prevalently located at synaptic sites (Olsen & Sieghart, 2009). However, α 4 or α 6 subunit-containing GABA_ARs are sensitive to neurosteroids, GABA-mimicking drugs such as muscimol and THIP (gaboxadol; 4,5,6,7-tetrahydroisoxazolol[4,5-c] pyridine-3-ol), general anesthetics such as isoflurane and etomidate and often found to be positioned at peri- or extrasynaptic sites (Alexander et al., 2013; Olsen & Sieghart, 2009)

Subtypes of GABA_ARs, mainly containing the α 1-3 subunit along with the γ 2-subunit, have been found to localize post-synaptically with gephyrin, the main scaffolding protein (Kasaragod & Schindelin, 2018; Tretter et al., 2012; Tyagarajan & Fritschy, 2014) of inhibitory glycinergic and GABAergic postsynapses. In contrast, extra-synaptic GABA_ARs, primarily composed of α 4-5 and δ -subunits, do not co-localize with gephyrin

1.3. Gephyrin

The central scaffolding protein at inhibitory postsynapses, gephyrin, derives its name from the Greek word, γέφυρα, which means bridge. It was initially discovered as a neuronal factor which concurrently binds to GlyRs along with tubulin at postsynaptic specializations, and hence was named gephyrin (Groeneweg et al., 2018; Kasaragod & Schindelin, 2018; Kirsch et al., 1991; Prior et al., 1992; Tretter et al., 2012). Later (Essrich et al., 1998), gephyrin was also found to be actively involved in the clustering of GABA_ARs. Moreover, acting as a moonlighting protein, gephyrin is well known to catalyze the final steps during molybdenum cofactor (Moco) biosynthesis (Copley, 2003; Schwarz et al., 2001). In rodents, the two independent functions of gephyrin were reported to be vital (Feng et al., 1998). Moco deficiency in mice results in compromised activity of Moco-dependent enzymes (Reiss & Hahnewald, 2011), subsequently leading to acute neurodegeneration resulting in premature death on postnatal days 1 to 11 (Lee et al., 2002). In contrast, gephyrin knock-out mice suffer from symptoms like hyperexcitability that are attributed to both, defects in neurotransmission at inhibitory synapses and Moco biosynthesis, eventually leading to death within the first few hours of birth (Feng et al., 1998). Moreover, alteration of gephyrin-mediated neurotransmission has been associated in serious disorders, including Alzheimer's disease, autism, schizophrenia, epilepsy, and hyperekplexia (Agarwal et al., 2008; Dejanovic, Lal, et al., 2014; Fang et al., 2011; Fritschy et al., 2008).

1.3.1. Gephyrin domain architecture

The gephyrin gene exhibits a complex intron-exon structure and subjected to extensive alternative splicing in tissue-specific manner (Dos Reis et al., 2022; Fritschy et al., 2008; Groeneweg et al., 2018; Tyagarajan & Fritschy, 2014). A recent proteomic analysis of gephyrin (Dos Reis et al., 2022) demonstrated that gephyrin is subjected to extensive alternative splicing involving its 40 exons with the splice variants displaying different functions. All gephyrin variants feature N and C-terminally positioned, structured domains, known as G-domain (GephG) and E-domain (GephE), respectively (Fig.1.3A). These terminally located domains are connected by a long unstructured linker (alternatively called C-domain) of ~150 amino acids depending on the splice variant (Fig.1.3A) (Kirsch et al., 1991; Sander et al., 2013). This flexible linker harbors numerous

sites for post-translational modifications (discussed extensively in the subsequent subtopic) including phosphorylation (Herweg & Schwarz, 2012; Kuhse et al., 2012; Kuper et al., 2004; Langosch et al., 1992; Tyagarajan et al., 2013; Tyagarajan, Ghosh, Yévenes, et al., 2011; Zhou et al., 2021), palmitoylation (Dejanovic, Lal, et al., 2014), acetylation (Tyagarajan et al., 2013), SUMOylation (Ghosh et al., 2016), and nitrosylation (Dejanovic & Schwarz, 2014).

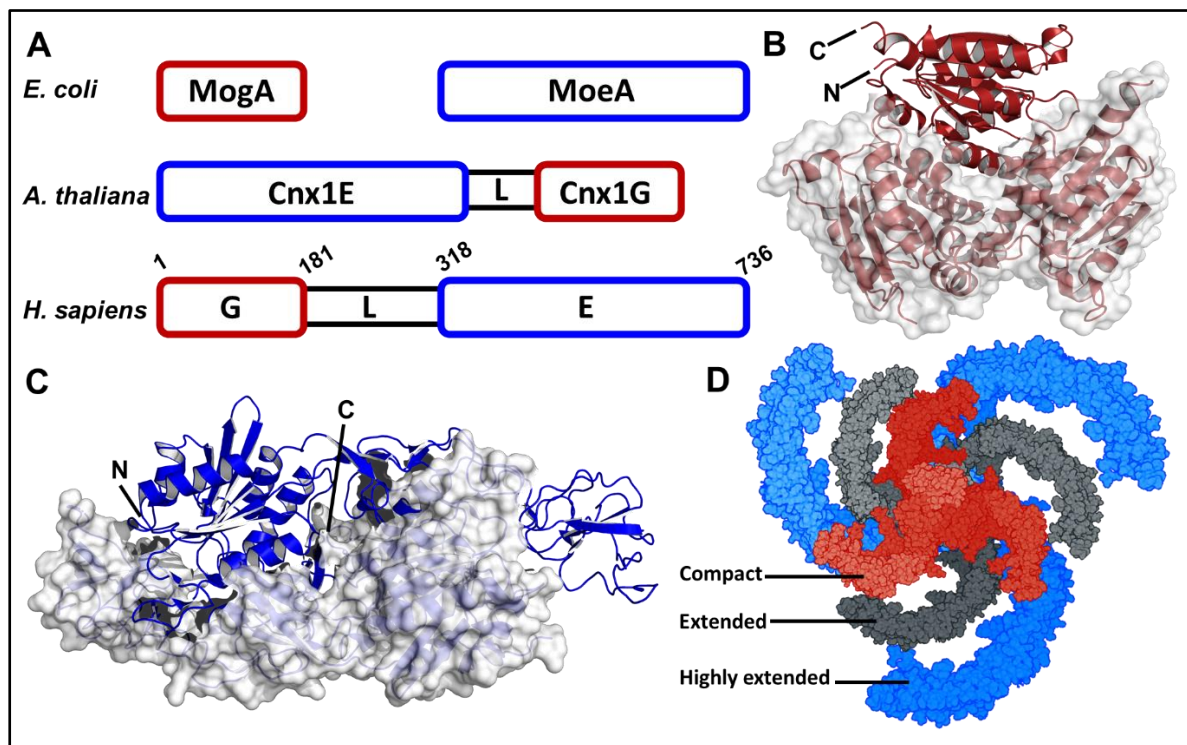


Figure 1.3. Structure of gephyrin. (A) Architecture of the individual structured orthologous domains in bacteria (*E. coli*), plants (*A. thaliana*) and mammals (*H. sapiens*). The bacterial orthologs of GephG and GephE, MogA and MoeA, respectively, are separate entities, whereas in plant the terminal domains are fused in inverted directionality and connected by a short linker. In isolation, GephG and its orthologues, MogA and Cnx1G form stable trimers, whereas isolated GephE and its corresponding orthologues, MoeA and Cnx1E, dimerize. (B) Crystal structure of the GephG trimer (PDB entry 1JLJ) showing one of the monomeric subunits in cartoon representation while the two others are displayed in surface representation (C) GephE dimer crystal structure (PDB entry 5ERQ) with one monomeric subunit in cartoon representation (blue) and the other subunit depicted in surface representation in light gray. (D) Schematic representation of the models of full-length gephyrin derived from SAXS studies (Sander et al., 2013). The compact state of the protein is represented in red, the moderately extended state in gray and the fully extended state in light blue.

Although a full-length structure of gephyrin is still lacking, previous structural studies with the isolated terminal domains showed that the G domain forms trimer, (Fig. 1.3B)

(Schwarz et al., 2001) the E domain dimerizes (Fig. 1.3C) (Kim et al., 2006) in solution. Structural studies employing small angle X ray scattering (SAXS) and atomic force microscopy (AFM) revealed that full-length gephyrin predominantly exists in a trimeric state, however, it is conformationally heterogeneous with a mixture of compact and extended forms (Fig. 1.3D) (Sander et al., 2013). Considering the oligomeric state of the G- and E-domains, a hexagonal gephyrin lattice model has been proposed (Xiang et al., 2001) and regarded as a popular framework for gephyrin-mediated molecular organizations at inhibitory synapses (Alvarez, 2017; Tyagarajan & Fritschy, 2014). However, the hexagonal lattice structure model has not been observed for gephyrin *in vitro* or in synapses. This might be probably because of the flexible C-domain which prevents gephyrin from forming a highly regular lattice structure (Sander et al., 2013).

1.3.2. Gephyrin orthologs

Gephyrin, being highly conserved protein, several gephyrin orthologs have been reported in numerous organisms where they primarily operate in Moco biosynthesis but also as neurotransmitter receptor scaffolding proteins. In mammals, the homologs are involved in both moonlighting functions, while in other organisms such as prokaryotes and plants, their counterparts are solely responsible for Moco biosynthesis. The prokaryotic equivalents of the GephG and GephE, called MogA (Liu et al., 2000) and MoeA (Fig. 1,3A) (Xiang et al., 2001), respectively, exist as separate enzymes and catalyze the terminal steps of Moco biosynthesis (Feng et al., 1998; Mendel, 2013; Stallmeyer et al., 1999). In addition to its prokaryotic counterparts, gephyrin homologs in the fungal kingdom, e.g. *Neurospora* and *Chaetomeum*, are principally involved in Moco biosynthesis. Intriguingly, over the course of time, an independent fusion of MogA and MoeA occurred twice during evolution. While this genetic fusion in mammals resulted in a linear arrangement with the G domain at the N-terminus followed by the E domain, in plants, the domain order is reversed (Fig1.3A) with Cnx1E (corresponding to the E domain) located N-terminal of Cnx1G (G-domain homolog). Cnx1 in plants is exclusively responsible for the catalysis of the final steps of Moco biosynthesis. However, the gephyrin orthologue in invertebrates like *Drosophila*, Cinnamon (Cnm), has been found not only to be responsible for Moco biosynthesis but has also been predicted to be involved in GABA_ARs clustering at postsynaptic sites (Kamdar et al., 1994; Wittle et al., 1999). Although the domain order in

Cnm and gephyrin is identical, the terminal domains in Cnm are connected by a much shorter linker. Compared to evolutionarily simpler orthologs, gephyrin in the mammalian system undergoes extensive alternative splicing, numerous post-translational modifications, and is involved in the clustering of both major classes of neurotransmitter receptors at inhibitory synapses, hence adding further complexity to the underlying functions during Moco biosynthesis and as a scaffolding factor (Tyagarajan & Fritschy, 2014).

1.3.3. Gephyrin post-translational modifications

Recent studies demonstrate that mammalian gephyrin undergoes extensive post-translational modifications and the list of residues undergoing PTM (Fig. 1.4) includes phosphorylation (Flores et al., 2015; Herweg & Schwarz, 2012; Langosch et al., 1992; Tyagarajan, Ghosh, Yévenes, et al., 2011), palmitoylation (Dejanovic, Semtner, et al., 2014), acetylation, SUMOylation (Ghosh et al., 2016), and nitrosylation (Dejanovic & Schwarz, 2014). The mapped sites for PTMs predominantly encompass the linker region of the protein (Fig. 1.4), indicating that the PTMs might play a critical role in modulating the protein's tertiary architecture, which presumably affect its scaffolding property, localization at inhibitory postsynaptic sites its trafficking and half-life, and certainly its ability to interact with partner proteins as well as in downstream signaling pathways.

Gephyrin phosphorylation was found to mostly result in an upregulation of gephyrin clustering, hence altering the strength of GABAergic transmission (Flores et al., 2015; Herweg & Schwarz, 2012; Huttlin et al., 2010). In addition to gephyrin phosphorylation, palmitoylation and acetylation of the protein were also reported (Kang et al., 2008; Tyagarajan et al., 2013). Gephyrin palmitoylation of Cys212 and Cys284 were shown to upregulate gephyrin clustering and potentiate GABAergic neurotransmission. In addition to membrane anchoring, gephyrin palmitoylation might be essential for its functional properties further indicating that gephyrin palmitoylation, along with either up or downstream phosphorylation, might play a crucial role in gephyrin anchoring at postsynaptic sites and hence further assist in the recruitment of GABAergic synapse-specific neuronal factors.

Contrary to other linker-associated PTMs, S-nitrosylation in gephyrin was mapped to the E-domain, where the neuron-specific nitric oxide synthase overexpression led to a

reduced gephyrin cluster size in primary hippocampal neurons (Dejanovic & Schwarz, 2014). Additionally, gephyrin acetylation at Lys666, located also in the E-domain, and the phosphorylation associated serine/threonine residues in the linker (Schwer et al., 2009; Tyagarajan et al., 2013) implies that acetylation might play an important role in the synaptic function of gephyrin. SUMOylation of GephG on Lys148 and of GephE on Lys724 were speculated to act upstream of the phosphorylation of Ser268 and the acetylation of Lys666. Overall, previous studies on gephyrin PTMs clearly indicate their vital role in modulating protein activity.

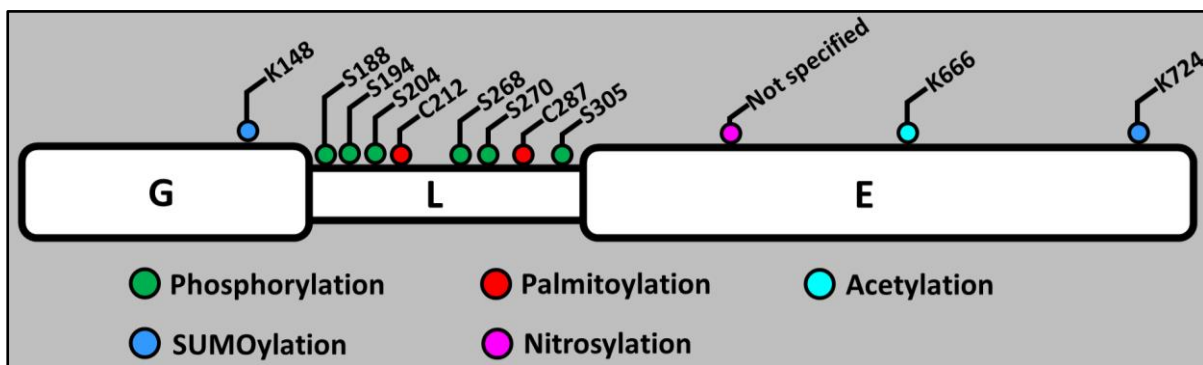


Figure 1.4. Schematic description of the post-translational modifications in gephyrin. Diagram depicting residues reported to undergo post-translational modifications (PTMs). Residues undergoing PTMs are colored according to the represented scheme and PTM sites are indicated by respective residue number.

1.3.4. Gephyrin-mediated receptor clustering

Glycine and GABA_A receptors are highly enriched at postsynaptic sites and specifically recruited opposed to cognate glycinergic and GABAergic nerve endings, respectively, via the direct assistance of gephyrin (Kirsch et al., 1993; Kneussel & Betz, 2000; Prior et al., 1992). Both, GlyRs and GABA_ARs share a close evolutionary relationship, as observed in their respective primary sequences and tertiary architectures (Fig. 1.2A) (Mülhardt et al., 1994). Moreover, on the presynaptic side, the neurotransmitters glycine and GABA share the identical transporter, the vesicular inhibitory amino acid transporter (Dumoulin et al., 2000; Lévi et al., 1999). Gephyrin-mediated GABA_AR and GlyR clustering has been well studied and the molecular bases of these interactions has been explored at atomic resolution (Kim et al., 2006; Maric, Kasaragod, Hausrat, et al., 2014; Maric, Kasaragod, & Schindelin, 2014; Sola et al., 2004). The C-terminally located E-domain of gephyrin is the prime section responsible for direct interactions with GABA_ARs and GlyRs, thereby

anchoring them to the postsynaptic membrane. Previous structural and biochemical findings revealed that the large intracellular loop of the GlyR β -subunit, located in between transmembrane α -helices 3 and 4, interacts with gephyrin (Kim et al., 2006; Sola et al., 2004). Moreover, a biophysical characterization of the gephyrin-GABA_AR interaction demonstrated that both the GlyR and the GABA_AR, interact with gephyrin through overlapping, yet distinct receptor binding sites (Maric et al., 2011). Biochemical characterizations for the interaction between gephyrin and the GlyR TM3-4 β -loop or shorter peptide derivatives indicated a strong affinity with dissociation constants varying between the high nanomolar to low micromolar range (Kim et al., 2006; Maric et al., 2015; Maric, Kasaragod, Hausrat, et al., 2014; Maric, Kasaragod, & Schindelin, 2014; Schrader et al., 2004; Tretter et al., 2012). In contrast, gephyrin interact with the unstructured TM3 - TM4 loops of GABA_ARs with a reduced affinity (Kasaragod & Schindelin, 2018; Maric et al., 2015; Maric, Kasaragod, Hausrat, et al., 2014; Mukherjee et al., 2011; Tretter et al., 2012). However, considering the oligomeric nature of the receptors, comprised of at least two gephyrin-binding subunits along with the oligomeric state of gephyrin, this more moderate affinity might be enhanced by avidity effects. Furthermore, gephyrin at postsynaptic sites is also known to interact with multiple neuronal factors including the cell adhesion molecule neuroligin 2 (NL2), the actin-binding protein profilin, the brain-specific guanine nucleotide exchange factor (GEF) collybistin, thus suggesting that gephyrin clearly is not just a simple scaffolding protein (Groeneweg et al., 2018; Tyagarajan & Fritschy, 2014).

1.4. Collybistin

Collybistin (CB) derives its name from the Greek word, κολλυ-βιστομαι, which roughly translates as “to exchange”. CB belongs to the diffuse B-cell lymphoma (dbl) superfamily of GEFs and is prevalently expressed in the brain and its gene is encoded on the human X chromosome. A yeast two-hybrid screen with gephyrin initially identified two CB splice variants (termed CB1 and CB2) as a novel gephyrin-binding partner (Kins et al., 2000) and was shown to selectively localize with gephyrin at the GABAergic and glycinergic postsynapses (Chiou et al., 2011; Patrizi et al., 2012). The CB mRNA undergoes alternative splicing, leading to the generation of multiple splice variants across different organisms. Murine CB is expressed as three splice variants (termed as CB1, CB2 and CB3) with

divergent primary sequences at the C-terminus. In terms of expression, CB variants also exhibit differential expression pattern with CB1 being significantly expressed only in the early stage of postnatal neuronal maturation (de Groot et al., 2017). In contrast, the other two isoforms (CB2 and CB3) are prominently expressed in adult neurons. The human CB ortholog, also referred to as hPEM-2 (human homolog of posterior end mark-2), is closely related to the murein CB3 isoform and occurs as two mRNA species which vary in the presence or absence of the N-terminal region (discussed below in detail).

1.4.1. Structure of CB

CB harbors a signature dbl homology (DH) domain and pleckstrin homology (PH) domain tandem, common to all members of the Dbl family of GEFs, which are connected by a short linker (Fig. 1.5A). The DH-domain mediates the catalytic nucleotide exchange activity by replenishing the GTP-bound (active) state of small Rho-like GTPase from its GDP-bound (inactive) state. The PH domain regulates the attachment of GEFs to membranes by binding to phosphoinositides (Hyvönen et al., 1995). The PH-domain of CB has been shown to preferentially interact with phosphatidylinositol-3-phosphate (PI3P) (Chiou et al., 2019; Kalscheuer et al., 2009; Papadopoulos et al., 2017; Papadopoulos et al., 2015). A majority of the murein and human CB variants feature an additional N-terminally located src-homology 3 (SH3) domain (Fig 1.5A). The SH3-domain of CB is believed to have a regulatory function, hence influencing the protein activity.

Previous structural studies with the full-length CB2 variant (CB2_{SH3+}) demonstrated that the protein adopts a closed conformation, where the SH3 domain primarily engages in intramolecular interaction with the tandem DH and PH domain (Fig. 1.5B). The overall tertiary structure of CB_{SH3+} is remarkably similar to the closely related GEF, Asef (Fig.1.5C), which displays a high sequence identity with the CB (Mitin et al., 2007). The relative orientations of the DH and PH domains in the full-length CB (CB_{SH3+}) differ significantly when compared with the CB1_{SH3-} and the CB2_{SH3-} variant of CB in complex with Cdc42 (Soykan et al., 2014; Xiang et al., 2006).

1.4.2. CB intramolecular interactions and autoinhibition relief

Previous structural and biochemical studies with Asef demonstrated that Trp203, Arg249, and Glu436 located in the interface between the SH3 domain and the DH-PH

tandem are crucial for the inter-domain association (Mitin et al., 2007). This inter-domain association is primarily responsible for the Asef autoinhibition. The residues Trp203, Arg249, and Glu436 in Asef are identical in CB and correspond to Trp24, Arg70, and

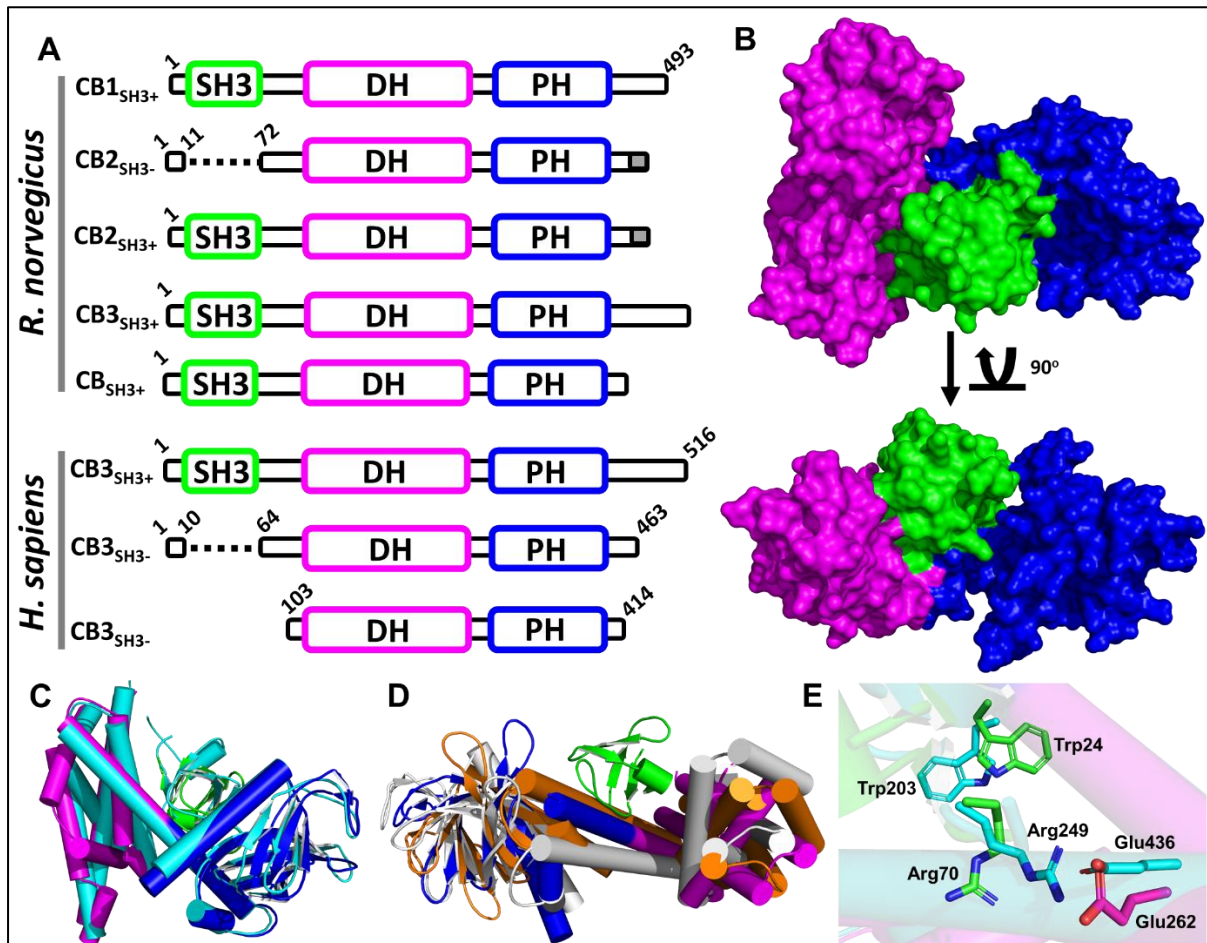


Figure 1.5. Domain arrangement and tertiary architecture of CB. (A) Domain architecture of CB isoforms from rat and human. Truncated sequences at the N-terminus and variable C-terminal sequences in the isoforms are indicated. (B) Surface representation of the crystal structure of CB_{SH3+} (PDB entry 4mt6) in two different orientations differing by a 90° rotation around the horizontal axis (indicated by the arrow). The SH3 domain lies in close proximity with the tandem DH and PH domains. Individual domains are color coded as indicated in (A). (C) Cartoon representation of the CB_{SH3+} (PDB entry 4mt6; color coded as in (A)) superimposed onto the closely related GEF Asef (PDB entry 2pz1; cyan), highlighting the similarities in overall architecture. (D) Comparison of various conformational state of CB. CB_{SH3+} (colored as in (A)), in its closed state is superimposed onto the open conformations of $CB2_{SH3-}$, as observed in the Cdc42- $CB2_{SH3-}$ complex (PDB entry 2atx; gray) and of $CB1_{SH3-}$ (orange). (E) Interface regions between the SH3 domain and the DH-PH tandem domain of CB_{SH3+} and Asef. The intermolecular interaction between the SH3 domain and the DH-PH tandem is primarily mediated by Trp24, Arg70 in the SH3 domain and Glu262 in the DH domain of CB. Trp24, Arg70 and Glu262 in CB_{SH3+} correspond to Trp203, Arg249 and Glu436 in Asef. Interface residues in CB and Asef are shown in stick representation and are color coded as in (C).

Glu262, respectively (Fig.1.5E). This sequence conservation suggested a similar mode of interaction (Soykan et al., 2014). To assess the role of these residues in CB autoinhibition, Soykan and colleagues (Soykan et al., 2014) introduced Ala substitution at Glu262 (E262A), and along with a replacement of Trp24 with Ala (W24A/E262A).

The conformational transition of CB in solution was analyzed by small angle X-ray scattering (SAXS). The pair distance distribution function of CBSH3+ and CBSH3+/E262A variant suggested a compact state for the wild-type whereas the E262A variant attained a more extended conformation. Additionally, assessment of flexibility for the E262A variant indicated that a pronounced heterogeneity of conformations is present in solution, featuring a mixture of compact, intermediate, and elongated conformations.

Additionally, studies (Soykan et al., 2014) using single molecule atomic force microscopy (AFM) corroborated the SAXS findings, indicating an equilibrium between three conformational (compact, intermediate, and elongated) states for the wild-type and E262A variant. The relative frequencies of the three conformations, however, varied considerably, with a substantially larger percentage of intermediate and more elongated conformation for the CBSH3+/E262A variant compared to the wild-type CB. The corresponding double mutant variant of CB (CBSH3+ W24A/E262A) could not be analyzed by either SAXS or AFM, presumably due to a pronounced tendency to aggregate and or degrade. Hence, a structural analysis of this variant is still lacking (Soykan et al., 2014).

1.4.3. CB role in inhibitory postsynapse organization

This subsection summarizes the structure and function of CB with an emphasis on the role of the individual domains in signaling pathways and inhibitory postsynapse organization.

1.4.3a. SH3 domain

Proteins belonging to the Src-family, for example myosin, cortactin, amphiphysin and spectrin, carry small modules composed of approximately 60 amino acids called Src homology 3 (SH3) domains. SH3 domains are ubiquitously present across all life forms ranging from viruses to the eukaryotes and have been long known to be involved in the regulation of important cellular pathways such as cell proliferation, migration and

cytoskeletal modifications (Bilwes et al., 1999; Falzone et al., 1994; Gmeiner & Horita, 2001; Kaneko et al., 2008; Whisstock & Lesk, 1999). Structural studies of the SH3 domain in isolation and in complex with ligands have been extensively carried out by crystallography and NMR. The canonical SH3 domain architecture (Fig. 1.6A) comprises five to eight β -strands arranged into two antiparallel β -sheets or in a β -barrel structure, connected by the RT, Src and distal loops (Kaneko et al., 2008). SH3 domains have been identified as protein modules that recognize proline-rich sequences and the canonical binding site is composed of the region between the RT and the Src loop (Kurochkina & Guha, 2013). In addition to its role as an adaptor during signal transduction, substrate recognition, and membrane localization, SH3 domains are involved in the regulation of enzymatic activity via conformational changes and the recruitment of substrates to cellular compartments (Gmeiner & Horita, 2001; Sriram et al., 2011).

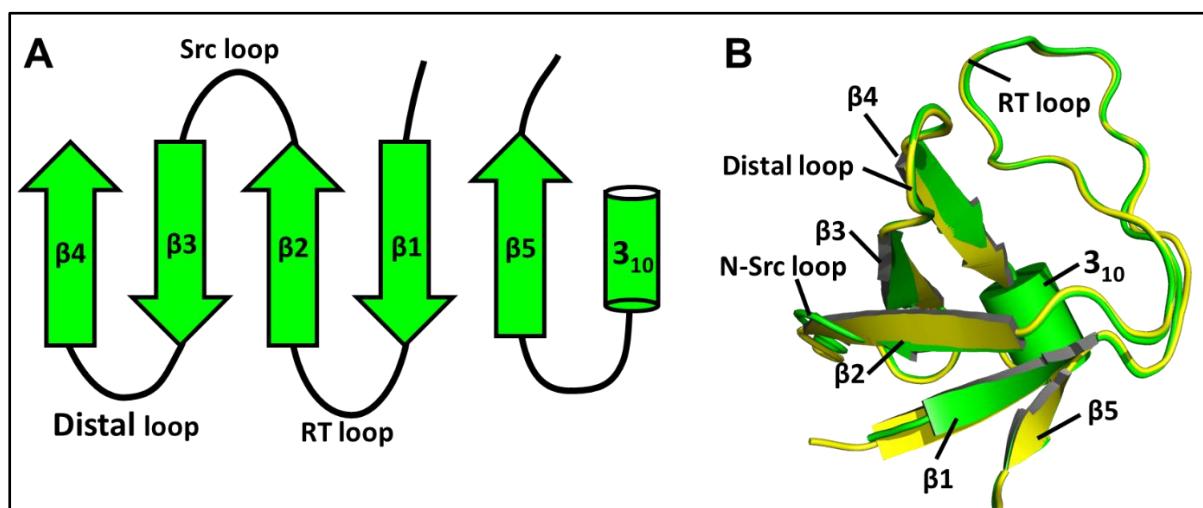


Figure 1.6. Structure of SH3 domain. (A) Topology of secondary structure elements constituting the SH3 domain. (B) Tertiary architecture of the SH3 domain from rat CB (PDB entry 4mt6; green) superimposed on the SH3 domain from human CB (PDB entry 2ysq; yellow) highlighting their secondary structure elements.

The regulatory SH3-domain in CB has long been speculated to function as an auto-inhibitory domain, hence rendering CB in a closed (or inactive with respect to neurotransmitter receptor recruitment) conformation. An initial study conducted by Harvey and colleagues (Harvey, 2004) revealed that the SH3 containing isoforms (CB2 and CB3) were predominantly expressed in postnatal rodent brain. Additionally, experiment with cortical neurons indicated that SH3-containing and SH3-lacking splice variants of CB similarly redistributed gephyrin into synaptic clusters (Harvey, 2004),

further suggesting that SH3-containing isoforms of CB might be activated locally at postsynaptic sites by an SH3-interacting neuronal factor. In line with this hypothesis, later studies confirmed that NL2 and the $\alpha 2$ subunit of the GABA_AR interact with the SH3-domain of CB and induce CB-dependent gephyrin clustering by relieving SH3-mediated auto-inhibition (Poulopoulos et al., 2009; Saiepour et al., 2010; Soykan et al., 2014). These developments led to the prevalent model that NL2 creates nucleation sites for gephyrin deposition and subsequent inhibitory receptor clustering by activating CB through a mechanism involving NL2–CB and NL2–gephyrin interactions (Poulopoulos et al., 2009). Although structural details of the NL2-CB interaction are lacking, previous studies led to the hypothesis that the cytosolic C-terminus of NL2 binds to the SH3 domain of CB. The NL2 C-terminus harbors a proline rich motif, suggesting that NL2 and CB association potentially involves a canonical (PxxP) motif (Soykan et al., 2014). A recent study by Hines and colleagues (Hines et al., 2018) revealed that the GABA_AR- $\alpha 2$ -subunit interaction with the SH3 domain of CB involves the long unstructured loop connecting the M3-M4 helices characterized by an affinity in the low micromolar range. Despite this moderately high affinity, the interacting $\alpha 2$ -subunit region is devoid of a canonical PxxP motif as observed in NL2, indicating a novel mode of interaction. Although previous studies clearly demonstrated interactions between the SH3 binding partners, a molecular understanding of how the SH3 mediates conformational activation is still lacking.

1.4.3b. DH Domain

Initially isolated in 1985, Dbl, the first mammalian GEF was found to be composed of approximately 180 amino acids (Eva & Aaronson, 1985). The isolated protein showed significant sequence similarity to CDC24, a protein reported as an upstream activator of CDC42 in yeast (Bender & Pringle, 1989; Ron et al., 1991). Later, Dbl was demonstrated to catalyze nucleotide exchange on human Cdc42 *in vitro* (Hart et al., 1991), and consecutively, the conserved domain in Dbl and CDC24, now known as the DH (Dbl homology) domain, was found to be necessary for the GEF activity (Hart et al., 1994). Since then, many proteins harboring a DH domain (Fig. 1.7A) have been isolated and characterized. The DH domain is a highly efficient catalytic machine (Rossman et al., 2005) that is able to accelerate the nucleotide exchange of Rho proteins by as much as a factor of 10^7 . Until now, 74 Dbl proteins have been identified in humans (Jaiswal et al.,

2013), which can be classified into different subfamilies: 46 Dbl proteins are monospecific for RHO-, RAC-, and CDC42-selective proteins, five are bispecific for RHO- and CDC42-selective proteins, and six are oligospecific for all three Rho protein subgroups. In addition to humans, around 23 Dbl proteins have been reported in *D. melanogaster*, roughly 18 of these GEFs in *C. elegans* and 6 in *S. cerevisiae* (Venter et al., 2001). Contrary to animals and yeast, surprisingly, there appear to be no DH-containing proteins in plants (Schultz et al., 1998; The Arabidopsis Genome, 2000).

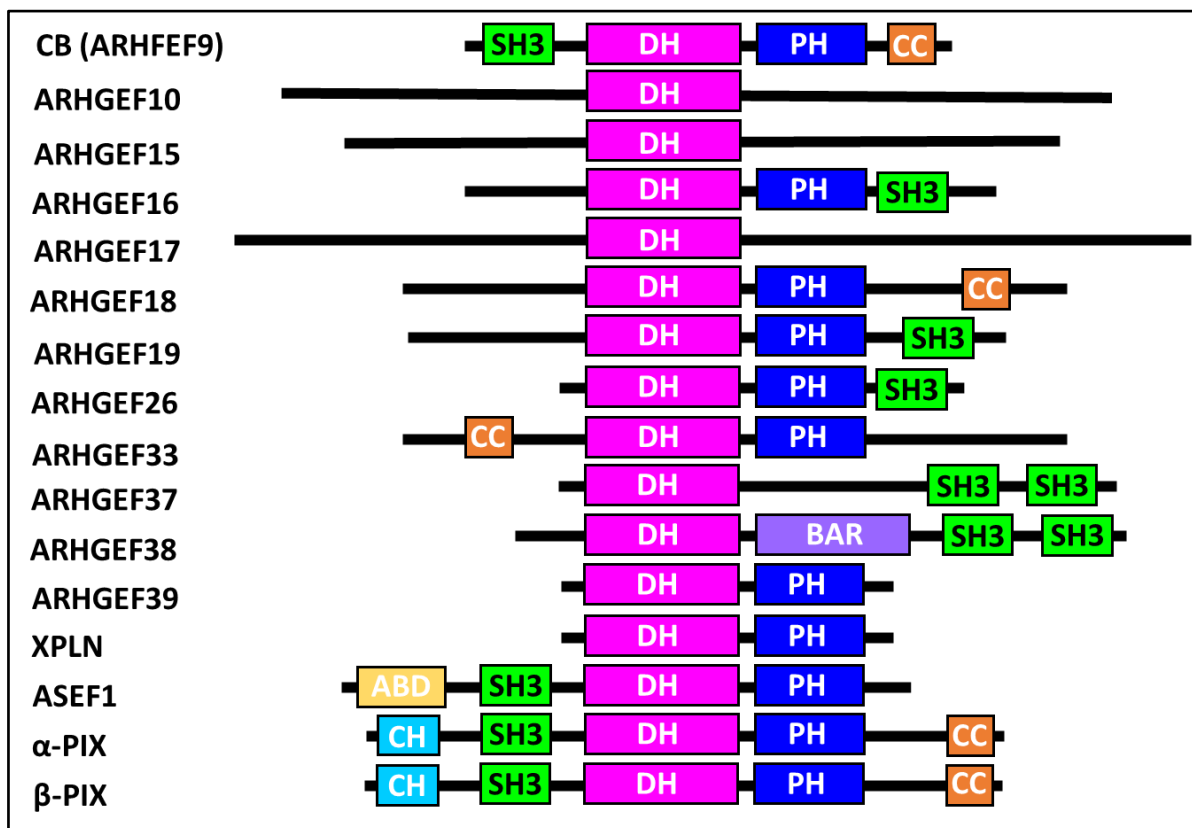


Figure 1.7. Domain architecture of Dbl family proteins. The Dbl superfamily RhoGEFs are mostly multi-domain proteins and feature several additional functional domains that mediate cross talk between Rho proteins and other signaling pathways. DH domains are almost always followed by C-terminally located PH domain, while only a few Dbl proteins lack tandem PH domains. The PH domain (blue) is involved in membrane tethering. Other functional modules, CH (Calponin homology; light blue), SH3 (src-homology 3; green), ABD (APC-binding domain; yellow) are involved in protein-protein interactions.

Structural analyses of Dbl GEFs revealed a highly conserved three-dimensional architecture for the DH domain which is primarily composed of an 11 α -helical bundle. Despite their highly conserved structure, DH domains share little homology with each

other, and GEFs with the same substrate specificity often harbor <20% sequence identity (Aghazadeh et al., 1998; Liu et al., 1998; Soisson et al., 1998; WorthyLake et al., 2000). Based on comparatively higher sequence similarity, three conserved regions (CR1, CR2, and CR3), each composed of 10-30 amino acids (Schmidt & Hall, 2002), have been assigned in the DH domain. Helices encompassing CR1 and CR3 are exposed on the surface of the DH domain and participate in the formation of the GTPase interaction pocket. The CR2 region, however, does not actively participate in interactions with the GTPase. GEFs initially bind to the GDP-bound form of the GTPase and subsequently destabilize the GDP-GTPase complex while stabilizing a nucleotide-free reaction intermediate (Cherfils & Chardin, 1999). Because of the high intracellular GTP to GDP ratio, the released GDP is replaced with GTP, leading to GTPase activation.

Previous biochemical studies on murine CB and its human ortholog, hPEM, with the three well characterized Rho-like GTPases (discussed extensively section 1.5), Cdc42, Rac1 and RhoA, demonstrated that CB is a Cdc42-specific GEF (Reid et al., 1999; Xiang et al., 2006). With Cdc42 being the sole GTPase to be activated by CB, it was previously believed that the CB interaction with Cdc42 might be crucial for gephyrin clustering at inhibitory postsynaptic sites (Kneussel & Betz, 2000). However, contrary to this belief, analyses of CB mutants (Reddy-Alla et al., 2010) deficient in catalyzing GDP/GTP exchange in Cdc42 and of Cdc42 conditional knock-out mice revealed that Cdc42 is not essential for inhibitory synapse formation. Moreover, the same study demonstrated that Cdc42 inactivation in the murine forebrain had no effect on gephyrin and GABA_ARs clustering in hippocampal neurons.

As mentioned above, Dbl-family proteins display varied selectivity towards Rho GTPases. This varied recognition is potentially because of non-conserved residues that reside within the GTPase interaction sites of the DH domains, hence determining their specific coupling (WorthyLake et al., 2000). The latter part of this thesis (Chapter 3) specifically highlights the differential recognition of Rho GTPases by CB.

1.4.3c. PH Domain

As outlined above, among the majority of Dbl family proteins, the catalytic DH domain is followed by a C-terminally located pleckstrin homology (PH) domain consisting of approximately 100-120 residues (Lenoir et al., 2015; Mosaddeghzadeh & Ahmadian,

2021). PH domains, which represent the 11th most common domain in the human proteome (Lemmon, 2007), were originally identified as modules of approximately 100 amino acids that share sequence similarity with two such regions in pleckstrin, a major substrate of protein kinase C in platelets. Initial studies of PH domains from pleckstrin (Yoon et al., 1994), along with concerted efforts to identify their interacting partners suggested that the PH domain can bind to the phosphoinositide, phosphatidylinositol 4,5-bisphosphate (PtdIns(4,5)P₂) (Harlan et al., 1994).

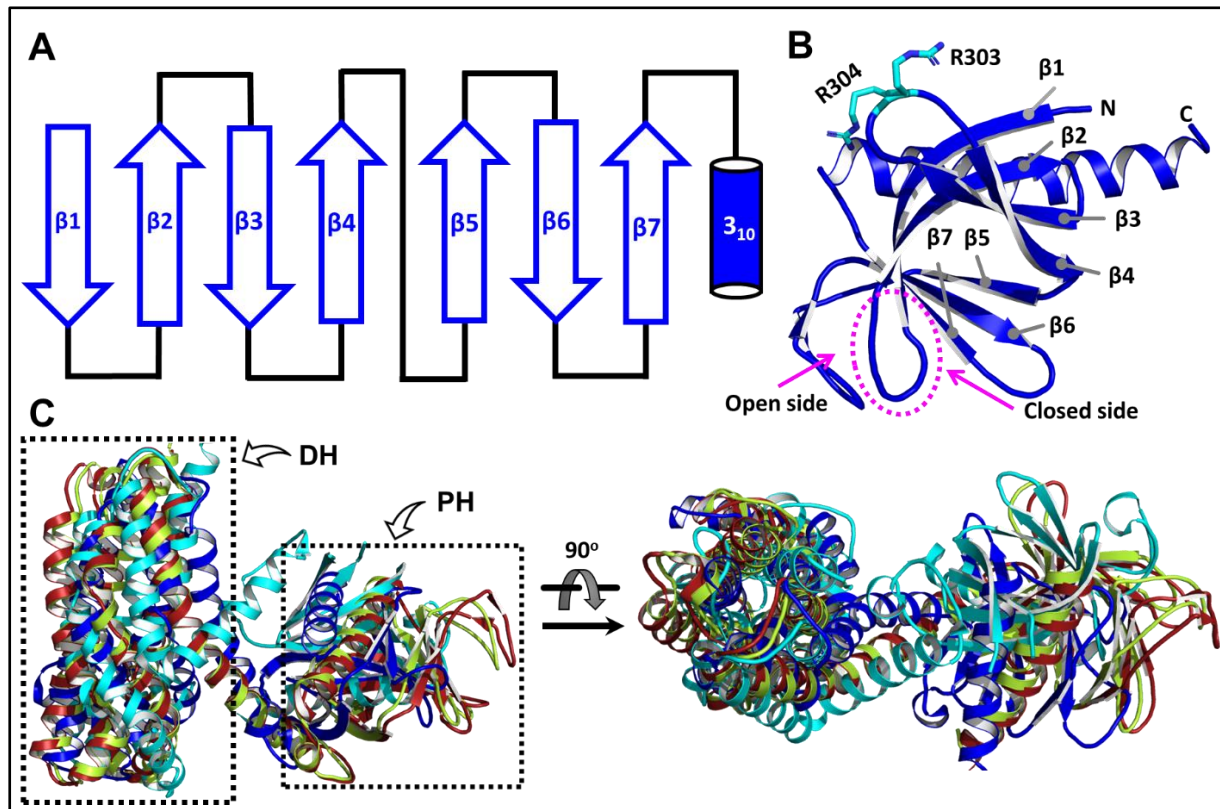


Figure 1.8. Structure of the PH domain. (A) The secondary structure elements of the PH domain fold are depicting the seven antiparallel β -strands and the C-terminal α -helix. (B) Tertiary architecture of the PH domain of CB (pdb entry 2atx). Secondary structure elements along with the PI3P interacting residues in the β 3- β 4 loop are indicated. Canonical binding site for lipids in the β 1- β 2 loop, as indicated by the MODA algorithm, along with the open/closed sides are indicated by the dotted ellipsoid and arrows, respectively. (C) Superimposition of the DH-PH tandem of Dbl family members, including CB (PDB entry 4mt6; red), Asef (PDB entry 2pz1; green), PI (3,4,5) P3-dependent Rac exchanger (PDB entry 7rx9; cyan) and Trio (PDB entry 1nty; blue), highlighting the similar tertiary architecture of the corresponding PH domain with respect to their DH domain. In all cases, the auto-inhibited form was used for the comparative analysis. The SH3 domain has been omitted for clarity.

Subsequent structural and biochemical studies with the PH domain of phospholipase-C presented a first molecular demonstration of specific phosphoinositide recognition by a PH domain (Garcia et al., 1995; Lemmon et al., 1995).

All members of the PH domain superfamily feature a conserved fold based on seven antiparallel β -strands arranged in a β -sandwich which is capped at its twisted corner by a C-terminally located solitary α -helix (Fig. 1.8A, B). Even though the PH domain sequence identity among the Dbl family members is less than 20%, the PH-domain containing Dbl proteins share a roughly similar three-dimensional architecture (Fig. 1.8C) (Lenoir et al., 2015; Mosaddeghzadeh & Ahmadian, 2021).

Membrane interactions studies using the MODA algorithm (Kufareva et al., 2014) initially specified the PH domain β 1- β 2 loop as the canonical binding site for lipids. Comparison of experimentally determined phosphoinositide binding modes (Lenoir et al., 2015), however, suggested another binding site which lies on the opposite side of the loop. The majority of the phosphoinositide interaction takes place via the “inner” or “closed” side of the loop, whereas, a few PH domains have been co-crystallized with inositol headgroups located at the “outer” or “open” side of the loop (Fig. 1.8B). Contrary to the canonical β 1- β 2 loop, the MODA algorithm suggested an alternate PIP binding site for CB (Lenoir et al., 2015), involving interactions with the DH-PH tandem in the autoinhibited state (Soykan et al., 2014). After relief of autoinhibition, the PH domain would interact with PIP and membranes using positively charged residues and a hydrophobic patch located at the tip of the β 3- β 4 loop (Kalscheuer et al., 2009; Soykan et al., 2014). In autoinhibited CB, the β 1- β 2 loop forms strong association with the long β 6- β 7 loop, thus preventing access to the canonical binding site (Lenoir et al., 2015; Soykan et al., 2014). Initial biochemical and cellular studies demonstrated that the PH domain of CB specifically interacts with phosphatidylinositol-3-phosphate (PI3P) (Kalscheuer et al., 2009). While PH-domain deletion in CB led to complete abolishment of its PI3P binding ability, the interaction of CB with gephyrin remained unaffected (Kalscheuer et al., 2009). Later Reddy-Alla and colleagues (Reddy-Alla et al., 2010) provided molecular evidence for PH domain interaction with PI3P, primarily mediated by the conserved arginine residues Arg303 (R303) and Arg304 (R304) located in the β 3- β 4 loop. Amino acid replacements of R303 and R304 with Asn in the CB2SH3+ variant (CB2SH3+RR303-304NN) led to complete abolishment of its ability to bind to PI3P (Kalscheuer et al., 2009).

These basic residues reside within the $\beta 3$ – $\beta 4$ connecting loop of the CB PH-domain (Fig. 1.8B) and their positively charged side chains are surface-exposed. Cellular studies (Reddy-Alla et al., 2010) indicated that overexpression of the RR303-304NN variant in non-neuronal cells led to the formation of large intracellular gephyrin aggregates. In cultured hippocampal neurons overexpression of the PI3P binding deficient CB mutant caused a strong reduction of synaptic gephyrin clusters, further demonstrating the crucial role of CB PH-PI3P interaction in gephyrin recruitment and maintenance at postsynaptic sites.

1.5. Ras GTPases

Ras GTPases (commonly known as small GTPases) represent a superfamily of guanine nucleotide-binding proteins, which are commonly found in eukaryotes (Fig. 1.9) (Pereira-Leal & Seabra, 2001). Ras GTPases are crucial for multiple reasons: (a) their ability to control the fundamental cellular processes in eukaryotes including morphogenesis, polarity, movement, cell division, gene expression, and reorganization of the cytoskeleton (Hall, 1998; Jaffe & Hall, 2005); (b) their association with a series of human diseases including cancer, cardiovascular and cognitive disorders (Ellenbroek & Collard, 2007); and (c) roughly 1% of proteins encoded by the human genome either regulate or are regulated by Ras proteins. Ras family GTPases generally function as molecular switches and cycle between a GDP-bound (or inactive state) and a GTP-bound (or active state) in the cytoplasm (Mosaddeghzadeh & Ahmadian, 2021).

1.5.1. Ras GTPase classification

Ras was initially discovered to be mutated in various cancers. With the passage of time, many such GTP-hydrolyzing enzymes were described and found to share similar tertiary architectures. At present, the Ras family includes over 150 members. Based on their primary sequence, structure, and function the Ras superfamily of G proteins has been divided into five subgroups which includes the Ras, Rho, Rab, Arf/Sar and Ran subfamilies. While each of the Ras subfamilies possess vital significance due to its ability in maintaining proper cellular function, this thesis primarily focuses on the role of the Rho subfamily, and hence it will subsequently be discussed in more detail.

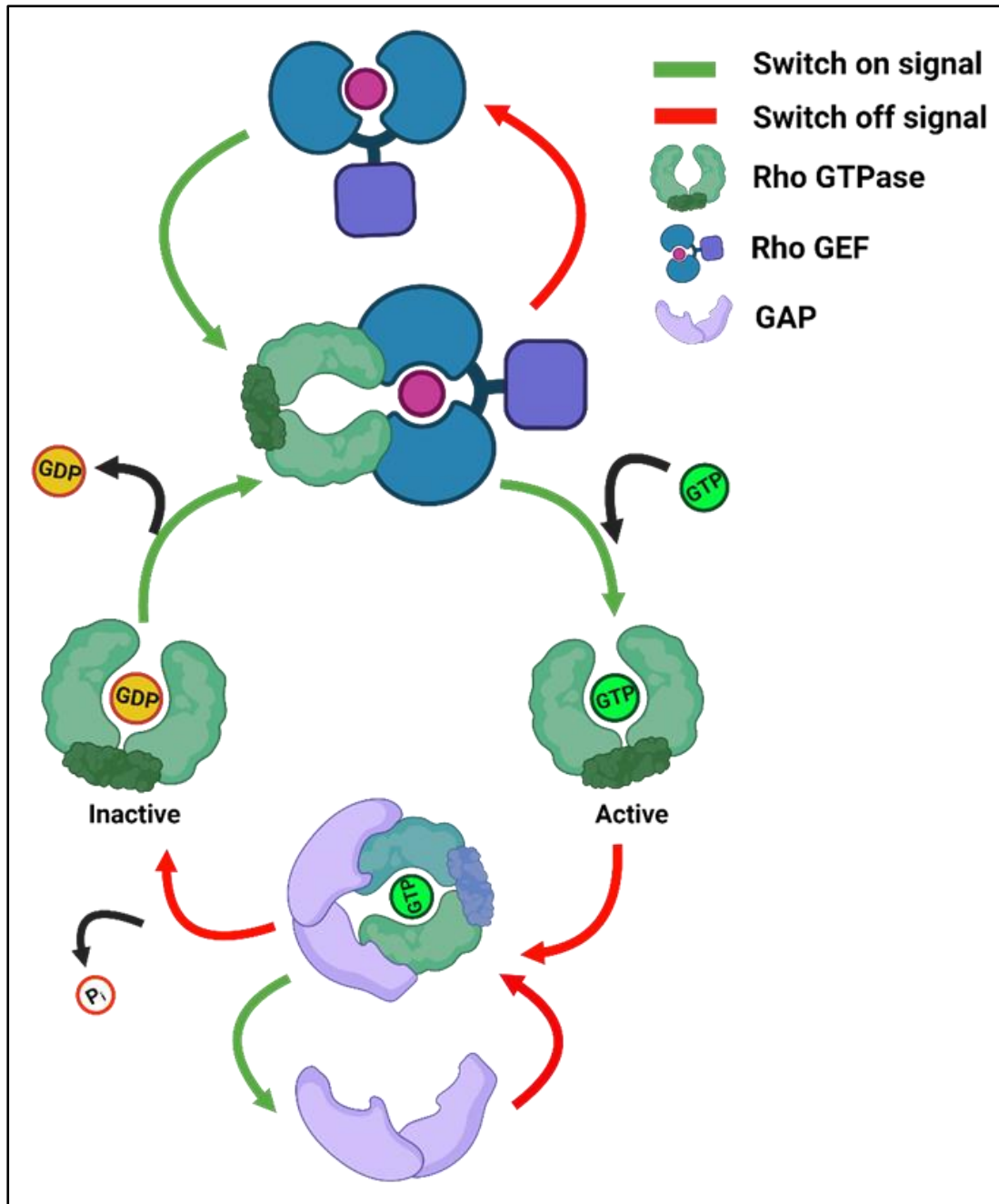


Figure 1.9 Schematic description of Rho GTPase activation and signaling. Rho GTPases serve as molecular switches by cycling between a GDP-bound or inactive state and a GTP-bound or active state. They interact with different classes of proteins including guanine nucleotide exchange factors (GEFs) and GTPase-activating proteins (GAPs). In actively growing cells, different sets of cytosolic proteins activate GEFs, which in turn activate Rho GTPases by accelerating the intrinsic exchange of GDP with GTP and hence switch on signal transduction. Rho GTPases also interact with various GAPs which negatively regulate Rho GTPases by enhancing the intrinsically slow rate of GTP hydrolysis activity, thereby switching off the signal transduction processes.

1.5.2. Rho subfamily

Members of the Ras homolog (Rho) GTPase subfamily have been long regarded as key regulatory proteins that couple changes in the extracellular environment to intracellular signal transduction pathways (Fig. 1.9). In humans, 20 canonical members of the Rho family have been identified. Based on their sequence homology, the Rho GTPases are further subdivided into six subclasses which include: (a) Rho (RhoA, RhoB and RhoC); (b) Rac (Rac1, Rac1B, Rac2, Rac3, and RhoG); (c) Cdc42 (Cdc42, G25K, TC10 (also referred to as RhoQ), TCL, WRCH1, and WRCH2); RhoD (RhoD, RIF); (d) RND (RND1, RND2, and RND3); and (e) RHOH (Jaiswal et al., 2013).

1.5.3. Rho GTPases structure and mechanism

Rho family GTPases are small proteins with a molecular weight of approximately 20-25 kDa. They typically are comprised of an N-terminally located, conserved GDP-/GTP-binding domain, called the G domain, followed by a C-terminal hypervariable region (HVR) (Fig. 1.10A) terminating with a consensus sequence, CAAX (where C is cysteine, A, any aliphatic amino acid, and X, any amino acid) motif (Schmidt & Hall, 2002; Venter et al., 2001). Structural and biochemical analysis of the Rho GTPases indicated that the G domain (Fig. 1.10A) features five relatively conserved motifs (G1-G5) which are involved in nucleotide binding and hydrolysis (Wittinghofer & Vetter, 2011). During the process of GTPase activation, purine nucleotide in the inactive GTPase is initially recognized by the G1 motif. G2 directs GDP/GTP binding, whereas the G3 motif binds to the Mg²⁺ ion associated with the bound nucleotide. G4 motif provides a hydrogen bond to the guanine base and G5 engages in interactions with the guanine nucleotide (Colicelli, 2004; Goitre et al., 2014; Wennerberg et al., 2005). The C-terminal hypervariable region of Rho GTPases is known to be crucial for their subcellular localization and hence their biological activity.

The subcellular localization of Rho GTPases is achieved through a series of posttranslational modifications at a cysteine residue in the CAAX motif including isoprenylation (geranylgeranyl or farnesyl), endoproteolysis, and carboxyl methylation of the prenylated cysteine (Roberts et al., 2008). Membrane association of Rho GTPases is considered to be a prerequisite for their biological function, which is primarily achieved by isoprenylation. In particular, prenylated Rho proteins are selectively recognized by

guanine nucleotide dissociation inhibitors (GDIs) (Fig.1.9) which control Rho GTPase shuttling between the cytosol and the plasma membrane. Rho GTPase activation results in their association with effector proteins that subsequently activate a wide variety of downstream signaling cascades, thereby regulating multiple crucial physiological and pathophysiological activities in the eukaryotic cells (Etienne-Manneville & Hall, 2002).

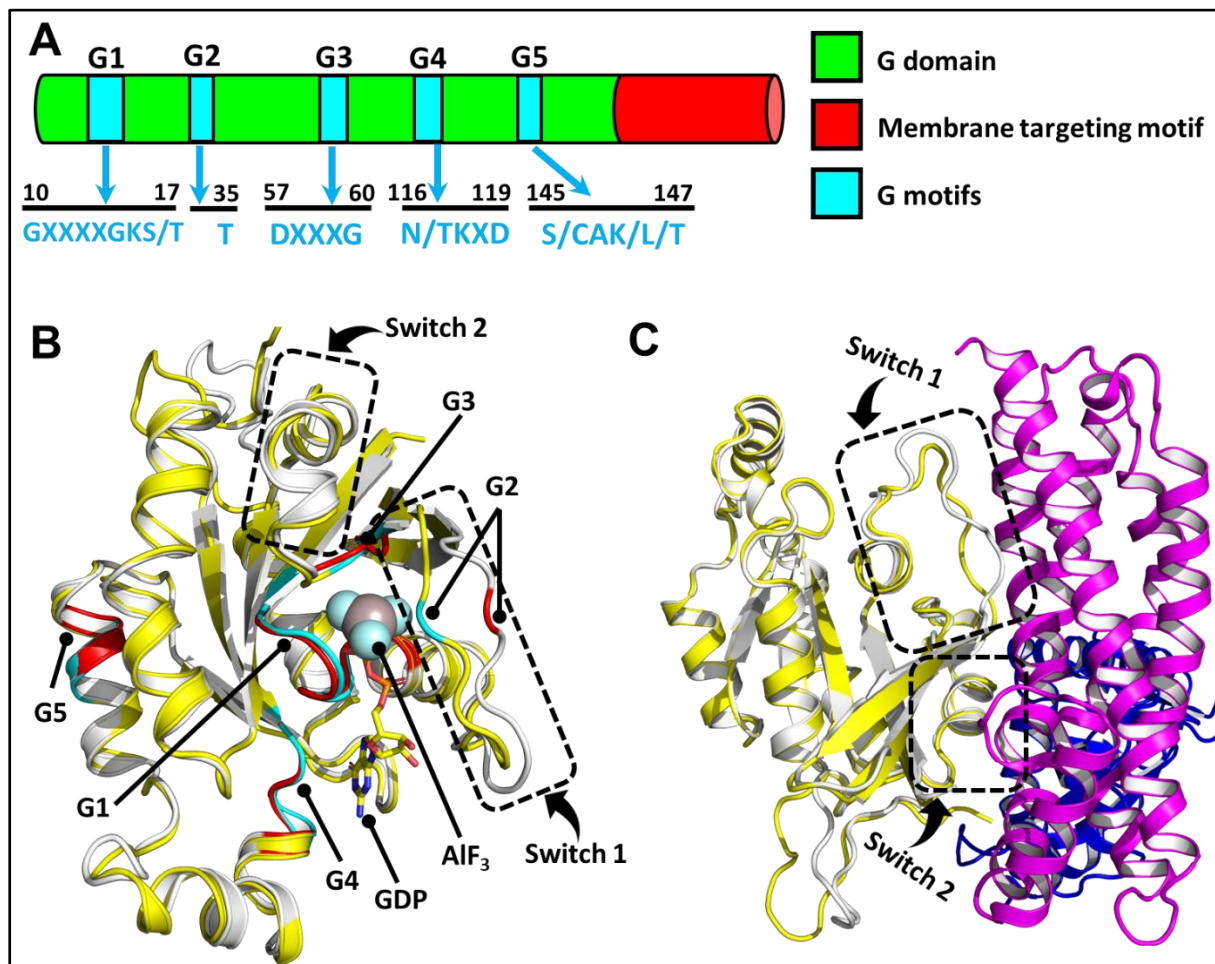


Figure 1.10 Structure of Rho GTPases. (A) Schematic diagram of the small GTPases domain architecture highlighting conserved sequence elements. (B) Superimposition of inactive (GDP bound) Cdc42 (PDB entry 1an0; grey) and active (GTP mimicked with GDP-AlF₃) Cdc42 (PDB entry 2ngr; yellow) highlighting the conformational changes in the switch 1 and switch 2 regions. The location of the G motifs (G1-5) in the inactive and active Cdc42 are represented in red and cyan, respectively. (C) Superimposition of inactive Cdc42 (grey; PDB entry 1an0) onto the CB2_{SH3}-Cdc42 complex (PDB entry 2dfk) with Cdc42 in yellow, the DH domain in magenta and the PH domain in blue. Cdc42 exclusively interacts with the catalytic DH domain of CB2SH3 whereas the PH domain remains free. Structural changes in the switch 1 and switch 2 region in Cdc42 are highlighted.

1.5.4. Rho GTPase interaction with CB

CB and its human ortholog, hPEM (also called CB3)(Fig. 1.5A and Fig. 1.7) , were originally identified as a GEF specific for Cdc42 (Reid et al., 1999). Later, using a yeast two-hybrid assay, Kins et al 2000 identified CB as a gephyrin interacting partner.

The crystal structure of the CB-Cdc42 complex (Fig. 1.10C) contain two copies of the heterodimer wherein both heterodimers form an identical set of interactions (Xiang et al., 2006). Cdc42 exclusively interacts with the DH domain (Fig. 1.10C) (Xiang et al., 2006) whereas the PH domain does not engage in any interactions with Cdc42. Biochemical data (Xiang et al., 2006) demonstrated that the SH3 domain-lacking CB2 variant (CB2_{SH3-}) efficiently catalysed the nucleotide exchange on Cdc42, compared to the SH3 containing CB1 isoform (CB1_{SH3+}), which displayed a slow exchange activity.

As Cdc42 plays a vital role in actin filament reorganization and CB being an activator of Cdc42, it was hypothesized that CB controls the gephyrin scaffold by regulating proximal elements of the cytoskeleton (Harvey, 2004). Interestingly, forebrain-specific deletion of Cdc42 in rodents (Reddy-Alla et al., 2010) did not affect gephyrin and hence GABA_AR clustering, potentially indicating that CB might also be responsible for the activation of other Rho-like GTPases in the brain. A prospective candidate in this perspective is the closely related Rho GTPase, TC10 (Hemsath et al., 2005; Neudauer et al., 1998), which is also referred to as RhoQ.

TC10 (Tetratocarcinoma10) belongs to the Cdc42-subfamily of Rho GTPase and shares approximately 70% sequence identity with Cdc42 (Mosaddeghzadeh & Ahmadian, 2021; Neudauer et al., 1998). However, contrary to Cdc42 which is ubiquitously expressed in the mammalian brain, TC10 expression is restricted to specific regions of the hippocampus. Previous biochemical and cellular studies indicated that TC10 interaction with CB leads to an activation of CB (Mayer et al., 2013). However, contrary to the canonical mode of Rho GTPase-GEF communication (Hodge & Ridley, 2016; Rossman et al., 2005; Xiang et al., 2006), where the interaction takes place via the catalytic DH domain of the GEF as described above, TC10 interaction with CB was reported to take place via the PH domain of CB (Kilisch et al., 2020; Mayer et al., 2013). Moreover, TC10 interaction studies with CB in cultured hippocampal neurons trigger synaptic gephyrin clustering and GABAergic neurotransmission enhancement (Mayer et al., 2013).

A recent study by Kilisch and colleagues (Kilisch et al., 2020) demonstrated that a

polybasic stretch at the C-terminus of TC10 is required for its interaction with monophosphorylated phosphoinositides, and that the interaction of TC10 with phospholipids via the polybasic region is essential for the TC10-triggered induction of CB-mediated gephyrin clustering.

1.6. Aims and objectives

As described above the brain specific GEF and adaptor protein CB plays a vital role in the formation and maintenance of the gephyrin scaffold and gephyrin-dependent GABA_A receptor clustering at inhibitory GABAergic postsynapses (Papadopoulos et al., 2008; Papadopoulos et al., 2007; Papadopoulos et al., 2017; Papadopoulos & Soykan, 2011; Reddy-Alla et al., 2010). However, important aspects of CB function, namely how its GDP/GTP-exchange activity, structure, and regulation contribute to gephyrin and GABA_AR clustering, as well as its role in synaptic plasticity, remain poorly understood. This dissertation aims to shed light on the varied functions of CB through its biochemical, structural, and biophysical characterization. The overall research objectives of this thesis can be subdivided into the following aims:

1. Collybistin conformational dynamics.
2. Characterization of the CB-gephyrin interaction.
3. NL2-mediated CB conformational activation.
4. Characterization of CB-Rho GTPases (Cdc42 and TC10) interaction and
5. CB conformational modulation by the Rho GTPases Cdc42 and TC10.

2. Deciphering the conformational dynamics of gephyrin-mediated collybistin activation ^Σ

Nasir Imam,^{1Ψ} Susobhan Choudhury,^{2Ψ} Katherina Hemmen,² Katrin G. Heinze,^{2*} Hermann Schindelin^{1*}

¹ University of Würzburg, Rudolf Virchow Center for Integrative and Translational Bioimaging, Institute of Structural Biology, Josef-Schneider Str. 2, 97080 Würzburg, Germany.

² University of Würzburg, Rudolf Virchow Center for Integrative and Translational Bioimaging, Molecular Microscopy, Josef-Schneider Str. 2, 97080 Würzburg, Germany.

^Σ Changes incorporated (Supplemental information has been merged with the main text).

*Correspondence to.

Hermann Schindelin, Email: hermann.schindelin@virchow.uni-wuerzburg.de

or

Katrin G. Heinze, Email: katrin.heinze@virchow.uni-wuerzburg.de

^Ψ These authors contributed equally to this work

Running Title: How gephyrin activates collybistin.

2.1. Abstract

Efficient neuronal signaling depends on the proper assembly of the postsynaptic neurotransmitter machinery. The majority of inhibitory synapses feature γ -aminobutyric acid type-A (GABA_A) receptors. The function of these GABAergic synapses is controlled by the scaffolding protein gephyrin and collybistin, a Dbl-family guanine nucleotide exchange factor and neuronal adaptor protein. Specifically, collybistin interacts with small GTPases, cell adhesion proteins and phosphoinositides to recruit gephyrin and GABA_A receptors to postsynaptic membrane specializations. Collybistin usually contains an N-terminal SH3 domain and exists in closed/inactive or open/active states. Here, we elucidate the molecular basis of the gephyrin-collybistin interaction with newly designed collybistin FRET sensors. Using fluorescence lifetime-based FRET measurements, we deduce the affinity of the gephyrin-collybistin complex, thereby confirming that the C-terminal dimer-forming E domain binds collybistin, an interaction, which does not require E domain dimerization. Simulations based on fluorescence lifetime and sensor distance distributions reveal at least a two-state equilibrium of the SH3 domain already in the free/unbound collybistin, thereby illustrating the accessible volume of the SH3 domain. Finally, our data provide strong evidence for a tightly regulated collybistin-gephyrin interplay, where, unexpectedly, switching of collybistin from closed/inactive to open/active states is efficiently triggered by gephyrin.

2.1.1. Keywords: Autoinhibition, conformational activation, collybistin, fluorescence resonance energy transfer (FRET), gephyrin, inhibitory postsynapse, neurologin-2, time-correlated single photon counting (TCSPC).

2.2. Why it matters

Information processing in the mammalian brain heavily depends on the presynaptic release of neurotransmitters and their postsynaptic reception. Inhibitory signaling is primarily mediated by the neurotransmitter γ -aminobutyric acid (GABA), which is precisely sensed by cognate GABA type A (GABA_A) receptors. Postsynaptic plasma membrane GABA_A receptor clustering in apposition to presynaptic neurotransmitter release sites ensures GABA-induced postsynaptic membrane hyperpolarization and reduced excitability with impaired GABAergic signaling triggering numerous brain

disorders. The proper assembly of the postsynaptic neurotransmitter machinery is regulated by the scaffolding protein gephyrin and the adaptor protein collybistin. The present study highlights the molecular basis of the gephyrin-collybistin interplay and demonstrates that gephyrin activates collybistin by inducing a molecular transition from a closed to an open state.

2.3. Introduction

Inhibitory synaptic signaling in the mammalian brain heavily depends on the neurotransmitter γ -aminobutyric acid (GABA) and glycine, which are recognized by postsynaptic GABA type-A (GABA_A) and glycine receptors, respectively. Postsynaptic GABA_A receptor clustering in direct apposition to the presynaptic transmitter release sites ensures fast signal transduction, inducing postsynaptic membrane hyperpolarization and reduced excitability (Andersen et al., 1963; Buhl et al., 1994; Miles & Wong, 1984; Nusser et al., 1997). GABA_A receptor assembly and maintenance is coordinated by various postsynaptic neuronal factors. These core neuronal components (Fig. 2.1) include cell adhesion proteins of the neuroligin family, specifically neuroligin 2 (NL2) and neuroligin 4 (NL4), the scaffolding protein gephyrin and the adaptor protein collybistin (Luscher et al., 2011; Papadopoulos & Soykan, 2011).

Gephyrin serves as a prime scaffolding protein at inhibitory GABAergic and glycinergic postsynaptic specializations and is principally responsible for GABA_A and glycine receptor clustering (Betz, 1998; Chooi & Ko, 2015; Fritschy et al., 2008; Tyagarajan & Fritschy, 2014). Gephyrin splice variants encompass two structured domains; a trimeric N-terminal G-domain, and a C-terminally located dimerizing E-domain, which are separated by a long unstructured linker (Chooi & Ko, 2015; Kim et al., 2006; Pizzarelli et al., 2020; Sola et al., 2004). Based on the oligomeric states of the isolated gephyrin G and E domains, a hexagonal lattice model has been suggested to provide a framework for gephyrin-mediated molecular organization at inhibitory synapses (Crosby et al., 2019; Tyagarajan & Fritschy, 2014; Xiang et al., 2001). However, in full-length gephyrin only G-domain trimerization takes place, whereas E-domain dimerization is prevented, predominantly resulting in gephyrin trimers after expression in *Escherichia coli* (Sander et al., 2013). Gephyrin loss is lethal and causes mice to die within the first post-natal day (Feng et al., 1998). Previous studies (Jedlicka et al., 2009; Papadopoulos et al., 2008;

Papadopoulos et al., 2007) demonstrated that clustering of glycine and GABA_A receptors in gephyrin-deficient mice is markedly reduced, underlining the essential role of gephyrin in receptor assembly at inhibitory postsynapses. Gephyrin mutations have also been associated with various brain disorders, including autism, schizophrenia, Alzheimer's disease, and epilepsy (Agarwal et al., 2008; Dejanovic, Lal, et al., 2014; Förster et al., 2010; Kiss et al., 2016; Lionel et al., 2013).

Gephyrin recruitment from intracellular deposits to postsynaptic membranes mainly depends on the adaptor protein collybistin (CB; also referred to as ARHGEF9). As a member of the Dbl-family of guanine nucleotide exchange factors (GEFs) it features tandem Dbl-homology (DH) and pleckstrin-homology (PH) domains (Zheng, 2001). In addition to the DH domain catalyzing the GEF activity and the phosphoinositide-binding PH domain, most CB mRNAs encode an additional N-terminal src-homology 3 (SH3) domain (Harvey, 2004). In rat, CB genes are expressed in the splice variants CB1, CB2 and CB3, which differ in their N and C termini, and the presence or absence of the SH3 domain (Harvey, 2004; Kins et al., 2000; Papadopoulos & Soykan, 2011). Structural and biochemical studies suggested that the most abundantly expressed, full-length, SH3-domain-containing CB isoform 2 (CB2-SH3⁺), adopts a closed conformation wherein the N-terminal SH3 domain interacts intra-molecularly with residues in the DH and PH domains, a conformation which does not interact with the cell division control protein 42 homolog (Cdc42), a CB-specific small GTPase (Soykan et al., 2014; Xiang et al., 2006). In contrast, the SH3 domain lacking CB2 splice variant (CB2-SH3⁻) constitutively regenerates the GTP-bound state of Cdc42 (Reddy-Alla et al., 2010; Tyagarajan, Ghosh, Harvey, et al., 2011; Xiang et al., 2006). However, a recent study demonstrated that only TC10, another Dbl-family GEF, which is closely related to Cdc42, but not Cdc42 can effectively mediate the conformational activation of full-length CB (Imam, Choudhury, Heinze, et al., 2022). Interestingly, earlier biochemical, and cellular studies (Schäfer et al., 2020; Soykan et al., 2014) indicated that CB interaction with the cytosolic region of NL2 led to a similar activation of CB (Fig. 2.1).

Previous studies revealed that CB-mediated gephyrin recruitment and clustering at the plasma membrane depend on the binding of its PH domain to phosphatidylinositol 3-phosphate [PI(3)P], whereas the GEF activity of its DH domain is dispensable (Kalscheuer et al., 2009; Reddy-Alla et al., 2010). Mutations causing a disruption of the CB inter-

domain association lead to an open/active (with respect to receptor anchoring) CB conformation with enhanced phosphatidylinositol affinity (Soykan et al., 2014).

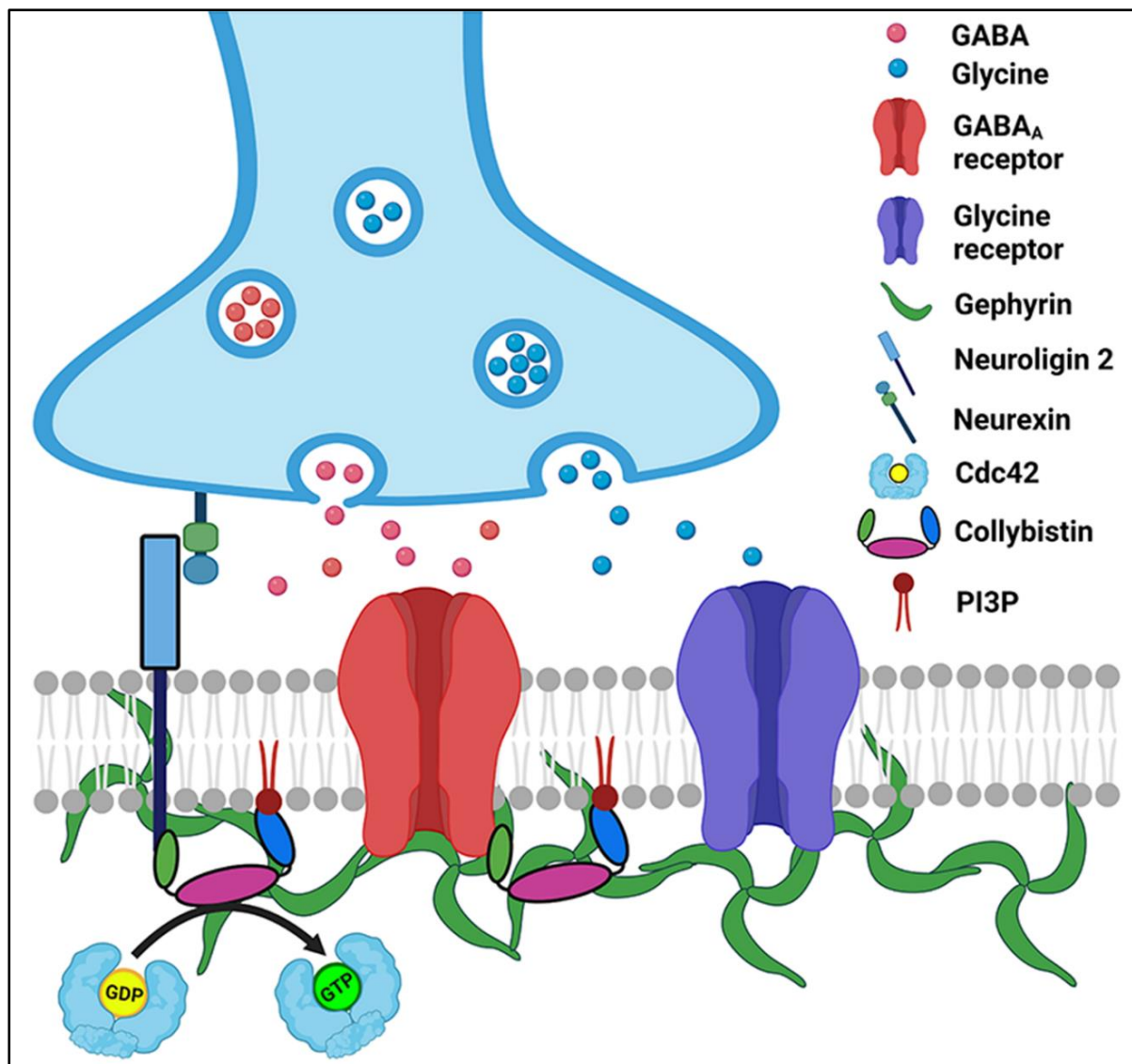


Figure 2.1 (Figure 1 in the manuscript). Schematic description of the inhibitory signal transmission and postsynaptic architecture. The synapse is stabilized by interactions between the cell-adhesion molecules, neuroligin and neuroligin, present at the pre- and postsynaptic site, respectively. GABA and glycine released from the presynaptic neuron bind to their cognate receptors embedded in the postsynaptic membrane. The GABA_A and glycine receptors are stabilized by the scaffolding protein gephyrin, which forms an extended structure underneath the postsynaptic membrane. Collybistin (CB) operates as an adaptor protein for gephyrin and recruits gephyrin to postsynaptic sites. CB (shown here in its conformationally active or open state) interacts with various other neuronal factors including the cytosolic region of neuroligin 2 and the GABA_A receptor. CB localization at the postsynaptic membranous site is largely mediated by its interaction with various phosphoinositides including phosphatidylinositol-3-phosphate (PI3P).

Mutations causing a disruption of the CB inter-domain association lead to an open/active (with respect to receptor anchoring) CB conformation with enhanced phosphatidylinositol affinity (Soykan et al., 2014).

In vivo experiments with CB-deficient mice indicated a reduction in synaptic gephyrin and GABA_A receptor γ 2-subunit clustering, decreased GABAergic synaptic transmission and impaired spatial learning (Papadopoulos et al., 2008). Surprisingly, CB-deficient mice do not exhibit deficits in glycinergic synaptic transmission, suggesting that CB is dispensable for gephyrin-mediated glycine receptor clustering at glycinergic synapses, but is required for the clustering of certain GABA_A receptors (Körber et al., 2012; Saiepour et al., 2010), further stressing the vital role of CB in the initial assembly and maintenance of gephyrin-GABA_A receptor clusters. However, owing to technical limitations, clear molecular insights into the association of CB and gephyrin and the overall clustering process have been lacking. Although the CB-gephyrin interaction has already been reported in previous studies (Kins et al., 2000; Tyagarajan, Ghosh, Harvey, et al., 2011), no quantification of the interaction strength has been reported and the reciprocal regulation of the activities of both proteins remains poorly understood.

The present study aims at elucidating the molecular basis of CB autoinhibition, its binding to gephyrin and whether this interaction leads to CB activation. We constructed novel intramolecular CB fluorescence resonance energy transfer (FRET) sensors to understand the conformational dynamics of CB by making use of picosecond-scale time-resolved fluorescence lifetime measurements. These studies confirmed that CB in isolation remains in a closed conformation while gephyrin binding takes place via its C-terminal E domain leading to an open conformation of CB. We quantified the interaction strength of gephyrin to wild type and constitutively active, open state mutant CB FRET sensors. Based on the inter-fluorophore distance distributions from the FRET sensors in the absence and presence of gephyrin, we modeled the overall three-dimensional conformational space accessible to CB with respect to the SH3 domain. Our data combined with simulation studies provide clear molecular evidence of gephyrin-mediated CB opening, thus suggesting a synergy between concurrent gephyrin scaffold assembly and CB targeting to the plasma membrane.

2.4. Methods

2.4.1 Cloning and Expression

The wild-type CB FRET sensor (F1_{D0}) was constructed by inserting a tetra-cysteine motif (tCM) (Adams et al., 2002) after the first amino acid residue of the rat CB2-SH3⁺ splice variant, while CFP (Heim et al., 1994) was C-terminally attached (Fig. 1*b*, Fig. S1*a*) using restriction free (RF) cloning (Bond & Naus, 2012) in pETM14 vector (Table S2). Amino acid replacements for the open state mutant sensors (F1_{smD0} and F1_{dmD0}) were generated by site directed mutagenesis. Additional sensors were created by inserting tCM at the specified position (Fig. 1*b*, Table S1). Full-length gephyrin (Geph^{FL}) and the domain variants (Geph^G, Geph^E and Geph^{LE}) were previously described (Maric, Kasaragod, Hausrat, et al., 2014; Saiyed et al., 2007; Sander et al., 2013). For the Geph^E monomeric mutant (Geph^{E_{mm}}) residues 318-750 were subcloned into the IMPACT system vector pTYB12 (New England Biolabs, Ipswich, MA, USA) and point mutations were introduced by site-directed mutagenesis. The SH3 domain of CB was generated by subcloning the cDNA coding for residues 10–79 (Soykan et al., 2014) of rat CB2-SH3⁺ into the pETM14 vector. The intracellular cytosolic domain of NL2 (NL2_{icd}) encompassing residues 700-836 (Hoon et al., 2011) was subcloned into the pETM11 vector.

All CB FRET sensors were expressed in the *E. coli* strain BL21 (DE3). Cell lysates were subjected to affinity chromatography on Protino Ni-IDA Resin (Macherey Nagel, Düren, Germany) equilibrated in buffer A (50 mM Tris-HCl pH 8, 250 mM NaCl, 5% glycerol and 5 mM β-mercaptoethanol). Samples were eluted using buffer A containing 300 mM imidazole and were subsequently applied to a MonoQ 10/100GL column (Cytiva, Marlborough, MA, USA) and eluted using a linear NaCl gradient from 50 mM to 1 M NaCl. Finally, sensors were subjected to size exclusion chromatography on a Superdex 200 column (GE Healthcare) and concentrated by ultrafiltration. Full-length gephyrin and its domain variants (Geph^G and Geph^{LE}) were purified as described before (Sander et al., 2013) with small modifications. Geph^E and its dimer-deficient mutant (Geph^{E_{mm}}) were initially subjected to affinity chromatography on chitin agarose beads (New England Biolabs), followed by ion exchange chromatography and subsequent size exclusion chromatography.

2.4.2. Circular-dichroism spectroscopy

Circular-dichroism (CD) spectroscopy was performed with a Jasco J-810 spectropolarimeter. Prior to measurements, the buffer was exchanged to phosphate-buffered saline (PBS) pH 8.0 using ultrafiltration (Sartorius Vivaspin 500, Göttingen, Germany). Far-UV CD spectra from 190 to 260 nm were recorded at a scanning speed of 50 nm/min with a response time of 1 second and a bandwidth of 1 nm. CD spectra were recorded repeatedly (n=15) for each sample and averaged to optimize the signal to noise ratio. The buffer spectrum was also recorded and subtracted from the protein spectra. All measurements were conducted at room temperature.

2.4.3. *In vitro* FLAsH Labeling

For FLAsH labeling (Adams et al., 2002; Griffin et al., 1998), purified sensors designated with the subscript D0 were first incubated at room temperature (RT) in labeling buffer (50 mM Tris-HCl pH 8, 250 mM NaCl, and 5 mM β -mercaptoethanol). Afterwards, FLAsH reagent (Cayman Chemicals, Ann Arbor, MI, USA) was added in a 10-fold molar excess to the sensors and the mixture was further incubated for 30 minutes at RT. Later, the mixture was dialyzed thoroughly against labeling buffer to remove unbound FLAsH, resulting in the corresponding DA fluorophore pair. Labeled sensors were flash frozen and stored at -80° C for later use.

2.4.4. Time-resolved setup and data acquisition

Time resolved fluorescent measurements were conducted with a custom-built confocal microscope setup (IX 71, Olympus, Hamburg, Germany) equipped with a time-correlated single photon counting (TCSPC) system (Hydraharp 400, Picoquant, Berlin, Germany) with data acquisition by the fluorescence lifetime correlation software SymPhoTime 64 (PicoQuant, Berlin, Germany). The excitation laser (440 nm pulsed laser LDH-D-C-440, Picoquant) was fiber coupled (Laser Combining Unit with polarization maintaining single mode fibre, PicoQuant, Berlin, Germany) and expanded to a diameter of 7 mm by a telescope to fill the back aperture of the objective (60x water immersion, NA 1.2, Olympus, Hamburg, Germany), thus creating a diffraction-limited focal spot. Before entering the objective lens, the laser polarization was adjusted by an achromatic half-wave plate (AHWP05M-600, Thorlabs, Bergkirchen, Germany). A beam splitter (HC458

rpc phase r uf1, AHF) guided the laser through the objective, epi-illuminating the sample. In the detection path a 100 μm pinhole (PNH-100, Newport, Darmstadt, Germany) rejected out of focus light before being projected on photon counting detectors (2x PMA Hybrid-40, Picoquant, Berlin, Germany) by a telescope in a 4f configuration (focal length of lenses: 60 mm, G063126000, Qioptiq, Rhyl, UK). The beam was split via a polarizing beam splitter cube (10FC16PB.3, Newport, Darmstadt, Germany) into parallel (VV, detector 1) and perpendicular emission (VH, detector 2) after the first lens of the telescope. Emission filters (band pass filter Brightline HC 480/40 AHF, Tübingen, Germany) rejected unspecific light in each detection path. The laser was operated in pulsed mode at 20 MHz with a laser power at the sample of $\sim 11 \mu\text{W}$ and the temporal resolution was set to 4 ps. Measurements with the CB FRET sensors (1 μM concentration) were performed on standard glass coverslips (Menzel-Gläser, Braunschweig, Germany; 24 x 40 mm, 1.5).

CB FRET sensors (F_{1D0}/F_{1DA}) were titrated with varying concentrations of gephyrin (or other ligands) in binding buffer (50 mM Tris-HCl pH 8, 250 mM NaCl, 10 mM EDTA and 5 mM β -mercaptoethanol) in a final sample volume of 20 μL . Prior to data acquisition, samples were incubated overnight at 4 $^{\circ}\text{C}$ under dark light conditions. Samples were excited at 440 nm and the donor emission between 460 and 500 nm was recorded. Donor only (D0) and buffer solutions were measured as control samples and for background corrections. The data were acquired at room temperature for 5-10 min depending on photon counts. To determine the instrument response function (IRF), a KI-saturated solution of 3 μM fluorescein in double distilled water was measured for 10-15 min. To determine the relative detection efficiency in the parallel to perpendicular channel, i.e. the g-factor, a 1 μM solution of Coumarin 343 was measured. Samples were measured in technical triplicates to calculate average and standard deviations for each condition.

2.4.5. Time-resolved fluorescence decay analysis

To accurately determine the inter-fluorophore distance distribution from the fluorescence intensity decays the magic angle intensity decay was determined based on the obtained g-factor from the VV and VH signals. Data were exported from the ptu Symphotime format into text files using the Jordi-tool of the Seidel-Software package (<https://www.mpc.hhu.de/software/3-software-package-for-mfd-fcs-and-mfis>). Here,

in the text file VV and VH data are stacked as a single column. All data were exported in 16 ps bins, i.e. 4096 channels for each detector. Thus, the single column text file contains 8192 channels in total with the first 4096 channels corresponding to the VV and the next 4096 channels to the VH decay. With a given g-factor, the analysis was done in the Chisurf software (Peulen et al., 2017) (<https://github.com/Fluorescence-Tools/chisurf>) as described elsewhere (Sanabria et al., 2020). We have calculated the g-factor to 0.9 from the tail fitting of the calibration dye coumarin 343. The decay curves were fitted with a multi-exponential model function using an iterative re-convolution approach (Sanabria et al., 2020; Tsytonok et al., 2020) as follows

$$F(t) = \sum_i x_i e^{-t/\tau_i} \quad (1)$$

where x_i represents the species fraction, i.e. the fractional amplitude of this component to the total intensity amplitude with $x_i = A_i/A_{total}$, and τ_i the lifetime of the corresponding component. The species fractions are normalized such that $\sum_i x_i = 1$. Ideally, D0 should show a single component but, due to local quenching in donor-only samples, multi-exponential decays were expected. The quality of the curve fitting was evaluated by the reduced χ^2 -values and the weighted residuals. Time-resolved fluorescence intensities for F1_{DA} labeled (F1_{DA}) and F1_{DA}-ligand complexes (all gephyrin variants, NL2_{icd} and SH3) were also analyzed by eq. 1 to obtain the species-weighted average fluorescence lifetime.

$$\langle \tau \rangle_x = \sum_i x_i \tau_i, \quad (2)$$

$$\text{where } \sum_i x_i = 1. \quad (3)$$

2.4.6. K_D determination

We titrated the F1_{DA} sensor with different concentrations of full-length gephyrin (or other ligands) and measured the resulting time-resolved fluorescence intensities. The fractional saturation (in %) at concentration i was determined based on the average fluorescence lifetime:

$$\text{fractional saturation (\%)}, f = \frac{\langle \tau_{DA,iM} \rangle - \langle \tau_{DA,0M} \rangle}{\langle \tau_{DA,max} \rangle} * 100 \quad (4)$$

where $\langle \tau_{DA,iM} \rangle$ is the average fluorescence lifetime at concentration i , $\langle \tau_{DA,0M} \rangle$ is the mean fluorescence lifetime of the F1_{DA} labeled CB FRET sensor without addition of ligand and $\langle \tau_{DA,max} \rangle$ is the longest mean fluorescence lifetime of the titration, usually obtained at the highest ligand concentration. The resulting data points were plotted against the

concentration of ligand and fitted as follows (Origin9, OriginLab):

$$f(x) = b + (a - b) * \frac{[(C_p * K_D * x) \pm \sqrt{(C_p * K_D * x)^2 - 4 * C_p * x}]}{2 * C_p} \quad (5)$$

where x is the concentration, b the offset, a , the final intensity, c_p the protein concentration, and K_D the dissociation constant.

2.4.7. Förster distance calculation

The Förster distance R_0 [Å] was calculated from the overlap integral of the emission spectrum of the donor and absorption spectrum of the acceptor from

$$R_0 = \left[\frac{9 \ln(10)}{128 \pi^2 * N_A} * \frac{J(\lambda) * \kappa^2 * \Phi_D}{n^4} \right]^{\frac{1}{6}} = 0.211 * [\kappa^2 \eta^{-4} \Phi_D J(\lambda)]^{1/6} \quad (6)$$

where κ^2 is a factor describing the relative orientation in space of the transition dipoles of the donor and the acceptor. The magnitude of κ^2 is assumed to be 0.66 for a random orientation of donor and acceptor. The refractive index (η) of the aqueous buffer is assumed to be 1.33. $J(\lambda)$ is the overlap integral of emission of donor (CFP), and absorption (Fig. S1c) of the acceptor (FIAsH) and calculated by

$$J(\lambda) = \frac{\int_0^\infty I_D(\lambda) \varepsilon(\lambda) \lambda^4 d\lambda}{\int_0^\infty I_D(\lambda) d\lambda} \quad (7)$$

where $I_D(\lambda)$ is the fluorescence emission of the donor in the wavelength region λ and $\varepsilon(\lambda)$ the extinction coefficient [$M^{-1} \text{ cm}^{-1}$] of the acceptor FIAsH ($41000 \text{ M}^{-1} \text{ cm}^{-1}$ at 508 nm).

2.4.8. Average FRET efficiency calculation

The fluorescence lifetime values obtained from the TCSPC decays were used to calculate an average FRET efficiency (E_{FRET}) using the following equation:

$$E_{FRET} = 1 - \frac{\langle \tau_{DA} \rangle}{\langle \tau_{D0} \rangle} \quad (8)$$

where $\langle \tau_{D0} \rangle$ and $\langle \tau_{DA} \rangle$ are the species-weighted average fluorescence lifetimes in the absence (D0) and presence (DA) of FIAsH as calculated based on eq. 2.

2.4.9. FRET distance distribution analysis

For distance distribution analysis for the FIAsH labeled (F1_{DA1}) and F1_{DA1}-ligand complexes we followed a method described earlier (Sanabria et al., 2020; Tsytlonok et al., 2020). The time-resolved fluorescence intensities of the FRET-sample and the donor-only

reference sample are presented as:

$$\begin{aligned}
 F_{FRET}(t) &= N_0[(1 - x_{NoFRET})F_{DA}(t) + x_{NoFRET}F_{D0}(t)] \otimes IRF + sc \cdot IRF + c \quad (9) \\
 F_{Ref}(t) &= N_0F_{D0}(t) \otimes IRF + sc \cdot IRF + c \\
 &\quad (10)
 \end{aligned}$$

Here, sc is the scattered light from the sample, c is the constant offset of the fluorescence intensity and N_0 is the total photon number. x_{NoFRET} is the no-FRET contribution from the unquenched donor. As stated earlier, we obtained multi-exponential fitting for the donor-only sample due to local quenching, however, the local quenching of the donor is not affected by FRET (Lehmann et al., 2020). Hence, the FRET-rate (k_{FRET}) depends on the relative orientation and donor-acceptor-distance and the FRET samples can be fitted globally with the donor-only reference sample. In the presence of FRET, the donor fluorescence decay can be expressed with a Gaussian distance distribution (ρ) of donor-acceptor as

$$F_{DA}(t) = F_{D0}(t) \cdot \int \rho_{Gauss}(\sigma, \langle R(i) \rangle) \cdot \exp(-k_{FRET}(R(i)) \cdot t) dR \quad (11)$$

where $\langle R(i) \rangle$ is the mean distance between donor and acceptor and σ the width of the inter-fluorophore distance distribution $R(i)$. In the analysis, σ was fixed to a physically meaningful value of 5 Å (Peulen et al., 2017). The Förster radius for CFP and FlAsH was 39 Å, as calculated following the method described in supplementary materials.

2.4.10. Uncertainty estimation of distance distribution

The experimental uncertainty in the TCSPC-based inter-fluorophore distance analysis mainly stems from three sources: (i) The uncertainty of the orientation factor $\langle \kappa^2 \rangle$, $\delta R_{DA, \langle \kappa^2 \rangle}$, (ii) the uncertainty in the D_{only} reference $\delta R_{DA, reference}$ (based on sample preparation etc.) and (iii) the statistical uncertainty based on the fitting, $\delta R_{DA, fit}$ (Peulen et al., 2017). Here, we estimated the uncertainty $\delta R_{DA, fit}$ in the obtained distances (Gaussian distance distribution, eq. 11) by sampling the χ_r^2 -surface in 50 steps in the range from -20% to +20% of the respective distance using the “Parameter Scan” option in ChiSurf (Peulen et al., 2017). The value of the scanned distance, R_1 or R_2 , respectively, is fixed, all other parameters are fitted and the resulting χ_r^2 is reported. The resulting χ_r^2 -surface (Lakowicz, 2013) was plotted against the scanned distance (Fig. S11b) and the limits were determined using a 3σ -criterion based on an F-test (1700 TCSPC channels, 9 parameters) to a relative $\chi_{r, rel}^2 = \chi_{r, i}^2 / \chi_{r, min}^2$ of 1.012. To incorporate $\delta R_{DA, reference}$ we

extended the limits for R_{\min} and R_{\max} in such a way that the overall R_{\min} and R_{\max} for the experimental triplicates were used (Fig. S11b). The uncertainty of the orientation factor $\langle \kappa^2 \rangle$, $\delta R_{DA(\kappa^2)}$, which is usually the largest source of uncertainty, was not considered.

2.4.11. Model-free distance distribution analysis

For a model-free description, we calculated the FRET-induced donor decay as described (Peulen et al., 2017). Briefly, in a first step, the fluorescence decay of the FRET sample $I_{DA}(t)$ is divided by the (modeled) decay of the single-labeled sample $I_{D0}(t)$. Next, the donor-only fraction, x_{NoFRET} , i.e. the offset, is subtracted, and finally, this ratio is multiplied with the time axis t to yield the FRET-induced donor decay $\varepsilon(t)$:

$$\varepsilon(t) = \left(\frac{I_{DA}(t)}{I_{D0}(t)} - x_{NoFRET} \right) \cdot t \quad (12)$$

For an intuitive display, we converted the x-axis from time t to critical distance $R_{DA,c}$ by the following relation:

$$R_{DA,c} = R_0 \cdot \left(\frac{t}{\tau_D} \right)^{1/6} \quad (13)$$

where R_0 is the Förster radius of the respective FRET dye pair (here 39 Å) and τ_D the reference fluorescence lifetime of the donor fluorophore (here, 3 ns). Plotting $\varepsilon(t)$ against $R_{DA,c}$ results in a peaking distribution, which reflects the probability density function of the underlying distance distribution of the original decay $I_{DA}(t)$.

2.4.12. FRET-restrained Markov-chain Monte-Carlo sampling

FRET-restrained Markov-chain Monte-Carlo (MCMC) sampling was performed using the FRET Positioning Software (FPS) (Kalinin et al., 2012) based on the X-ray crystal structures of CB-SH3⁻ (PDBID 4mt7) and CB-SH3⁺ (PDBID 4mt6) (Soykan et al., 2014). Additionally, the NMR structure of the ReAsH-tag (BioMagResBank ID code 16041) (Madani et al., 2009) was used as a model for the FlAsH-tag and the X-ray crystal structure of eGFP served as a template for CFP (PDBID 4eul). Two types of restraints were defined: (a) Connectivity restraints and (b) FRET-based restraints (Fig. S11a).

Connectivity restraints are based on the linear connectivity between the protein domains and labels, i.e. the SH3-domain is separated from the DH domain by 35 amino acids based on the structural models and 28 residues from the FlAsH-label incorporated at position 99 (Table S8). These flexible connections are modelled as worm-like chain polymers,

where the uncertainty (or width of distribution) for FPS was determined as the 1σ -region. One exception is the connection between the PH domain and the CFP. Here, we assumed that residues 439-456 stay in their α -helical conformation as found in PDB entry 2dfk (Xiang et al., 2006), while residue 439 serves as a flexible hinge around which the helix and the ensuing CFP move about. Here, the uncertainty was set to the length of one amino acid residue (3.6 Å). FRET-based restraints were based on the experimental distances obtained by the Gaussian distance fitting. The mean distance was set as the average from the experimental triplicates and the uncertainties were determined.

Next, the five entities (FlAsH-1, SH3-domain (from 4mt6), FlAsH-99, CB (4mt6 or 4mt7) and CFP) were loaded into FPS and the respective CB structure (4mt6 or 4mt7) was fixed in place. The structural models were docked for 100 times, followed by 100x sampling using MCMC of each generated structure. In this step, the reciprocal kT was lowered to a value of 2. The resulting 10,000 models were exported as pml files, translated into PDB format and the docking and sampling results were verified by comparing the obtained restrained mean value with our input values. Next, the trajectories were generated using mdtraj (Robert et al., 2015) and the density based on the occupancy of the FlAsH-1, FlAsH-99, CFP and SH3-domain was exported from VMD (Humphrey et al., 1996). The data were visualized using PyMol (The PyMOL Molecular Graphics System, Schrödinger, LLC).

2.4.13. Statistical analysis

All quantitative data are expressed as mean values \pm standard deviation (SD) unless stated otherwise. Origin 9 (OriginLab) was used for statistical analysis. One-way ANOVA followed by Tukey's post hoc multiple comparison test was performed for comparison between multiple pairs.

2.5. Results

2.5.1. Sensor engineering and characterization

To generate suitable FRET sensors we incorporated an *Aequorea victoria* derived cyan variant (CFP) of the green fluorescent protein (Heim et al., 1994) and the biarsenical dye,

fluorescein arsenical hairpin binder-ethanedithiol (FlAsH) (Griffin et al., 1998), as suitable donor and acceptor, respectively (Hoffmann et al., 2005) into CB (Fig. 2.2a,c; Fig. 2.3a-b). The non-fluorescent molecule FlAsH forms a fluorescent complex with any protein to which a short tetracysteine-motif (tCM) is genetically fused (Fig. 2.3c), with the amino acid sequence CCPGCC possessing the highest specificity for FlAsH (Adams et al., 2002). We optimized the position for CFP attachment and the tCM insertion site so that the intramolecular CB-FRET sensor can be used to study ligand-induced conformational changes. Initial screening for suitable intramolecular CB-FRET sensors was done by attaching the CFP moiety at various C-terminal positions by utilizing different truncated forms of CB, while the tCM insertion site was kept constant at the N-terminus of CB. Insertion of tCM after the first amino acid residue and CFP after residue 456 of the CB2-SH3⁺ splice variant (Fig. 2.3b), denoted as F1, yielded the best working wild-type CB FRET sensor in terms of FRET efficiency (E_{FRET}) along with sensor purity, while still maintaining proper folding (Fig. 2.2 a-b).

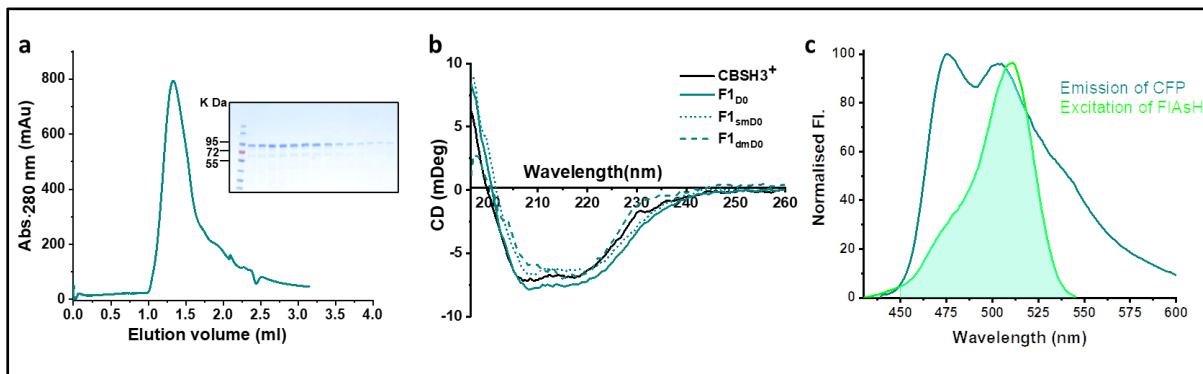


Figure 2.2 (Supplementary Figure 1 in the manuscript). CB FRET sensor purification and characterization. (a) Elution profile of the CB FRET sensor ($F1_{D0}$, teal) and corresponding SDS-PAGE gel showing the eluted protein from the size exclusion chromatography. (b) CD spectra of CBSH3⁺ (black), $F1_{D0}$ (teal, solid line) $F1_{smD0}$ (teal; dotted line) and $F1_{dmD0}$ (teal; dashed line). (c) Emission and excitation spectra of $F1_{D0}$ (teal) and $F1_{DA}$ (green), respectively. The filled area marks the overlap integral used for determining the Förster radius R_0 .

To better understand CB conformational dynamics, we generated three additional CB-FRET sensors (Fig. 2.3b), where we inserted the tCM for the FlAsH labeling after residues 28 (F28), 73 (F73) and 99 (F99) of CB, while keeping the CFP position fixed after residue 456.

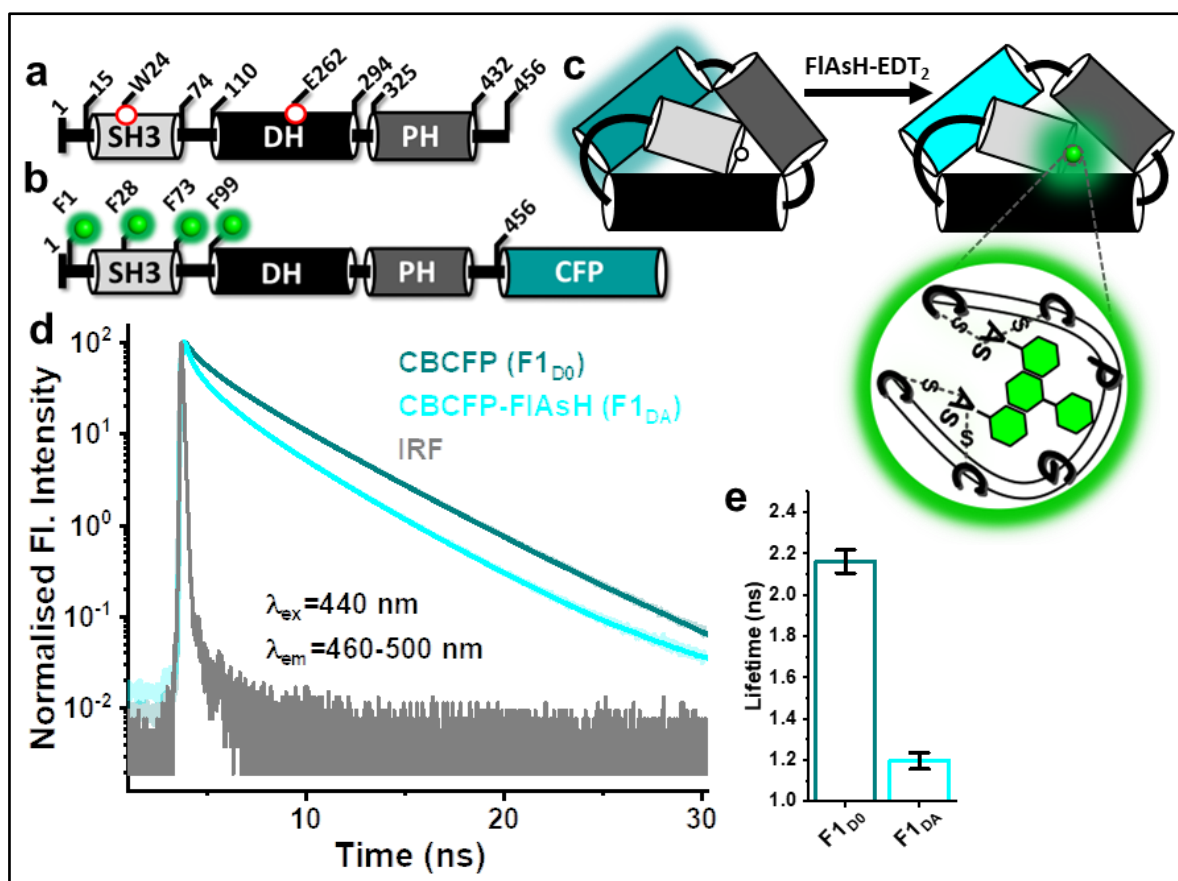


Figure 2.3. (Figure 2 in the manuscript). **CB FRET sensor design and characterization.** (a) CB domain architecture with the SH3, DH and PH domains in light grey, black and dark grey, respectively. Amino acid positions Trp24 (W24) and Glu262 (E262) are highlighted. (b) Domain architecture of the ensemble of CB FRET sensors constructed in this study, highlighting the position of the tetra-cysteine motif (tCM) used for labeling with the fluorescein arsenical hairpin binder-ethanedithiol (FIAsh-EDT₂) (green spheres) and C-terminal attachment site of CFP (teal). Individual sensors contained a single tCM inserted after residue 1 (F1), 28 (F28), 73 (F73) and 99 (F99), whereas the CFP position (after residue 456) was kept constant. F1_{D0}, F28_{D0}, F73_{D0} and F99_{D0} represent the individual FRET sensors in the absence of FIAsh and F1_{DA}, F28_{DA}, F73_{DA} and F99_{DA} after FIAsh-labeling. In the single mutant FRET sensor (F1_{smD0}) E262 was replaced with Ala (E262A) and in the double mutant FRET sensor (F1_{dmD0}), W24 and E262 were replaced with Ala (W24A/E262A). (c) Cartoon representing the CB FRET sensor (F1_{D0}) in the closed conformation highlighting its labeling with FIAsh-EDT₂ reagent, resulting in F1_{DA}. FIAsh-EDT₂ (non-fluorescent) turns fluorescent (green) after forming covalent bonds with the cysteine residues present in tCM (green circle). (d) Time-resolved fluorescence intensities of CFP of the CB FRET sensor (F1_{D0}; teal) and the FIAsh-labeled CB FRET sensor (F1_{DA}; cyan). The instrument response function (IRF) is shown in grey. F1_{D0} and F1_{DA} were excited (λ_{ex}) at 440 nm and emission (λ_{em}) data were collected between 460-500 nm. Data were scaled to a maximum of 100 for easier comparison. (e) Species-weighted $\langle \tau \rangle_x$ of CFP in F1_{DA} (1.20 ± 0.04 ns) is reduced compared to F1_{D0} (2.16 ± 0.06 ns), corresponding to a FRET efficiency of 44% (eq. 8). Data from three different batches of experiments are presented as mean values ± SD.

Additionally, we also constructed two open state mutant CB sensors (Fig. 2.3a-b). In the single mutant sensor (sm), Glu262 was replaced with alanine, whereas in the double mutant sensor (dm), an additional Trp24Ala variant was engineered while keeping the FAsH and CFP at the same positions as in the F1 construct. The sensors in the absence of acceptor are referred with the subscript D0 and in the presence of the acceptor as DA. Full-length CB is rather unstable and prone to degradation, while full-length gephyrin (GephFL) is susceptible to aggregation and degradation during purification (Sander et al., 2013; Soykan et al., 2014). After optimization, we recombinantly purified stable constructs of full-length CB and GephFL (see Methods for details). We ensured that all sensors (F1_{D0}, F1_{smD0} and F1_{dmD0}) retained proper folding (Fig. 2.2b).

Previous crystallographic studies (Soykan et al., 2014) suggested that CB exists in a closed conformation in its inactive state which would allow optimum resonance energy transfer between CFP and FAsH (Fig. 2.3c). For our initial studies we used the F1 construct which is expected to closely mimic wild type CB2-SH3⁺. Time-resolved fluorescence intensities of CFP in the absence (F1_{D0}) and presence of FAsH (F1_{DA}) revealed a significant reduction in the average fluorescence lifetime ($\langle\tau\rangle_x$) from 2.16 (± 0.06) ns to 1.20 (± 0.04) ns (Fig. 2.3d-e; Table 2.1). The decrease in $\langle\tau\rangle_x$ in F1_{DA} is attributed to FRET from the C-terminally attached CFP to the FAsH moiety bound to tCM. F1_{DA} displayed a FRET efficiency (E_{FRET}) of $\sim 44\%$ (eq. 6) and a Förster radius (R_0) of 39 Å (eq. 6 and Fig. 2.2c). These properties support the use of F1_{DA} as FRET sensor to study ligand-induced CB conformational dynamics.

2.5.2. Gephyrin, NL2 and free SH3 mediate CB activation

Using the CB FRET sensor as a novel tool, we sought to delineate the molecular basis of the CB and GephFL interaction. For interaction studies, we measured the $\langle\tau\rangle_x$ of CFP in F1_{D0} as well as F1_{DA} alone and in the presence of a 100-fold molar excess (100 μM) of GephFL. A significant increase in average fluorescence lifetime to 1.56 ± 0.04 ns (Table 2.1) of the F1_{DA}-GephFL complex compared to free F1_{DA} was observed (Fig. 2.4a). In this case an E_{FRET} of $\sim 27\%$ was calculated for the F1_{DA}-GephFL complex (Table 2.1), while no substantial change in $\langle\tau\rangle_x$ of CFP was observed for F1_{D0} in the presence of GephFL (Table 2.2), indicating that GephFL binding does not alter the fluorescent properties of CFP.

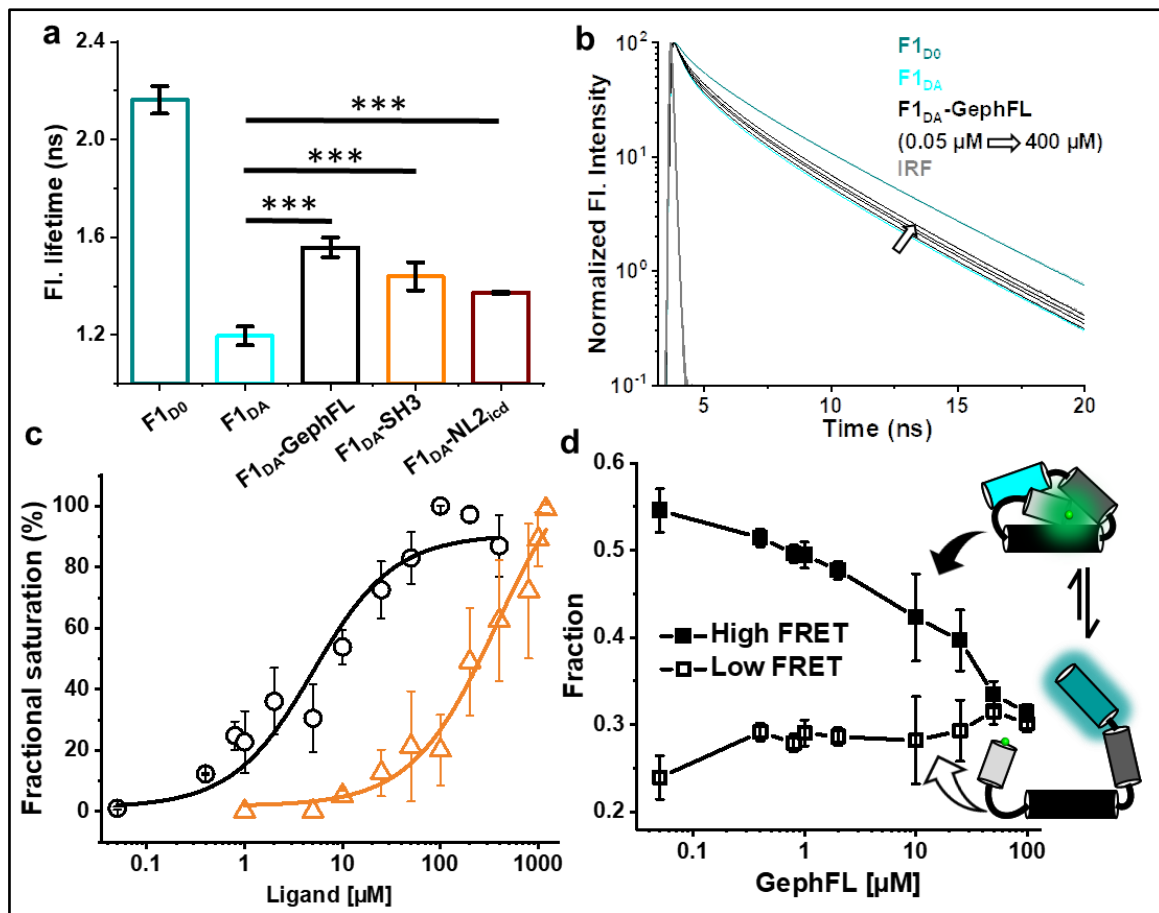


Figure 2.4 (Figure 3 in the main manuscript). Full-length gephyrin-mediated CB activation. (a) Average fluorescence lifetime of CFP in $F1_{D0}$ (teal), $F1_{DA}$ alone (cyan) and in the presence of GephFL (black), SH3 domain (orange) and $NL2_{icd}$ (dark red). $***P < 0.005$. **(b)** Fluorescence lifetime of CFP in $F1_{DA}$ and $F1_{DA}$ -GephFL complexes with increasing concentrations of full-length gephyrin (GephFL, black). Data were scaled to a maximum of 100 for easier comparison. The decay histograms are fitted in two ways: i) With a multi-exponential fitting model (eq. 1) to determine K_D and ii) with two FRET species ($R(i)$) with a Gaussian distance distribution (half-widths 5 \AA) and a single NoFRET species (see Methods). **(c)** GephFL binding affinity was determined based on the average fluorescence lifetime converted into the fractional saturation using eq. 4. The data were fitted with eq. 5. For the $F1_{DA}$ -GephFL complex (black) a dissociation constant (K_D) of $4.5 \pm 1.7 \mu\text{M}$ and for the $F1_{DA}$ -SH3 complex (orange) a K_D of $373 \pm 116 \mu\text{M}$ (data \pm SD) were obtained. Data from three different batches of experiments are presented as mean values \pm SD. **(d)** Plot of the contribution of the two FRET species (high and low FRET states) against the concentration of GephFL obtained when analyzing the time-resolved fluorescence intensities with the Gaussian distribution model (eq. 9). Curves showing the fraction of $F1_{DA}$ molecules in the closed/high FRET state (filled squares, black) with a FRET pair distance (R_1) of $25 \pm 1.1 \text{ \AA}$ and their gradual transition into the open/low FRET state (open squares) exhibiting a FRET pair distance (R_2) of $46 \pm 1.5 \text{ \AA}$ upon addition of GephFL. The transition of $F1_{DA}$ from the high to the low FRET state is illustrated in cartoon representation.

Samples	$\langle \tau \rangle_x (\pm SD)$, [ns]	$E_{\langle \tau \rangle_x}$ [%]	$R_1 (\pm SD)$ [Å]	x_1	$R_2 (\pm SD)$ [Å]	x_2	x_{NoFRET}
F1 _{D0}	2.16 (± 0.06)	-	-	-	-	-	-
F1 _{DA}	1.20 (± 0.04)	44	25.5 (± 0.5)	0.59 (± 0.02)	45.5 (± 0.9)	0.19 (± 0.02)	0.21 (± 0.03)
F1 _{DA} + GephFL	1.56 (± 0.04)	27	26.3 (± 0.6)	0.31 (± 0.02)	47.1 (± 1.8)	0.30 (± 0.02)	0.38 (± 0.01)
F1 _{DA} + GephG	1.26 (± 0.01)	-	26.8 (± 0.6)	0.43 (± 0.01)	44.5 (± 0.6)	0.29 (± 0.01)	0.27 (± 0.01)
F1 _{DA} + GephLE	1.54 (± 0.04)	28	26.3 (± 0.47)	0.37 (± 0.01)	49.6 (± 0.47)	0.25 (± 0.01)	0.37 (± 0.03)
F1 _{DA} + GephE	1.36 (± 0.02)	37	23.6 (± 0.4)	0.42 (± 0.01)	46.5 (± 1.8)	0.27 (± 0.01)	0.31 (± 0.02)
F1 _{DA} + GephE _{mm}	1.78 (± 0.02)	17	24.5 (± 0.2)	0.26 (± 0.02)	43.7 (± 0.3)	0.16 (± 0.02)	0.57 (± 0.01)
F1 _{DA} + cytNL _{icd}	1.37 (± 0.00)	36	25.7 (± 0.12)	0.44 (± 0.01)	46 (± 0.62)	0.23 (± 0.01)	0.32 (± 0.01)
F1 _{DA} + SH3	1.44 (± 0.06)	33	26.9 (± 0.88)	0.42 (± 0.03)	49.3 (± 0.9)	0.27 (± 0.04)	0.29 (± 0.03)

Table 2.1 (Supplementary Table 3 in the manuscript). Species-weighted average fluorescence lifetime ($\langle \tau \rangle_x$) and inter-dye distances (R_i) along with their relative species fractions (x_i) obtained from time-resolved FRET analysis for the F1 CB-FRET sensor in the absence (F1_{D0}), presence of F1_{DA} alone and after incubation with NL2_{icd}, SH3 domain, full-length gephyrin (GephFL) and its domain variants. Species fractions are normalized such that $x_1 + x_2 + x_{NoFRET} = 1$. Data from three different batches of experiments are presented as mean values \pm SD.

Samples	$\langle \tau \rangle_x (\pm SD)$, [ns]
F1 _{D0}	2.16 (± 0.06)
F1 _{D0} + GephFL	2.15 (± 0.02)
F1 _{D0} + GephG	2.12 (± 0.01)
F1 _{D0} + GephLE	2.12 (± 0.03)
F1 _{D0} + GephE	2.12 (± 0.01)
F1 _{D0} + GephE _{mm}	2.15 (± 0.01)
F1 _{D0} + SH3	2.15 (± 0.01)
F1 _{D0} + NL2 _{icd}	2.12 (± 0.02)

Table 2.2 (Supplementary Table 4 in the manuscript). Species-weighted average fluorescence lifetime ($\langle \tau \rangle_x$) for F1_{D0} in the absence and presence of full-length Gephyrin (GephFL), its domain variants (GephG, GephLE, GephE) and the dimer-deficient monomeric E-domain mutant (GephE_{mm}). The table also depicts the observed lifetime in F1_{D0} in the presence of SH3 and NL2_{icd}. Data from three different batches of experiments are

presented as mean values \pm SD.

The decrease in E_{FRET} upon GephFL binding reflects changes in the CB conformation, leading to an increased distance between the fluorophores attached to the SH3 and PH domain.

Earlier studies hypothesized that the intracellular cytosolic domain of NL2 (NL2_{icd}) binds to the SH3 domain of CB, resulting in an open/active state capable of interacting with plasma membrane phosphoinositides (Poulopoulos et al., 2009; Schäfer et al., 2020; Soykan et al., 2014). In the presence of 100 μ M NL2_{icd} the $\langle \tau \rangle_x$ of CFP in the F1_{DA}-NL2_{icd} complex was 1.37 ns (Fig. 2.4a) with an E_{FRET} of $\sim 36\%$ (Table 2.1), a slightly higher E_{FRET} than in the F1_{DA}-GephFL complex.

A previous biochemical analysis (Soykan et al., 2014) suggested that the SH3 domain engages in a weak intra-molecular interaction with the DH-PH domain tandem. To investigate whether this interaction is dynamic so that the SH3 domain also exists in a partially detached state, we incubated a 100-fold stoichiometric excess (100 μM) of recombinantly purified SH3 domain with F1_{DA}. The $\langle\tau\rangle_x$ and E_{FRET} for the SH3-F1_{DA} complex were measured as 1.44 ± 0.06 ns and $\sim 33\%$, respectively (Fig. 2.4a; Table 2.1), indicating that the free SH3 domain can displace the covalently linked SH3 domain, which hence must exist not only in a state where it interacts with the DH-PH tandem.

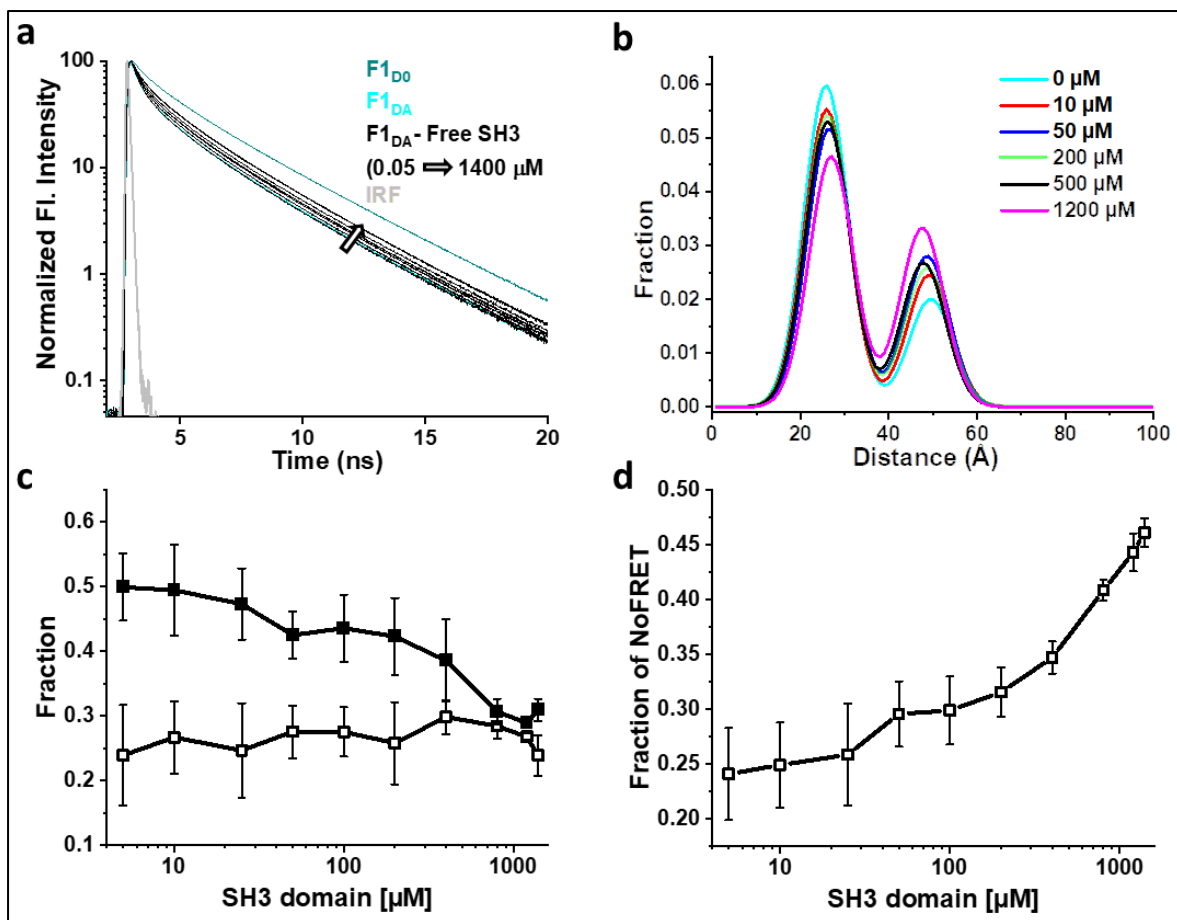


Figure 2.5 (Supplementary Figure 3 in the manuscript). Free-SH3 domain mediates CB opening. (a) Time-resolved fluorescence intensities of the CB FRET sensor F1_{D0} (teal), F1_{DA} in the absence (cyan) and presence (black) of increasing concentrations of free-SH3 domain. Data were scaled to a maximum of 100 for easier comparison. **(b)** Distance distribution for the F1_{DA} sensor with increasing concentrations of free SH3 domain. **(c)** Fraction of F1_{DA} molecules in the closed/high FRET state (solid black squares) and their gradual transition into the open/low FRET state (unfilled black squares) upon addition of free SH3 domain. **(d)** x_{noFRET} of the F1_{DA}-SH3 complex increases with increasing concentrations of GephFL. Again, this indicates another state with distances >49 \AA .

Encouraged by these initial results, we performed titration experiments to quantify the binding affinity between CB and GephFL (Fig. 2.4b). With increasing (0.05 to 400 μM) GephFL concentrations, a concomitant increase in $F_{1\text{DA}} \langle \tau \rangle_x$ was observed, reaching saturation at a GephFL: $F_{1\text{DA}}$ molar ratio of 100:1 (Fig. 2.4 b-c). In contrast, when titrating with the free SH3 domain, saturation was only obtained at a SH3: $F_{1\text{DA}}$ 1200:1 molar ratio (Fig. 2.4c and Fig. 2.5a). By plotting the fractional saturation determined from the corresponding $\langle \tau \rangle_x$ (eq. 4) against the GephFL and SH3 concentrations, the dissociation constants (K_D) of the $F_{1\text{DA}}$ -GephFL and $F_{1\text{DA}}$ -SH3 complexes were assessed as $4.5 \pm 1.7 \mu\text{M}$ and $373 \pm 116 \mu\text{M}$, respectively (eq. 5, Fig. 2.4c and Fig. 2.5a). These results indicate that GephFL and CB interaction is moderately tight, while the SH3 domain has a low affinity towards CB. Previous microscale thermophoresis (MST) data (Soykan et al., 2014) with the free SH3 and the tandem DH-PH domains yielded a K_D of $273 \pm 34 \mu\text{M}$, similar to the value obtained here. The interaction strength between $F_{1\text{DA}}$ and NL2_{icd} could not be quantified as no systematic increase in $\langle \tau \rangle_x$ of CFP was observed when further incubated with excess (more than 100 μM) of NL2_{icd}.

2.5.3. Two state dynamics during CB activation

To understand the mode of CB activation, we analyzed the time-resolved fluorescence intensities of $F_{1\text{DA}}$ and $F_{1\text{DA}}$ -GephFL complexes at various concentrations by Gaussian distance distribution models (eq. 9). From Fig. 2.6a, it is evident that fitting with two FRET species with a Gaussian distance ($R(i)$) distribution and a NoFRET (X_{NoFRET}) state is significantly better than assuming only a single FRET species, while three FRET species led to no further improvement. The half-widths of the Gaussian distributions were kept fixed to 5 \AA . The results suggested that the $F_{1\text{DA}}$ molecules exist in two conformational states, a high-FRET and a low-FRET state (Fig. 2.6b). The high FRET state exhibited an average inter-fluorophore distance (R_1) of $25.5 \pm 0.5 \text{\AA}$, while the low FRET state showed an average inter-fluorophore distance (R_2) of $45.5 \pm 0.9 \text{\AA}$ (Table 2.1). Considering the size of CFP (diameter $\sim 20 \text{\AA}$), the distance of the high FRET state indicates that the F₁AsH and CFP fluorophores are in very close proximity, in line with a compact/closed conformation, while $F_{1\text{DA}}$ adopts an open state in the low FRET state.

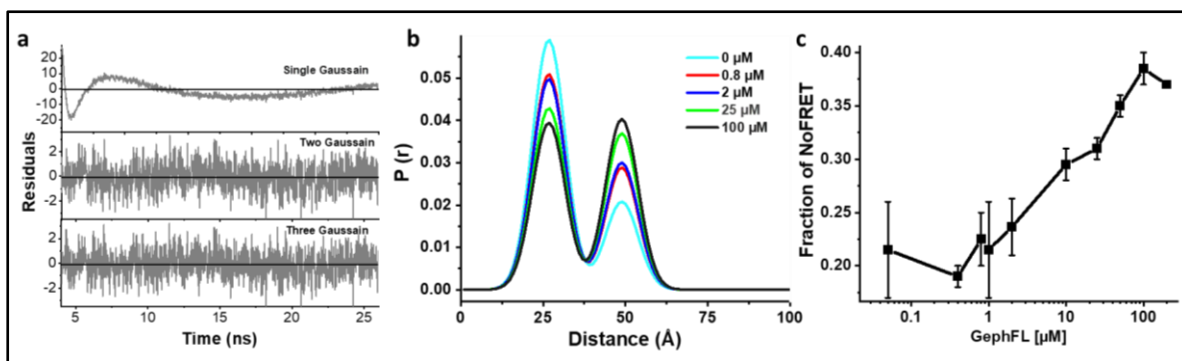


Figure 2.6 (Supplementary Figure 2 in the manuscript). Gaussian distributed distance fitting. (a) Weighted residuals for fitting of the F1_{DA}-labeled CB FRET sensor (F1_{DA}) with one ($\chi_r^2 = 47.14$), two ($\chi_r^2 = 1.14$) or three ($\chi_r^2 = 1.12$) Gaussian distributed distances with a width of 5 Å. **(b)** The distance distribution based on the two-state Gaussian distribution model shows that the fraction of the high FRET state decreases, and the fraction of the low FRET state increases with higher concentrations of GephFL. **(c)** Increase of the No-FRET fraction, x_{NoFRET} , of the F1_{DA}-GephFL complex with increasing concentrations of GephFL, which may indicate the existence of an additional state exhibiting an inter-fluorophore distance $>49\text{Å}$ where the F1_{DA}-CFP FRET pair is blind.

While gradual addition of GephFL did not induce any significant changes in the inter-fluorophore distances, it shifted the equilibrium towards the low FRET state (Fig. 2.4d and Fig. 2.6b). It must be noted that increasing GephFL concentrations led to a stronger population of the x_{NoFRET} state (Fig. 2.6c), possibly indicating another state beyond the measurable FRET distance limit ($>49\text{Å}$) for this FRET pair (Algar et al., 2019). The fluorescence lifetime-based FRET study along with distance distribution analysis of F1_{DA} provides concrete evidence of GephFL-mediated CB opening and its transition from the closed to an open state. Binding of the free SH3 domain also resulted in a concentration-dependent increase in the low-FRET F1_{DA} state and a simultaneous decline in the high-FRET F1_{DA} population (Fig. 2.5b-c), suggesting a displacement of the SH3 domain present in F1_{DA} by the isolated SH3 domain. Again, we observed that rising SH3 concentrations resulted in a x_{NoFRET} increase (Fig. 2.5d).

2.5.4. The E domain of gephyrin mediates CB binding and activation

Next, we investigated which region of gephyrin mediates the interaction with CB by employing constructs containing only the G domain (GephG), the linker followed by the E domain (GephLE), and the isolated E domain (GephE) of gephyrin. The purified variants

(GephG, GephLE and GephE) were incubated with F1_{D0} and F1_{DA}, and fluorescence lifetime measurements were performed.

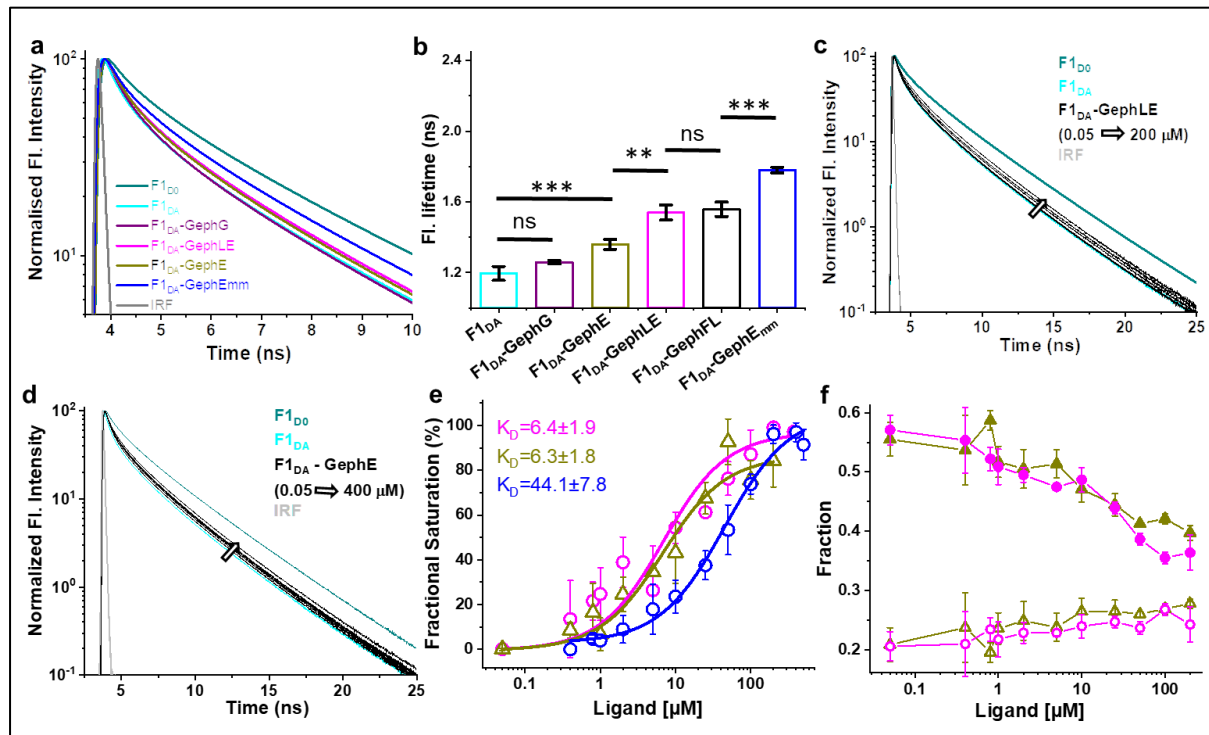


Figure 2.7 (Figure 4 in the main manuscript). Gephyrin E domain mediates CB activation (a) Time-resolved fluorescence intensities of CFP in F1_{D0} (teal), F1_{DA} (cyan) and in the presence of 100 μM GephG (purple), GephE (dark yellow) and GephLE (magenta) with IRF in light grey. Data were scaled to a maximum of 100 for easier comparison. **(b)** Bar graph showing the observed species-weighted average fluorescence lifetime of CFP in F1_{DA} (cyan) and in the presence of GephG (purple), GephE (olive), GephLE (magenta) and the monomeric E domain variant (GephEmm, blue). **P < 0.05, ***P < 0.005; ns, statistically not significant. **(c-d)** Fluorescence lifetimes of the CB FRET sensor F1_{D0} (teal), F1_{DA} in the absence (cyan) and presence (black) of increasing molar concentrations of GephLE (c) and GephE domain (d), respectively. **(e)** Binding affinity curves for GephLE (magenta), GephE (olive) and GephEmm (blue) determined based on the average fluorescence lifetime converted into fractional saturation using eq. 5. Curves are fitted with eq. 8 (see Methods) to determine the K_D for GephLE, GephE and GephEmm. Data from three different batches of experiments are presented as mean values ± SD. **(f)** Plot of the contribution of the two FRET species (high FRET state and low FRET state) against the concentrations of GephLE (triangle) and GephE (circle) obtained when analyzing the time-resolved fluorescence intensities with the Gaussian distribution model (eq. 9). The high FRET state (R₁, filled circle and triangle) decreases, and the low FRET (R₂, open circle and triangle) state increases with increasing concentrations of both ligands.

Fig. 2.7a-b shows the $\langle\tau\rangle_x$ changes in F1_{DA} when incubated with the domain variants. At comparable concentrations of 100 μM, GephLE showed the highest increase in $\langle\tau\rangle_x$ with

1.54 ± 0.04 ns, followed by GephE (1.36 ± 0.02 ns) (Fig. 2.7a-b, Table 2.1). In contrast, GephG (1.26 ± 0.01 ns) did not display a fluorescence lifetime change, thus confirming previous studies reporting that the G domain is not involved in the interaction with CB (Tyagarajan & Fritschy, 2014; Tyagarajan, Ghosh, Harvey, et al., 2011). Note, the incubation of F1_{D0} with the domain variants, as observed before for GephFL, did not alter $\langle\tau\rangle_x$ of CFP (Table 2.2). Taken together, these data suggest that GephE with a possible minor contribution from the linker mediates interaction and opening of CB.

To further map the binding site, we individually titrated F1_{DA} with GephLE and GephE. F1_{DA} displayed a concentration-dependent increase in $\langle\tau\rangle_x$ for both domain variants (Fig. 2.7 c-d). We quantified the binding strengths by plotting the fractional saturation based on the change in F1_{DA} $\langle\tau\rangle_x$ (eq. 4) upon increasing GephLE and GephE concentrations, respectively. Both, GephLE and GephE displayed identical affinities with K_D values of 6.4 ± 1.9 μM and 6.3 ± 1.8 μM, respectively (Fig. 2.7e, eq. 5). Subsequently, we examined, how GephLE and GephE mediate the high-FRET to low-FRET transition in F1_{DA}. In line with their identical affinities, GephLE and GephE displayed comparable concentration-dependent effects in transitioning from the high-FRET/closed state to the low-FRET/open F1_{DA} state (Fig. 2.7f). Like GephFL, both GephLE and GephE exhibited an increase of x_{NoFRET} with higher concentrations of both ligands (Fig. 2.7f). Hence, the fluorescence lifetime-based affinity interaction study with F1_{DA} demonstrated that the E-domain solely mediates the interaction with CB.

2.5.5. A monomeric E-domain induces a stronger CB conformational change

As GephE forms a dimer in its native state, we next checked whether GephE dimerization plays a role in its recognition by CB. To investigate this aspect we recombinantly purified a dimerization-deficient, monomeric mutant of GephE (GephE_{mm}) described earlier (Saiyed et al., 2007) (Fig. 2.8a). We then measured the $\langle\tau\rangle_x$ change observed for F1_{DA} in the presence of GephE_{mm} and compared it to that of GephE (Fig. 2.7a-b). Surprisingly, at comparable concentrations, GephE_{mm} displayed a longer lifetime (1.78 ± 0.02 ns) compared to GephE (1.36 ± 0.03 ns) (Table 2.1), implying that GephE_{mm} possesses a higher potential for changing the conformation of CB.

To investigate the binding strength of GephE_{mm} we titrated F1_{DA} with increasing concentrations of GephE_{mm} (Fig. 2.8b) and quantified the results. Unexpectedly, GephE_{mm} displayed a significantly lower affinity with a K_D value of $44.1 \pm 7.8 \mu\text{M}$ (Fig. 2.7e, eq. 5) compared to GephE ($6.3 \pm 1.8 \mu\text{M}$).

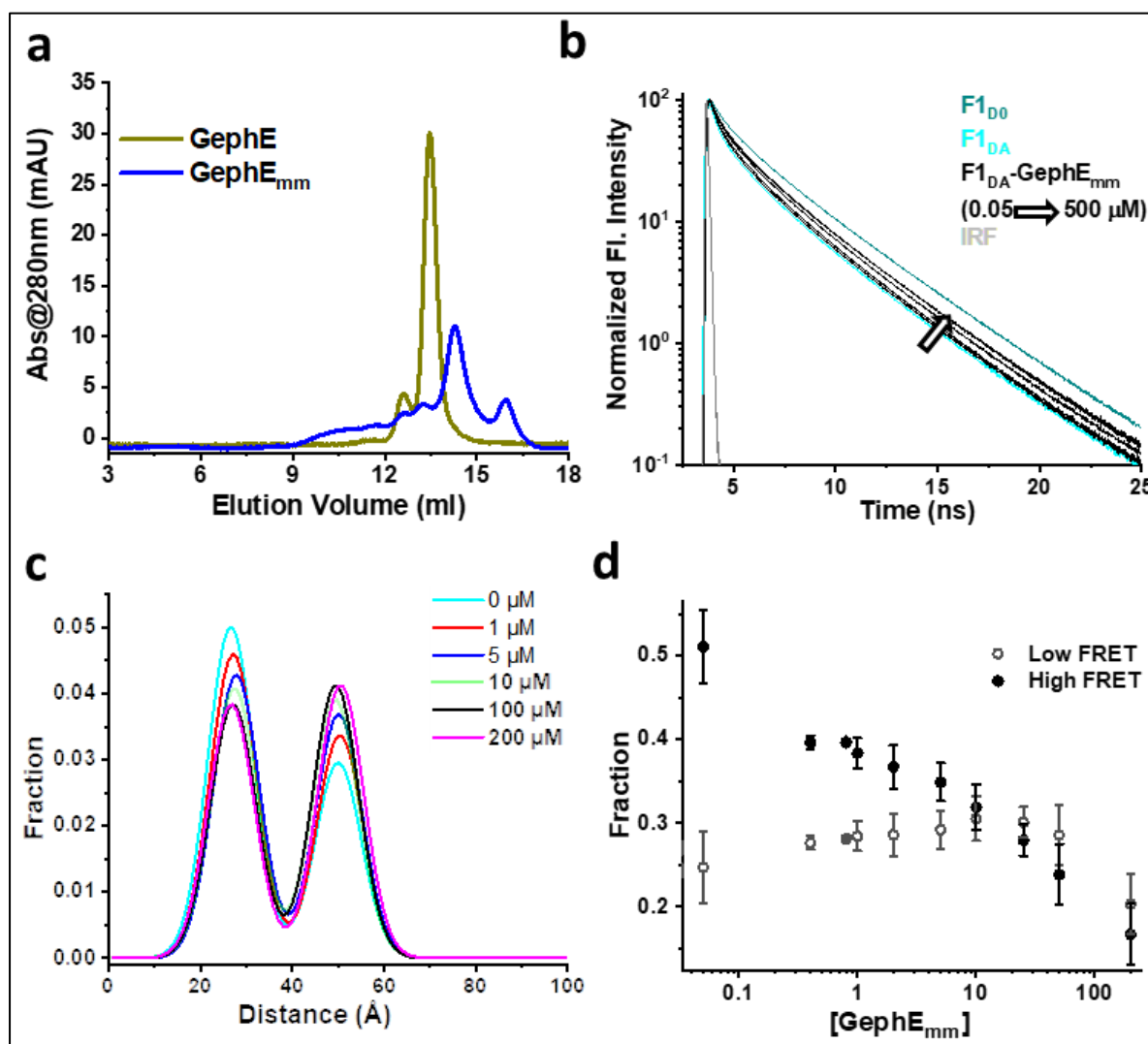


Figure 2.8 (Supplementary Figure 5 in the main manuscript). GephE_{mm} mediates CB opening. (a) Size exclusion chromatography profile of GephE (yellow) and GephE_{mm} (blue). (b) Time-resolved fluorescence intensities of CFP in F1_{D0} (teal), F1_{DA} alone (cyan) and in the presence of increasing concentrations of GephE_{mm} (black). Data were scaled to a maximum of 100 for easier comparison. (c) Gaussian distance distribution analysis shows the decrease of the fraction of high FRET and concomitant increase in the fraction of the low FRET state with increasing concentrations of GephE_{mm}. (d) Fraction of F1_{DA} molecules in the closed/high FRET state (filled circles, black) and their transition into the low FRET F1_{DA} state (empty circle) upon addition of GephE_{mm}.

To better understand the conformational changes induced in F1_{DA} by GephE_{mm} we

performed distance distribution fittings for both constructs as described for GephFL. GephE_{mm} was found to be more potent in turning the high FRET F1_{DA} molecules into a low FRET population compared to GephE/LE (Fig. 2.8c-d), however, the inter-fluorophore distance for the high FRET (R₁) and low FRET (R₂) molecules remained relatively unchanged for GephE (R₁ = 23.6 ± 0.4 Å and R₂ = 46.5 ± 1.8 Å) and GephE_{mm} (R₁ = 24.5 ± 0.2 Å and R₂ = 43.7 ± 0.3 Å) (Table 2.1). Hence, comparative fluorescence lifetime changes along with analyses of distance distribution results for GephE and GephE_{mm} clearly depict that GephE dimerization is not crucial for the CB-gephyrin interaction.

2.5.6. Active state mutant sensors design and characterization

A previous study reported that residues Trp24 and Arg70, which are located in the SH3 domain, and Glu262 in the DH domain play crucial roles in modulating the equilibrium between the inactive and active conformations in full-length CB (Soykan et al., 2014). The W24A and E262A variants promote the formation of the open state, which, with respect to its role in inhibitory synapse formation, is considered to be the active state (Soykan et al., 2014). Small angle X-ray scattering (SAXS) and atomic force microscopy (AFM) data indicated a more extended conformation for the E262A single mutant, in contrast to the compact state of wild-type CB (Soykan et al., 2014). The W24A/E262A double mutant could not be analyzed by these biophysical techniques due to enhanced instability of the protein (Soykan et al., 2014). In our current study, however, where only low protein concentrations are required, we could carry out experiments with the single (F1_{smDA}) as well as the double mutant (F1_{dmDA}) CB FRET sensor.

The $\langle\tau\rangle_x$ of CFP in F1_{smD0} (2.14 ± 0.02 ns) and F1_{dmD0} (2.10 ± 0.01 ns) in the absence of the F_{lAsH}, were identical to that observed for F1_{D0} (2.16 ± 0.06 ns) (Fig. 2.9 a-b; Fig 2.10a, Tables 2.1 and 2.3). In contrast, the F_{lAsH} labeled sensors F1_{smDA} (0.32 ± 0.01 ns) and F1_{dmDA} (0.35 ± 0.01 ns) displayed a substantial decrease in the average CFP fluorescence lifetime compared to the wild-type sensor with 1.2 ± 0.04 ns (Fig. 2.9 a-b; Fig 2.10a; Tables 2.1 and 2.3). At the same time, F1_{smDA} and F1_{dmDA} exhibited comparable E_{FRET} (~84%), indicating that the mutations bring the donor and acceptor of the FRET pair into close spatial proximity which is drastically different from the F1_{DA} E_{FRET} of 44%. Next, we checked the effect of GephFL upon interaction with the mutant sensors. As expected, no

$\langle\tau\rangle_x$ change was observed in $F1_{smD0}$ and $F1_{dmD0}$ upon GephFL interaction (Table 2.3). However, to our surprise, an interaction of GephFL with $F1_{smDA}$ and $F1_{dmDA}$ resulted in a drastic increase in their average fluorescence lifetimes to 0.62 ± 0.01 ns and 0.64 ± 0.02 ns, respectively (Fig. 2.9 a-b; Fig. 2.10a; Table 2.3), indicating a substantial increase in inter-fluorophore distance upon GephFL binding.

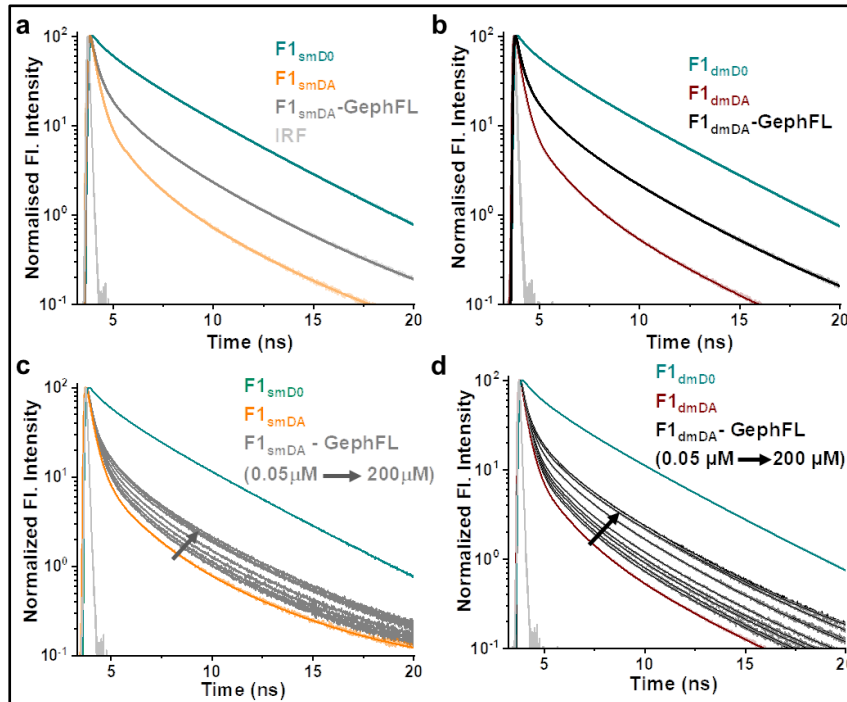


Figure 2.9 (Supplementary Figure 6 in the manuscript). Open state mutant sensor characterization. (a) CFP fluorescence intensity decay of the single mutant FRET sensor $F1_{smD0}$ (teal) and the FAsH labeled single mutant $F1_{smDA}$ sensor in the absence (light red) and presence (grey) of GephFL. **(b)** Fluorescence intensity decay of the double mutant FRET sensor $F1_{dmD0}$ (teal) and the FAsH labeled double mutant FRET sensor $F1_{dmDA}$ in the absence and presence of GephFL in dark red and black, respectively. **(c-d)** Fluorescence intensity decays of $F1_{smDA}$ (c) and $F1_{dmDA}$ (d) in the presence of varying concentrations of GephFL. Data were scaled to a maximum of 100 for easier comparison. IRF is shown in light grey.

FRET sensor $F1_{smDA}$ in the absence and presence of GephFL in dark red and black, respectively. (c-d) Fluorescence intensity decays of $F1_{smDA}$ (c) and $F1_{dmDA}$ (d) in the presence of varying concentrations of GephFL. Data were scaled to a maximum of 100 for easier comparison. IRF is shown in light grey.

Samples	$\langle\tau\rangle_x$ (\pm SD) ns	$E_{\langle\tau\rangle_x}$ [%]
$F1_{smD0}$	2.14 (\pm 0.02)	-
$F1_{smDA}$	0.32 (\pm 0.01)	84
$F1_{smD0}$ + GephFL	2.12 (\pm 0.01)	-
$F1_{smDA}$ + GephFL	0.62 (\pm 0.01)	71
$F1_{dmD0}$	2.10 (\pm 0.01)	-
$F1_{dmDA}$	0.35 (\pm 0.01)	83
$F1_{dmD0}$ + GephFL	2.11 (\pm 0.01)	-
$F1_{dmDA}$ + GephFL	0.64 (\pm 0.02)	69

Table 2.3 (Supplementary Table 10 in the manuscript). Average fluorescence lifetimes ($\langle\tau_x\rangle$) of single ($F1_{smD0}$) and double mutant ($F1_{dmD0}$) CB FRET sensors, their FAsH labeled counterparts $F1_{smDA}$ and $F1_{dmDA}$ in the absence and presence of full-length gephyrin (GephFL). Data from three different batches of experiments are presented as mean values \pm SD.

We also investigated the GephFL affinity for the open state mutant sensors and hence separately titrated $F1_{smDA}$ and $F1_{dmDA}$ with increasing concentrations of GephFL. GephFL titration with $F1_{smDA}$ and $F1_{dmDA}$ led to a

gradual increase in their $\langle\tau\rangle_x$ followed by saturation (Fig. 2.9c-d). As assessed from the binding affinity values (Fig. 2.10b) of $F1_{smDA}$ ($K_D = 47 \pm 14 \mu\text{M}$) and $F1_{dmDA}$ ($K_D = 43 \pm 11 \mu\text{M}$), both exhibited a comparable and moderately strong binding affinity for GephFL. Interestingly, the GephFL binding affinity for the open state sensors was comparable to that of the wild-type sensor ($F1_{DA}$).

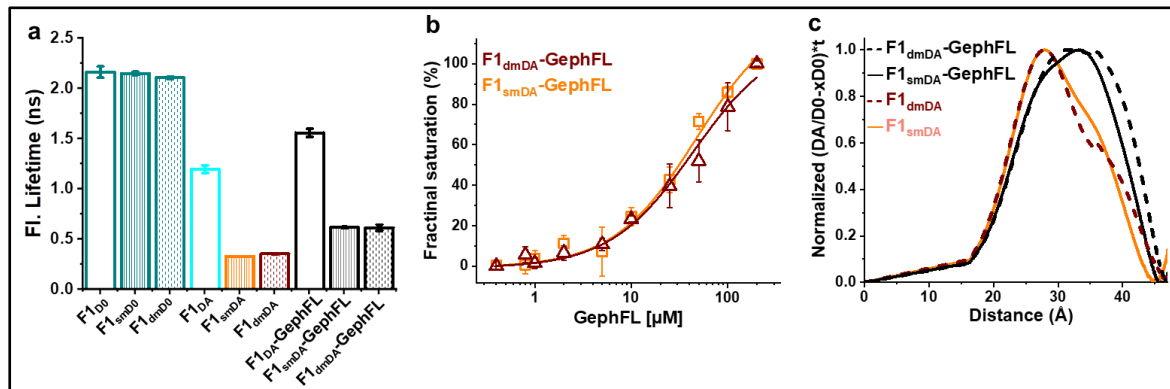


Figure 2.10 (Figure 5 in the manuscript). Mutant sensor construction and characterization. (a) Bar graph showing the species-weighted average fluorescence-lifetime of the CB wild-type, single mutant (*sm*) and double mutant (*dm*) FRET sensors prior to ($F1_{D0}$, $F1_{smD0}$ and $F1_{dmD0}$), after FLaSH labeling ($F1_{DA}$, $F1_{smDA}$ and $F1_{dmDA}$) and the FLaSH labeled sensors in the presence of a 100-fold molar excess of GephFL. **(b)** GephFL binding affinity plot of $F1_{smDA}$ (orange) and $F1_{dmDA}$ (wine). Binding affinities were determined by first converting $\langle\tau\rangle_x$ into the fractional saturation using eq. 4. and the data were further fitted with eq. 5. The GephFL binding affinity constant (K_D) for $F1_{smDA}$ and $F1_{dmDA}$ were measured as $47 \pm 14 \mu\text{M}$ and $43 \pm 11 \mu\text{M}$, respectively. Data from three different batches of experiments are presented as mean values \pm SD. **(c)** Model-free description of the inter-fluorophore distance distribution underlying the time-resolved fluorescence intensities (eq. 12-13). Normalized distance distribution curves shown for $F1_{smDA}$ and $F1_{dmDA}$ in the absence and presence of GephFL. $F1_{smDA}$ and $F1_{dmDA}$ show a major peak at 28\AA and a shoulder at 36\AA , which is significantly different from $F1_{DA}$, particularly for the major peak located in this case at $\sim 43 \text{\AA}$ (Fig. S9 d). Upon complexation with GephFL the major peak shifts to 36\AA with a weak shoulder at $\sim 28 \text{\AA}$.

Our studies with the mutant sensors corroborate previous data (Soykan et al., 2014), which suggest that the disruption of the intramolecular interaction leads to a conformational switch within CB. We also tried to analyze the fluorescent lifetimes with a Gaussian distance distribution model (eq. 11), however, the fast exponential decay of the fluorescent intensities in the beginning for both $F1_{smDA}$ and $F1_{dmDA}$ sensors made the fitting with the Gaussian distance distribution model challenging. Thus, we followed a model-free approach reported earlier (Peulen et al., 2017) to visualize the distance distribution underlying the time-resolved fluorescence intensities of $F1_{smDA}$ and $F1_{dmDA}$

(Fig. 2.10c; Fig. 2.11-2.12). For comparison, we analyzed the $F1_{DA}$ and $F1_{DA}$ -GephFL time-resolved fluorescent intensities in the same way (Fig. 2.13).

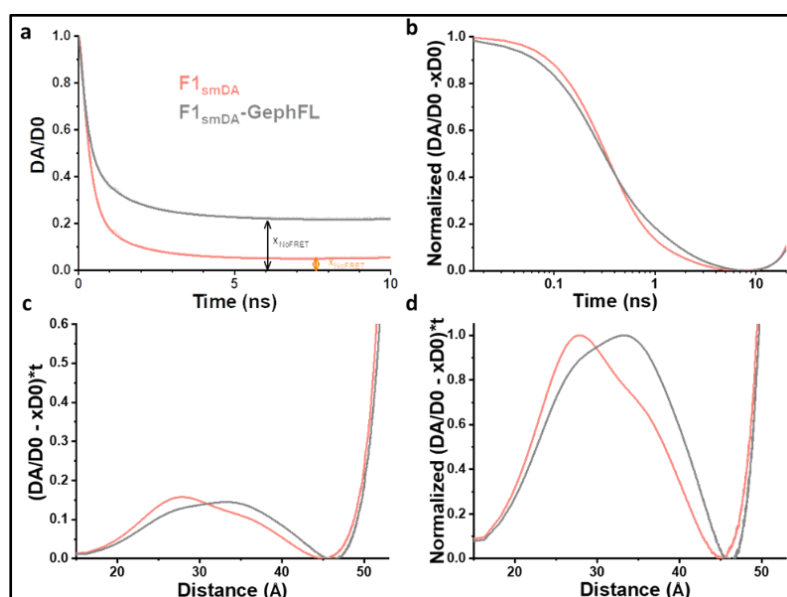


Figure 2. 11 (Supplemental Figure 7 in the manuscript). Model-free visualization of the distance distribution underlying the time-resolved fluorescence intensities of $F1_{smDA}$ in the absence and presence of GephFL. (a) Time-resolved fluorescence intensity of the double-labeled sample $I_{F1_{smDA}}(t)$ is divided by the single-labeled sample $I_{F1_{smD0}}(t)$. The offset values are the corresponding X_{NoFRET} values (~ 0.05 for $F1_{smDA}$ and ~ 0.25 for $F1_{smDA}$ -GephFL). (b) Fraction of molecules not showing FRET (X_{noFRET} or X_{D0}) – the constant offset in (A) – is subtracted and the time scale is logarithmic. (c) Time-axis is converted to the distance axis (eq. 11 main text). (d) Probability density distribution of the underlying distance distribution is normalized to 1 for easier comparison.

for $F1_{smDA}$ and ~ 0.25 for $F1_{smDA}$ -GephFL). (b) Fraction of molecules not showing FRET (X_{noFRET} or X_{D0}) – the constant offset in (A) – is subtracted and the time scale is logarithmic. (c) Time-axis is converted to the distance axis (eq. 11 main text). (d) Probability density distribution of the underlying distance distribution is normalized to 1 for easier comparison.

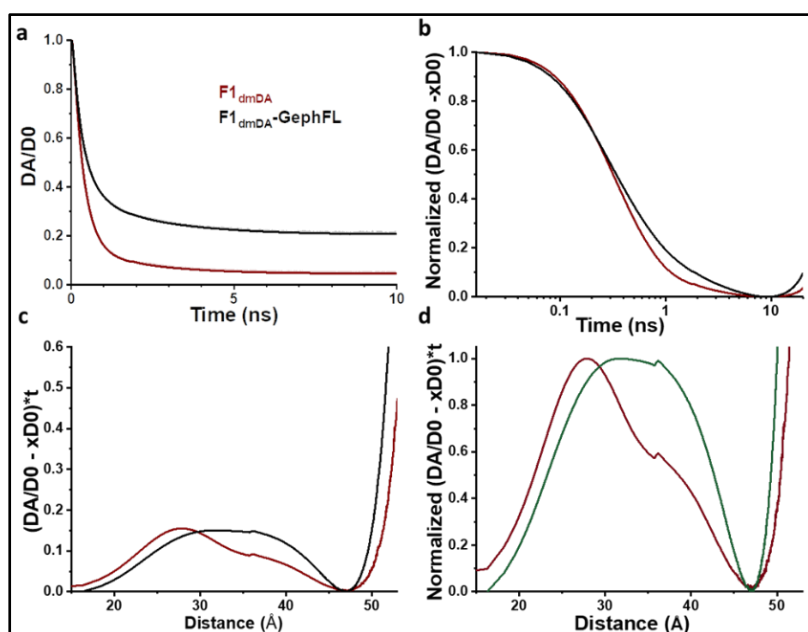


Figure 2.12 (Supplemental Figure 8 in the manuscript). Model-free visualization of the distance distribution underlying the time-resolved fluorescence intensities of $F1_{dmDA}$ in the absence and presence of GephFL. (a) Time-resolved fluorescence intensity of the double-labeled sample $I_{F1_{dmDA}}(t)$ is divided by the single-labeled sample $I_{F1_{dmD0}}(t)$. (b) Fraction of molecules not showing FRET (X_{noFRET} or X_{D0}) – the constant offset in (A) – is subtracted and the time scale is logarithmic. (c) Time-axis is converted to distance axis (eq. 11 main text). (d) Probability density distribution of the underlying distance distribution is normalized to 1 for easier comparison.

the constant offset in (A) – is subtracted and the time scale is logarithmic. (c) Time-axis is converted to distance axis (eq. 11 main text). (d) Probability density distribution of the underlying distance distribution is normalized to 1 for easier comparison.

The distance distributions of $F1_{smDA}$ and $F1_{dmDA}$ revealed a main peak around 28 Å and a shoulder around 36 Å, indicating a disruption in the intra-molecular interaction between the SH3 and DH domains, which concomitantly became more flexible, in both the single and double mutant (Fig. 2.10c). Thus, the F1AsH present at the N-terminus and CFP at the C-terminus move closer to each other, as reflected in the main peak at 28 Å (high FRET state), while a second peak around 36 Å is observed (low FRET state).

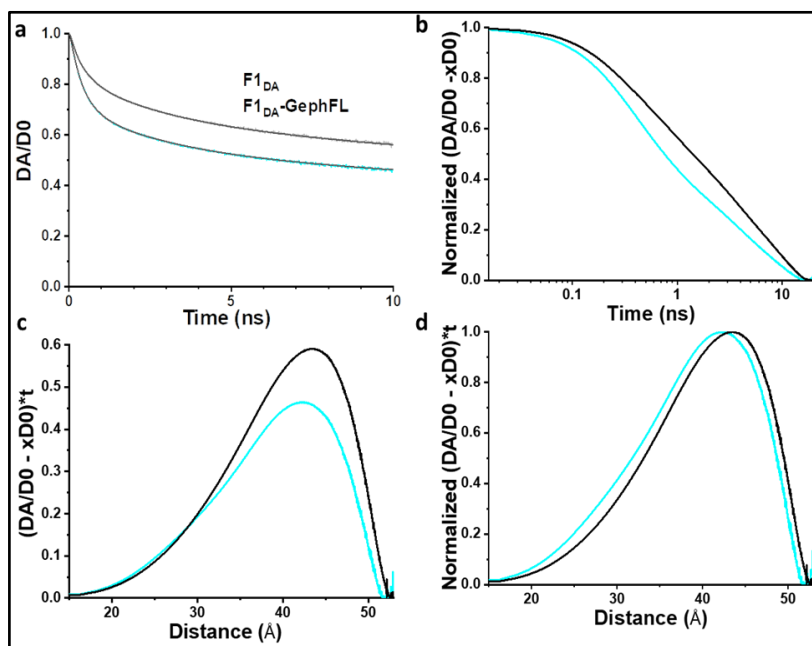


Figure 2.13. (Supplemental Figure 9 in the manuscript). Model-free visualization of the distance distribution underlying the time-resolved fluorescence intensities of $F1_{DA}$ in the absence and presence of GephFL. (a) Time-resolved fluorescence intensity of the double-labeled sample $I_{F1smDA}(t)$ is divided by the single-labeled sample $I(a)_{F1smD0}(t)$. (b) Fraction of molecules not showing FRET (X_{noFRET} or $xD0$) – the constant

offset in (A) – is subtracted and the time scale is logarithmic. (c) Time-axis is converted to distance axis (eq. 11 main text). (d) Probability density distribution of the underlying distance distribution is normalized to 1 for easier comparison.

Upon ligand interaction the $F1_{smDA}$ sensor showed a shift of the main peak from 28 Å to 36 Å with a minor shoulder at 28 Å, further indicating that the distance between the donor and acceptor increases upon ligand interaction. A similar type of distance shift was also observed for $F1_{dmDA}$ upon interaction with GephFL. In contrast, in case of $F1_{DA}$ and the $F1_{DA}$ -GephFL complex (Fig. 2.13), the main peak is at ~43 Å (low FRET) with a small shoulder at ~25 Å (high FRET). Thus, the high FRET population is strongly increased in case of $F1_{smDA}$ and $F1_{dmDA}$ compared to $F1_{DA}$ and the $F1_{DA}$ -GephFL complex, indicating that the opening of the structure due to mutations is different from the opening caused by ligand interaction of the wild type CBFRET sensor.

2.5.7. Gephyrin binding elicits differential responses in a series of FRET sensors

To investigate the orientation of the SH3 domain with respect to the DH-PH tandem during activation, we performed interaction studies of GephFL with CB constructs displaying the tCM at three additional positions: After residue 28 and 73, i.e. at the start and end of the SH3 domain, assuming that these positions should be sensitive to SH3 domain reorientations during activation, and after residue 99, close to the DH domain, for understanding DH-PH domain reorientation. Initially, CFP $\langle\tau\rangle_x$ measurements were carried out for the FAsH-labeled sensors denoted as F28_{DA}, F73_{DA} and F99_{DA} (Table 2.4). An identical $\langle\tau\rangle_x$ decrease was observed for F73_{DA} (0.79 ± 0.01 ns) and F99_{DA} (0.8 ± 0.01 ns), whereas F28_{DA} (1.2 ± 0.06 ns) showed a similar value as F1_{DA} with 1.2 ± 0.04 ns (Fig. 2.14a and 2.15a). Upon interaction with GephFL, F73_{DA} and F99_{DA} displayed a significant increase in $\langle\tau\rangle_x$ with 1.03 ± 0.02 ns and 1.2 ± 0.01 ns (2.14b and Fig. 2.15a), respectively, whereas F28_{DA} (1.4 ± 0.01) displayed a comparable change in $\langle\tau\rangle_x$ as observed for F1_{DA} (1.56 ± 0.04 ns) (Tables 2.1 and 2.4). GephFL addition to F28_{D0}, F73_{D0} and F99_{D0} did not cause any substantial change in their $\langle\tau\rangle_x$, further suggesting that GephFL binding does not alter the fluorescent properties of the attached CFP.

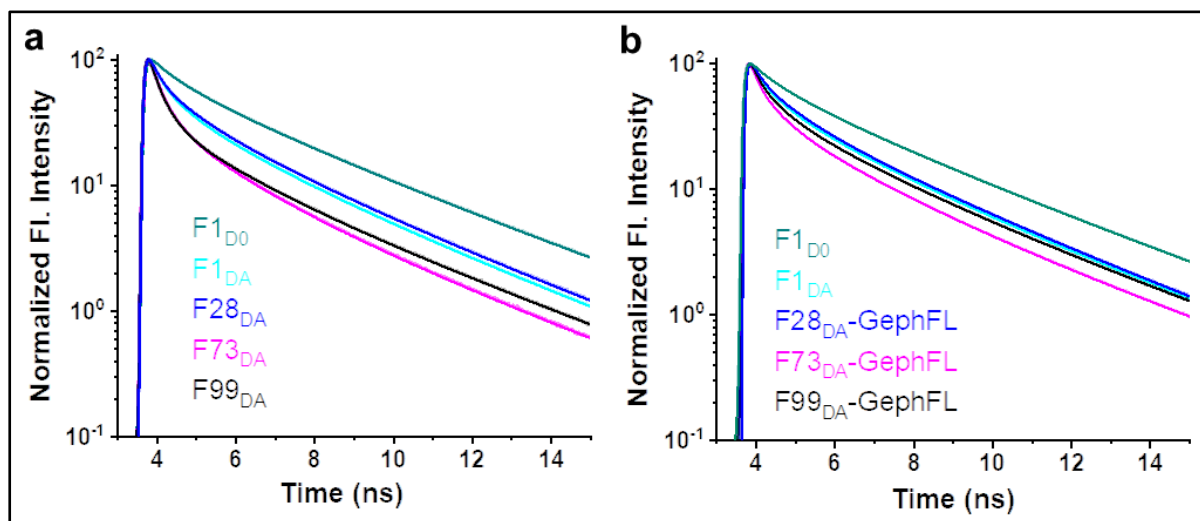


Figure 2.14 (Supplemental Figure 10 in the manuscript). Characterization of the additional CB FRET sensors. (a) Comparative fluorescence intensity decay for the series of FAsH labeled CB FRET sensors. Data were scaled to a maximum of 100 for easier comparison. Maximum quenching of the fluorescence lifetime was observed with F73_{DA}, whereas F1_{DA} and F28_{DA} showed similarly low quenching. **(b)** Fluorescence intensity decays for the FAsH labeled CB FRET sensors in the presence of full-length gephyrin. Data were scaled to a maximum of 100 in both figures for better comparison.

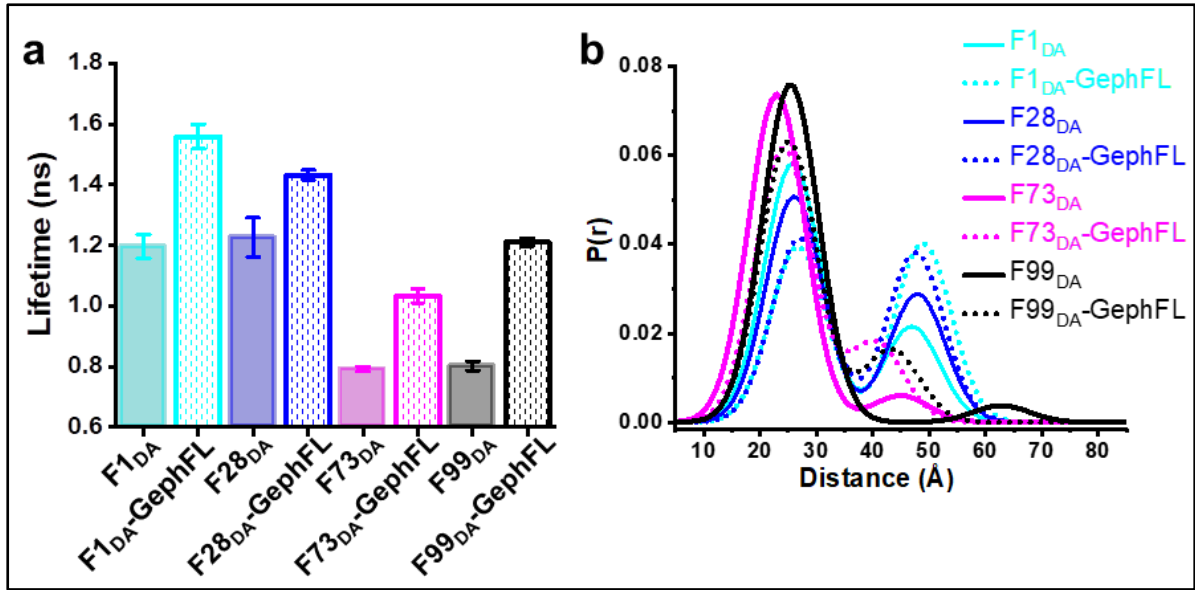


Figure 2.15 (Figure 6a-b in the manuscript). Characterization of additional CB FRET sensors. **(a)** Average fluorescence lifetime observed of $F1_{DA}$, $F28_{DA}$, $F73_{DA}$ and $F99_{DA}$ in the absence (solid bars) and presence (dotted bars) of GephFL. **(b)** Distance distribution obtained from the two Gaussian distributed distances fit model of different FLaSH labeled sensors in the absence (solid lines) and presence (dotted lines) of GephFL. In case of $F1_{DA}$ and $F28_{DA}$ the change in the low FRET state upon interaction with GephFL is larger.

Samples	$\langle\tau\rangle_x$ (\pm SD), [ns]	$E_{\langle\tau\rangle_x}$ [%]	R_1 (\pm SD) [Å]	x_1	R_2 (\pm SD) [Å]	x_2	x_{NoFRET}
$F28_{D0}$	2.11 (\pm 0.01)	-	-	-	-	-	-
$F28_{D0} + GephFL$	2.10 (\pm 0.01)	-	-	-	-	-	-
$F28_{DA}$	1.2 (\pm 0.06)	41	25.9 (\pm 1.1)	0.47 (\pm 0.02)	48.1 (\pm 0.4)	0.25 (\pm 0.02)	0.28 (\pm 0.01)
$F28_{DA} + GephFL$	1.4 (\pm 0.01)	32	26.9 (\pm 0.2)	0.33 (\pm 0.01)	47.4 (\pm 0.3)	0.29 (\pm 0.01)	0.38 (\pm 0.01)
$F73_{D0}$	2.12 (\pm 0.02)	-	-	-	-	-	-
$F73_{D0} + GephFL$	2.11 (\pm 0.03)	-	-	-	-	-	-
$F73_{DA}$	0.79 (\pm 0.01)	62	23.1 (\pm 0.4)	0.86 (\pm 0.01)	45.5 (\pm 0.2)	0.07 (\pm 0.01)	0.06 (\pm 0.01)
$F73_{DA} + GephFL$	1.03 (\pm 0.02)	51	23.8 (\pm 0.5)	0.64 (\pm 0.01)	42.2 (\pm 1.7)	0.15 (\pm 0.01)	0.20 (\pm 0.01)
$F99_{D0}$	2.1 (\pm 0.02)	-	-	-	-	-	-
$F99_{D0} + GephFL$	2.11 (\pm 0.02)	-	-	-	-	-	-
$F99_{DA}$	0.80 (\pm 0.01)	62	22.9 (\pm 0.3)	0.86 (\pm 0.01)	52.4 (\pm 1.5)	0.05 (\pm 0.01)	0.08 (\pm 0.01)
$F99_{DA} + GephFL$	1.2 (\pm 0.01)	42	24.1 (\pm 0.2)	0.59 (\pm 0.01)	42.5 (\pm 0.8)	0.12 (\pm 0.01)	0.29 (\pm 0.01)

Table2.4 (Supplementary Table 13 in the manuscript). Average fluorescence lifetimes ($\langle\tau\rangle_x$), inter-fluorophore distances (R_i) and their relative species fractions (x_i) estimated from time-resolved FRET analysis for different CB-FRET sensors having the FLaSH moiety at positions 1, 28, 73, or 99 of CB in the presence of 100 μ M full length gephyrin (GephFL). Species fractions are normalized such that $x_1 + x_2 + x_{NoFRET} = 1$. Data from three different batches of experiments are presented as mean values \pm SD.

Distance distribution studies for all sensors suggested that the absence or presence of GephFL does not alter the high-FRET and low-FRET states, indicating that all sensors including F1_{DA} displayed comparable inter-fluorophore distances (Fig.2.15b, Table 2.4). The equilibrium between the high-FRET (x_1) and low-FRET (x_2) states upon GephFL interaction is comparable to F1_{DA} in case of F73_{DA} and F99_{DA} (Table 2.4). In contrast, F28_{DA} showed a smaller equilibrium shift following GephFL binding, as is evident from the fractions of the x_1 and x_2 species (Table 2.4). It must be noted that x_{NoFRET} is very low for F73_{DA} and F99_{DA} but increases significantly for all sensors upon interaction with GephFL (Table 2.4). In summary, the results clearly indicated that GephFL induces an overall spatial shift/translocation of the SH3 and DH domain in CB during the transition from the closed to the open conformation.

2.5.8. Markov-chain Monte-Carlo sampling studies reveal CB conformations

To comprehend the overall conformational changes between the open and closed states of CB, especially with respect to SH3 domain, which can be described as “attached” and “detached” states, we performed Markov chain Monte-Carlo (MCMC) sampling studies based on the experimental distance distributions derived from our four FRET sensors (F1_{DA}, F28_{DA}, F73_{DA} and F99_{DA}), their respective uncertainties (Table 2.5), and the molecular architecture of CB.

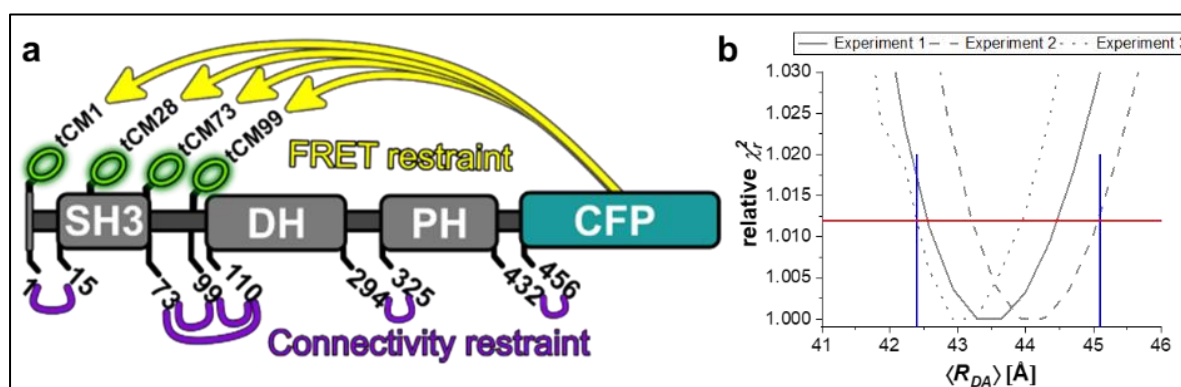


Figure 2.16 (Supplemental Figure 11 in the manuscript). FPS-based collybistin modelling. (a) Connectivity and FRET-based restraints for collybistin modelling. Small numbers denote residue numbers based on the full-length collybistin sequence to which CFP is directly attached. **(b)** Exemplary χ^2_r -surface for the F1_{DA} – CFP low FRET distance of the open, GephFL-bound state. The red horizontal line indicates the 3 σ -criterion of the $\chi_{r,rel}^2 = 1.012$, while blue vertical lines indicate the limits used for the FPS-based modelling.

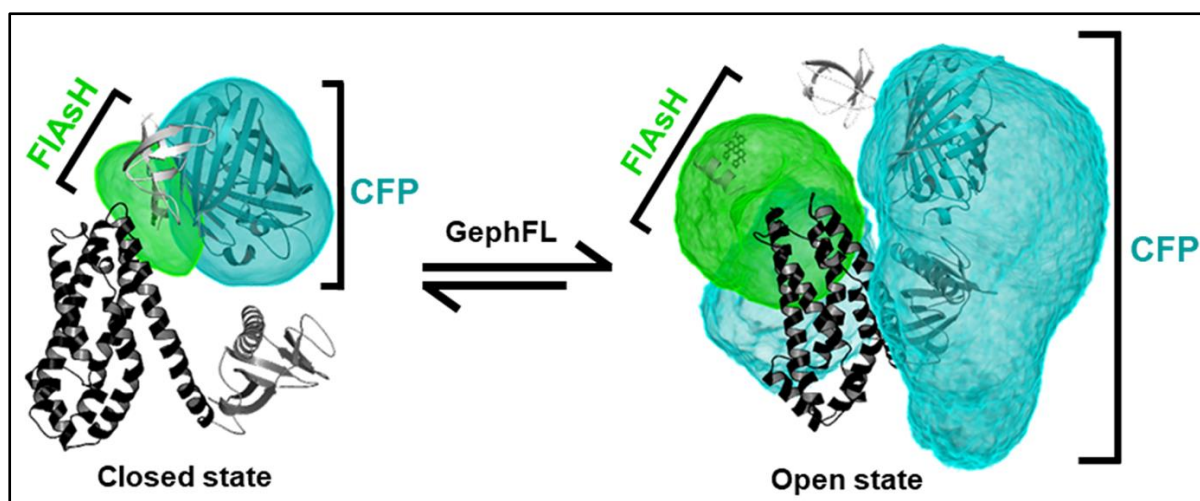


Figure 2.17 (Figure 6c in the manuscript). FRET-restraint based Markov-chain Monte Carlo (MCMC) sampling. MCMC sampling of the fluorophore positions in CB based on the experimentally obtained FRET restraints (Table 2.6), connectivity restraints (Table 2.5) and the available structures for CB-SH3- (PDB ID 4mt7) and CB-SH3+ (PDB ID 4mt6). The cyan density reflects the spatially accessible volume of CFP, whereas the green color shows the spatially accessible volume of FIAsh incorporated at residue 99. The conformational change in CB from the free to the bound state allows both fluorophores to sample a much larger volume. In the bound, open state the excluded volume due to gephyrin binding should be considered.

Comp. 1	Residue	Atom ID	Comp. 2	Residue	Atom ID	Length [aa]	Length [Å]	width [Å]
SH3	Trp 72	442	DH	Asn 106	445 (4mt6), 10 (4mt7)	35	39.4	9.5
PH	Lys 439	3291 (4mt6) 2840 (4mt7)	CFP	Lys 3	1	---	18.4	3.6
FIAsh-1	Pro 6	106	SH3	Val 18	1	17	26.7	6.5
SH3	Trp 72	442	FIAsh-99	Pro 6	106	28	35.0	8.5
FIAsh-99	Pro 6	106	DH	Asn 106	445 (4mt6), 10 (4mt7)	7	15.6	4.0

Table 2.5 (Supplementary Table 14 in the manuscript). Connectivity restraints. Components (Comp.) 1 and 2 denote the respective structural components / models to be connected. The length in amino acid residues is converted into Å assuming a worm-like chain polymer behaviour. The width of the distribution, used as uncertainty in FPS, was determined as the 1σ -interval (68% are under the curve).

As input for the MCMC sampling (Kalinin et al., 2012) the structures of CB without the SH3 domain (PDBID 4mt7) and with the SH3 domain in the closed state (PDBID 4mt6) were used and dissected into their domains connected by flexible hinges (see Methods, Table 2.6). For the sampling of the open, GephFL-bound state, the respective low FRET distances were used, while for the closed, GephFL-free state, the respective high FRET distances were used (Table 2.5). We evaluated the accessible volume of CFP, F99_{DA} (Fig.

2.17 and Fig. 2.18a) and the SH3 domain in the open and closed state. As Fig. 2.17 shows, the opening and the PH-domain rotation/tilt with respect to the DH-domain generates an “empty” space between those two domains and thus gives the C-terminally attached CFP and F99_{DA} access to a larger space, while in the closed state, both CFP and F99 are rather restricted and confined by the excluded volume of the DH-PH domains.

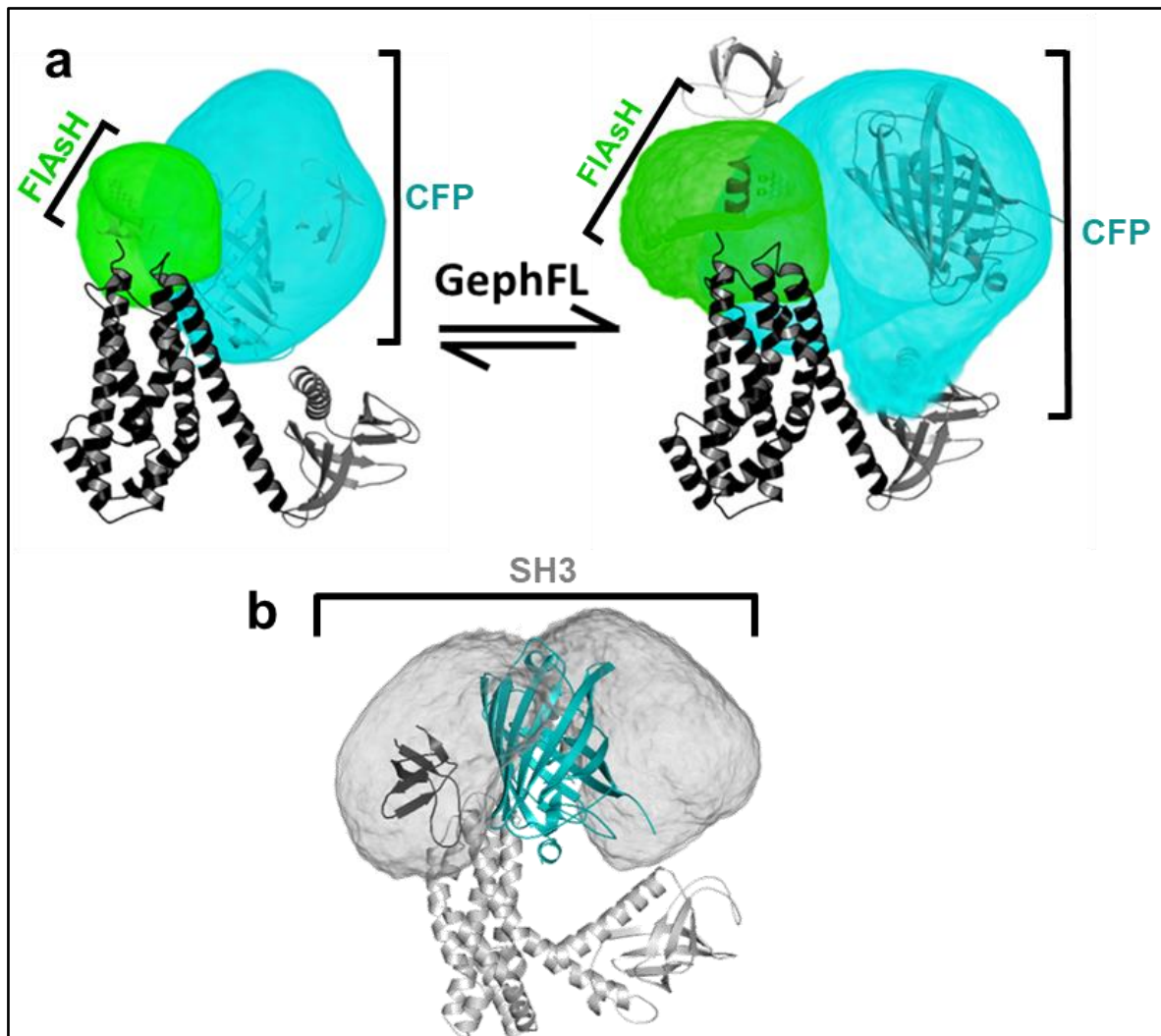


Figure 2.18 (Supplemental Figure12 in the manuscript): Results of the FRET-restrained modelling. (a) Closed state of CB modeled based on PDB ID 4mt7 and the high FRET distances (left), and the open state of CB, modeled based on PDB ID 4mt7 and the low FRET distances. The DH domain is shown in black, PH in dark grey and SH3 in light grey. The cyan cloud depicts the accessible volume of CFP, whereas the green color represents the accessible volume of F99. **(b)** Accessible volume of the SH3 domain (grey density) in the open state conformation of CB. In the open state the intramolecular interaction of the SH3 and DH domains decreases and thus the mobility of the SH3 domain increases, which, in turn, brings the N-terminal FLaSH much closer to the C-terminally attached CFP leading to an increase in FRET efficiency.

Comp. 1	Residue number	Atom ID	Comp. 2	Residue number	Atom ID	$\langle R_{DA,closed} \rangle$ [Å]	$\delta R_{DA,closed}$ [Å]	$\langle R_{DA,open} \rangle$ [Å]	$\delta R_{DA,open}$ [Å]
FLAsH-1	Pro 6	106	CFP	Leu 64*	490	22.3	2.2	43.8	1.3
FLAsH-28	Pro 6	106	CFP	Leu 64*	490	23.4	1.4	49.5	1.5
FLAsH-73	Pro 6	106	CFP	Leu 64*	490	23.4	1.6	40.1	1.6
FLAsH-99	Pro 6	106	CFP	Leu 64*	490	21.8	1.1	40.5	1.7

Table 2.6 (Supplementary Table 15 in the manuscript). Experimental FRET-based restraints. Components (Comp.) 1 and 2 denote the respective structural components / models to be connected. The mean distances and uncertainties were determined as described in methods section.

In contrast, the experimental restraints for the closed state allow a relatively large accessible volume for the SH3 domain already in the closed state, on either side of the DH domain. The sampling of the open state for the SH3 domain resulted in a large, bilobed volume surrounding the DH-PH domains (Fig. 2.18b), indicative of a less well resolved, freely diffusing SH3 domain. This large spatial offset of the SH3 domain with respect to DH-PH domain is in agreement with previous SAXS data (Soykan et al., 2014).

2.6. Discussion

Despite the fundamental importance of CB as an adaptor protein ensuring the proper function of inhibitory GABAergic synapses, its interaction with the neuronal scaffolding protein gephyrin remained poorly understood. In the present study, we address this longstanding conundrum through the aid of custom designed CB FRET sensors. Here, we provide fluorescence lifetime-based FRET data, which, along with FRET-restrained modelling studies, elucidates the molecular mechanism of autoinhibition of CB and its activation by gephyrin.

Previous studies demonstrated that activation of CB upon interacting with NL2_{icd} or TC10 leads to an open structure of CB, which allows CB to interact with phosphoinositides located in the postsynaptic membrane (Imam, Choudhury, Heinze, et al., 2022; Pouloupoulos et al., 2009; Schäfer et al., 2020; Soykan et al., 2014). The two-state Gaussian distributed distance fit of the CB F1_{DA} sensor showed an increase in the population of the low FRET state upon interaction with NL2_{icd} indicating NL2_{icd}-mediated CB opening. However, at comparable concentrations, NL2_{icd} displayed a smaller increase in average fluorescence lifetime as compared to GephFL, thus suggesting that GephFL not only interacts with but also efficiently activates CB. Compared to NL2_{icd}, GephFL even

possesses a higher capability for CB activation. Contrary to a previously hypothesized notion (Jedlicka et al., 2009; Soykan et al., 2014) our data suggest that initial CB relief by NL2 binding is not essential for gephyrin-CB complex formation.

Through the aid of the F1_{DA} FRET sensor we could successfully quantify the previously unknown binding strength of the GephFL-CB complex, yielding a reasonably tight interaction ($K_D = 4.5 \pm 1.7 \mu\text{M}$) between the two proteins (Fig. 2.4c). Furthermore, using a two-state Gaussian distributed distance fit model for F1_{DA}, we demonstrate that CB can be described as a two-state system, encompassing a compact or high FRET state and a relaxed or low FRET state (Fig. 2.6b). Quantification of CB molecules in the high and low FRET state indicated that GephFL binding shifts the equilibrium from the closed state of CB (high-FRET F1_{DA}) towards the open (low-FRET F1_{DA}) state (Fig. 2.4d). Additionally, the gradual increase of X_{NoFRET} upon addition of GephFL indicates that there might be another state beyond the measurable FRET distance of 49 Å for this FRET pair. Our FRET study therefore provides concrete evidence of GephFL-mediated CB opening, further strengthening the role of gephyrin as a CB activator. Identical affinities for GephLE ($6.4 \pm 1.9 \mu\text{M}$) and GephE ($6.3 \pm 1.8 \mu\text{M}$), along with their highly similar behavior in mediating the transition from closed to open states of CB (Fig. 2.7e), indicate that the E domain is responsible for CB activation. Additionally, a monomeric (dimerization-deficient) variant of the E domain (GephE_{mm}) was also able to facilitate CB activation, which demonstrates that GephE dimerization is not a prerequisite for its interaction with CB. However, the low binding strength ($44.1 \pm 7.8 \mu\text{M}$, Fig. 2.7e) of GephE_{mm} for F1_{DA} indicates that GephE dimerization is required to enhance its affinity for CB, potentially by stabilizing the E-domain.

The constitutively active mutant CB FRET F1_{smDA} and F1_{dmDA} sensors, somewhat counterintuitively, exhibited an increased average FRET efficiency compared to the wild-type F1_{DA} sensor. This might be because the disruption of the intramolecular SH3-DH/PH interactions rearranges the SH3 and PH domains and brings the FAsH and CFP moieties into closer proximity. A comparable $\langle\tau\rangle_x$ decrease (Fig. 2.9a-b, Table 2.3) in both mutant sensors along with their similar affinity for GephFL (Fig. 2.10), suggests that the single E262A variant is already capable of eliminating the intramolecular interactions between the SH3 domain and the DH-PH tandem, and both mutant sensors potentially attain similar tertiary structures.

Structural insights into full-length CB is limited to a low resolution apo-CB-SH3⁺ crystal structure (Soykan et al., 2014) and hence information about the SH3 domain orientation in active CB state is limited. With our series of CB FRET sensors, we could visualize the accessible space of the SH3 domain in the active state of CB (Fig. 2.17, Fig. 2.18a-b). In all sensors, GephFL addition led to an increase in the $\langle \tau \rangle_x$, thus suggesting an increase in the average inter-fluorophore distance in the respective sensors (Fig. 2.15a-b). Overall, the studies with the F28_{DA}, F73_{DA} and F99_{DA} sensors provide strong evidence for a displacement of the SH3 domain following the interaction of CB with gephyrin. Furthermore, Markov-chain Monte-Carlo (MCMC) sampling (Greife et al., 2016; Kravets et al., 2016) based on the experimentally obtained inter-fluorophore distances of the four sensors and protein domain connectivity clearly identified distinct closed and open states of CB. In the closed conformation of F99_{DA} the two fluorophores were found to be in close spatial proximity. In contrast, GephFL addition led to a clearly distinguishable open state of CB, in which the probability densities of the two fluorophores were clearly separated (Fig. 2.17; Fig. 2.18a) with enhanced CFP density being present on the opposite side of the connecting helix between the DH and PH domains. This further suggests that GephFL-mediated CB opening causes a disruption of the intramolecular interaction between the SH3 domain and DH-PH tandem, thereby also rendering the PH domain flexible and generating space between the DH-PH domains, which, in turn, can be occupied by the fluorophores. Please note that gephyrin was not present in the MCMC modelling studies, however, it would significantly restrict the space accessible to the fluorophores. As is evident from the extended density of the SH3 domain in the closed state and the presence of both low and high FRET states in the gephyrin-free measurement, our lifetime-based FRET experiments and modelling studies suggest an equilibrium between an SH3-attached and SH3-detached state already in the inactive, unbound state (Fig. 2.18b). This was not apparent in the available structure of the closed state where crystal packing forces presumably selected for a single closed state. However, only a flexibly attached SH3 domain, in equilibrium between an attached and detached state, would allow other proteins to bind in the region usually occupied by the SH3 domain. Our *in vitro* and modelling data with CB FRET sensors led us to formulate a model (Fig. 2.19) summarizing the gephyrin-mediated CB activation. Taken together, our results reveal a clear interaction between full-length gephyrin (and its domain variants) and CB an interaction

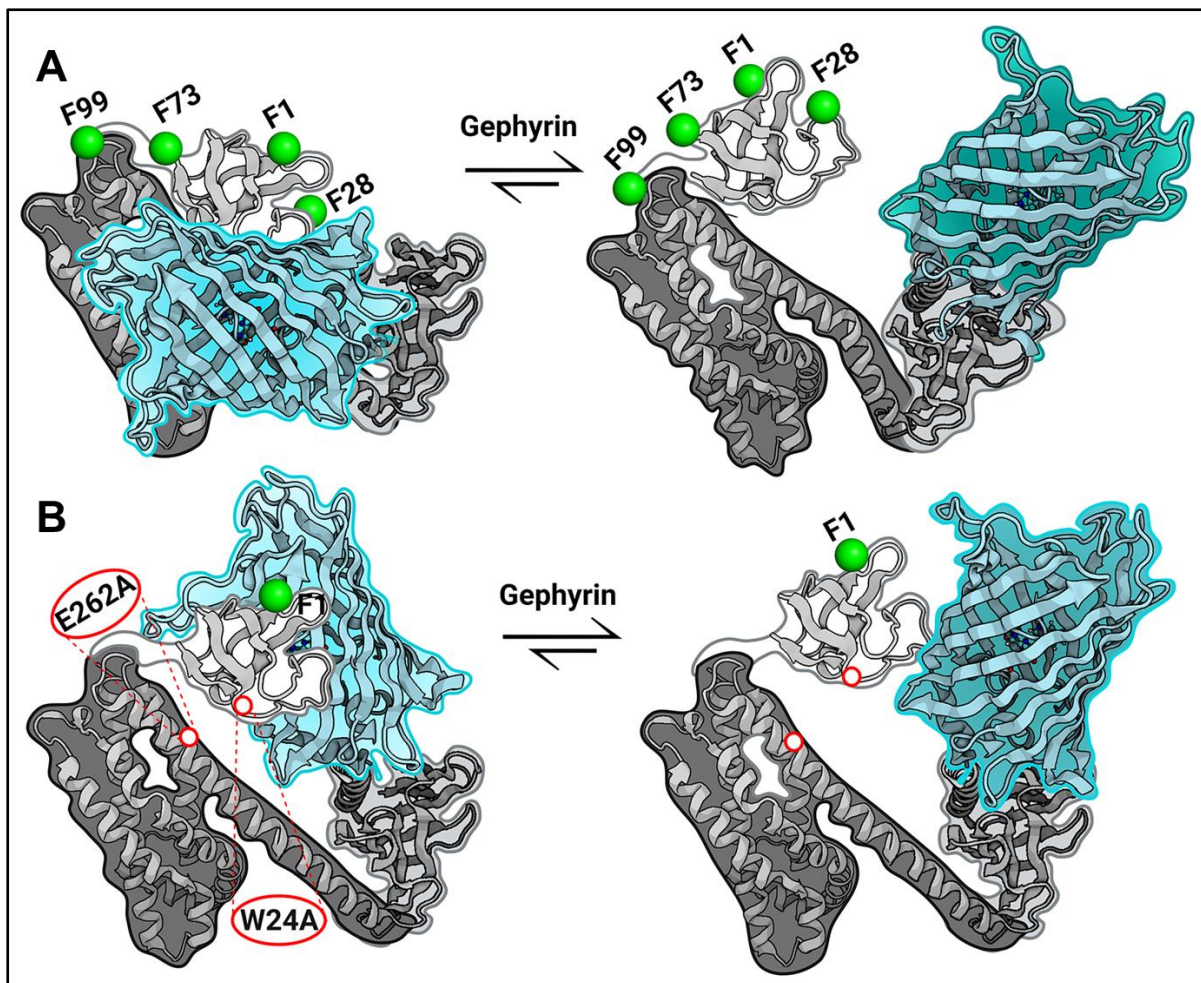


Figure 2.19 (Figure 7 in the manuscript). Schematic representation of gephyrin-mediated CB opening and complex assembly. (a) Cartoon and surface representation of full-length CB (PDBID 4mt6) in its auto-inhibited conformation depicting the individual domains (SH3; light grey with white surface, DH; black with dark grey surface and PH; grey with light grey surface). The figure illustrates the ensemble of sensors used in this study with the FLAsH attachment sites after amino acid residues 1 (F1_{DA}), 28 (F28_{DA}), 73 (F73_{DA}) and 99 (F99_{DA}) represented as green spheres, whereas CFP (cyan) was inserted after residue 456. Addition of gephyrin shifts the equilibrium towards an open state. In the closed, high FRET state, the C-terminally attached CFP exhibits significant quenching (cyan), whereas the low FRET, open state (CFP in teal) is characterized by reduced CFP quenching. (b) Cartoon representing the active state double mutant CB FRET sensor (F1_{dmDA}, the mutated residues are indicated by white dots), which is already in an open state, and its conformational change upon interaction with gephyrin.

that has been first identified more than 20 years ago (Kins et al., 2000), however, owing to technical limitations, could not be comprehensively characterized. Taken together, our data provide a framework to understand how CB acts as a dynamic molecular switch cycling between closed/inactive and open/active states in response to gephyrin binding.

2.7. Acknowledgements

We would like to thank the Seidel Lab (Molecular Physical Chemistry, Heinrich-Heine-Universität, Düsseldorf, Germany) for providing the MFD software package and Nicole Bader for excellent technical assistance.

2.8. Author contributions

N.I. generated the constructs, purified, labeled the proteins and performed the *in vitro* experiments. N.I. performed the time-resolved measurements. N.I. and S.C. analysed the results. Uncertainty analysis and MCMC modelling were done by K.H. NI, H.S., S.C., K.H. and K.G.H. prepared the manuscript. The project was supervised by H.S. and K.G.H.

3. Differential modulation of collybistin conformational dynamics by the closely related GTPases Cdc42 and TC10 ^Σ

Nasir Imam,¹ Susobhan Choudhury,² Katrin G. Heinze,^{2*} Hermann Schindelin^{1*}

¹ Institute of Structural Biology, Rudolf Virchow Center for Integrative and Translational Bioimaging, University of Würzburg, Josef-Schneider Str. 2, 97080 Würzburg, Germany.

² University of Würzburg, Rudolf Virchow Center for Integrative and Translational Bioimaging, Molecular Microscopy, Josef-Schneider Str. 2, 97080 Würzburg, Germany.

* **Correspondence:** hermann.schindelin@virchow.uni-wuerzburg.de
or
katrin.heinze@virchow.uni-wuerzburg.de

^Σ Changes incorporated (Supplemental information have been merged with main text).

Running Title: GTPase-driven activation of collybistin.

3.1. Abstract

Interneuronal synaptic transmission relies on the proper spatial organization of presynaptic neurotransmitter release and its reception on the postsynaptic side by cognate neurotransmitter receptors. Neurotransmitter receptors are incorporated into and arranged within the plasma membrane with the assistance of scaffolding and adaptor proteins. At inhibitory GABAergic postsynapses, collybistin, a neuronal adaptor protein, recruits the scaffolding protein gephyrin and interacts with various neuronal factors including cell adhesion proteins of the neuroligin family, the GABA_A receptor α 2-subunit and the closely related small GTPases Cdc42 and TC10 (RhoQ). Most collybistin splice variants harbor an N-terminal SH3 domain and exist in an autoinhibited/closed state. Cdc42 and TC10, despite sharing 67.4% amino acid sequence identity, interact differently with collybistin. Here, we delineate the molecular basis of the collybistin conformational activation induced by TC10 with the aid of recently developed collybistin FRET sensors. Time-resolved fluorescence-based FRET measurements reveal that TC10 binds to

closed/inactive collybistin leading to relief of its autoinhibition, contrary to Cdc42, which only interacts with collybistin when forced into an open state by the introduction of mutations destabilizing the closed state of collybistin. Taken together, our data describe a TC10-driven signaling mechanism in which collybistin switches from its autoinhibited closed state to an open/active state.

3.1.1. Keywords: Autoinhibition, fluorescence resonance energy transfer (FRET), gephyrin, guanine nucleotide exchange factor (GEF), inhibitory postsynapse, Rho GTPase.

3.2. Introduction

In the central nervous system, synaptic neurotransmission is mediated by ligand-gated ion channels which are assembled at postsynaptic specializations. The postsynaptic localization of ion channel receptors is vital for efficient synaptic neurotransmission and the precise regulation of distinct neuronal functions (Andersen et al., 1963; Buhl et al., 1994; Nusser et al., 1997). Inhibitory neurotransmission is mediated by glycine and gamma amino-butyric acid (GABA) and cognate receptors for these neurotransmitters are recruited and stabilized by the scaffolding protein gephyrin (Betz, 1998; Fritschy et al., 2008; Tyagarajan & Fritschy, 2014). Gephyrin has been postulated to form extended structures beneath the plasma membrane, where its interaction with the receptors stabilizes the receptors and inhibits their lateral movement (Kneussel & Betz, 2000; Moss & Smart, 2001). Gephyrin recruitment from intracellular deposits to the plasma membrane mainly relies on the adaptor protein collybistin (CB; alternatively known as ARHGEF9) (Kins et al., 2000; Papadopoulos & Soykan, 2011; Soykan et al., 2014).

CB belongs to the diffuse B-cell lymphoma (Dbl) family of guanine nucleotide exchange factors (GEFs) (Zheng, 2001). The murine CB gene is expressed in three splice variants (CB1-CB3) which differ in the presence or absence of a regulatory src homology 3 (SH3) domain and their C-terminal residues (Harvey, 2004). In addition to the SH3 domain, all CB splice variants contain tandem Dbl homology (DH) and pleckstrin homology (PH) domains, which are responsible for its role as a GEF and plasma membrane tethering, respectively (Ludolphs et al., 2016; Papadopoulos & Soykan, 2011; Reddy-Alla et al., 2010; Xiang et al., 2006). GEFs play essential roles in the reactivation of RAS homologue (Rho)-like GTPases (Papadopoulos & Soykan, 2011; Sinha & Yang, 2008; Xiang et al.,

2006), which ensures that these GTPases play important roles in regulating cytoskeletal rearrangements, cell motility, cell polarity, axon guidance, vesicle trafficking and the cell cycle (Heasman & Ridley, 2008; Hodge & Ridley, 2016).

Previous studies demonstrated that the most widely expressed, SH3-domain containing CB isoform-2 splice variant (CB2-SH3⁺) preferentially adopts a closed conformation, in which the N-terminally located SH3 domain interacts intra-molecularly with the tandem DH-PH domains (Soykan et al., 2014). Cellular data suggested that all SH3 domain-encoding CB variants remain untargeted and colocalize with intracellular gephyrin deposits and hence require additional factors including NL2, NL4 or the α 2-subunit of GABA_A receptor which interact with the SH3 domain, thus inducing an open or active state conformation (Harvey, 2004; Hines et al., 2018; Hoon et al., 2011; Kins et al., 2000; Pouloupoulos et al., 2009; Saiepour et al., 2010; Soykan et al., 2014). Here “active” does not refer to the ability of CB to act as a GEF, instead it reflects its ability to contribute to neurotransmitter receptor clustering. The SH3 domain-deficient CB isoform (CB2-SH3⁻), on the contrary, adopts an open conformation, which possess enhanced postsynaptic gephyrin-clustering and effectively replenishes the active (or GTP-bound) small GTPase-Cdc42 from its inactive (or GDP-bound) state (Chiou et al., 2011; Reddy-Alla et al., 2010; Soykan et al., 2014; Tyagarajan, Ghosh, Harvey, et al., 2011; Xiang et al., 2006). Additionally, biochemical and cell-based studies suggested that amino-acid replacements weakening the inter-domain association of CB lead to an open/active CB conformation in which the DH domain is exposed (Schäfer et al., 2020; Soykan et al., 2014).

Based on previous biochemical experiments, CB was originally considered to be a Cdc42-specific GEF (Reid et al., 1999). However, contrary to this prevalent assumption, recent studies suggested that CB interacts differently with the closely related small GTPase, TC10 (also referred to as RhoQ), which is 67.4% identical with Cdc42 (Hemsath et al., 2005; Kilisch et al., 2020; Mayer et al., 2013; Neudauer et al., 1998). In contrast to Cdc42, which is ubiquitously expressed in all brain regions, TC10 expression is limited to specific hippocampal regions in the mammalian brain (Tanabe et al., 2000).

The crystal structure of the Cdc42-CB2SH3⁻ complex revealed that CB binds to Cdc42 via its catalytic DH domain (Xiang et al., 2006). TC10, however, preferentially interacts with the C-terminally located PH domain of CB (Kilisch et al., 2020; Mayer et al., 2013). Furthermore, *in cellulo* studies suggested that TC10 promotes a CB-dependent gephyrin

redistribution, thereby regulating GABAergic postsynaptic strength (Mayer et al., 2013). Although previous studies indicated that TC10 binding to CB interferes with the inter-domain autoinhibitory interactions of CB (Kilisch et al., 2020; Mayer et al., 2013), an understanding of the molecular basis of TC10-mediated CB activation is still lacking. With respect to the closely related Cdc42 it is unclear whether it can activate CB and, if yes, how this is accomplished.

In the present study, we delineate how Cdc42 and TC10 modulate CB conformational dynamics. Through a series of custom engineered CB FRET sensors, we describe the molecular basis of TC10-mediated CB conformational activation. Using time-resolved fluorescence lifetime measurements we demonstrate that TC10 and Cdc42 elicit differential responses in auto-inhibited CB; specifically, TC10, unlike Cdc42, can efficiently induce CB opening. Binding affinity quantification for TC10 shows enhanced affinity for an open state mutant sensor compared to the wild-type CB, whereas Cdc42 binds only to the active state mutant of CB, but with substantially reduced affinity compared to TC10. By analyzing the sequences and structures of the two GTPases we identify molecular determinants for the differential interactions between CB and TC10/Cdc42. Taken together, our data provide a structural framework for TC10-driven CB conformational activation of its auto-inhibited form.

3.3. Methods

3.3.1. Cloning, expression, purification and *in vitro* FLAsH labeling

An N-terminal His₆-tagged wild-type TC10 construct was generated by subcloning the murine cDNA coding for residues 1-205 into the pETM14 vector using restriction free (RF) cloning (Bond & Naus, 2012). TC10KR/GS was subsequently constructed by site-directed mutagenesis. The C-terminal TC10 deletion variant, TC10 Δ C, was constructed by deleting the last 20 amino acids by using RF cloning. The full-length Cdc42 construct has been previously described (Xiang et al., 2006) as have the wild-type CB FRET sensor (F1_{D0}), open state mutant sensors (F1_{smD0} and F1_{dmD0}) and the series of additional CB FRET sensors (Imam, Choudhury, Hemmen, et al., 2022). All FRET sensors are derived from the CB2-SH3+ variant.

Wild-type TC10 and its C-terminal variants were expressed in the *E. coli* strain BL21

(DE3). Bacterial cell lysates were subjected to affinity chromatography on Protino Ni-IDA resin (Macherey Nagel) equilibrated in lysis buffer (50 mM Tris-HCl pH 8, 250 mM NaCl and 5 mM β -mercaptoethanol). Immobilized proteins were eluted using lysis buffer containing 300 mM imidazole and were subsequently subjected to size exclusion chromatography on a Superdex 200 column (GE Healthcare). Eluted protein fractions were concentrated to 10-12 mg/ml by ultrafiltration, flash frozen and stored at -80 °C for later usage. All CB FRET sensors were purified as described (Imam, Choudhury, Hemmen, et al., 2022) as was full-length Cdc42 (Xiang et al., 2006), in this case with minor modifications. All CB FRET sensors were FIAsh labeled as described (Imam, Choudhury, Hemmen, et al., 2022).

3.3.2. Time-resolved setup and data acquisition

A custom-built confocal microscopy setup (IX 71, Olympus, Hamburg, Germany) equipped with a time-correlated single photon counting (TCSPC) system (HydraHarp 400, Picoquant, Berlin, Germany) and with data acquisition by the fluorescence lifetime correlation software SymPhoTime 64 (PicoQuant, Berlin, Germany) was used to measure time resolved data. A 440 nm pulsed laser (LDH-D-C-440, Picoquant) was the excitation laser source, which was coupled through a polarization maintaining single mode fiber (PicoQuant, Berlin, Germany). The laser beam was expanded by a telescope to a diameter of 7 mm to fill the back aperture of the objective (60x water immersion, NA 1.2, Olympus, Hamburg, Germany). For epi-illuminating the sample, a beam splitter (HC458 rpc phase r uf1, AHF) was placed before the objective. In the detection path a 50 μ m pinhole (PNH-50, Newport, Darmstadt, Germany) rejected out of focus light and the beam was split via a polarizing beam splitter cube (10FC16PB.3, Newport, Darmstadt, Germany) into parallel (VV, detector 1) and perpendicular emissions (VH, detector 2) before being projected on photon counting detectors (2x PMA Hybrid-40, Picoquant, Berlin, Germany). An emission band pass filter (Brightline HC 480/40 AHF, Tübingen, Germany) was placed before the detectors to reject unspecific light. The laser was operated in 20 MHz pulsed mode and the power at the sample was maintained at \sim 11 μ W, while the temporal resolution was kept at 4 ps. All measurements were conducted on standard glass coverslips (Menzel-Gläser, Braunschweig, Germany; 24 x 40 mm, 1.5). The setup was optimized daily with a 1 μ M solution of Coumarin 343. These measurements also provide

the relative detection efficiency in the parallel and perpendicular channels, i.e., the g-factor of the setup. To determine the instrument response function (IRF), a KI-saturated solution of 3 μ M fluorescein in double distilled water was measured for 10-15 min. 20 μ L of each sample (CB FRET sensor mixed with different ligands) were excited at 440 nm and the donor (CFP) emission between 460 and 500 nm was recorded at room temperature for 5-10 minutes depending on photon counts. Donor only (D0) and buffer solutions were measured as control samples and for background corrections, respectively. Samples were measured in technical triplicates to calculate average values and standard deviations for each condition.

3.3.3. Time-resolved fluorescence decay analysis

Time resolved fluorescence intensities were analyzed using the Seidel-Software package (<https://www.mpc.hhu.de/software/3-software-package-for-mfd-fcs-and-mfis>). The VV and VH signals collected in ptu format with the Symphotime 64 software were converted into a single column stack using the Jordi-tool of software package. All data were exported in 16 ps bins, i.e., 4096 channels for each detector for a total of 8192 channels. With a given g-factor, the magic angle fluorescence intensity decays were created and analyzed with the chisurf software (Peulen et al., 2017). The g-factor for the set was calculated from tail fitting the Coumarin 343 calibration dye to be 0.98. The decay curves were fitted with a multi-exponential model function using an iterative re-convolution approach (Sanabria et al., 2020; Tsytlonok et al., 2020) as follows

$$F(t) = \sum_i a_i e^{-t/\tau_i} \quad (1)$$

where a_i represents the amplitude and τ_i the lifetime of the corresponding component. Under ideal conditions the donor-only sample (D0) should show a single component, however, due to local quenching we had to conduct a 3-component fitting as reported earlier (Lehmann et al., 2020; Peulen et al., 2017). The reduced χ^2 -values and the weighted residuals were evaluated to check the goodness of the fit. Time-resolved fluorescence intensities for F1_{DA} labeled (F1_{DA}) and F1_{DA}-ligand complexes were also analyzed by eq. 1 to obtain the species-weighted average fluorescence lifetime.

$$\langle \tau \rangle = \sum_i a_i \tau_i, \quad (2)$$

$$\text{where } \sum_i a_i = 1. \quad (3)$$

3.3.4. K_D determination

To determine the K_D of F1_{DA} interacting with TC10 or Cdc42, we titrated the F1_{DA} sensor with different concentrations of the respective ligand and measured the corresponding time-resolved fluorescence intensities. The species-weighted average fluorescence lifetimes were used to calculate the fractional saturation (in %) as follows

$$\text{fractional saturation (\%)}, f = \frac{\langle\tau_{DA,iM}\rangle - \langle\tau_{DA,0M}\rangle}{\langle\tau_{DA,max}\rangle} * 100 \quad (4)$$

where $\langle\tau_{DA,iM}\rangle$ is the average fluorescence lifetime at concentration i , $\langle\tau_{DA,0M}\rangle$ is the mean fluorescence lifetime of the F1AsH labeled CB FRET sensor without addition of ligand and $\langle\tau_{DA,max}\rangle$ is the longest mean fluorescence lifetime of the titration, usually obtained at the highest ligand concentration. The resulting data points were plotted against the ligand concentration and fitted as follows (Origin9, OriginLab):

$$f(x) = b + (a - b) * \frac{[(C_p * K_D * x) \pm \sqrt{(C_p * K_D * x)^2 - 4 * C_p * x}]}{2 * C_p} \quad (5)$$

where x is the concentration, b the offset, a , the final intensity, c_p the protein concentration, and K_D the dissociation constant.

3.3.5. Average FRET efficiency calculation

The average FRET efficiency (E_{FRET}) is calculated from the average fluorescence lifetimes using the following equation:

$$E_{FRET} = 1 - \frac{\langle\tau_{DA}\rangle}{\langle\tau_{D0}\rangle} \quad (6)$$

where $\langle\tau_{D0}\rangle$ and $\langle\tau_{DA}\rangle$ are the species-weighted average fluorescence lifetimes in the absence (D0) and presence (DA) of F1AsH as calculated based on eq. 2.

3.3.6. Förster distance calculation

To determine the inter-fluorophore distance distribution from the fluorescence intensity decays the Förster distance R_0 needs to be calculated accurately. R_0 [Å] was calculated from the following equation

$$R_0 = 0.211 * [\kappa^2 \eta^{-4} \Phi_D J(\lambda)]^{1/6} \quad (7)$$

where κ^2 is a factor describing the relative orientation in space of the transition dipoles of the donor and the acceptor. The magnitude of κ^2 is assumed to be 0.66 for a random orientation of donor and acceptor. The refractive index (η) of the aqueous buffer is

assumed to be 1.33. The quantum yield (Φ_D) of the donor ECFP is 0.4. $J(\lambda)$ is the overlap integral of emission of donor (CFP), and absorption of acceptor (FlAsH) and is calculated by

$$J(\lambda) = \frac{\int_0^\infty I_D(\lambda)\varepsilon(\lambda)\lambda^4 d\lambda}{\int_0^\infty I_D(\lambda)d\lambda} \quad (8)$$

Here, $I_D(\lambda)$ is the fluorescence emission of the donor in the wavelength region λ and $\varepsilon(\lambda)$ the extinction coefficient in units of [$M^{-1} cm^{-1}$] of the acceptor FlAsH ($41000 M^{-1} cm^{-1}$ at 508 nm).

3.3.7. FRET distance distribution analysis

To accurately determine the inter-fluorophore distance distribution from the fluorescence intensity decays of the FlAsH labeled (F1_{DA}) and F1_{DA}-ligand complexes we followed a method described earlier (Sanabria et al., 2020; Tsytlonok et al., 2020). The time-resolved fluorescence intensities of the FRET-sample and the donor-only (reference) sample can be represented as:

$$F_{FRET}(t) = N_0[(1 - x_{NoFRET})F_{DA}(t) + x_{NoFRET}F_{D0}(t)] \otimes IRF + sc \cdot IRF + c \quad (9)$$

$$F_{Ref}(t) = N_0F_{D0}(t) \otimes IRF + sc \cdot IRF + c \quad (10)$$

where N_0 is the total photon number, c the constant offset of the fluorescence intensity, sc the scattered light from the sample, and x_{NoFRET} the no-FRET contribution from the unquenched donor. As however, this quenching is not affected by FRET (Lehmann et al., 2020). Thus, the FRET-rate (k_{FRET}) depends on the relative orientation of the fluorophores and donor-acceptor-distance and the FRET samples can be fitted globally with the donor-only reference sample. In the presence of FRET, the donor fluorescence decay can be expressed with a Gaussian distance distribution (ρ) of the donor-acceptor pair as

$$F_{DA}(t) = F_{D0}(t) \cdot \int \rho_{Gauss}(\sigma\langle R(i) \rangle) \cdot \exp(-k_{FRET}(R(i)) \cdot t) dR \quad (11)$$

where $\langle R(i) \rangle$ is the mean distance between donor and acceptor and σ the width of the inter-fluorophore distance distribution $R(i)$. The calculated Förster radius for CFP and FlAsH pair was 39 and σ was kept fixed to a physically meaningful value of 5 Å (Peulen et al., 2017).

3.3.8. Uncertainty estimation of distance distribution

There are three sources of the experimental uncertainty in the TCSPC-based inter-fluorophore distance distribution analysis: (i) Orientation factor $\langle \kappa^2 \rangle$ uncertainty, $\delta R_{DA(\kappa^2)}$, (ii) the uncertainty in the D_{only} reference $\delta R_{DA,\text{reference}}$ (based on sample preparation etc.) and (iii) the statistical distance distribution fitting uncertainty, $\delta R_{DA,\text{fit}}$ (Peulen et al., 2017). To estimate the uncertainty $\delta R_{DA,\text{fit}}$ we sampled the χ^2 -surface of the fit over the range -20% to + 20% in 50 steps of the respective distance using the “Parameter Scan” option in ChiSurf (Peulen et al., 2017). The resulting χ^2 -surface (Lakowicz, 2013) was plotted against the scanned distance and the limits were determined using a 3σ -criterion based on an F-test (1700 TCSPC channels, 9 parameters) to a relative $\chi_{r,\text{rel}}^2 = \chi_{r,i}^2 / \chi_{r,\text{min}}^2$ of 1.012. To evaluate $\delta R_{DA,\text{reference}}$, we had extended the limits for R_{min} and R_{max} in such a way that the overall R_{min} and R_{max} for the experimental triplicates were used. The uncertainty of the orientation factor $\langle \kappa^2 \rangle$, $\delta R_{DA(\kappa^2)}$, which is usually the largest source of uncertainty, was not considered.

3.3.9. Model Free distance distribution analysis

For the model-free distance distribution analysis, we calculated the FRET-induced donor decay as described earlier (Peulen et al., 2017). Briefly, as a first step, the fluorescence decay of the FRET sample $I_{DA}(t)$ is divided by the (fit) decay of the donor-only sample $I_{D0}(t)$. Next, the D_{only} fraction, x_{NoFRET} , i.e., the offset of the decay, is subtracted, and finally, this ratio is multiplied with the time axis t to yield the FRET-induced donor decay $\varepsilon(t)$:

$$\varepsilon(t) = \left(\frac{I_{DA}(t)}{I_{D0}(t)} - x_{NoFRET} \right) \cdot t \quad (12)$$

For an intuitive display, we converted the x-axis from time t to critical distance $R_{DA,c}$ by the following relation:

$$R_{DA,c} = R_0 \cdot \left(\frac{t}{\tau_D} \right)^{1/6} \quad (13)$$

Here R_0 is the Förster radius of the respective FRET dye pair (39 Å in this case) and τ_D the reference fluorescence lifetime of the donor fluorophore (here, 3.1 ns). Plotting $\varepsilon(t)$ against $R_{DA,c}$ results in a peak distribution, which reflects the probability density function of the underlying distance distribution of the original decay $I_{DA}(t)$

3.4. Results

3.4.1. Comparative analysis of TC10 and Cdc42 structures

The CB interacting GTPases TC10 and Cdc42 are closely related (Fig. 3.1A) which is reflected in a high amino-acid sequence identity of 67.4% (Neudauer et al., 1998). Despite the high conservation, the N and C-termini of both GTPases each contain a small stretch of non-conserved residues. Furthermore, additional short patches of non-identical residues can be observed in the core regions of the GTPases (Fig. 3.1A).

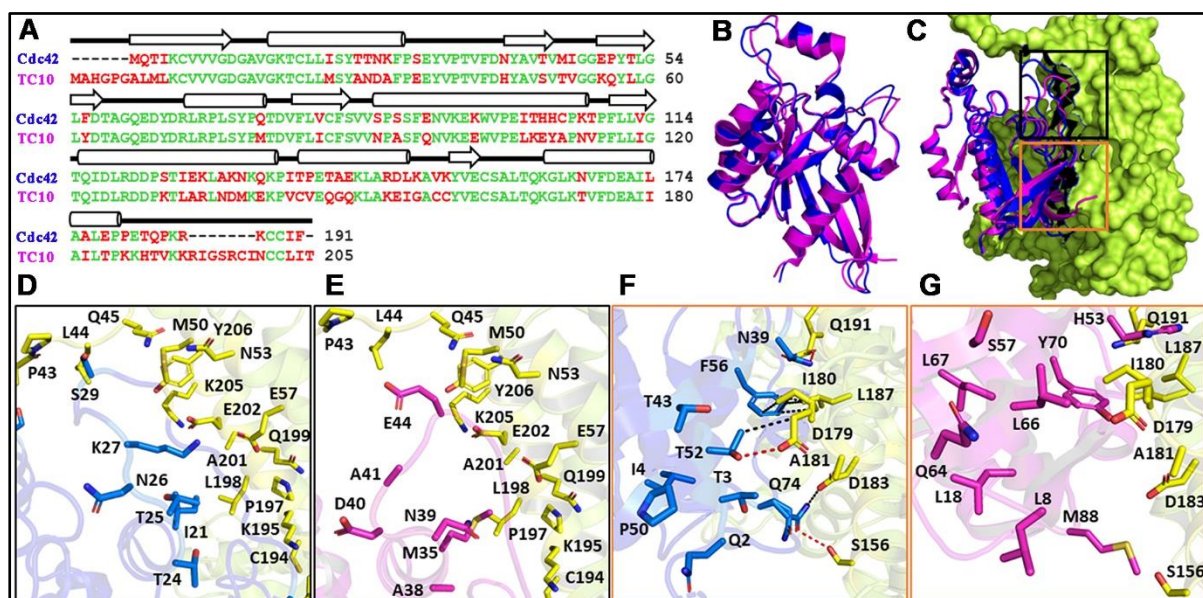


Figure 3.1 (Figure 1 in the manuscript) Cdc42 and TC10 comparison. (A) Sequence alignment calculated with Clustal (Sievers et al., 2011) of murine TC10 and Cdc42. Conserved amino acid residues are displayed in green, diverging residues in red. On the top, β -strands (arrows) and α -helices (cylinders) are indicated. (B) Superimposition of Cdc42 (PDB entry 1an0; blue) and TC10 (PDB entry 2atx; magenta), highlighting their conserved three-dimensional structures. (C) Crystal structure of the Cdc42-CB2SH3- complex (PDB entry 2dfk) superimposed with TC10 (PDB entry 2atx). TC10 (magenta) and Cdc42 (blue) are shown in cartoon, whereas CB2SH3- (lemon) is depicted in surface representation. Black and orange boxes represent the top and bottom portion of the Cdc42-CB interface. (D, E) Zoomed image of the top interface region of the CB-Cdc42 complex (D) and the hypothetical CB-TC10 interface region following superimposition of TC10 onto Cdc42 (E). Residues of Cdc42, which are part of the interface but are not conserved in TC10, are represented with their side chains in blue (D) and the corresponding residues of TC10 in magenta (E). (F, G) Enlarged image of the bottom section of Cdc42-CB interface (F) and that of the hypothetical TC10-CB complex (G). Residues are highlighted as described for panels (D, E). Hydrogen bonds and hydrophobic interactions in the Cdc42-CB complex (F) are represented by red and black dotted lines, respectively.

As expected, the superimposition of both GTPases (Fig. 3.1B) revealed a high degree of structural similarity as reflected in a root mean square (RMS) deviation of 0.52 Å for the C α -atoms. To understand why TC10 does not interact in the same way with CB as Cdc42, we superimposed TC10 onto the crystal structure of the Cdc42-CBSH3⁻ complex (Xiang et al., 2006) (Fig. 3.1C) and analyzed the distribution of non-conserved residues in the interface of the complex (Fig. 3.1C-G).

The interface can be divided into two areas, designated as top and bottom, where non-conserved residues are observed. Fig. 3.1D and E represent the top section of the interface for Cdc42 (based on the crystal structure) and TC10 (based on the superimposition), respectively. In this region six non-identical residues between Cdc42 and TC10 are observed. The bottom part of the Cdc42-CBSH3⁻ interface (Fig. 3.1F) and the hypothetical TC10-CBSH3⁻ interface (Fig. 3.1G) features nine non-identical residues. An analysis of the protein-protein interface with PDBePISA (Krissinel & Henrick, 2007) revealed that the residues present in the top interface in the Cdc42-CBSH3⁻ complex do not form any hydrogen bonds (Fig. 3.1D). The side chains of the non-conserved residues were also predicted not to be involved in any van der Waals' interactions. In contrast, in the bottom interface, the non-conserved residues N39, T52, and Q74 of Cdc42 (Fig. 3.1F) engage in hydrogen bonds with Q191, D179 and S156, respectively. The corresponding residues in TC10, H53, L66 and M88 (Fig. 3.1G), either lack the potential to form hydrogen bonds (L66 and M88) or, due to size differences (H53), can no longer form hydrogen bonds. Moreover, the hydrophobic interactions between F56 in Cdc42 and I180 as well as L187 in the DH domain of CB are weakened by the substitution of Y70 in TC10 for F56 in Cdc42. Please note that eight non-native residues (SPGAGRSS) are present at the N-terminus of TC10 (PDB entry 2atx) (Hemsath et al., 2005), which are partially responsible for the offset in residue numbers (Fig. 3.1A). This analysis indicates that the aforementioned substitutions mediate the differential binding preferences of Cdc42 and TC10 to the DH-PH tandem of CB (Mayer et al., 2013; Xiang et al., 2006) and explains why TC10 cannot be bound in a manner analogous to Cdc42. Since the interaction between the PH domain of CB and TC10 has not yet been structurally characterized, it is unclear which residues in either protein are involved and why Cdc42 cannot engage in the same interaction with the PH domain of CB.

3.4.2. TC10 mediates conformational activation of auto-inhibited CB

In order to examine the role of the two GTPases in CB activation, we employed previously described fluorescence lifetime-based CB FRET sensors (Imam, Choudhury, Hemmen, et al., 2022) derived from the CB2-SH3⁺ splice variant (Figure 2.1 B). We recombinantly purified TC10 and Cdc42 (Figure 3.2 A-B) and incubated both proteins in a 100-fold molar excess (100 μ M) with the CB wild-type FRET sensors (Imam, Choudhury, Hemmen, et al., 2022).

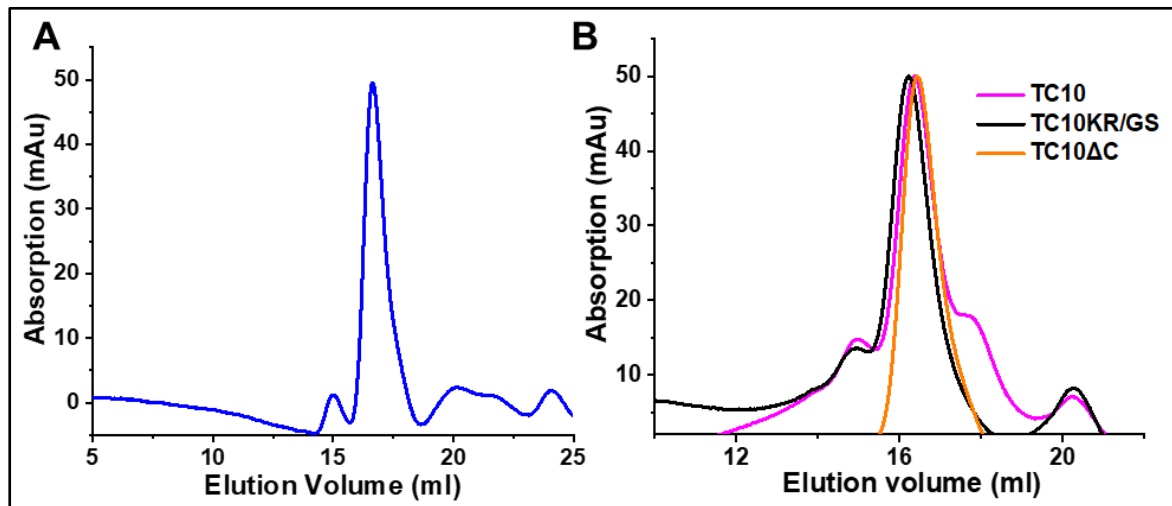


Figure 3.2 (Supplementary Figure 1 in the manuscript). Purification of small GTPases. (A) Size exclusion chromatography elution profile of Cdc42 (blue). **(B)** Elution profile of TC10 (magenta) and its C-terminal variants TC10KR/GS (black) and TC10 Δ C (orange).

For interaction studies, we individually measured the average fluorescence lifetime ($\langle\tau\rangle$) of CFP (Figure 3.3A) of the CB FRET sensor (F1_{D0}) and its FLAsH-labeled counterpart (F1_{DA}), in the absence and presence of either TC10 or Cdc42. Time-resolved fluorescence intensities of CFP in the presence of FLAsH (F1_{DA}) showed a significant $\langle\tau\rangle$ reduction, from 3.1 ± 0.03 ns (mean \pm standard deviation; SD) to 2.52 ± 0.02 ns (Table 3.1). When incubated with F1_{D0} neither TC10 nor Cdc42 induced any change in $\langle\tau\rangle$ of CFP (Table 3.1), thus indicating that both GTPases do not alter the fluorescence characteristics of the C-terminally attached CFP in the F1_{D0}. Interestingly, upon incubation of F1_{DA} with TC10 a substantial increase (2.87 ± 0.01 ns) in the $\langle\tau\rangle$ of F1_{DA} was observed (Figure 3.3A-B, Table 3.1). The TC10-induced $\langle\tau\rangle$ increase in the F1_{DA} can be attributed to an inter-dye distance increase between the donor fluorophore, CFP, and the acceptor fluorophore, FLAsH. In contrast, Cdc42 did not show a significant $\langle\tau\rangle$ change in F1_{DA} compared to free F1_{DA}

(Figure 3.3A-B, Table 1). The unaltered $F1_{DA}$ $\langle\tau\rangle$ in the presence of Cdc42 (2.53 ± 0.03 ns) suggests that the SH3-containing CB2 variant, which is known to be in an autoinhibited state (Soykan et al., 2014), at best only weakly interacts with Cdc42.

Samples	$\langle\tau\rangle$ (\pm SD), [ns]	R_1 (\pm SD) [\AA]	X_1 (\pm SD)	R_2 (\pm SD) [\AA]	X_2 (\pm SD)	x_{NoFRET} (\pm SD)
$F1_{D0}$	3.1 (\pm 0.03)	-	-	-	-	-
$F1_{DA}$	2.52 (\pm 0.02)	25.5 (\pm 1.5)	0.45 (\pm 0.02)	45.5 (\pm 0.9)	0.21 (\pm 0.02)	0.32 (\pm 0.03)
$F1_{D0} + \text{Cdc42}$	3.12(\pm 0.02)	-	-	-	-	-
$F1_{D0} + \text{TC10}$	3.1 (\pm 0.01)	-	-	-	-	-
$F1_{DA} + \text{Cdc42}$	2.53 (\pm 0.03)	26.2 (\pm 1.2)	0.48 (\pm 0.02)	42.5 (\pm 1.9)	0.21 (\pm 0.04)	0.29 (\pm 0.11)
$F1_{DA} + \text{TC10}$	2.87 (\pm 0.01)	26.8 (\pm 2.6)	0.20 (\pm 0.01)	47.5 (\pm 4.3)	0.23 (\pm 0.09)	0.68 (\pm 0.18)
$F1_{DA} + \text{TC10KR/GS}$	2.89 (\pm 0.03)	25.3 (\pm 1.9)	0.16 (\pm 0.06)	45.1 (\pm 4.0)	0.17 (\pm 0.06)	0.67 (\pm 0.17)
$F1_{DA} + \text{TC10}\Delta\text{C}$	2.83 (\pm 0.02)	27.1 (\pm 1.1)	0.18 (\pm 0.1)	48.1 (\pm 0.6)	0.24 (\pm 0.1)	0.56 (\pm 0.13)

Table 3.1. (Table 1 in the manuscript). Table representing the species-weighted average fluorescence lifetime ($\langle\tau\rangle$) and inter-fluorophore distances (R_i) along with their relative species fractions (x_i) obtained from time-resolved FRET analysis for the CB-FRET sensors ($F1_{D0}$ and $F1_{DA}$) alone and after incubation with Cdc42, TC10 and its C-terminal variants. Species fractions are normalized in an order that $x_1 + x_2 + x_{\text{NoFRET}} = 1$.

3.4.3. TC10 stabilizes an open conformation of CB

To further characterize the CB-TC10 interaction we carried out titration experiments to determine the binding affinity between TC10 and CB by incubating increasing concentrations (0.05 to 400 μM) of TC10 with $F1_{DA}$, while keeping the $F1_{DA}$ concentration constant. With increasing TC10 concentrations, $F1_{DA}$ showed a consequent increase in $\langle\tau\rangle$, finally reaching saturation at higher molar concentrations of TC10. We plotted the fractional saturation determined from the corresponding $\langle\tau\rangle$ change (eq. 4) against the TC10 concentration and determined a dissociation constant (K_d) of the $F1_{DA}$ -TC10 complex of 37 ± 4 μM (eq. 5, Figure 3.3C), suggesting a moderately tight interaction between CB and TC10. Since for Cdc42 no change in $\langle\tau\rangle$ was observed even at significantly higher concentrations (Fig. 3.3A-B, Table 3.1), the binding strength could not be measured.

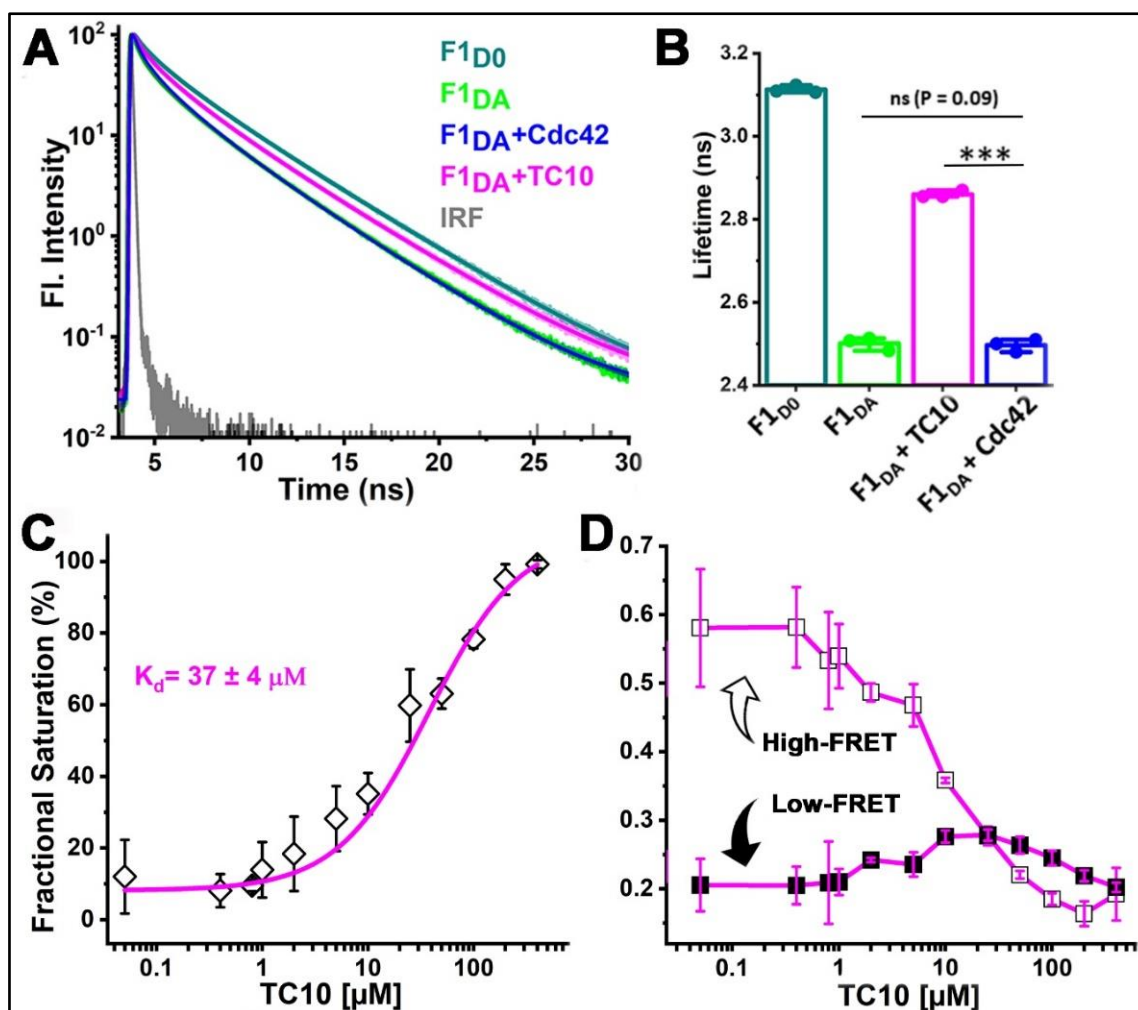


Figure 3.3 (Figure 2 in the published manuscript). TC10 and Cdc42 interaction with CB FRET sensor. (A) Time-resolved CFP fluorescence intensities for the CB FRET sensor $F1_{D0}$ (teal), its FRET-labeled counterpart $F1_{DA}$ alone (green) and in the presence of a 100-fold molar excess (100 μM) of Cdc42 (blue) and TC10 (magenta). The instrument response function (IRF) is shown in grey. $F1_{D0}$ and $F1_{DA}$ were excited (λ_{ex}) at 440 nm. Emission (λ_{em}) data were collected between 460-500 nm and fitted with eq. 1 to obtain the average fluorescence lifetime (τ) for the respective samples. For easier comparison data were scaled to a maximum of 10^2 . (B) Bar plot showing species-weighted $\langle\tau\rangle$ of CFP in $F1_{D0}$ (teal), $F1_{DA}$, alone (green) and in the presence of a 100-fold molar excess of TC10 (magenta) and Cdc42 (blue). Data from three individual biological replicates ($n = 3$) are presented as mean values \pm SD. *** $P < 0.001$; ns, statistically not significant. (C) $F1_{DA}$ binding affinity plot of TC10. Binding affinity was determined by first converting $\langle\tau\rangle$ into the fractional saturation using eq. 4. and the data were further fitted with eq. 5. The $F1_{DA}$ binding affinity constant (K_d) for TC10 was measured as $37 \pm 4 \mu\text{M}$. (D) Plot showing the FRET species (high-FRET state and low-FRET state) composition plotted against increasing concentrations of TC10, obtained after analysing the time-resolved fluorescence intensities with the Gaussian distribution model (eqs. 9-11). With increasing concentrations of TC10, the high FRET state (R1, open square) gradually decreases, while the low FRET (R2, filled square) state increases.

To further investigate the role of TC10 in CB activation we analyzed the time-resolved fluorescence intensities of F1_{DA} and F1_{DA}-TC10 complexes at varying concentrations by Gaussian distance distribution models (eq. 9-11) as described before (Imam, Choudhury, Hemmen, et al., 2022). Consistent with our previous study, F1_{DA} molecules adopted two distinct conformational states, a high-FRET state exhibiting a compact conformation and a low-FRET state reflecting an open conformation (Figure 3.3D). The inter-fluorophore distances (Table 3.1) in the high (R_1) and low FRET states (R_2) were calculated as $26.8 \pm 2.6 \text{ \AA}$ and $47.5 \pm 4.3 \text{ \AA}$, respectively. Increasing TC10 concentrations resulted in a significant shift in the equilibrium from the high to the low FRET state (Figure 3.3D, Table 3.1A). Interestingly, higher TC10 concentrations also led to a stronger population of a NoFRET (x_{NoFRET}) state, possibly indicating another state beyond the measurable FRET distance limit ($>49 \text{ \AA}$) for the FRET pair used in this study. The fluorescence lifetime-based FRET study along with distance distribution analysis of F1_{DA} provided concrete evidence of a TC10-mediated CB opening and its transition from the closed to an open state.

3.4.4. TC10 C-terminal variants efficiently recognize CB

Small GTPases possess variable C-terminal regions which contain diverse types of subcellular localization signals and harbor sites for various post-translational modifications (Lionel et al., 2013; Michaelson et al., 2001; Murphy et al., 2001; Roberts et al., 2008; Watson Robert et al., 2003). Specifically, most Rho GTPases at their C-termini possess a stretch of basic residues which is believed to mediate their positioning at the appropriate cellular membrane sites to ensure proper signal transduction (Hodge & Ridley, 2016). In line with this observation, the C-terminal tail of TC10 also contains a cluster of positively charged residues, which serves as a binding site for various phosphoinositides (Kilisch et al., 2020).

Therefore, we aimed to inspect the role of basic amino acid stretch of TC10 in CB recognition and binding. To this end, we purified a TC10KR/GS variant in which basic residues were replaced with glycine and serine residues as described before (Kilisch et al., 2020) (Fig. 3.3A). Additionally, we also constructed a C-terminal deletion variant of TC10 (TC10 Δ C) in which residues 186-205 containing the positively charged residues were removed (Figure 3.4A).

For initial interaction studies, we incubated F1_{D0} and F1_{DA} with a 100-fold molar excess concentration (100 μ M) of both TC10 variants and measured the change in $\langle\tau\rangle$. Both TC10KR/GS and TC10 Δ C led to a significant increase (Fig. 3.4B, Fig. 3.5B, Table 3.1) in $\langle\tau\rangle$ of F1_{DA}, however, no $\langle\tau\rangle$ change was detected in F1_{D0}.

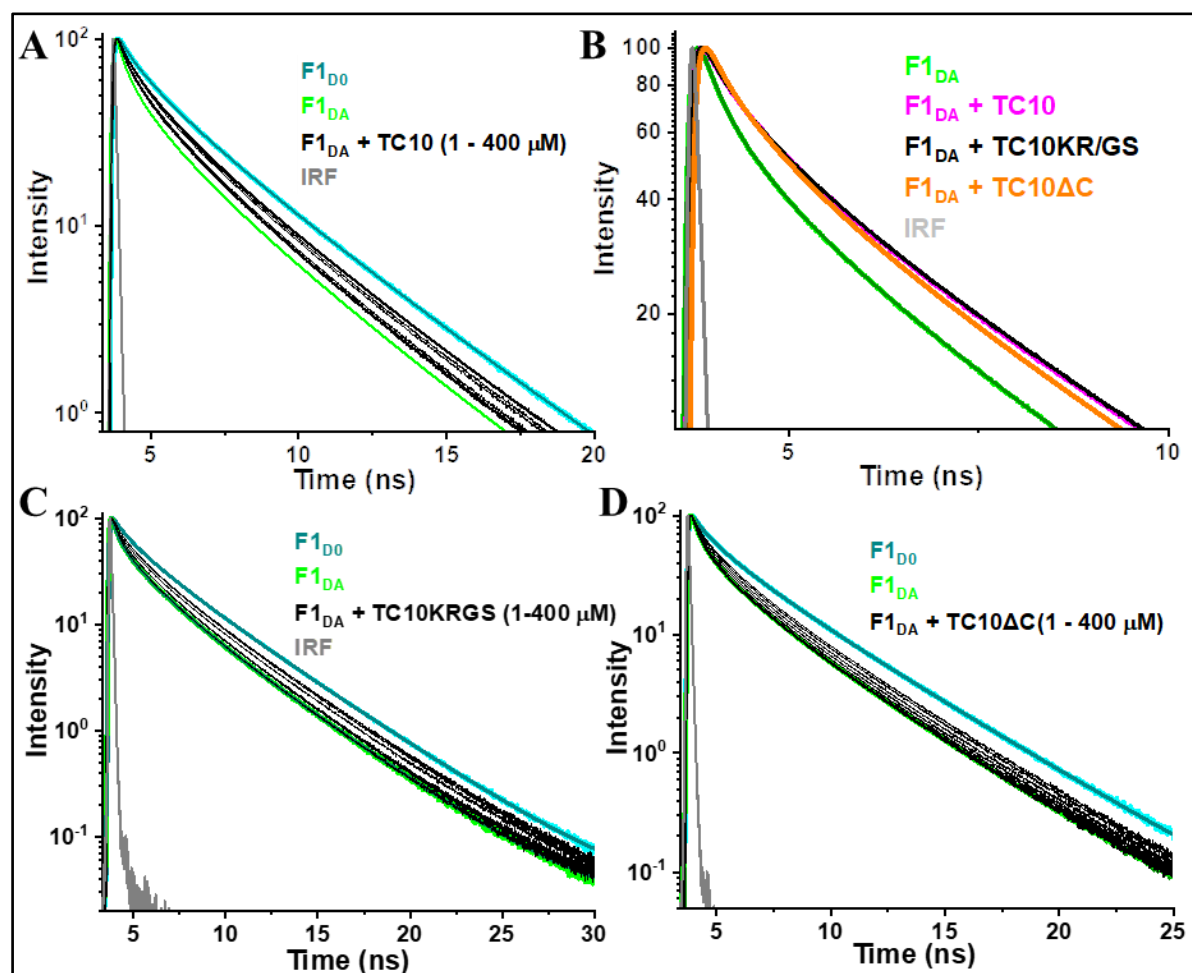


Figure 3.4 Supplementary Figure 2. Titrations of TC10 and its C-terminal variants with F1DA. (A) Fluorescence lifetimes of CFP in F1D0 (teal), F1DA (green) and F1DA-TC10 complexes with increasing TC10 concentrations (black). (B) Time-resolved fluorescence intensities of CFP of F1AsH-labeled CB FRET sensor (F1DA) in the absence (green) and presence of TC10 (magenta), TC10KR/GS (black) and TC10 Δ C (orange). (C-D) Fluorescence lifetimes of CFP in F1D0 (teal), F1DA (green) and F1DA with increasing concentrations of TC10KR/GS (C; black) and TC10 Δ C (D; black). Data in A-D are scaled to a maximum of 10^2 for easier comparison.

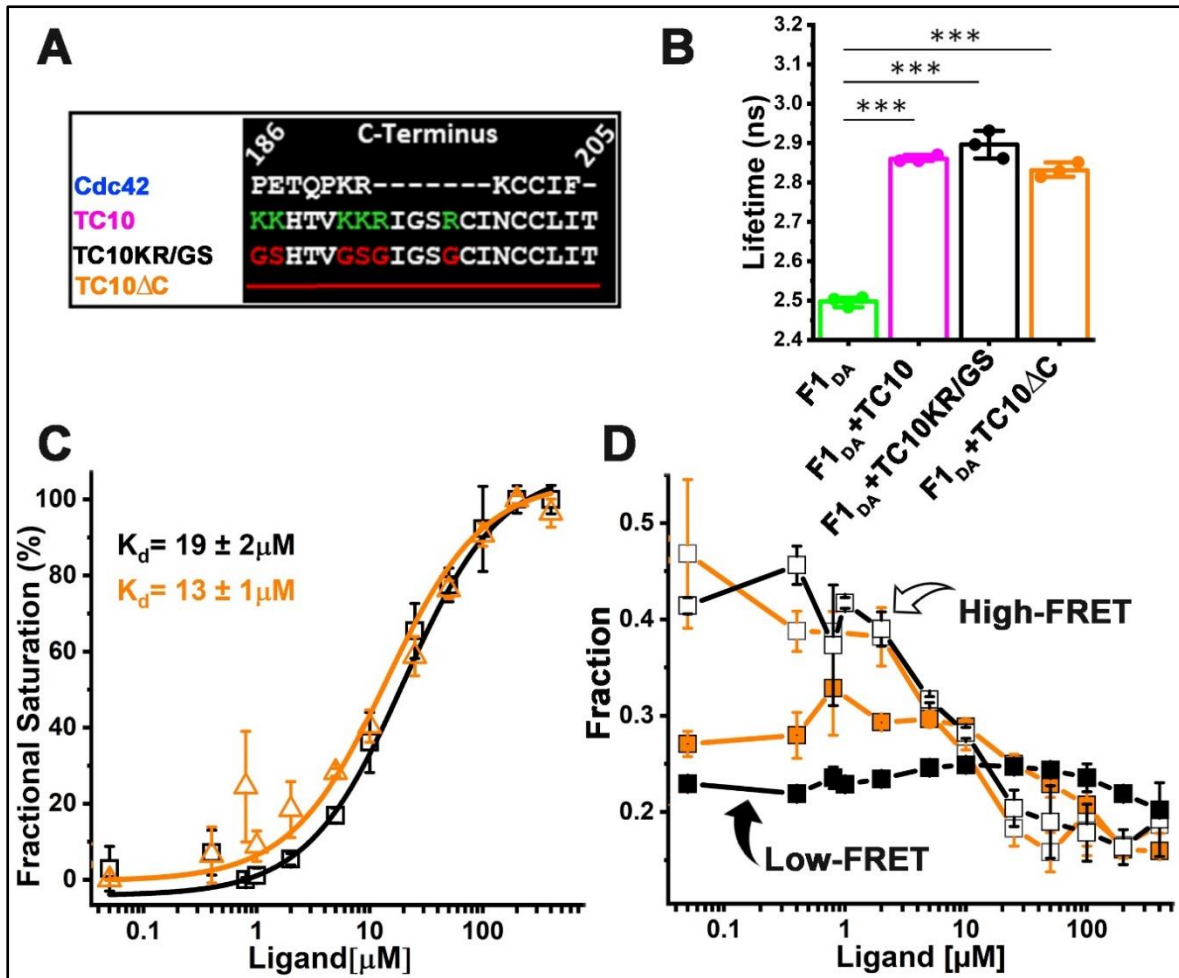


Figure 3.5 (Figure 3. in the main manuscript). **CB binding affinity for TC10 and variants impaired in phosphoinositide-binding.** (A) Alignment of the C-terminal residues of Cdc42 and TC10 (wild-type and variants). In the TC10KR/GS variant the basic residues K and R (shown in green) were replaced with G and S (red). In case of TC10ΔC, the C-terminal amino acid stretch was completely removed. (B) Bar plots depicting the species-weighted average CFP fluorescence lifetime of F1_{DA} alone (green) and in the presence of a 100-fold molar excess of TC10 (magenta), TC10KR/GS (black) or TC10ΔC (orange). *** $P < 0.001$ (C) F1_{DA} binding affinity plot of TC10KR/GS (black) and TC10ΔC (orange). Affinities were determined by first converting $\langle \tau \rangle$ into the fractional saturation using eq. 4. and the data were further fitted with eq. 5. TC10KR/GS and TC10ΔC binding affinity for F1_{DA} were measured as $19 \pm 2 \mu\text{M}$ and $13 \pm 1 \mu\text{M}$, respectively. Data from three individual biological replicates ($n = 3$) are presented as mean values \pm SD. (D) High-FRET state and low-FRET species composition plotted against increasing concentrations of TC10KR/GS (black) and TC10ΔC (orange) obtained after analysing the time-resolved fluorescence intensities with the Gaussian distribution model (eqs. 9-11). In both cases the high FRET state (R1, open square) gradually decreases, while the low FRET (R2, filled square) state increases with increasing concentrations of TC10 variants.

The observed $\langle\tau\rangle$ change for F1_{DA} in case of TC10KR/GS (2.89 ± 0.03 ns) and TC10 Δ C (2.83 ± 0.02 ns) was comparable to the wild-type TC10 (2.87 ± 0.01 ns) (Fig. 3.5B). The highly similar change in $\langle\tau\rangle$ elicited by binding of TC10 C-terminal variants indicated that elimination of the phosphoinositide binding site in case of TC10KR/GS, or even the complete removal of the basic residues in TC10 Δ C does not affect CB recognition by TC10.

3.4.5. Deletion of TC10 C-terminal stretch enhances its affinity for CB

Since TC10 and its C-terminal variants induced similar $\langle\tau\rangle$ change in the F1_{DA} molecules, we next investigated whether the TC10 variants possess similar affinities for CB. To examine the binding strength of TC10 variants, we titrated F1_{DA} separately (Fig. 3.4C-D) with increasing concentrations of TC10KR/GS and TC10 Δ C and quantified the results. TC10KR/GS and TC10 Δ C displayed comparable binding affinities (Fig. 3.5C) characterized by K_d -values of 19 ± 2 μ M and 13 ± 1 μ M, respectively. Hence, the observed affinity values for the TC10 variants were roughly two-fold reduced compared to wild-type TC10 (Fig. 3.5C) with a binding constant of 37 ± 4 μ M.

To better understand the conformational changes induced in F1_{DA} by TC10KR/GS and TC10 Δ C, we performed distance distribution fittings for both constructs as described for wild-type TC10 (Fig. 3.3D). Both, TC10KR/GS and TC10 Δ C were found to be potent (Fig. 3.4C-D, Fig. 3.5D) in turning the high FRET F1_{DA} molecules into a low FRET population as seen for the wild-type TC10 (Fig. 3.3D). The inter-fluorophore distances for the high FRET (R_1) and low FRET (R_2) molecules remained relatively unchanged for TC10KR/GS ($R_1 = 25.3 \pm 1.9$ Å and $R_2 = 45.1 \pm 4$ Å) and TC10 Δ C ($R_1 = 27.1 \pm 1.1$ Å and $R_2 = 48.1 \pm 0.6$ Å) and were found to be highly similar to the TC10 wild-type ($R_1 = 26.8 \pm 2.6$ Å and $R_2 = 47.5 \pm 4.3$ Å) (Table 3.1). Thus, the comparative changes in $\langle\tau\rangle$ and the related distance distribution results for the C-terminal TC10 variants indicate a similar conformational modulation in CB, as the one elicited by the TC10 wild-type.

3.4.6. Cdc42 and TC10 efficiently interact with active state mutant sensors of CB

Full-length CB is stabilized by intramolecular interactions between the SH3 domain and the tandem DH-PH domains (Soykan et al., 2014). The equilibrium between the inactive and active conformations in full-length CB is known to be modulated by the amino acid

residues Trp24 and Arg70 in the SH3 domain, and Glu262 in the DH domain (Soykan et al., 2014).

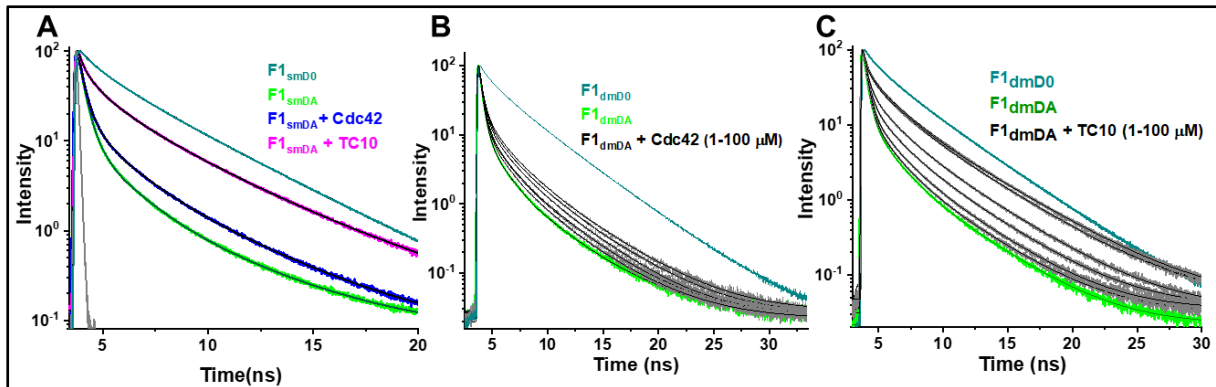


Figure 3.6 (Supplementary Figure 5 in the manuscript). Interactions of the open state mutant sensors with TC10 or Cdc42. (A) CFP fluorescence intensity in single mutant sensor ($F1_{smD0}$; teal), its FLAsH labeled counterpart ($F1_{smDA}$) alone (green) and in the presence of either Cdc42 (blue) or TC10 (magenta). The instrument response function (IRF) is shown in grey. **(B)** Fluorescence lifetime decay of CFP in the double mutant FRET sensor with $F1_{dmD0}$ (teal), $F1_{dmDA}$ alone (green) and $F1_{dmDA}$ -Cdc42 complexes with increasing concentrations of Cdc42 (black). **(C)** $F1_{dmDA}$ alone (green) and $F1_{dmDA}$ -TC10 complexes with increasing concentrations of TC10 (black). Data in A-C are scaled to a maximum of 10^2 for easy comparison.

Sample	$\langle\tau\rangle$ (\pm SD) ns	Sample	$\langle\tau\rangle$ (\pm SD) ns
$F1_{smD0}$	3.15 (\pm 0.02)	$F1_{dmD0}$	3.12 (\pm 0.02)
$F1_{smDA}$	1.17 (\pm 0.03)	$F1_{dmDA}$	1.2 (\pm 0.08)
$F1_{smD0}$ +Cdc42	3.13(\pm 0.02)	$F1_{dmD0}$ + Cdc42	3.1 (\pm 0.03)
$F1_{smD0}$ +TC10	3.12 (\pm 0.02)	$F1_{dmD0}$ + TC10	3.12 (\pm 0.01)
$F1_{smDA}$ +Cdc42	1.63 (\pm 0.03)	$F1_{dmDA}$ + Cdc42	1.7 (\pm 0.02)
$F1_{smDA}$ +TC10	2.83 (\pm 0.04)	$F1_{dmDA}$ + TC10	2.9 (\pm 0.04)

Table 3.2 (Supplementary Table 1 in the manuscript). Average fluorescence lifetime ($\langle\tau\rangle$) of open state single ($F1_{smD0}$) and double mutant ($F1_{dmD0}$) CB FRET sensors, their FLAsH labeled counterparts $F1_{smDA}$ and $F1_{dmDA}$ in the absence and presence of Cdc42, TC10 and its variants. Data from three individual biological replicates ($n = 3$) are presented as mean values \pm SD.

Earlier studies (Soykan et al., 2014) demonstrated that alanine substitutions of Trp24 (W24A) and Glu262 (E262A) weaken the intramolecular interactions and stabilize the

open state of CB. Therefore, we employed open state mutant sensors (Imam, Choudhury, Hemmen, et al., 2022) to investigate the interactions of TC10 and Cdc42 with CB in the open conformation.

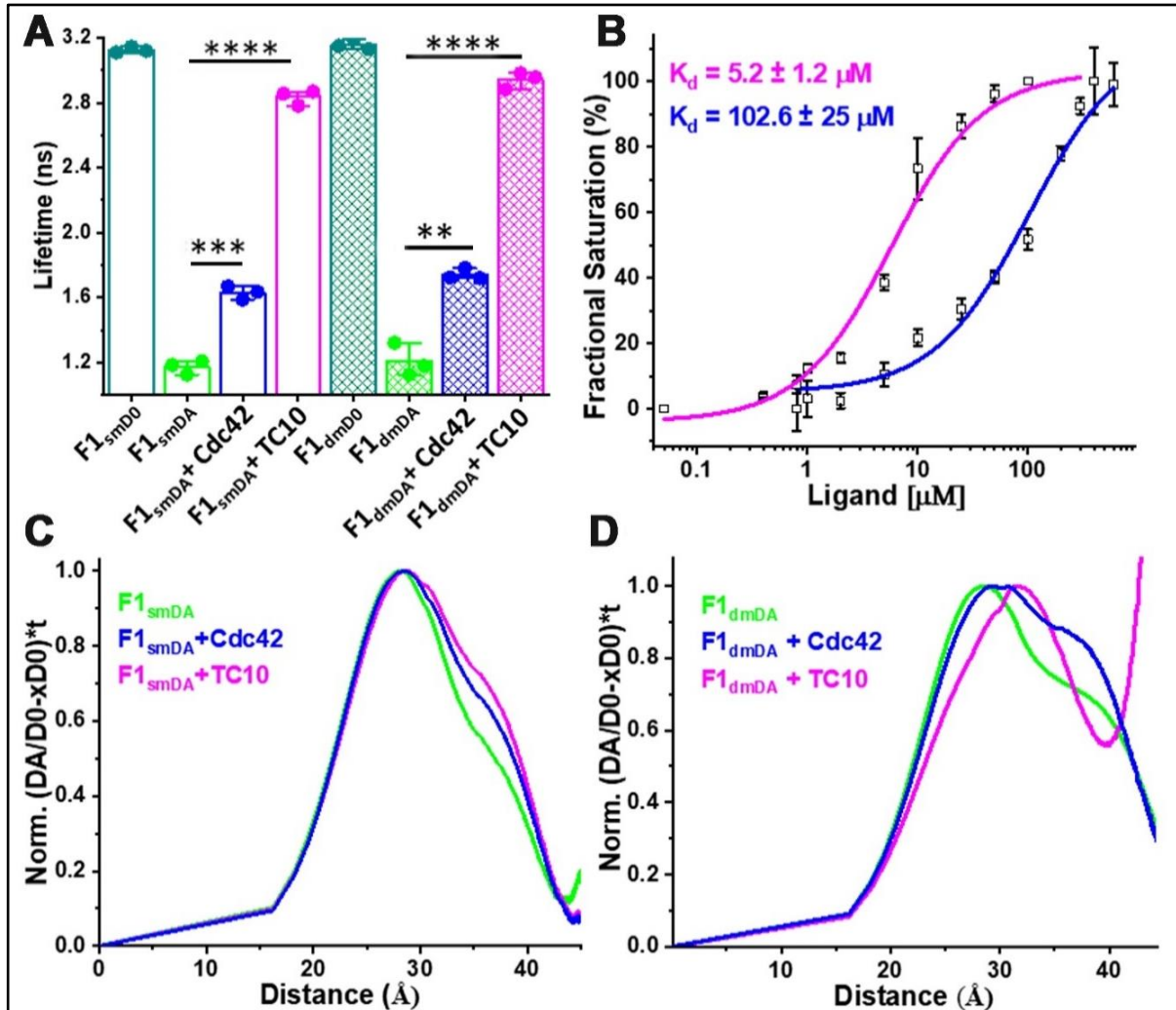


Figure 3.7 (Figure 4 in the main text). Interactions of open state mutant sensors with Cdc42 and TC10. (A) Bar plot depicting the species-weighted CFP $\langle \tau \rangle$ of the CB wild-type, open state single mutant (*sm*) and double mutant (*dm*) FRET sensors ($F1_{smD0}$ and $F1_{dmD0}$), their F_lAsH-labeled counterparts ($F1_{smDA}$ and $F1_{dmDA}$) and the F_lAsH labeled sensors in the presence of Cdc42 or TC10. ** $P < 0.01$, *** $P < 0.001$, **** $P < 0.0001$. (B) $F1_{dmDA}$ binding affinity (K_D) plots for TC10 (magenta) and Cdc42 (blue). TC10 and Cdc42 binding affinity for the $F1_{dmDA}$ were measured as $5.2 \pm 1.2 \mu M$ and $102 \pm 25 \mu M$, respectively. Data from three individual biological replicates ($n = 3$) are presented as mean values \pm SD. (C-D) Model-free distance distribution fits for the inter-fluorophore distance corresponding to the time-resolved CFP fluorescence intensities (eq. 12, 13). Normalised distance distribution curves shown for $F1_{smDA}$ (C) and $F1_{dmDA}$ (D) in the absence (green) and presence of TC10 (magenta) and Cdc42 (blue).

We measured the average fluorescence lifetime $\langle\tau\rangle$ for single ($F1_{smDA}$) and double mutant ($F1_{dmDA}$) CB FRET sensors containing either the single W24A or double W24A/E262A amino acid replacements (Imam, Choudhury, Hemmen, et al., 2022) by incubating the sensors and $F1_{smD0}$ and $F1_{dmD0}$ as controls with a 100-fold molar excess (100 μ M) of Cdc42 and TC10 (Figure 3.6A). For the control measurements with $F1_{smD0}$ and $F1_{dmD0}$ no change in $\langle\tau\rangle$ was observed. In contrast to the wild-type sensor $F1_{DA}$ with a $\langle\tau\rangle$ of 2.53 ± 0.03 ns, Cdc42 interaction with $F1_{smDA}$ and $F1_{dmDA}$ resulted in a significant increase in their $\langle\tau\rangle$ to 1.63 ± 0.03 ns and 1.7 ± 0.02 ns, respectively (Fig. 3.7A, Table 3.2). Compared to Cdc42, the interaction of TC10 with $F1_{smDA}$ and $F1_{dmDA}$ led to even stronger $\langle\tau\rangle$ increase with 2.83 ± 0.04 ns and 2.9 ± 0.04 ns, respectively (Figure 3.7A, Table 3.2). Since the $\langle\tau\rangle$ change inflicted by TC10 and Cdc42 were quite significant, we next investigated their binding affinity for the open state mutant sensor and titrated $F1_{dmDA}$ with increasing concentrations of TC10 and Cdc42 (Fig. 3.6 B-C). In both cases, rising concentrations led to a concomitant increase in $\langle\tau\rangle$ of $F1_{dmDA}$ followed by saturation (Fig. 3.6 B-C).

Interestingly, compared to the wild-type sensor ($F1_{DA}$) the double mutant sensor ($F1_{dmDA}$) exhibited an enhanced binding affinity for TC10 with a K_d of 5.2 ± 1.2 μ M (Fig. 3.7B) vs. a K_d of 37 ± 4 μ M for $F1_{DA}$ (Fig. 3.3C). Although the titration with Cdc42 also resulted in a gradual $\langle\tau\rangle$ increase in $F1_{dmDA}$, the overall change was considerably lower than for TC10 resulting in a low affinity interaction with K_d of 102.6 ± 2.5 μ M for the Cdc42-CB complex (Fig. 3.7B).

3.4.7. Active state sensors display differential responses upon GTPase binding

In case of the $F1_{smDA}$ and $F1_{dmDA}$ sensors a rapid exponential decay of the fluorescence intensities in both sensors made the fitting with the Gaussian distance distribution model cumbersome. Thus, we relied on a model-free approach (Peulen et al., 2017) to visualize the distance distribution underlying the time-resolved fluorescence intensities of both sensors (Fig. 3.7 C-D, Fig. 3.8-3.9). For comparison, the $F1_{DA}$ and $F1_{DA}$ complexes with TC10 and Cdc42 were analyzed in the same fashion (Fig. 3.10). Consistent with previous results (Imam, Choudhury, Hemmen, et al., 2022), model-free distance distribution analyses of $F1_{smDA}$ and $F1_{dmDA}$ (Fig. 3.7C-D) yielded a main peak at around 28 Å (high-FRET state) along with a small shoulder at 37 Å, which was less prominent in $F1_{smDA}$.

These distances depict the high and low FRET states, respectively, for the open state sensors (Figure 3.7 C-D).

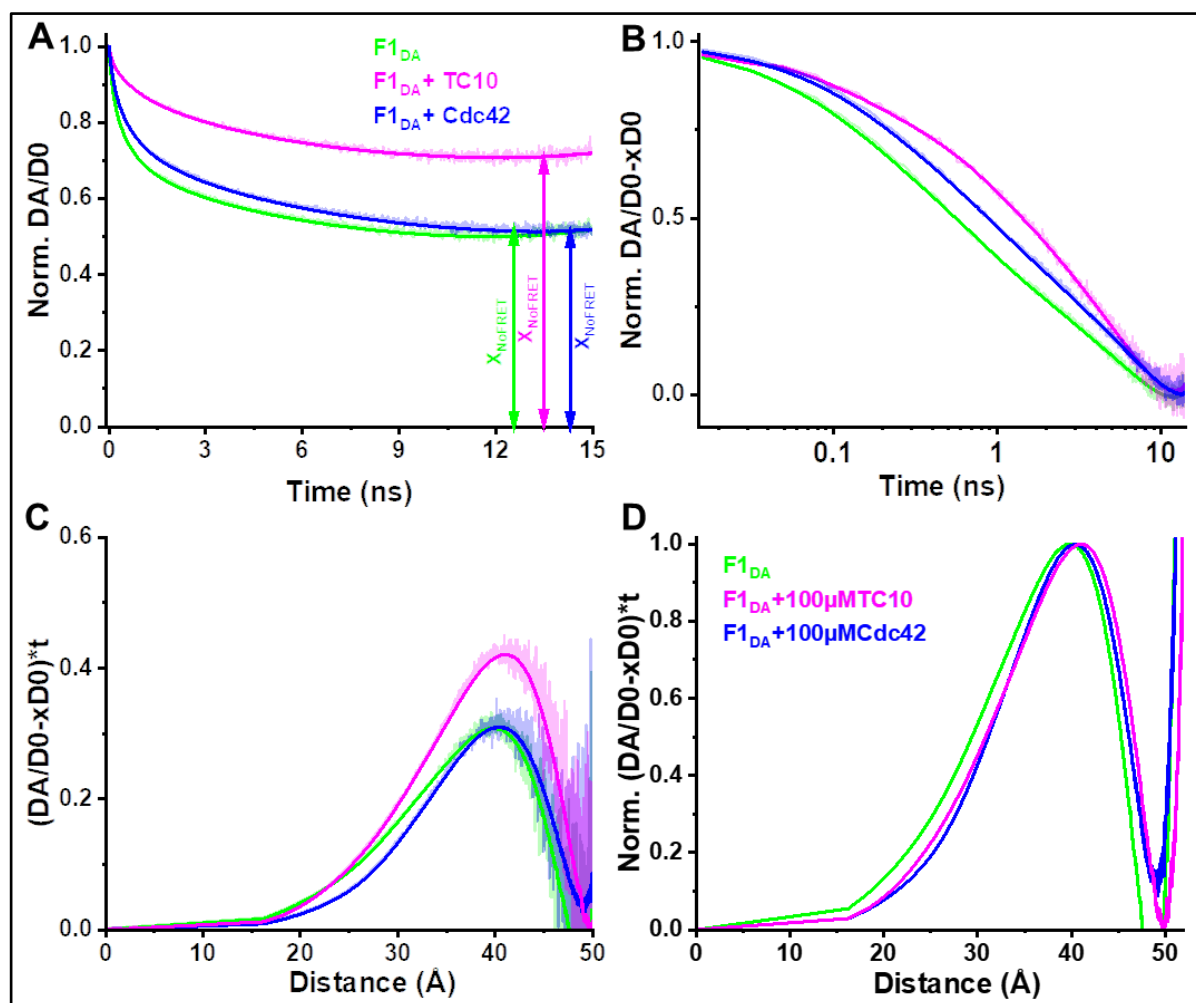


Figure 3.8 (Supplementary Figure 6 in the manuscript). Model-free distance distribution analysis of F1_{DA}. (A) Time-resolved fluorescence intensities $I_{F1DA}(t)$ of the wild type mimicking FAsH labeled sensors alone (green) and in the presence of a 100-fold molar excess of TC10 (magenta) and Cdc42 (blue) divided by $I_{F1D0}(t)$, the corresponding intensity without FAsH labeling. The off-set values of each curve represent the X_{NoFRET} fraction. (B) The offset in (A) is subtracted and time is displayed on a logarithmic scale. (C) The time-axis is converted to a distance axis (eqs. 12-13; main text). (D) The probability density distribution of the underlying distance distribution is normalized to 1 for easier comparison.

Next, we analyzed the F1_{dmDA} distance distribution change upon ligand interaction. Cdc42 binding to F1_{dmDA} resulted in a strong increase in the shoulder, located in this case at approximately 37 Å (Fig. 3.7D). The interaction of TC10 with F1_{dmDA} led to a rightward shift of the main peak in F1_{dmDA} from 28 Å to 32 Å (Fig. 3.7D), while the shoulder at 37 Å

observed in both $F1_{dmDA}$ and the $F1_{dmDA}$ -Cdc42 complex disappeared. This was coupled to a concomitant increase in the X_{NoFRET} fraction as observed in the inter-fluorophore distance increase beyond 40 Å (Fig. 3.7D). The observed inter-fluorophore distance change in $F1_{smDA}$ and $F1_{dmDA}$ suggested that the individual sensors induce distinct conformational states after TC10 and Cdc42 binding.

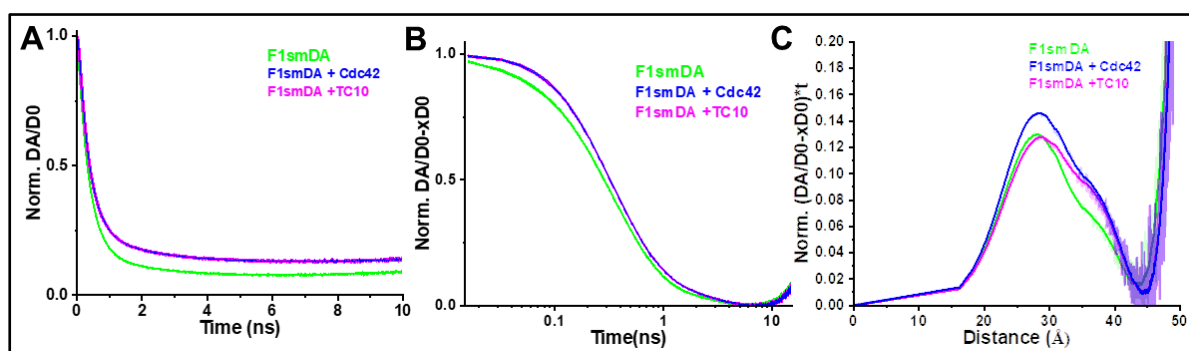


Figure 3.9 (Supplementary Figure 7). Model-free distance distribution of time-resolved fluorescence intensities of the open state single mutant sensor ($F1_{smDA}$). (A) Time-resolved fluorescence intensities of the F1AsH-labeled single mutant sensor, $IF1_{smDA}(t)$, alone (green) and in the presence of a 100-fold molar excess of TC10 (magenta) and Cdc42 (blue) divided by $IF1_{smD0}(t)$, the corresponding intensity of the singly labeled sample. The off-set values of each curve represent the $xNoFRET$ fraction. (B) The offset in (A) is subtracted and the time scale is logarithmic. (C) The time-axis is converted to the distance axis (eqs. 12-13).

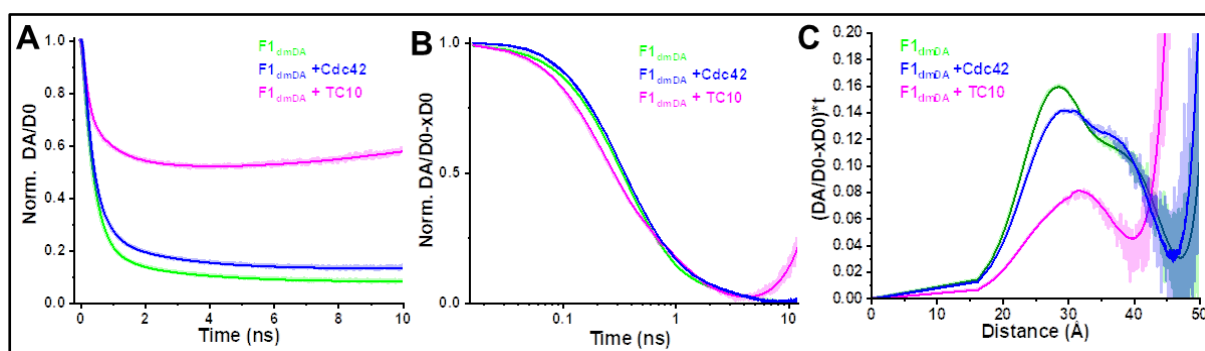


Figure 3.10 (Supplementary Figure 8 in the manuscript). Model-free distance distribution of time-resolved fluorescence intensities of the open state double mutant sensor ($F1_{dmDA}$). (A) Time-resolved fluorescence intensities of the F1AsH-labeled double mutant sensor, $IF1_{dmDA}(t)$, alone and in the presence of a 100-fold molar excess of Cdc42 (blue) and TC10 (magenta) divided by $IF1_{dmD0}(t)$, the corresponding intensity of the singly labeled sample. The off-set values of the curves represent the $xNoFRET$ fraction. (B) The offset in (A) is subtracted and the time scale is logarithmic. (C) The time-axis is converted to the distance axis (eqs. 12-13; main text).

3.4.8. Cdc42 and TC10 induce variable responses in additional FRET sensors

CB opening disrupts the inter-domain interactions between the SH3-domain and the tandem DH-PH domain leading to dislocation of the SH3 domain (Soykan et al., 2014).

Sample	$\langle\tau\rangle$ (\pm SD), [ns]	R_1 (\pm SD) [\AA]	X_1 (\pm SD)	R_2 (\pm SD) [\AA]	X_2 (\pm SD)	X_{NoFRET} (\pm SD)
F1 _{DA}	2.52 (\pm 0.02)	25.5 (\pm 1.5)	0.45 (\pm 0.02)	45.5 (\pm 0.9)	0.21 (\pm 0.02)	0.32 (\pm 0.03)
F1 _{DA} + Cdc42	2.53 (\pm 0.03)	26.2 (\pm 1.2)	0.48 (\pm 0.02)	42.5 (\pm 1.9)	0.21 (\pm 0.04)	0.29 (\pm 0.11)
F1 _{DA} + TC10	2.87 (\pm 0.01)	26.8 (\pm 2.6)	0.20 (\pm 0.01)	47.5 (\pm 4.3)	0.23 (\pm 0.09)	0.68 (\pm 0.18)
F28 _{DA}	2.54 (\pm 0.03)	25.8 (\pm 1.1)	0.47 (\pm 0.02)	48.3 (\pm 0.4)	0.24 (\pm 0.02)	0.27 (\pm 0.01)
F28 _{DA} + Cdc42	2.56(\pm 0.01)	24.6 (\pm 0.8)	0.40 (\pm 0.01)	45 (\pm 0.8)	0.25 (\pm 0.01)	0.33 (\pm 0.01)
F28 _{DA} + TC10	2.8 (\pm 0.03)	27.1 (\pm 0.1)	0.18 (\pm 0.01)	46.7 (\pm 0.02)	0.25 (\pm 0.01)	0.56 (\pm 0.01)
F73 _{DA}	2.12 (\pm 0.04)	24.2 (\pm 1.1)	0.78 (\pm 0.01)	45.6 (\pm 0.2)	0.11 (\pm 0.01)	0.11 (\pm 0.06)
F73 _{DA} + Cdc42	2.19 (\pm 0.01)	25.3 (\pm 0.3)	0.63 (\pm 0.01)	44.8 (\pm 0.5)	0.16 (\pm 0.01)	0.16 (\pm 0.02)
F73 _{DA} + TC10	2.73 (\pm 0.03)	22.5 (\pm 0.3)	0.30 (\pm 0.02)	39.6 (\pm 1.5)	0.22 (\pm 0.02)	0.46 (\pm 0.01)
F99 _{DA}	2.3 (\pm 0.02)	24.7 (\pm 2.1)	0.73(\pm 0.01)	54 (\pm 1.6)	0.12 (\pm 0.12)	0.13 (\pm 0.03)
F99 _{DA} + Cdc42	2.39 (\pm 0.01)	25.8 (\pm 2.3)	0.38 (\pm 0.01)	51.7 (\pm 1.6)	0.23 (\pm 0.11)	0.38 (\pm 0.07)
F99 _{DA} + TC10	2.6 (\pm 0.01)	32.9 (\pm 0.4)	0.10 (\pm 0.03)	52.7 (\pm 2.0)	0.14 (\pm 0.03)	0.74 (\pm 0.01)

Table 3.3 (Supplementary Table 2 in the manuscript). Time-resolved FRET analysis for different CB-FRET sensors having the FLAsH moiety at positions 1, 28, 73, or 99 of CB in the presence of a 100-fold molar excess of Cdc42 or TC10. The table depicts their measured average fluorescence lifetimes ($\langle\tau\rangle$), inter-fluorophore distances (R_i) and their relative species fractions (x_i). Species fractions are normalized such that $x_1 + x_2 + x_{\text{NoFRET}} = 1$. Data from three individual biological replicates ($n = 3$) are presented as mean values \pm SD.

We probed the SH3-domain orientation with respect to the remainder of CB following activation by both GTPases. We employed a previously described additional set of SH3-domain responsive CB FRET sensors (Imam, Choudhury, Hemmen, et al., 2022) incorporating the FLAsH moiety after amino-acid residue 28 (F28_{DA}), 73 (F73_{DA}) and 99 (F99_{DA})(Figure 2.2B) and measured $\langle\tau\rangle$ in the absence and presence of 100-fold molar excess of TC10 and Cdc42 (Table 3.3, Fig. 3.11A). For F28_{DA} no $\langle\tau\rangle$ change was observed (Figure 3.11A) upon interaction with Cdc42 ($\langle\tau\rangle = 2.56 \pm 0.01$ ns) whereas TC10 caused

a substantial increase ($\langle\tau\rangle = 2.8 \pm 0.03$ ns). F73_{DA} showed a minute $\langle\tau\rangle$ increase in the presence of Cdc42 ($\langle\tau\rangle = 2.19 \pm 0.005$ ns) and a considerable increase with TC10 ($\langle\tau\rangle = 2.73 \pm 0.03$ ns) (Fig. 3.11A, Table 3.3). Similar to F73_{DA}, a minor increase in ($\langle\tau\rangle = 2.39 \pm 0.01$ ns) was observed for F99_{DA} (Fig. 3.5A), while TC10 led to a slightly smaller increase ($\langle\tau\rangle = 2.6 \pm 0.004$ ns) in F99_{DA} compared to the other sensors (Figure 3.11).

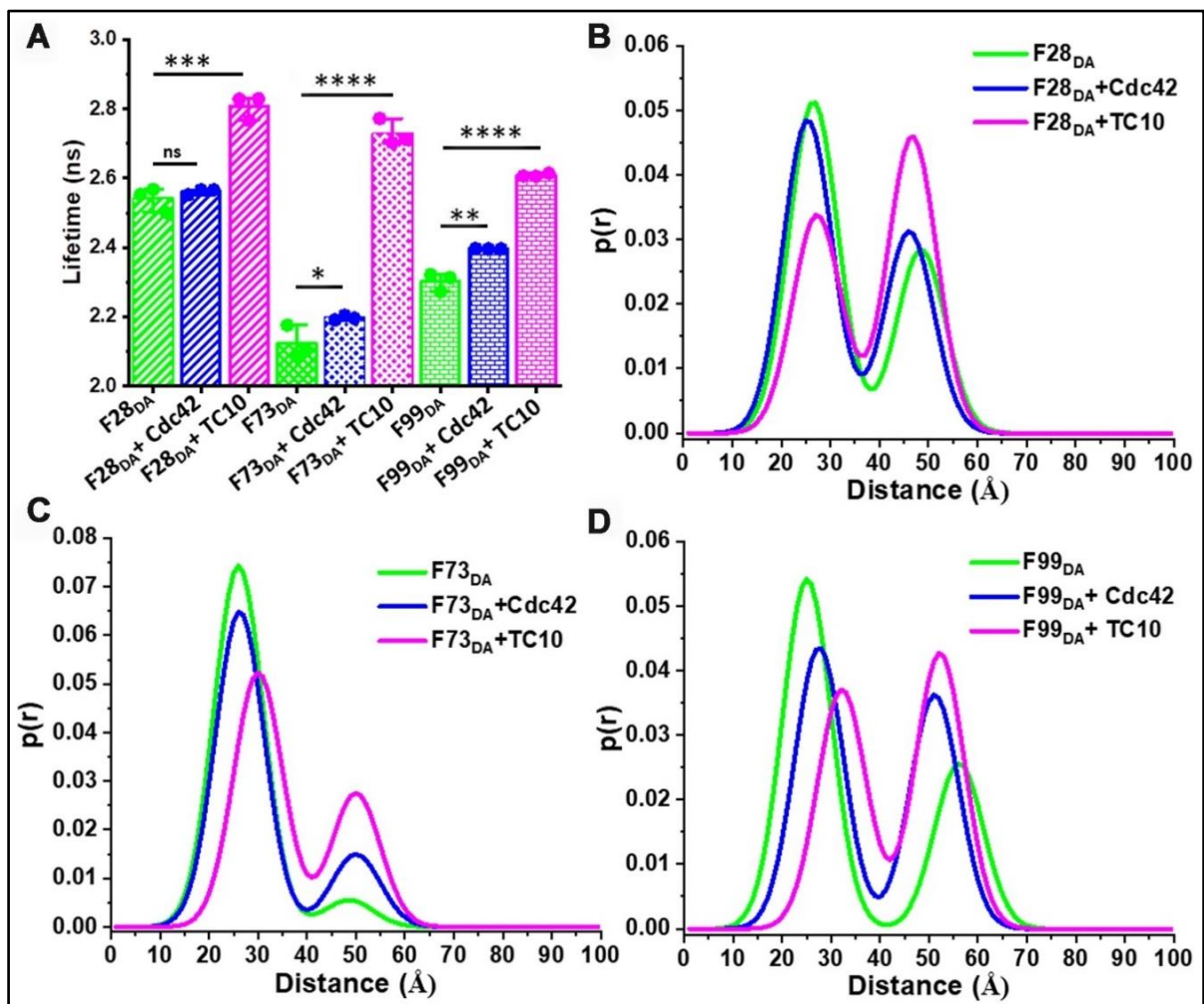


Figure 3.11 (Figure 5 in the manuscript). TC10 and Cdc42 induce varied responses in additional FRET sensors. (A) Bar graph showing the species-weighted average fluorescence-lifetime of F28_{DA}, F73_{DA} and F99_{DA} alone (green) and in the presence of a 100-fold molar excess of Cdc42 (blue) or TC10 (magenta). * $P < 0.05$, ** $P < 0.01$, *** $P < 0.001$, **** $P < 0.0001$; ns, statistically not significant. **(B-D)** Plots showing the distance distribution obtained from the two Gaussian distributed distance fit model for (B) F28_{DA}, (C) F73_{DA} and (D) F99_{DA} in the absence (green) and presence of Cdc42 (blue) and TC10 (magenta).

We also carried out distance distribution studies for all sensors in the absence and presence of a 100-fold molar excess of Cdc42 and TC10. Consistent with our previous

study (Imam, Choudhury, Hemmen, et al., 2022), all sensors displayed comparable inter-fluorophore distances in the absence of ligands. Cdc42 could not change the equilibrium between the high-FRET (x_1) and low-FRET states (x_2) in the F1_{DA} and F28_{DA} (Fig. 3.11B). However, Cdc42 addition led to significant changes in the x_1 and x_2 species in F73_{DA} and F99_{DA} (Fig. 3.11C-D), hence shifting the equilibrium towards the low FRET state. In contrast to Cdc42, TC10 addition led to a strong shift in the equilibrium from the high FRET to the low FRET state in all (F1_{DA}, F28_{DA}, F73_{DA} and F99_{DA}) sensors (Fig. 3.5B-D). The overall results evidently suggest that both GTPases occupy different binding sites (Mayer et al., 2013; Xiang et al., 2006) relative to the respective sensor and hence induce variable responses in the different sensors.

3.4.9. Cdc42 and TC10 display different electrostatic potentials

To better understand the molecular basis of differential recognition of both GTPases by CB, we calculated the electrostatic potential of the two proteins (Hemsath et al., 2005; Soykan et al., 2014; Xiang et al., 2006) using APBS (Jurrus et al., 2018) at an ionic strength of 150 mM. Full-length CB was found to contain small patches of positive, neutral, and negative residues, uniformly distributed over the surface of the SH3 and DH domains (Fig. 3.12A). In contrast, the PH domain possesses a positively charged area in close proximity to the SH3-PH domain interface (Fig. 3.12A). Removing Cdc42 from the complex with the SH3-domain truncated CB variant (Fig. 3.12B) illustrated that the top interface region located in the DH domain largely consists of positively charged residues, whereas the bottom section contained a small patch of acidic residues.

Analysis of the Cdc42 interface region in the Cdc42-CBSH3⁻ complex (Fig. 3.12C) revealed no prominent electronegative or electropositive features, thus indicating that complex formation is driven by hydrophobic interactions and hydrogen bonds as outlined above (Fig. 3.1D, F). In contrast, the corresponding surface of TC10 (Fig. 3.12E) contains strong negative patches at its center and a smaller patch of positively charged electrostatic potential at the bottom. Surprisingly, these patches are complementary to those observed in CB where Cdc42 interacts. Hence, the inability of TC10 to interact with CB in an analogous manner as Cdc42 must arise from the amino acid replacements discussed earlier (Fig. 3.1D-G), which abrogate the hydrophobic contacts and H-bonds present in the CB-Cdc42 complex. Rotation of both GTPases by 90° highlighted additional

differences; TC10 featured a significant electronegative patch, in contrast to Cdc42 with an electropositive patch at the same region (right edge in Fig. 3.6D and 3.12F).

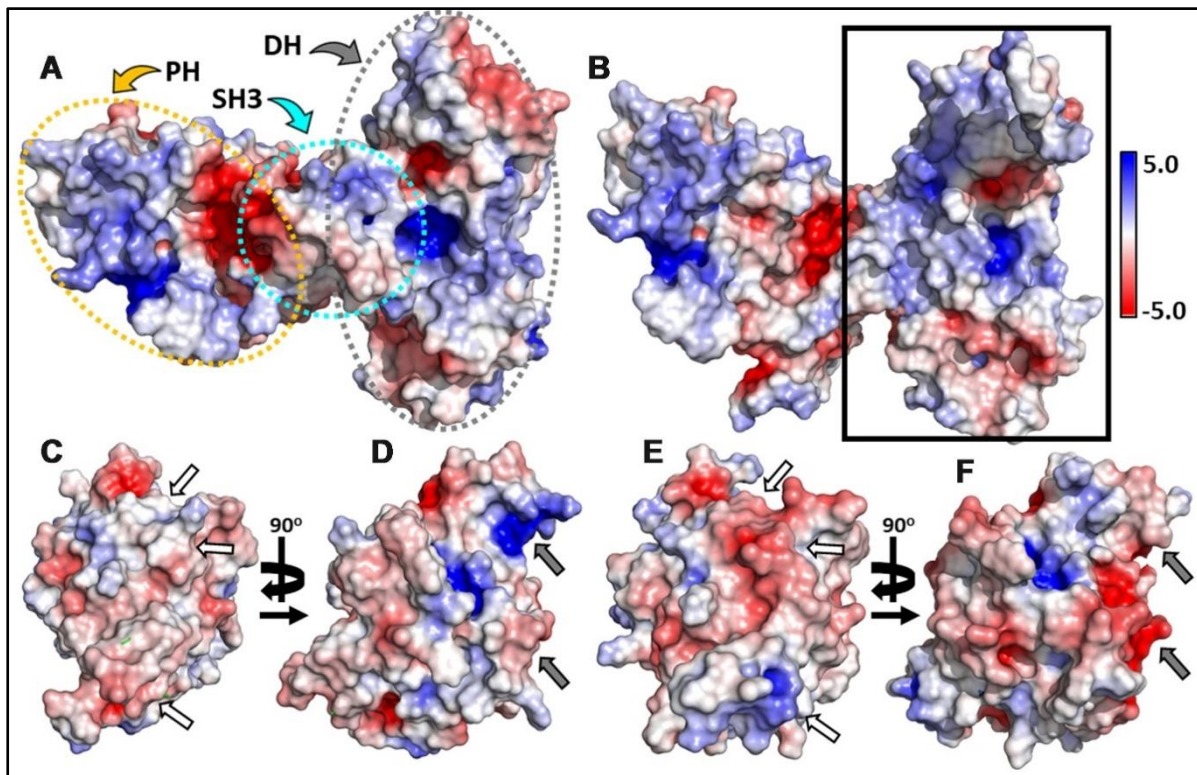


Figure 3.12 (Figure 6 in the manuscript). Electrostatic potentials of CB, Cdc42 and TC10. (A) Surface representations showing the electrostatic potentials of full-length CB (PDB entry 4mt6). The SH3, DH and PH domains are outlined by dotted ellipsoids shown in cyan, gray, and yellow, respectively. (B) Electrostatic potential of CBSH3⁻ (PDB entry 2dfk) viewed into interface region (solid rectangle) of the CBSH3⁻-Cdc42 complex with Cdc42 omitted from the calculation. (C, E) Electrostatic potential of Cdc42 showing the interface region of the Cdc42-CBSH3⁻ complex after rotation by 180° around the vertical axis (C) and hypothetical CB-TC10 interface region following superimposition of TC10 on Cdc42 (E). Regions possessing substantial charge differences between Cdc42 (C) and TC10 (E) are emphasized by white arrows. (D, F) Surface charge potential of Cdc42 (D) and TC10 (F) when rotated by 90° around the vertical axis. Sections having substantial charge differences between Cdc42 (D) and TC10 (F) are highlighted by grey arrows. All electrostatic potentials are represented by isosurfaces contoured at $-5.0 k_bT/e_c$ (red) or $5.0 k_bT/e_c$ (blue), respectively.

This region in TC10 would be ideally suited to interact with the positively charged PH domain, in line with its known binding preference (Mayer et al., 2013). At the same time, Cdc42 cannot interact with the PH domain in the same manner since it is oppositely charged in this region.

3.5. Discussion

Activation of Ras-related GTPases and their isoforms induces a plethora of cellular processes, including reorganizations of the actin cytoskeleton governing the cell cycle and cellular motility (Hall, 1998; Hodge & Ridley, 2016; Mosaddeghzadeh & Ahmadian, 2021). In humans, based on sequence similarity, 20 canonical members of the Rho family have been identified to date (Wittinghofer & Vetter, 2011). The GTPases belonging to the Cdc42 subfamily, TC10 and Cdc42, share common cellular functions (Murphy et al., 2001), however, TC10 expression is limited to specific hippocampal regions (Tanabe et al., 2000) where the most prominent reduction in gephyrin is observed in CB knock-out mice (Papadopoulos et al., 2007), thus suggesting a potential role in GABA_A receptor clustering (Mayer et al., 2013).

Previous cell-based and biochemical studies documented that TC10 binding to CB triggers synaptic gephyrin clustering and enhances GABAergic neurotransmission (Kilisch et al., 2020; Mayer et al., 2013). Moreover, prior work demonstrated that CB interaction with the intracellular domain of NL2 or Cdc42 leads to an open structure of CB, which favors its interaction with phosphoinositides located in the postsynaptic membrane (Poulopoulos et al., 2009; Schäfer et al., 2020; Soykan et al., 2014). Our study with the wild-type mimicking CB FRET sensor (F1_{DA}) (Fig. 3.3A-B) upon interaction with TC10 resulted in a significant increase in $\langle\tau\rangle$, indicating a TC10-mediated CB opening. In contrast, the inability of Cdc42 to induce any $\langle\tau\rangle$ change in F1_{DA} reflects the preferential binding of CB to TC10. Furthermore, we could determine the binding strength of the CB-TC10 complex with a K_d of $37 \pm 4 \mu\text{M}$, which so far had not been determined (Fig. 3.3C). The interaction with Cdc42 is considerably weaker, which precluded an experimental determination of the binding strength by our approach.

The C-terminal extension of TC10 harbors several basic residues, which have been shown to play an important role in CB-dependent gephyrin micro-clustering (Kilisch et al., 2020). A TC10 variant in which several lysine and arginine C-terminal residues were replaced with glycine and serine (TC10KR/GS) failed to stimulate gephyrin clustering and abrogated phosphoinositide binding (Kilisch et al., 2020). Our studies showed that the TC10KR/GS variant bound more tightly ($K_d = 19 \pm 2 \mu\text{M}$) as did the TC10 Δ C variant in which the C-terminal residues were removed ($K_d = 13 \pm 1 \mu\text{M}$), compared to the TC10

wild-type ($K_d = 37 \pm 4 \mu\text{M}$) (Fig. 3.3C and 3.5C). This demonstrated that, while the C-terminal residues are crucial for phosphoinositide-binding (Kilisch et al., 2020), they do not contribute to TC10-CB complex formation *in vitro*. In fact, our electrostatic analysis suggested that the interaction between TC10 and the PH domain of CB is driven by electrostatic interactions with the PH domain being positively charged and TC10 being negatively charged. The presence of additional positive charges at the TC10 C-terminus could hence weaken this electrostatic complementarity.

The Cdc42 interaction with the open state mutant sensors F1_{smDA} and F1_{dmDA}, as reflected in the $\langle\tau\rangle$ increase, (Fig. 3.7A) suggested that Cdc42 only binds to the open-state CB. Quantification of the F1_{dmDA} data revealed a rather low affinity characterized by a K_d -value of $102 \pm 25 \mu\text{M}$ (Fig. 3.7B), in contrast to the Cdc42-F1_{DA} interaction where no binding could be detected (Fig. 3.3A-B). This finding further corroborated previous biochemical data (Xiang et al., 2006), which revealed that full-length CB showed a significantly reduced GEF activity compared to the CB2-SH3⁻ variant.

A similar trend was also observed for TC10 where binding to both F1_{smDA} and F1_{dmDA} sensors led to a strong $\langle\tau\rangle$ increase (Fig. 3.7A), which resulted in an increase in binding affinity ($K_d = 5.2 \pm 1.2 \mu\text{M}$) to the F1_{dmDA} sensor (Fig. 3.7B). The preferential binding of Cdc42 to F1_{dmDA} and the enhanced binding of TC10 to this sensor presumably reflects an increased accessibility of the respective binding site. While this can be straightforwardly understood in the case of Cdc42 where the SH3 domain in the closed state of CB (Soykan et al., 2014) partially overlaps with Cdc42 (Fig. 3.12A), it cannot be easily rationalized for the CB-TC10 interaction in the absence of structural data. One possible explanation would be that the SH3 domain in the closed conformation slightly overlaps with the TC10 binding site in the PH domain (Kilisch et al., 2020; Mayer et al., 2013). Based on our time-resolved fluorescence-based FRET data, we propose a simplified model (Fig. 3.13) for GTPase-mediated conformational activation of CB.

In summary, this study provides clear evidence of a TC10-induced CB conformational switch from its auto-inhibited or closed state to an open/active state. As described earlier (Soykan et al., 2014), the open conformation is critical for the ability of CB to promote the formation of inhibitory postsynaptic structures. Despite the fact that Cdc42 is a closely related GTPase, it fails to induce this conformational change in full-length CB, which, on the molecular level, correlates with its entirely different mode of interaction with CB.

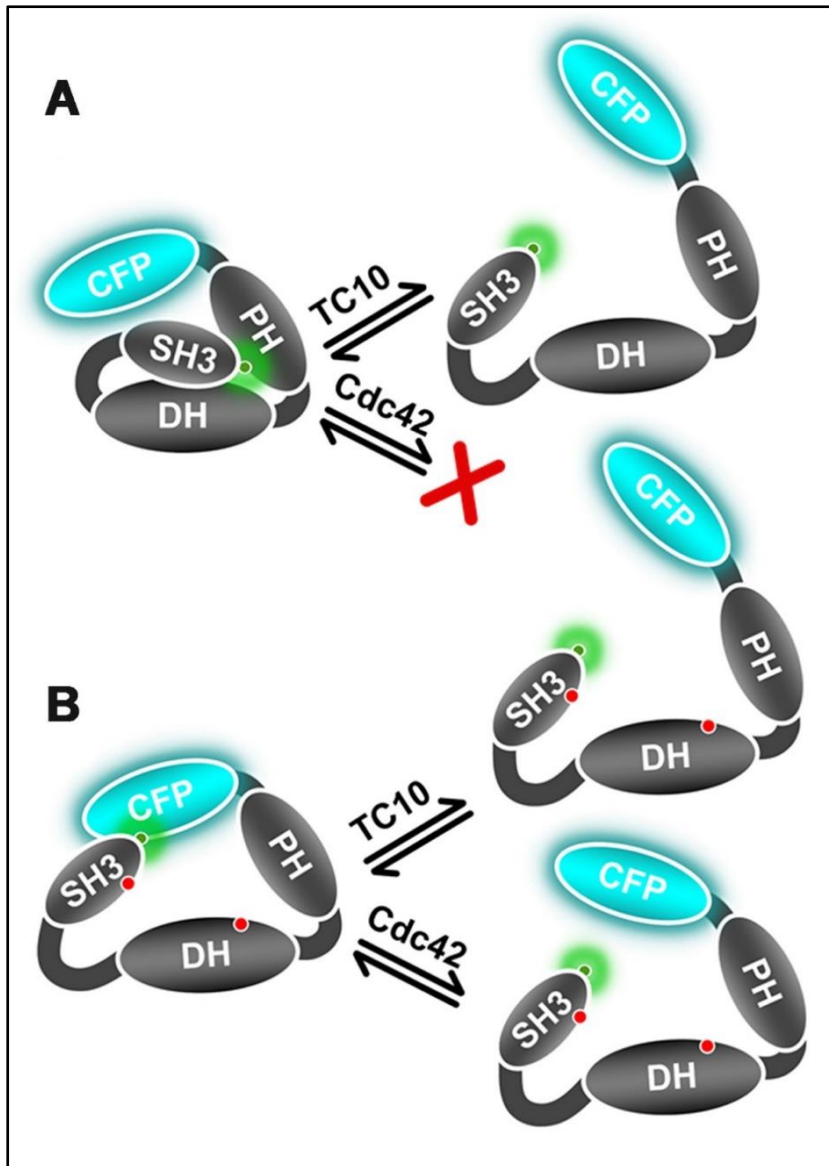


Figure 3.13 (Figure 7 in the manuscript). *Schematic representation of TC10 and Cdc42 mediated CB conformational activation. (A) This figure represents the wild-type mimicking CB FRET sensor ($F1_{DA}$) in the auto-inhibited form and its conformational state after interaction with TC10 or the inability of Cdc42 to interact with this sensor. (B) Cartoon depicting the active state CB FRET sensor ($F1_{dmDA}$) conformational change after TC10 and Cdc42 binding. TC10 binding induces a strong change in $\langle \tau \rangle$ and hence a large inter-fluorophore movement, whereas it is relatively small for Cdc42. Red dots on the SH3 and DH domain represent the incorporated amino-acid replacements in the $F1_{dmDA}$ construct.*

construct.

Contrary to the ubiquitous expression of Cdc42, the limited expression of TC10 in the hippocampus was reported to be essential for CB-dependent gephyrin clustering (Kilisch et al., 2020; Mayer et al., 2013). Our data hence suggest that the TC10-induced stabilization of CB in the open state is critical for gephyrin clustering. Interestingly, both GTPases have also been reported to interact with another Dbl family Rho GEF, ARHGEF7 (also called β Pix) via its catalytic DH domain (Feng et al., 2002; López Tobón et al., 2018). Intriguingly, β Pix-deficient neurons lack the ability of axon formation in culture and in the developing cortex. Nevertheless, the loss can be rescued by the expression of TC10, but not Cdc42 (López Tobón et al., 2018). Since there are no reports regarding GTPase-mediated β Pix conformational activation, it would be interesting to investigate as to how

TC10 and Cdc42 interact with β Pix and whether they possibly induce similar conformational changes as observed for CB in this study.

3.6. Acknowledgements

The project was funded by the Deutsche Forschungsgemeinschaft (SCHI425-8/3). We would like to thank Nicole Bader and Monika Kuhn for their technical help and the Seidel Lab (Molecular Physical Chemistry, Heinrich-Heine-Universität, Düsseldorf, Germany) for providing the MFD software package.

3.7. Author contributions

N.I. generated the TC10 constructs, purified the proteins, carried out *in vitro* experiments and performed the time-resolved fluorescence measurements. N.I. and S.C. analysed the results. NI and HS prepared the manuscript. The project was supervised by H.S. and K.G.H.

4. Cumulative Discussion

In the developing brain, the dynamic generation of synapses between adjacent neuronal cells is a fundamental determinant of synaptogenesis and neuronal network development. During the process of synaptogenesis, contact spots of the presynaptic and postsynaptic neurons undergo significant changes in their morphology as well as molecular content to eventually form a fully functional synapse, a dynamically complex neuron-to-neuron junction. This process is orchestrated by various neuronal cell adhesion proteins and involves the accumulation of synaptic vesicles and active zone components at the presynaptic sites. In apposition to the transmitter release sites, at the postsynaptic membrane, synapse-type-specific neurotransmitter receptors are precisely clustered via the assistance of scaffolding and recruiting factors.

4.1. Gephyrin-mediated Collybistin activation

In mammals, the most prevalent scaffolding protein at inhibitory glycinergic and GABAergic postsynapses, gephyrin, is primarily responsible for glycine and GABA_A receptor clustering opposite to cognate neurotransmitter release sites (Kneussel & Betz, 2000; Moss & Smart, 2001). Gephyrin directly interacts with glycine and GABA_A receptors thus regulating their cell surface dynamics (Bai et al., 2021; Kasaragod & Schindelin, 2018; Maric, Kasaragod, Hausrat, et al., 2014; Tretter et al., 2012; Tyagarajan & Fritschy, 2014). The amount of gephyrin recruited from the intracellular deposits to the postsynaptic membrane governs the receptor content and sensitivity of inhibitory synapses (Specht et al., 2013). In many brain regions, the recruitment of gephyrin from cytosolic deposits to postsynaptic membranes relies on the adaptor protein collybistin (CB) (Papadopoulos & Soykan, 2011). However, despite CB having a fundamental role as neuronal adaptor safeguarding the proper function of inhibitory GABAergic synapses, its interaction with the neuronal scaffolding protein gephyrin remained poorly understood. This thesis primarily addresses this open question through the aid of a series of CB FRET sensors. Previous studies hypothesized that CB interaction with the neuronal factors, NL2_{icd} and the GABA_A α 2 subunit leads to an open structure of CB, which allows CB to interact with phosphoinositides located in the postsynaptic membrane (Poulopoulos et al., 2009; Schäfer et al., 2020; Soykan et al., 2014). However, contrary to the previously

hypothesized notion (Jedlicka et al., 2009; Soykan et al., 2014), CB FRET sensor interaction with the NL2_{icd} suggested that initial CB relief by NL2 binding is not essential for gephyrin-CB interaction and hence their stable complex formation (see Section 2.5.2). Binding affinity quantification for the GephFL-CB complex (see Section 2.5.3) indicated a reasonably tight interaction between the two neuronal factors. The GephLE and GephE domain variants of gephyrin also displayed identical binding affinity to that of GephFL. Interestingly, a monomeric (or dimerization-deficient) variant of the E domain (GephE_{mm}) was also able to interact with CB. However, binding strength quantification for the GephE_{mm}-F1_{DA} complex demonstrated a lower binding affinity, suggesting that GephE dimerization may be required to enhance its affinity for CB, potentially by stabilizing the E-domain.

Gaussian distributed distance fit modelling demonstrated the existence of two CB conformational states, encompassing a compact or high FRET state and a relaxed or low FRET state. Interestingly, quantification of CB molecules in the high and low FRET states indicated that GephFL binding shifts the equilibrium from the closed state of CB (high-FRET F1_{DA}) towards the open (low-FRET F1_{DA}) state. In line with the results obtained with GephFL, the GephE and GephE_{mm} domain variants also showed a similar behavior in mediating the transition from the closed to the open state of CB.

In this study, constitutively active mutant CB FRET F1_{smDA} and F1_{dmDA} sensors were also employed to better understand the conformational dynamics of the CB. Compared to the CB wild-type, the constitutively active mutant sensors exhibited an increased average FRET efficiency, indicating that disruption of the intramolecular SH3-DH/PH interaction potentially rearranges the SH3 and PH domains, hence bringing the FAsH and CFP moieties into closer proximity.

Markov-chain Monte-Carlo (MCMC) sampling (Greife et al., 2016; Kravets et al., 2016) clearly identified distinct closed and open states of CB. GephFL addition led to a clearly distinguishable open state of CB, in which the probability densities of the two fluorophores were clearly separated with increased CFP density being present on the opposite side of the connecting helix between the DH and PH domains.

The *in vitro* studies accompanied by the simulation data presented in this thesis, clearly demonstrates GephFL-mediated CB opening, disrupting the intramolecular interaction between the SH3 domain and the DH-PH tandem.

4.2. Differential Rho GTPase recognition by Collybistin and its conformational activation

Based on sequence identity within the Ras superfamily approximately 20 members (further sub-divided into six subfamilies) of the Rho family have been identified in humans. Members of the Cdc42-subfamily, Cdc42 and TC10, although sharing common cellular functions, display variable cellular expressions (Murphy et al., 2001; Tanabe et al., 2000). In contrast to Cdc42, which is ubiquitously expressed, TC10 expression is confined to specific hippocampal region in the brain. Interestingly, previous studies suggested that TC10 binding to CB triggers synaptic gephyrin clustering and enhances GABAergic neurotransmission. This dissertation addresses the molecular basis of differential recognition of closely related GTPases TC 10 and the Cdc42 by CB.

Interaction studies of full-length CB with TC10 indicated a moderately tight interaction between the proteins, while full-length CB displayed a considerably weaker interaction for Cdc42, which precluded quantification of the binding strength. In contrast to wild-type CB, open state mutant of CB could efficiently interact with both GTPases, suggesting a preferential binding of Cdc42 to the open state of CB. Cdc42 preferential interaction for the open state mutant CB is potentially because of the mutation induced autoinhibition relief which, otherwise, is absent in wild-type CB, leading to steric interference of the SH3 domain with the Cdc42 binding region on CB (Soykan et al., 2014; Xiang et al., 2006). Overall, the biophysical and structural data presented in this dissertation provide clear evidence of a TC10-induced CB conformational switch from its auto-inhibited or closed state to an open/active state.

5. Future perspective

5.1. Gephyrin-Collybistin Interaction

The results presented in this thesis clearly indicate that the gephyrin interaction with CB leads to a conformational activation of the latter. The fluorescence life-time based FRET measurements of the intramolecular CB FRET sensors described in Chapter 2 provide significant insights into the mechanism of CB activation *in vitro*. In the future the described intramolecular sensors should be extended to *in vitro* cell-based studies in isolated hippocampal neurons, to better understand CB-mediated gephyrin clustering along with the gephyrin-mediated CB conformational activation. To accomplish this goal fluorescence-lifetime imaging microscopy (FLIM) would be an ideal technique to unravel the intricate details of interaction of both proteins in a cell-based system.

5.2. Collybistin and Rho GTPase interaction

The work described in Chapter 3 of this dissertation demonstrates an interesting set of characteristics for CB. *In vitro* studies suggest that the Rho GTPases interact differently with the wild-type and constitutively active, open state mutant CB. Although an *in cellulo* interaction study of CB and TC10 has already been carried out (Kilisch et al., 2020; Mayer et al., 2013), a comparative study between TC10 and Cdc42 is still lacking and hence would be interesting to conduct. Since Rho GTPases play crucial roles in controlling fundamental cellular processes, it would be interesting to study the effect of a constitutively active mutant CB in hippocampal neurons where TC10 is specifically expressed.

5.3. CB interaction with the GABA_AR α 2 subunit

This dissertation specifically highlights interactions of CB with postsynaptic neuronal factors including NL2, gephyrin, and Rho GTPases Cdc42 and TC10. However, a well-known interacting partner of CB, the α 2 subunit of GABA_A receptor, has not been included in this dissertation. The α 2 subunit has been hypothesized to interact with the SH3 domain of CB and hence would be required for CB autoinhibition relief. Initial preliminary

interaction data (not included in this dissertation) utilizing CB FRET sensors and $\alpha 2$ subunit indicate that the interaction also results in conformational activation of CB, however, additional experiments need to be carried out to better understand the $\alpha 2$ subunit mediated CB activation.

5.4. CB interaction with phosphoinositides

The PH domain of CB has been reported to specifically interact with phosphatidylinositol-3-phosphate, and the membrane tethering property of CB has been regarded as crucial for its function. The interaction of CB with other phosphoinositides has not been extensively studied. The series of CB FRET sensors described in the dissertation would provide an excellent system to characterize the CB interaction with other phosphoinositides.

6. References

- Adams, S. R., Campbell, R. E., Gross, L. A., Martin, B. R., Walkup, G. K., Yao, Y., Llopis, J., & Tsien, R. Y. (2002). New Biarsenical Ligands and Tetracysteine Motifs for Protein Labeling in Vitro and in Vivo: Synthesis and Biological Applications. *Journal of the American Chemical Society*, 124(21), 6063-6076. <https://doi.org/10.1021/ja017687n>
- Agarwal, S., Tannenber, R. K., & Dodd, P. R. (2008). Reduced Expression of the Inhibitory Synapse Scaffolding Protein Gephyrin in Alzheimer's Disease. *Journal of Alzheimer's Disease*, 14, 313-321. <https://doi.org/10.3233/JAD-2008-14305>
- Aghazadeh, B., Zhu, K., Kubiseski, T. J., Liu, G. A., Pawson, T., Zheng, Y., & Rosen, M. K. (1998). Structure and mutagenesis of the Dbl homology domain. *Nat Struct Biol*, 5(12), 1098-1107. <https://doi.org/10.1038/4209>
- Alexander, S. P. H., Benson, H. E., Faccenda, E., Pawson, A. J., Sharman, J. L., Spedding, M., Peters, J. A., Harmar, A. J., & Collaborators, C. (2013). The Concise Guide to PHARMACOLOGY 2013/14: Ligand-Gated Ion Channels. *British Journal of Pharmacology*, 170(8), 1582-1606. <https://doi.org/https://doi.org/10.1111/bph.12446>
- Algar, W. R., Hildebrandt, N., Vogel, S. S., & Medintz, I. L. (2019). FRET as a biomolecular research tool — understanding its potential while avoiding pitfalls. *Nature Methods*, 16(9), 815-829. <https://doi.org/10.1038/s41592-019-0530-8>
- Alvarez, F. J. (2017). Gephyrin and the regulation of synaptic strength and dynamics at glycinergic inhibitory synapses. *Brain Research Bulletin*, 129, 50-65. <https://doi.org/https://doi.org/10.1016/j.brainresbull.2016.09.003>
- Andersen, P., Eccles, J. C., & Løynings, Y. (1963). Hippocampus of the Brain: Recurrent Inhibition in the Hippocampus with Identification of the Inhibitory Cell and its Synapses. *Nature*, 198(4880), 540-542. <https://doi.org/10.1038/198540a0>
- Bai, G., Wang, Y., & Zhang, M. (2021). Gephyrin-mediated formation of inhibitory postsynaptic density sheet via phase separation. *Cell Research*, 31(3), 312-325. <https://doi.org/10.1038/s41422-020-00433-1>
- Bear, M., Connors, B., & Paradiso, M. A. (2020). *Neuroscience: Exploring the Brain, Enhanced Edition: Exploring the Brain*. Jones & Bartlett Learning.
- Bender, A., & Pringle, J. R. (1989). Multicopy suppression of the cdc24 budding defect in yeast by CDC42 and three newly identified genes including the ras-related gene RSR1. *Proceedings of the National Academy of Sciences*, 86(24), 9976-9980. <https://doi.org/10.1073/pnas.86.24.9976>

- Betz, H. (1998). Gephyrin, a major player in GABAergic postsynaptic membrane assembly? *Nature Neuroscience*, 1(7), 541-543. <https://doi.org/10.1038/2777>
- Bilwes, A. M., Alex, L. A., Crane, B. R., & Simon, M. I. (1999). Structure of CheA, a signal-transducing histidine kinase. *Cell*, 96(1), 131-141. [https://doi.org/10.1016/s0092-8674\(00\)80966-6](https://doi.org/10.1016/s0092-8674(00)80966-6)
- Bond, S. R., & Naus, C. C. (2012). RF-Cloning.org: an online tool for the design of restriction-free cloning projects. *Nucleic Acids Res*, 40(Web Server issue), W209-213. <https://doi.org/10.1093/nar/gks396>
- Buhl, E. H., Halasy, K., & Somogyi, P. (1994). Diverse sources of hippocampal unitary inhibitory postsynaptic potentials and the number of synaptic release sites. *Nature*, 368(6474), 823-828. <https://doi.org/10.1038/368823a0>
- Cherfils, J., & Chardin, P. (1999). GEFs: structural basis for their activation of small GTP-binding proteins. *Trends Biochem Sci*, 24(8), 306-311. [https://doi.org/10.1016/s0968-0004\(99\)01429-2](https://doi.org/10.1016/s0968-0004(99)01429-2)
- Chiou, T.-T., Bonhomme, B., Jin, H., Miralles, C. P., Xiao, H., Fu, Z., Harvey, R. J., Harvey, K., Vicini, S., & De Blas, A. L. (2011). Differential Regulation of the Postsynaptic Clustering of γ -Aminobutyric Acid Type A (GABAA) Receptors by Collybistin Isoforms. *Journal of Biological Chemistry*, 286(25), 22456-22468. <https://doi.org/10.1074/jbc.m111.236190>
- Chiou, T.-T., Long, P., Schumann-Gillett, A., Kanamarlapudi, V., Haas, S. A., Harvey, K., O'Mara, M. L., De Blas, A. L., Kalscheuer, V. M., & Harvey, R. J. (2019). Mutation p.R356Q in the Collybistin Phosphoinositide Binding Site Is Associated With Mild Intellectual Disability [Original Research]. *Frontiers in Molecular Neuroscience*, 12. <https://www.frontiersin.org/articles/10.3389/fnmol.2019.00060>
- Choi, G., & Ko, J. (2015). Gephyrin: a central GABAergic synapse organizer. *Experimental & Molecular Medicine*, 47(4), e158-e158. <https://doi.org/10.1038/emm.2015.5>
- Colicelli, J. (2004). Human RAS superfamily proteins and related GTPases. *Sci STKE*, 2004(250), Re13. <https://doi.org/10.1126/stke.2502004re13>
- Copley, S. D. (2003). Enzymes with extra talents: moonlighting functions and catalytic promiscuity. *Current Opinion in Chemical Biology*, 7(2), 265-272. [https://doi.org/https://doi.org/10.1016/S1367-5931\(03\)00032-2](https://doi.org/https://doi.org/10.1016/S1367-5931(03)00032-2)
- Crosby, K. C., Gookin, S. E., Garcia, J. D., Hahm, K. M., Dell'Acqua, M. L., & Smith, K. R. (2019). Nanoscale Subsynaptic Domains Underlie the Organization of the Inhibitory Synapse. *Cell Reports*, 26(12), 3284-3297.e3283. <https://doi.org/10.1016/j.celrep.2019.02.070>

- de Groot, C., Floriou-Servou, A., Tsai, Y. C., Früh, S., Kohler, M., Parkin, G., Schwerdel, C., Bosshard, G., Kaila, K., Fritschy, J. M., & Tyagarajan, S. K. (2017). RhoGEF9 splice isoforms influence neuronal maturation and synapse formation downstream of $\alpha 2$ GABAA receptors. *PLoS Genet*, 13(10), e1007073. <https://doi.org/10.1371/journal.pgen.1007073>
- Dejanovic, B., Lal, D., Catarino, C. B., Arjune, S., Belaidi, A. A., Trucks, H., Vollmar, C., Surges, R., Kunz, W. S., Motameny, S., Altmüller, J., Köhler, A., Neubauer, B. A., Epicure, C., Nürnberg, P., Noachtar, S., Schwarz, G., & Sander, T. (2014). Exonic microdeletions of the gephyrin gene impair GABAergic synaptic inhibition in patients with idiopathic generalized epilepsy. *Neurobiology of Disease*, 67, 88-96. <https://doi.org/10.1016/j.nbd.2014.02.001>
- Dejanovic, B., & Schwarz, G. (2014). Neuronal Nitric Oxide Synthase-Dependent S-Nitrosylation of Gephyrin Regulates Gephyrin Clustering at GABAergic Synapses. *The Journal of Neuroscience*, 34(23), 7763. <https://doi.org/10.1523/JNEUROSCI.0531-14.2014>
- Dejanovic, B., Semtner, M., Ebert, S., Lamkemeyer, T., Neuser, F., Lüscher, B., Meier, J. C., & Schwarz, G. (2014). Palmitoylation of Gephyrin Controls Receptor Clustering and Plasticity of GABAergic Synapses. *PLoS Biology*, 12(7), e1001908. <https://doi.org/10.1371/journal.pbio.1001908>
- Dos Reis, R., Kornobis, E., Pereira, A., Tores, F., Carrasco, J., Gautier, C., Jahannault-Talignani, C., Nitschké, P., Muchardt, C., Schlosser, A., Maric, H. M., Ango, F., & Allemand, E. (2022). Complex regulation of Gephyrin splicing is a determinant of inhibitory postsynaptic diversity. *Nature Communications*, 13(1), 3507. <https://doi.org/10.1038/s41467-022-31264-w>
- Du, J., Lü, W., Wu, S., Cheng, Y., & Gouaux, E. (2015, Oct 8). Glycine receptor mechanism elucidated by electron cryo-microscopy. *Nature*, 526(7572), 224-229. <https://doi.org/10.1038/nature14853>
- Dumoulin, A., Lévi, S., Riveau, B., Gasnier, B., & Triller, A. (2000). Formation of mixed glycine and GABAergic synapses in cultured spinal cord neurons. *Eur J Neurosci*, 12(11), 3883-3892. <https://doi.org/10.1046/j.1460-9568.2000.00271.x>
- Ellenbroek, S. I., & Collard, J. G. (2007). Rho GTPases: functions and association with cancer. *Clin Exp Metastasis*, 24(8), 657-672. <https://doi.org/10.1007/s10585-007-9119-1>
- Essrich, C., Lorez, M., Benson, J. A., Fritschy, J.-M., & Lüscher, B. (1998). Postsynaptic clustering of major GABAA receptor subtypes requires the $\gamma 2$ subunit and gephyrin. *Nature Neuroscience*, 1(7), 563-571. <https://doi.org/10.1038/2798>
- Etienne-Manneville, S., & Hall, A. (2002). Rho GTPases in cell biology. *Nature*, 420(6916), 629-635. <https://doi.org/10.1038/nature01148>

- Eva, A., & Aaronson, S. A. (1985). Isolation of a new human oncogene from a diffuse B-cell lymphoma. *Nature*, 316(6025), 273-275. <https://doi.org/10.1038/316273a0>
- Falzone, C. J., Kao, Y. H., Zhao, J., Bryant, D. A., & Lecomte, J. T. (1994). Three-dimensional solution structure of PsaE from the cyanobacterium *Synechococcus* sp. strain PCC 7002, a photosystem I protein that shows structural homology with SH3 domains. *Biochemistry*, 33(20), 6052-6062. <https://doi.org/10.1021/bi00186a004>
- Fang, M., Shen, L., Yin, H., Pan, Y.-M., Wang, L., Chen, D., Xi, Z.-Q., Xiao, Z., Wang, X.-F., & Zhou, S.-N. (2011). Downregulation of gephyrin in temporal lobe epilepsy neurons in humans and a rat model [<https://doi.org/10.1002/syn.20928>]. *Synapse*, 65(10), 1006-1014. <https://doi.org/https://doi.org/10.1002/syn.20928>
- Feng, G., TINTRUP, H., KIRSCH, J., NICHOL, M. C., KUHSE, J., BETZ, H., & SANES, J. R. (1998). Dual Requirement for Gephyrin in Glycine Receptor Clustering and Molybdoenzyme Activity. *Science*, 282(5392), 1321. <https://doi.org/10.1126/science.282.5392.1321>
- Feng, Q., Albeck, J. G., Cerione, R. A., & Yang, W. (2002). Regulation of the Cool/Pix proteins: key binding partners of the Cdc42/Rac targets, the p21-activated kinases. *J Biol Chem*, 277(7), 5644-5650. <https://doi.org/10.1074/jbc.M107704200>
- Flores, C. E., Nikonenko, I., Mendez, P., Fritschy, J. M., Tyagarajan, S. K., & Muller, D. (2015). Activity-dependent inhibitory synapse remodeling through gephyrin phosphorylation. *Proc Natl Acad Sci U S A*, 112(1), E65-72. <https://doi.org/10.1073/pnas.1411170112>
- Förstera, B., Belaidi, A. A., Jüttner, R., Bernert, C., Tsokos, M., Lehmann, T.-N., Horn, P., Dehnicke, C., Schwarz, G., & Meier, J. C. (2010). Irregular RNA splicing curtails postsynaptic gephyrin in the cornu ammonis of patients with epilepsy. *Brain*, 133(12), 3778-3794. <https://doi.org/10.1093/brain/awq298>
- Fritschy, J.-M., Harvey, R. J., & Schwarz, G. (2008). Gephyrin: where do we stand, where do we go? *Trends in Neurosciences*, 31(5), 257-264. <https://doi.org/10.1016/j.tins.2008.02.006>
- Garcia, P., Gupta, R., Shah, S., Morris, A. J., Rudge, S. A., Scarlata, S., Petrova, V., McLaughlin, S., & Rebecchi, M. J. (1995). The pleckstrin homology domain of phospholipase C-delta 1 binds with high affinity to phosphatidylinositol 4,5-bisphosphate in bilayer membranes. *Biochemistry*, 34(49), 16228-16234. <https://doi.org/10.1021/bi00049a039>
- Ghosh, H., Auguadri, L., Battaglia, S., Simone Thirouin, Z., Zemoura, K., Messner, S., Acuña, M. A., Wildner, H., Yévenes, G. E., Dieter, A., Kawasaki, H., O. Hottiger,

- M., Zeilhofer, H. U., Fritschy, J.-M., & Tyagarajan, S. K. (2016). Several posttranslational modifications act in concert to regulate gephyrin scaffolding and GABAergic transmission. *Nature Communications*, 7(1), 13365. <https://doi.org/10.1038/ncomms13365>
- Gmeiner, W. H., & Horita, D. A. (2001). Implications of SH3 domain structure and dynamics for protein regulation and drug design. *Cell Biochemistry and Biophysics*, 35(2), 127-140. <https://doi.org/10.1385/CBB:35:2:127>
- Goitre, L., Trapani, E., Trabalzini, L., & Retta, S. F. (2014). The Ras superfamily of small GTPases: the unlocked secrets. *Methods Mol Biol*, 1120, 1-18. https://doi.org/10.1007/978-1-62703-791-4_1
- Greife, A., Felekyan, S., Ma, Q., Gertzen, C. G. W., Spomer, L., Dimura, M., Peulen, T. O., Wöhler, C., Häussinger, D., Gohlke, H., Keitel, V., & Seidel, C. A. M. (2016). Structural assemblies of the di- and oligomeric G-protein coupled receptor TGR5 in live cells: an MFIS-FRET and integrative modelling study. *Scientific Reports*, 6(1), 36792. <https://doi.org/10.1038/srep36792>
- Griffin, B. A., Adams, S. R., & Tsien, R. Y. (1998). Specific Covalent Labeling of Recombinant Protein Molecules Inside Live Cells. *Science*, 281(5374), 269. <https://doi.org/10.1126/science.281.5374.269>
- Groeneweg, F. L., Trattnig, C., Kuhse, J., Nawrotzki, R. A., & Kirsch, J. (2018). Gephyrin: a key regulatory protein of inhibitory synapses and beyond. *Histochemistry and Cell Biology*, 150(5), 489-508. <https://doi.org/10.1007/s00418-018-1725-2>
- Hall, A. (1998). Rho GTPases and the actin cytoskeleton. *Science*, 279(5350), 509-514. <https://doi.org/10.1126/science.279.5350.509>
- Harlan, J. E., Hajduk, P. J., Yoon, H. S., & Fesik, S. W. (1994). Pleckstrin homology domains bind to phosphatidylinositol-4,5-bisphosphate. *Nature*, 371(6493), 168-170. <https://doi.org/10.1038/371168a0>
- Hart, M. J., Eva, A., Evans, T., Aaronson, S. A., & Cerione, R. A. (1991). Catalysis of guanine nucleotide exchange on the CDC42Hs protein by the dbloncogene product. *Nature*, 354(6351), 311-314. <https://doi.org/10.1038/354311a0>
- Hart, M. J., Eva, A., Zangrilli, D., Aaronson, S. A., Evans, T., Cerione, R. A., & Zheng, Y. (1994). Cellular transformation and guanine nucleotide exchange activity are catalyzed by a common domain on the dbl oncogene product. *J Biol Chem*, 269(1), 62-65. [https://doi.org/10.1016/S0021-9258\(17\)42313-1](https://doi.org/10.1016/S0021-9258(17)42313-1)
- Harvey, K. (2004). The GDP-GTP Exchange Factor Collybistin: An Essential Determinant of Neuronal Gephyrin Clustering. *Journal of Neuroscience*, 24(25), 5816-5826. <https://doi.org/10.1523/jneurosci.1184-04.2004>

- Heasman, S. J., & Ridley, A. J. (2008). Mammalian Rho GTPases: new insights into their functions from in vivo studies. *Nat Rev Mol Cell Biol*, 9(9), 690-701. <https://doi.org/10.1038/nrm2476>
- Heim, R., Prasher, D. C., & Tsien, R. Y. (1994). Wavelength mutations and posttranslational autoxidation of green fluorescent protein. *Proceedings of the National Academy of Sciences*, 91(26), 12501. <https://doi.org/10.1073/pnas.91.26.12501>
- Hemsath, L., Dvorsky, R., Fiegen, D., Carlier, M.-F., & Ahmadian, M. R. (2005). An Electrostatic Steering Mechanism of Cdc42 Recognition by Wiskott-Aldrich Syndrome Proteins. *Molecular Cell*, 20(2), 313-324. <https://doi.org/10.1016/j.molcel.2005.08.036>
- Herculano-Houzel, S., & Lent, R. (2005). Isotropic Fractionator: A Simple, Rapid Method for the Quantification of Total Cell and Neuron Numbers in the Brain. *The Journal of Neuroscience*, 25(10), 2518. <https://doi.org/10.1523/JNEUROSCI.4526-04.2005>
- Herweg, J., & Schwarz, G. (2012). Splice-specific glycine receptor binding, folding, and phosphorylation of the scaffolding protein gephyrin. *J Biol Chem*, 287(16), 12645-12656. <https://doi.org/10.1074/jbc.M112.341826>
- Hines, R. M., Maric, H. M., Hines, D. J., Modgil, A., Panzanelli, P., Nakamura, Y., Nathanson, A. J., Cross, A., Deeb, T., Brandon, N. J., Davies, P., Fritschy, J.-M., Schindelin, H., & Moss, S. J. (2018). Developmental seizures and mortality result from reducing GABAA receptor $\alpha 2$ -subunit interaction with collybistin. *Nature Communications*, 9(1), 3130. <https://doi.org/10.1038/s41467-018-05481-1>
- Hodge, R. G., & Ridley, A. J. (2016). Regulating Rho GTPases and their regulators. *Nature Reviews Molecular Cell Biology*, 17(8), 496-510. <https://doi.org/10.1038/nrm.2016.67>
- Hoffmann, C., Gaietta, G., Bünemann, M., Adams, S. R., Oberdorff-Maass, S., Behr, B., Vilardaga, J.-P., Tsien, R. Y., Ellisman, M. H., & Lohse, M. J. (2005). A FIAsh-based FRET approach to determine G protein-coupled receptor activation in living cells. *Nature Methods*, 2(3), 171-176. <https://doi.org/10.1038/nmeth742>
- Hoon, M., Soykan, T., Falkenburger, B., Hammer, M., Patrizi, A., Schmidt, K.-F., Sassoè-Pognetto, M., Löwel, S., Moser, T., Taschenberger, H., Brose, N., & Varoqueaux, F. (2011). Neuroligin-4 is localized to glycinergic postsynapses and regulates inhibition in the retina. *Proceedings of the National Academy of Sciences*, 108(7), 3053. <https://doi.org/10.1073/pnas.1006946108>
- Humphrey, W., Dalke, A., & Schulten, K. (1996). VMD: Visual molecular dynamics. *Journal of Molecular Graphics*, 14(1), 33-38. [https://doi.org/10.1016/0263-7855\(96\)00018-5](https://doi.org/10.1016/0263-7855(96)00018-5)

- Huttlin, E. L., Jedrychowski, M. P., Elias, J. E., Goswami, T., Rad, R., Beausoleil, S. A., Villén, J., Haas, W., Sowa, M. E., & Gygi, S. P. (2010). A tissue-specific atlas of mouse protein phosphorylation and expression. *Cell*, *143*(7), 1174-1189. <https://doi.org/10.1016/j.cell.2010.12.001>
- Hyvönen, M., Macias, M. J., Nilges, M., Oschkinat, H., Saraste, M., & Wilmanns, M. (1995). Structure of the binding site for inositol phosphates in a PH domain. *The EMBO journal*, *14*(19), 4676-4685. <https://doi.org/10.1002/j.1460-2075.1995.tb00149.x>
- Imam, N., Choudhury, S., Heinze, K. G., & Schindelin, H. (2022). Differential modulation of collybistin conformational dynamics by the closely related GTPases Cdc42 and TC10 [Original Research]. *Frontiers in Synaptic Neuroscience*, *14*. <https://www.frontiersin.org/articles/10.3389/fnsyn.2022.959875>
- Imam, N., Choudhury, S., Hemmen, K., Heinze, K., & Schindelin, H. (2022). Deciphering the conformational dynamics of gephyrin-mediated collybistin activation. *bioRxiv*, 2022.2005.2030.493832. <https://doi.org/10.1101/2022.05.30.493832>
- Jaffe, A. B., & Hall, A. (2005). Rho GTPases: biochemistry and biology. *Annu Rev Cell Dev Biol*, *21*, 247-269. <https://doi.org/10.1146/annurev.cellbio.21.020604.150721>
- Jaiswal, M., Dvorsky, R., & Ahmadian, M. R. (2013). Deciphering the Molecular and Functional Basis of Dbl Family Proteins: A NOVEL SYSTEMATIC APPROACH TOWARD CLASSIFICATION OF SELECTIVE ACTIVATION OF THE Rho FAMILY PROTEINS. *Journal of Biological Chemistry*, *288*(6), 4486-4500. <https://doi.org/https://doi.org/10.1074/jbc.M112.429746>
- Jaiteh, M., Taly, A., & Hénin, J. (2016). Evolution of Pentameric Ligand-Gated Ion Channels: Pro-Loop Receptors. *PLOS ONE*, *11*(3), e0151934. <https://doi.org/10.1371/journal.pone.0151934>
- Jedlicka, P., Papadopoulos, T., Deller, T., Betz, H., & Schwarzacher, S. W. (2009). Increased network excitability and impaired induction of long-term potentiation in the dentate gyrus of collybistin-deficient mice in vivo. *Molecular and Cellular Neuroscience*, *41*(1), 94-100. <https://doi.org/10.1016/j.mcn.2009.02.005>
- Jurrus, E., Engel, D., Star, K., Monson, K., Brandi, J., Felberg, L. E., Brookes, D. H., Wilson, L., Chen, J., Liles, K., Chun, M., Li, P., Gohara, D. W., Dolinsky, T., Konecny, R., Koes, D. R., Nielsen, J. E., Head-Gordon, T., Geng, W., Krasny, R., Wei, G.-W., Holst, M. J., McCammon, J. A., & Baker, N. A. (2018). Improvements to the APBS biomolecular solvation software suite. *Protein Science*, *27*(1), 112-128. <https://doi.org/https://doi.org/10.1002/pro.3280>

- Kalinin, S., Peulen, T., Sindbert, S., Rothwell, P. J., Berger, S., Restle, T., Goody, R. S., Gohlke, H., & Seidel, C. A. M. (2012). A toolkit and benchmark study for FRET-restrained high-precision structural modeling. *Nature Methods*, 9(12), 1218-1225. <https://doi.org/10.1038/nmeth.2222>
- Kalscheuer, V. M., Musante, L., Fang, C., Hoffmann, K., Fuchs, C., Carta, E., Deas, E., Venkateswarlu, K., Menzel, C., Ullmann, R., Tommerup, N., Dalprà, L., Tzschach, A., Selicorni, A., Lüscher, B., Ropers, H.-H., Harvey, K., & Harvey, R. J. (2009). A balanced chromosomal translocation disrupting ARHGEF9 is associated with epilepsy, anxiety, aggression, and mental retardation. *Human Mutation*, 30(1), 61-68. <https://doi.org/10.1002/humu.20814>
- Kamdar, K. P., Shelton, M. E., & Finnerty, V. (1994). The *Drosophila molybdenum* cofactor gene *cinnamon* is homologous to three *Escherichia coli* cofactor proteins and to the rat protein gephyrin. *Genetics*, 137(3), 791-801. <https://doi.org/10.1093/genetics/137.3.791>
- Kaneko, T., Li, L., & Li, S. S.-C. (2008). The SH3 domain- a family of versatile peptide- and protein-recognition module. *FBL*, 13(13), 4938-4952. <https://doi.org/10.2741/3053>
- Kang, R., Wan, J., Arstikaitis, P., Takahashi, H., Huang, K., Bailey, A. O., Thompson, J. X., Roth, A. F., Drisdell, R. C., Mastro, R., Green, W. N., Yates III, J. R., Davis, N. G., & El-Husseini, A. (2008). Neural palmitoyl-proteomics reveals dynamic synaptic palmitoylation. *Nature*, 456(7224), 904-909. <https://doi.org/10.1038/nature07605>
- Kasaragod, V. B., & Schindelin, H. (2018). Structure–Function Relationships of Glycine and GABAA Receptors and Their Interplay With the Scaffolding Protein Gephyrin. *Frontiers in Molecular Neuroscience*, 11(317). <https://doi.org/10.3389/fnmol.2018.00317>
- Kilisch, M., Mayer, S., Mitkovski, M., Roehse, H., Hentrich, J., Schwappach, B., & Papadopoulos, T. (2020). A GTPase-induced switch in phospholipid affinity of collybistin contributes to synaptic gephyrin clustering. *Journal of Cell Science*, 133(2), jcs232835. <https://doi.org/10.1242/jcs.232835>
- Kim, E. Y., Schrader, N., Smolinsky, B., Bedet, C., Vannier, C., Schwarz, G., & Schindelin, H. (2006). Deciphering the structural framework of glycine receptor anchoring by gephyrin. *The EMBO journal*, 25(6), 1385-1395. <https://doi.org/10.1038/sj.emboj.7601029>
- Kim, J. J., & Hibbs, R. E. (2021). Direct Structural Insights into GABA(A) Receptor Pharmacology. *Trends Biochem Sci*, 46(6), 502-517. <https://doi.org/10.1016/j.tibs.2021.01.011>
- Kins, S., Betz, H., & Kirsch, J. (2000). Collybistin, a newly identified brain-specific GEF, induces submembrane clustering of gephyrin. *Nature Neuroscience*, 3(1), 22-29. <https://doi.org/10.1038/71096>

- Kirsch, J., Langosch, D., Prior, P., Littauer, U. Z., Schmitt, B., & Betz, H. (1991). The 93-kDa glycine receptor-associated protein binds to tubulin. *J Biol Chem*, 266(33), 22242-22245. [https://doi.org/10.1016/S0021-9258\(18\)54560-9](https://doi.org/10.1016/S0021-9258(18)54560-9)
- Kirsch, J., Wolters, I., Triller, A., & Betz, H. (1993). Gephyrin antisense oligonucleotides prevent glycine receptor clustering in spinal neurons. *Nature*, 366(6457), 745-748. <https://doi.org/10.1038/366745a0>
- Kiss, E., Gorgas, K., Schlicksupp, A., Groß, D., Kins, S., Kirsch, J., & Kuhse, J. (2016). Biphasic Alteration of the Inhibitory Synapse Scaffold Protein Gephyrin in Early and Late Stages of an Alzheimer Disease Model. *The American Journal of Pathology*, 186(9), 2279-2291. <https://doi.org/10.1016/j.ajpath.2016.05.013>
- Klausberger, T., Roberts, J. D. B., & Somogyi, P. (2002). Cell Type- and Input-Specific Differences in the Number and Subtypes of Synaptic GABA Receptors in the Hippocampus. *The Journal of Neuroscience*, 22(7), 2513. <https://doi.org/10.1523/JNEUROSCI.22-07-02513.2002>
- Kneussel, M., & Betz, H. (2000). Receptors, gephyrin and gephyrin-associated proteins: novel insights into the assembly of inhibitory postsynaptic membrane specializations. *The Journal of Physiology*, 525 Pt 1(Pt 1), 1-9. <https://doi.org/10.1111/j.1469-7793.2000.t01-4-00001.x>
- Körber, C., Richter, A., Kaiser, M., Schlicksupp, A., Mükusch, S., Kuner, T., Kirsch, J., & Kuhse, J. (2012). Effects of distinct collybistin isoforms on the formation of GABAergic synapses in hippocampal neurons. *Molecular and Cellular Neuroscience*, 50(3-4), 250-259. <https://doi.org/10.1016/j.mcn.2012.05.006>
- Kravets, E., Degrandi, D., Ma, Q., Peulen, T.-O., Klümpers, V., Felekyan, S., Kühnemuth, R., Weidtkamp-Peters, S., Seidel, C. A., & Pfeffer, K. (2016). Guanylate binding proteins directly attack *Toxoplasma gondii* via supramolecular complexes. *eLife*, 5. <https://doi.org/10.7554/elife.11479>
- Krissinel, E., & Henrick, K. (2007). Inference of Macromolecular Assemblies from Crystalline State. *Journal of Molecular Biology*, 372(3), 774-797. <https://doi.org/https://doi.org/10.1016/j.jmb.2007.05.022>
- Kufareva, I., Lenoir, M., Dancea, F., Sridhar, P., Raush, E., Bissig, C., Gruenberg, J., Abagyan, R., & Overduin, M. (2014). Discovery of novel membrane binding structures and functions. *Biochem Cell Biol*, 92(6), 555-563. <https://doi.org/10.1139/bcb-2014-0074>
- Kuhse, J., Kalbouneh, H., Schlicksupp, A., Mükusch, S., Nawrotzki, R., & Kirsch, J. (2012). Phosphorylation of Gephyrin in Hippocampal Neurons by Cyclin-dependent Kinase CDK5 at Ser-270 Is Dependent on Collybistin. *Journal of Biological Chemistry*, 287(37), 30952-30966. <https://doi.org/https://doi.org/10.1074/jbc.M112.349597>

- Kumar, A., Basak, S., Rao, S., Gicheru, Y., Mayer, M. L., Sansom, M. S. P., & Chakrapani, S. (2020). Mechanisms of activation and desensitization of full-length glycine receptor in lipid nanodiscs. *Nature Communications*, 11(1), 3752. <https://doi.org/10.1038/s41467-020-17364-5>
- Kuper, J., Llamas, A., Hecht, H.-J., Mendel, R. R., & Schwarz, G. (2004). Structure of the molybdopterin-bound Cnx1G domain links molybdenum and copper metabolism. *Nature*, 430(7001), 803-806. <https://doi.org/10.1038/nature02681>
- Kurochkina, N., & Guha, U. (2013). SH3 domains: modules of protein-protein interactions. *Biophys Rev*, 5(1), 29-39. <https://doi.org/10.1007/s12551-012-0081-z>
- Lakowicz, J. R. (2013). *Principles of fluorescence spectroscopy*. Springer science & business media.
- Langosch, D., Hoch, W., & Betz, H. (1992). The 93 kDa protein gephyrin and tubulin associated with the inhibitory glycine receptor are phosphorylated by an endogenous protein kinase. *FEBS Letters*, 298(2), 113-117. [https://doi.org/https://doi.org/10.1016/0014-5793\(92\)80034-E](https://doi.org/https://doi.org/10.1016/0014-5793(92)80034-E)
- Lee, H. J., Adham, I. M., Schwarz, G., Kneussel, M., Sass, J. O., Engel, W., & Reiss, J. (2002). Molybdenum cofactor-deficient mice resemble the phenotype of human patients. *Hum Mol Genet*, 11(26), 3309-3317. <https://doi.org/10.1093/hmg/11.26.3309>
- Lehmann, K., Felekyan, S., Kühnemuth, R., Dimura, M., Tóth, K., Seidel, C. A. M., & Langowski, J. (2020). Dynamics of the nucleosomal histone H3 N-terminal tail revealed by high precision single-molecule FRET. *Nucleic Acids Research*, 48(3), 1551-1571. <https://doi.org/10.1093/nar/gkz1186>
- Lemmon, M. A. (2007). Pleckstrin homology (PH) domains and phosphoinositides. *Biochem Soc Symp*(74), 81-93. <https://doi.org/10.1042/bss0740081>
- Lemmon, M. A., Ferguson, K. M., O'Brien, R., Sigler, P. B., & Schlessinger, J. (1995). Specific and high-affinity binding of inositol phosphates to an isolated pleckstrin homology domain. *Proc Natl Acad Sci U S A*, 92(23), 10472-10476. <https://doi.org/10.1073/pnas.92.23.10472>
- Lenoir, M., Kufareva, I., Abagyan, R., & Overduin, M. (2015). Membrane and Protein Interactions of the Pleckstrin Homology Domain Superfamily. *Membranes*, 5(4), 646-663. <https://doi.org/10.3390/membranes5040646>
- Lévi, S., Chesnoy-Marchais, D., Sieghart, W., & Triller, A. (1999). Synaptic control of glycine and GABA(A) receptors and gephyrin expression in cultured motoneurons. *The Journal of neuroscience : the official journal of the Society for Neuroscience*, 19(17), 7434-7449. <https://doi.org/10.1523/jneurosci.19-17-07434.1999>

- Lionel, A. C., Vaags, A. K., Sato, D., Gazzellone, M. J., Mitchell, E. B., Chen, H. Y., Costain, G., Walker, S., Egger, G., Thiruvahindrapuram, B., Merico, D., Prasad, A., Anagnostou, E., Fombonne, E., Zwaigenbaum, L., Roberts, W., Szatmari, P., Fernandez, B. A., Georgieva, L., Brzustowicz, L. M., Roetzer, K., Kaschnitz, W., Vincent, J. B., Windpassinger, C., Marshall, C. R., Trifiletti, R. R., Kirmani, S., Kirov, G., Petek, E., Hodge, J. C., Bassett, A. S., & Scherer, S. W. (2013). Rare exonic deletions implicate the synaptic organizer Gephyrin (GPHN) in risk for autism, schizophrenia and seizures. *Human Molecular Genetics*, 22(10), 2055-2066. <https://doi.org/10.1093/hmg/ddt056>
- Liu, M. T., Wuebbens, M. M., Rajagopalan, K. V., & Schindelin, H. (2000). Crystal structure of the gephyrin-related molybdenum cofactor biosynthesis protein MogA from *Escherichia coli*. *J Biol Chem*, 275(3), 1814-1822. <https://doi.org/10.1074/jbc.275.3.1814>
- Liu, X., Wang, H., Eberstadt, M., Schnuchel, A., Olejniczak, E. T., Meadows, R. P., Schkeryantz, J. M., Janowick, D. A., Harlan, J. E., Harris, E. A., Staunton, D. E., & Fesik, S. W. (1998). NMR structure and mutagenesis of the N-terminal Dbl homology domain of the nucleotide exchange factor Trio. *Cell*, 95(2), 269-277. [https://doi.org/10.1016/s0092-8674\(00\)81757-2](https://doi.org/10.1016/s0092-8674(00)81757-2)
- López Tobón, A., Suresh, M., Jin, J., Vitriolo, A., Pietralla, T., Tedford, K., Bossenz, M., Mahnken, K., Kiefer, F., Testa, G., Fischer, K.-D., & Püschel, A. W. (2018). The guanine nucleotide exchange factor Arhgef7/ β Pix promotes axon formation upstream of TC10. *Scientific Reports*, 8(1), 8811. <https://doi.org/10.1038/s41598-018-27081-1>
- Ludolphs, M., Schneeberger, D., Soykan, T., Schäfer, J., Papadopoulos, T., Brose, N., Schindelin, H., & Steinem, C. (2016). Specificity of Collybistin-Phosphoinositide Interactions: IMPACT OF THE INDIVIDUAL PROTEIN DOMAINS. *The Journal of biological chemistry*, 291(1), 244-254. <https://doi.org/10.1074/jbc.M115.673400>
- Ludwig, P. E., Reddy, V., & Varacallo, M. (2022). Neuroanatomy, Central Nervous System (CNS). In *StatPearls*. StatPearls Publishing
Copyright © 2022, StatPearls Publishing LLC.
- Luscher, B., Fuchs, T., & Casey. (2011). GABAA Receptor Trafficking-Mediated Plasticity of Inhibitory Synapses. *Neuron*, 70(3), 385-409. <https://doi.org/10.1016/j.neuron.2011.03.024>
- Madani, F., Lind, J., Damberg, P., Adams, S. R., Tsien, R. Y., & Gräslund, A. O. (2009). Hairpin Structure of a Biarsenical-Tetracysteine Motif Determined by NMR Spectroscopy. *Journal of the American Chemical Society*, 131(13), 4613-4615. <https://doi.org/10.1021/ja809315x>
- Maric, H. M., Kasaragod, V. B., Haugaard-Kedström, L., Hausrat, T. J., Kneussel, M., Schindelin, H., & Strømgaard, K. (2015). Design and Synthesis of High-Affinity Dimeric Inhibitors Targeting the Interactions between Gephyrin and Inhibitory

- Neurotransmitter Receptors. *Angewandte Chemie International Edition*, 54(2), 490-494. <https://doi.org/https://doi.org/10.1002/anie.201409043>
- Maric, H. M., Kasaragod, V. B., Hausrat, T. J., Kneussel, M., Tretter, V., Strømgaard, K., & Schindelin, H. (2014). Molecular basis of the alternative recruitment of GABA_A versus glycine receptors through gephyrin. *Nature Communications*, 5(1), 5767. <https://doi.org/10.1038/ncomms6767>
- Maric, H. M., Kasaragod, V. B., & Schindelin, H. (2014). Modulation of Gephyrin-Glycine Receptor Affinity by Multivalency. *ACS Chemical Biology*, 9(11), 2554-2562. <https://doi.org/10.1021/cb500303a>
- Mayer, S., Kumar, R., Jaiswal, M., Soykan, T., Ahmadian Mohammad, R., Brose, N., Betz, H., Rhee, J.-S., & Papadopoulos, T. (2013). Collybistin activation by GTP-TC10 enhances postsynaptic gephyrin clustering and hippocampal GABAergic neurotransmission. *Proceedings of the National Academy of Sciences*, 110(51), 20795-20800. <https://doi.org/10.1073/pnas.1309078110>
- Mendel, R. R. (2013). Metabolism of Molybdenum. In L. Banci (Ed.), *Metallomics and the Cell* (pp. 503-528). Springer Netherlands. https://doi.org/10.1007/978-94-007-5561-1_15
- Michaelson, D., Silletti, J., Murphy, G., D'Eustachio, P., Rush, M., & Philips, M. R. (2001). Differential Localization of Rho Gtpases in Live Cells. *Journal of Cell Biology*, 152(1), 111-126. <https://doi.org/10.1083/jcb.152.1.111>
- Miles, R., & Wong, R. K. (1984). Unitary inhibitory synaptic potentials in the guinea-pig hippocampus in vitro. *The Journal of Physiology*, 356(1), 97-113. <https://doi.org/10.1113/jphysiol.1984.sp015455>
- Mitin, N., Betts, L., Yohe, M. E., Der, C. J., Sondek, J., & Rossman, K. L. (2007). Release of autoinhibition of ASEF by APC leads to CDC42 activation and tumor suppression. *Nature Structural & Molecular Biology*, 14(9), 814-823. <https://doi.org/10.1038/nsmb1290>
- Mosaddeghzadeh, N., & Ahmadian, M. R. (2021). The RHO Family GTPases: Mechanisms of Regulation and Signaling. *Cells*, 10(7), 1831. <https://doi.org/10.3390/cells10071831>
- Moss, S. J., & Smart, T. G. (2001). Constructing inhibitory synapses. *Nature Reviews Neuroscience*, 2(4), 240-250. <https://doi.org/10.1038/35067500>
- Mukherjee, J., Kretschmannova, K., Gouzer, G., Maric, H. M., Ramsden, S., Tretter, V., Harvey, K., Davies, P. A., Triller, A., Schindelin, H., & Moss, S. J. (2011). The residence time of GABA(A)Rs at inhibitory synapses is determined by direct binding of the receptor α 1 subunit to gephyrin. *The Journal of neuroscience : the official journal of the Society for Neuroscience*, 31(41), 14677-14687. <https://doi.org/10.1523/jneurosci.2001-11.2011>

- Mülhardt, C., Fischer, M., Gass, P., Simon-Chazottes, D., Guénet, J. L., Kuhse, J., Betz, H., & Becker, C. M. (1994). The spastic mouse: aberrant splicing of glycine receptor beta subunit mRNA caused by intronic insertion of L1 element. *Neuron*, 13(4), 1003-1015. [https://doi.org/10.1016/0896-6273\(94\)90265-8](https://doi.org/10.1016/0896-6273(94)90265-8)
- Murphy, G. A., Jillian, S. A., Michaelson, D., Philips, M. R., D'Eustachio, P., & Rush, M. G. (2001). Signaling mediated by the closely related mammalian Rho family GTPases TC10 and Cdc42 suggests distinct functional pathways. *Cell Growth Differ*, 12(3), 157-167.
- Neudauer, C. L., Joberty, G., Tatsis, N., & Macara, I. G. (1998). Distinct cellular effects and interactions of the Rho-family GTPase TC10. *Current Biology*, 8(21), 1151-1161. [https://doi.org/10.1016/s0960-9822\(07\)00486-1](https://doi.org/10.1016/s0960-9822(07)00486-1)
- Noviello, C. M., Kreye, J., Teng, J., Prüss, H., & Hibbs, R. E. (2022). Structural mechanisms of GABA(A) receptor autoimmune encephalitis. *Cell*, 185(14), 2469-2477.e2413. <https://doi.org/10.1016/j.cell.2022.06.025>
- Nusser, Z., Cull-Candy, S., & Farrant, M. (1997). Differences in Synaptic GABAA Receptor Number Underlie Variation in GABA Mini Amplitude. *Neuron*, 19(3), 697-709. [https://doi.org/10.1016/s0896-6273\(00\)80382-7](https://doi.org/10.1016/s0896-6273(00)80382-7)
- Nusser, Z., Sieghart, W., Benke, D., Fritschy, J. M., & Somogyi, P. (1996). Differential synaptic localization of two major gamma-aminobutyric acid type A receptor alpha subunits on hippocampal pyramidal cells. *Proceedings of the National Academy of Sciences*, 93(21), 11939-11944. <https://doi.org/10.1073/pnas.93.21.11939>
- Nyíri, G., Freund, T. F., & Somogyi, P. (2001). Input-dependent synaptic targeting of alpha(2)-subunit-containing GABA(A) receptors in synapses of hippocampal pyramidal cells of the rat. *Eur J Neurosci*, 13(3), 428-442. <https://doi.org/10.1046/j.1460-9568.2001.01407.x>
- Olsen, R. W., & Sieghart, W. (2009). GABAA receptors: subtypes provide diversity of function and pharmacology. *Neuropharmacology*, 56(1), 141-148. <https://doi.org/10.1016/j.neuropharm.2008.07.045>
- Papadopoulos, T., Eulenburg, V., Reddy-Alla, S., Mansuy, I. M., Li, Y., & Betz, H. (2008). Collybistin is required for both the formation and maintenance of GABAergic postsynapses in the hippocampus. *Molecular and Cellular Neuroscience*, 39(2), 161-169. <https://doi.org/10.1016/j.mcn.2008.06.006>
- Papadopoulos, T., Korte, M., Eulenburg, V., Kubota, H., Retiounskaia, M., Harvey, R. J., Harvey, K., O'Sullivan, G. A., Laube, B., Hülsmann, S., Geiger, J. R. P., & Betz, H. (2007). Impaired GABAergic transmission and altered hippocampal synaptic plasticity in collybistin-deficient mice. *The EMBO journal*, 26(17), 3888-3899. <https://doi.org/10.1038/sj.emboj.7601819>

- Papadopoulos, T., Rhee, H. J., Subramanian, D., Paraskevopoulou, F., Mueller, R., Schultz, C., Brose, N., Rhee, J.-S., & Betz, H. (2017). Endosomal Phosphatidylinositol 3-Phosphate Promotes Gephyrin Clustering and GABAergic Neurotransmission at Inhibitory Postsynapses. *Journal of Biological Chemistry*, 292(4), 1160-1177. <https://doi.org/https://doi.org/10.1074/jbc.M116.771592>
- Papadopoulos, T., Schemm, R., Grubmüller, H., & Brose, N. (2015). Lipid Binding Defects and Perturbed Synaptogenic Activity of a Collybistin R290H Mutant That Causes Epilepsy and Intellectual Disability*. *Journal of Biological Chemistry*, 290(13), 8256-8270. <https://doi.org/https://doi.org/10.1074/jbc.M114.633024>
- Papadopoulos, T., & Soykan, T. (2011). The role of collybistin in gephyrin clustering at inhibitory synapses: facts and open questions. *Frontiers in cellular neuroscience*, 5, 11-11. <https://doi.org/10.3389/fncel.2011.00011>
- Patrizi, A., Viltono, L., Frola, E., Harvey, K., Harvey, R. J., & Sassoè-Pognetto, M. (2012). Selective localization of collybistin at a subset of inhibitory synapses in brain circuits. *Journal of Comparative Neurology*, 520(1), 130-141. <https://doi.org/https://doi.org/10.1002/cne.22702>
- Pereira-Leal, J. B., & Seabra, M. C. (2001). Evolution of the Rab family of small GTP-binding proteins. *J Mol Biol*, 313(4), 889-901. <https://doi.org/10.1006/jmbi.2001.5072>
- Peulen, T.-O., Opanasyuk, O., & Seidel, C. A. M. (2017). Combining Graphical and Analytical Methods with Molecular Simulations To Analyze Time-Resolved FRET Measurements of Labeled Macromolecules Accurately. *The Journal of Physical Chemistry B*, 121(35), 8211-8241. <https://doi.org/10.1021/acs.jpcc.7b03441>
- Pizzarelli, R., Griguoli, M., Zacchi, P., Petrini, E. M., Barberis, A., Cattaneo, A., & Cherubini, E. (2020). Tuning GABAergic Inhibition: Gephyrin Molecular Organization and Functions. *Neuroscience*, 439, 125-136. <https://doi.org/10.1016/j.neuroscience.2019.07.036>
- Poulopoulos, A., Aramuni, G., Meyer, G., Soykan, T., Hoon, M., Papadopoulos, T., Zhang, M., Paarmann, I., Fuchs, C., Harvey, K., Jedlicka, P., Schwarzacher, S. W., Betz, H., Harvey, R. J., Brose, N., Zhang, W., & Varoqueaux, F. (2009). Neuroligin 2 Drives Postsynaptic Assembly at Perisomatic Inhibitory Synapses through Gephyrin and Collybistin. *Neuron*, 63(5), 628-642. <https://doi.org/10.1016/j.neuron.2009.08.023>
- Prior, P., Schmitt, B., Grenningloh, G., Pribilla, I., Multhaup, G., Beyreuther, K., Maulet, Y., Werner, P., Langosch, D., Kirsch, J., & et al. (1992). Primary structure and alternative splice variants of gephyrin, a putative glycine receptor-tubulin linker protein. *Neuron*, 8(6), 1161-1170. [https://doi.org/10.1016/0896-6273\(92\)90136-2](https://doi.org/10.1016/0896-6273(92)90136-2)

- Reddy-Alla, S., Schmitt, B., Birkenfeld, J., Eulenburg, V., Dutertre, S., Böhringer, C., Götz, M., Betz, H., & Papadopoulos, T. (2010). PH-Domain-driven targeting of collybistin but not Cdc42 activation is required for synaptic gephyrin clustering. *European Journal of Neuroscience*, 31(7), 1173-1184. <https://doi.org/10.1111/j.1460-9568.2010.07149.x>
- Reid, T., Bathorn, A., Ahmadian, M. R., & Collard, J. G. (1999). Identification and Characterization of hPEM-2, a Guanine Nucleotide Exchange Factor Specific for Cdc42*. *Journal of Biological Chemistry*, 274(47), 33587-33593. <https://doi.org/https://doi.org/10.1074/jbc.274.47.33587>
- Reiss, J., & Hahnewald, R. (2011). Molybdenum cofactor deficiency: Mutations in GPHN, MOCS1, and MOCS2. *Human Mutation*, 32. <https://doi.org/10.1002/humu.21390>
- Robert, Kyle, Matthew, Klein, C., Jason, Carlos, Christian, Wang, L.-P., Thomas, & Vijay. (2015). MDTraj: A Modern Open Library for the Analysis of Molecular Dynamics Trajectories. *Biophysical Journal*, 109(8), 1528-1532. <https://doi.org/10.1016/j.bpj.2015.08.015>
- Roberts, P. J., Mitin, N., Keller, P. J., Chenette, E. J., Madigan, J. P., Currin, R. O., Cox, A. D., Wilson, O., Kirschmeier, P., & Der, C. J. (2008). Rho Family GTPase Modification and Dependence on CAAX Motif-signaled Posttranslational Modification*. *Journal of Biological Chemistry*, 283(37), 25150-25163. <https://doi.org/https://doi.org/10.1074/jbc.M800882200>
- Ron, D., Zannini, M., Lewis, M., Wickner, R. B., Hunt, L. T., Graziani, G., Tronick, S. R., Aaronson, S. A., & Eva, A. (1991). A region of proto-dbl essential for its transforming activity shows sequence similarity to a yeast cell cycle gene, CDC24, and the human breakpoint cluster gene, bcr. *New Biol*, 3(4), 372-379.
- Rossmann, K. L., Der, C. J., & Sondek, J. (2005). GEF means go: turning on RHO GTPases with guanine nucleotide-exchange factors. *Nature Reviews Molecular Cell Biology*, 6(2), 167-180. <https://doi.org/10.1038/nrm1587>
- Rudolph, U., & Möhler, H. (2006). GABA-based therapeutic approaches: GABAA receptor subtype functions. *Curr Opin Pharmacol*, 6(1), 18-23. <https://doi.org/10.1016/j.coph.2005.10.003>
- Saiepour, L., Fuchs, C., Patrizi, A., Sassoè-Pognetto, M., Harvey, R. J., & Harvey, K. (2010). Complex Role of Collybistin and Gephyrin in GABAA Receptor Clustering. *Journal of Biological Chemistry*, 285(38), 29623-29631. <https://doi.org/10.1074/jbc.m110.121368>
- Saiyed, T., Paarmann, I., Schmitt, B., Haeger, S., Sola, M., Schmalzing, G., Weissenhorn, W., & Betz, H. (2007, 2007/02/23/). Molecular Basis of Gephyrin Clustering at Inhibitory Synapses: ROLE OF G- AND E-DOMAIN

- INTERACTIONS. *Journal of Biological Chemistry*, 282(8), 5625-5632. <https://doi.org/https://doi.org/10.1074/jbc.M610290200>
- Sanabria, H., Rodnin, D., Hemmen, K., Peulen, T.-O., Felekyan, S., Fleissner, M. R., Dimura, M., Koberling, F., Kühnemuth, R., Hubbell, W., Gohlke, H., & Seidel, C. A. M. (2020). Resolving dynamics and function of transient states in single enzyme molecules. *Nature Communications*, 11(1). <https://doi.org/10.1038/s41467-020-14886-w>
- Sander, B., Tria, G., Shkumatov, A. V., Kim, E.-Y., Grossmann, J. G., Tessmer, I., Svergun, D. I., & Schindelin, H. (2013). Structural characterization of gephyrin by AFM and SAXS reveals a mixture of compact and extended states. *Acta Crystallographica Section D*, 69(10), 2050-2060. <https://doi.org/doi:10.1107/S0907444913018714>
- Schäfer, J., Förster, L., Mey, I., Papadopoulos, T., Brose, N., & Steinem, C. (2020). Neuroligin-2 dependent conformational activation of collybistin reconstituted in supported hybrid membranes. *Journal of Biological Chemistry*, 295(52), 18604-18613. <https://doi.org/https://doi.org/10.1074/jbc.RA120.015347>
- Schmidt, A., & Hall, A. (2002). Guanine nucleotide exchange factors for Rho GTPases: turning on the switch. *Genes Dev*, 16(13), 1587-1609. <https://doi.org/10.1101/gad.1003302>
- Schrader, N., Kim, E. Y., Winking, J., Paulukat, J., Schindelin, H., & Schwarz, G. (2004). Biochemical Characterization of the High Affinity Binding between the Glycine Receptor and Gephyrin*. *Journal of Biological Chemistry*, 279(18), 18733-18741. <https://doi.org/https://doi.org/10.1074/jbc.M311245200>
- Schultz, J., Milpetz, F., Bork, P., & Ponting, C. P. (1998). SMART, a simple modular architecture research tool: Identification of signaling domains. *Proceedings of the National Academy of Sciences*, 95(11), 5857-5864. <https://doi.org/10.1073/pnas.95.11.5857>
- Schwarz, G., Schrader, N., Mendel, R. R., Hecht, H.-J., & Schindelin, H. (2001). Crystal structures of human gephyrin and plant Cnx1 G domains: comparative analysis and functional implications Edited by D. Rees. *Journal of Molecular Biology*, 312(2), 405-418. <https://doi.org/https://doi.org/10.1006/jmbi.2001.4952>
- Schwer, B., Eckersdorff, M., Li, Y., Silva, J. C., Fermin, D., Kurtev, M. V., Giallourakis, C., Comb, M. J., Alt, F. W., & Lombard, D. B. (2009). Calorie restriction alters mitochondrial protein acetylation. *Aging Cell*, 8(5), 604-606. <https://doi.org/10.1111/j.1474-9726.2009.00503.x>
- Sieghart, W. (2006). Structure, pharmacology, and function of GABAA receptor subtypes. *Adv Pharmacol*, 54, 231-263. [https://doi.org/10.1016/s1054-3589\(06\)54010-4](https://doi.org/10.1016/s1054-3589(06)54010-4)

- Sieghart, W. (2015). Allosteric modulation of GABAA receptors via multiple drug-binding sites. *Adv Pharmacol*, 72, 53-96. <https://doi.org/10.1016/bs.apha.2014.10.002>
- Sigel, E., & Buhr, A. (1997). The benzodiazepine binding site of GABAA receptors. *Trends Pharmacol Sci*, 18(11), 425-429. [https://doi.org/10.1016/s0165-6147\(97\)01118-8](https://doi.org/10.1016/s0165-6147(97)01118-8)
- Sigel, E., & Steinmann, M. E. (2012). Structure, function, and modulation of GABA(A) receptors. *J Biol Chem*, 287(48), 40224-40231. <https://doi.org/10.1074/jbc.R112.386664>
- Sinha, S., & Yang, W. (2008). Cellular signaling for activation of Rho GTPase Cdc42. *Cellular Signalling*, 20(11), 1927-1934. <https://doi.org/https://doi.org/10.1016/j.cellsig.2008.05.002>
- Soisson, S. M., Nimnual, A. S., Uy, M., Bar-Sagi, D., & Kuriyan, J. (1998). Crystal structure of the Dbl and pleckstrin homology domains from the human Son of sevenless protein. *Cell*, 95(2), 259-268. [https://doi.org/10.1016/s0092-8674\(00\)81756-0](https://doi.org/10.1016/s0092-8674(00)81756-0)
- Sola, M., Bavro, V. N., Timmins, J., Franz, T., Ricard-Blum, S., Schoehn, G., Ruigrok, R. W. H., Paarmann, I., Saiyed, T., O'Sullivan, G. A., Schmitt, B., Betz, H., & Weissenhorn, W. (2004). Structural basis of dynamic glycine receptor clustering by gephyrin. *The EMBO journal*, 23(13), 2510-2519. <https://doi.org/10.1038/sj.emboj.7600256>
- Sousa, A. M. M., Meyer, K. A., Santpere, G., Gulden, F. O., & Sestan, N. (2017). Evolution of the Human Nervous System Function, Structure, and Development. *Cell*, 170(2), 226-247. <https://doi.org/https://doi.org/10.1016/j.cell.2017.06.036>
- Soykan, T., Schneeberger, D., Tria, G., Buechner, C., Bader, N., Svergun, D., Tessmer, I., Pouloupoulos, A., Papadopoulos, T., Varoqueaux, F., Schindelin, H., & Brose, N. (2014). A conformational switch in collybistin determines the differentiation of inhibitory postsynapses. *The EMBO journal*, 33(18), 2113-2133. <https://doi.org/https://doi.org/10.15252/embj.201488143>
- Specht, C. G., Izeddin, I., Rodriguez, P. C., El Beheiry, M., Rostaing, P., Darzacq, X., Dahan, M., & Triller, A. (2013). Quantitative nanoscopy of inhibitory synapses: counting gephyrin molecules and receptor binding sites. *Neuron*, 79(2), 308-321. <https://doi.org/10.1016/j.neuron.2013.05.013>
- Sriram, G., Reichman, C., Tunceroglu, A., Kaushal, N., Saleh, T., Machida, K., Mayer, B., Ge, Q., Li, J., Hornbeck, P., Kalodimos, C. G., & Birge, R. B. (2011). Phosphorylation of Crk on tyrosine 251 in the RT loop of the SH3C domain promotes Abl kinase transactivation. *Oncogene*, 30(46), 4645-4655. <https://doi.org/10.1038/onc.2011.170>

- Stallmeyer, B., Drugeon, G., Reiss, J., Haenni, A. L., & Mendel, R. R. (1999). Human Molybdopterin Synthase Gene: Identification of a Bicistronic Transcript with Overlapping Reading Frames. *The American Journal of Human Genetics*, 64(3), 698-705. <https://doi.org/10.1086/302295>
- Sternbach, L. H. (1979). The benzodiazepine story. *Journal of Medicinal Chemistry*, 22(1), 1-7. <https://doi.org/10.1021/jm00187a001>
- Tanabe, K., Tachibana, T., Yamashita, T., Che, Y. H., Yoneda, Y., Ochi, T., Tohyama, M., Yoshikawa, H., & Kiyama, H. (2000). The small GTP-binding protein TC10 promotes nerve elongation in neuronal cells, and its expression is induced during nerve regeneration in rats. *The Journal of neuroscience : the official journal of the Society for Neuroscience*, 20(11), 4138-4144. <https://doi.org/10.1523/JNEUROSCI.20-11-04138.2000>
- The Arabidopsis Genome, I. (2000, 2000/12/01). Analysis of the genome sequence of the flowering plant *Arabidopsis thaliana*. *Nature*, 408(6814), 796-815. <https://doi.org/10.1038/35048692>
- Tretter, V., Mukherjee, J., Maric, H.-M., Schindelin, H., Sieghart, W., & Moss, S. J. (2012). Gephyrin, the enigmatic organizer at GABAergic synapses. *Frontiers in cellular neuroscience*, 6, 23-23. <https://doi.org/10.3389/fncel.2012.00023>
- Tsytlonok, M., Hemmen, K., Hamilton, G., Kolimi, N., Felekyan, S., Seidel, C. A. M., Tompa, P., & Sanabria, H. (2020). Specific Conformational Dynamics and Expansion Underpin a Multi-Step Mechanism for Specific Binding of p27 with Cdk2/Cyclin A. *Journal of Molecular Biology*, 432(9), 2998-3017. <https://doi.org/10.1016/j.jmb.2020.02.010>
- Tyagarajan, S. K., & Fritschy, J.-M. (2014). Gephyrin: a master regulator of neuronal function? *Nature Reviews Neuroscience*, 15(3), 141-156. <https://doi.org/10.1038/nrn3670>
- Tyagarajan, S. K., Ghosh, H., Harvey, K., & Fritschy, J.-M. (2011). Collybistin splice variants differentially interact with gephyrin and Cdc42 to regulate gephyrin clustering at GABAergic synapses. *Journal of Cell Science*, 124(16), 2786-2796. <https://doi.org/10.1242/jcs.086199>
- Tyagarajan, S. K., Ghosh, H., Yévenes, G. E., Imanishi, S. Y., Zeilhofer, H. U., Gerrits, B., & Fritschy, J.-M. (2013). Extracellular Signal-regulated Kinase and Glycogen Synthase Kinase 3 β Regulate Gephyrin Postsynaptic Aggregation and GABAergic Synaptic Function in a Calpain-dependent Mechanism*. *Journal of Biological Chemistry*, 288(14), 9634-9647. <https://doi.org/https://doi.org/10.1074/jbc.M112.442616>
- Tyagarajan, S. K., Ghosh, H., Yévenes, G. E., Nikonenko, I., Ebeling, C., Schwerdel, C., Sidler, C., Zeilhofer, H. U., Gerrits, B., Muller, D., & Fritschy, J.-M. (2011). Regulation of GABAergic synapse formation and plasticity by GSK3 β -

- dependent phosphorylation of gephyrin. *Proceedings of the National Academy of Sciences*, 108(1), 379-384. <https://doi.org/10.1073/pnas.1011824108>
- Uusi-Oukari, M., & Korpi, E. R. (2010). Regulation of GABA_A Receptor Subunit Expression by Pharmacological Agents. *Pharmacological Reviews*, 62(1), 97. <https://doi.org/10.1124/pr.109.002063>
- Vashchinkina, E., Panhelainen, A., Aitta-aho, T., & Korpi, E. R. (2014). GABA_A receptor drugs and neuronal plasticity in reward and aversion: focus on the ventral tegmental area [Hypothesis and Theory]. *Frontiers in Pharmacology*, 5. <https://www.frontiersin.org/articles/10.3389/fphar.2014.00256>
- Venter, J. C., Adams, M. D., Myers, E. W., Li, P. W., Mural, R. J., Sutton, G. G., Smith, H. O., Yandell, M., Evans, C. A., Holt, R. A., Gocayne, J. D., Amanatides, P., Ballew, R. M., Huson, D. H., Wortman, J. R., Zhang, Q., Kodira, C. D., Zheng, X. H., Chen, L., Skupski, M., Subramanian, G... & Zhu, X. (2001). The sequence of the human genome. *Science*, 291(5507), 1304-1351. <https://doi.org/10.1126/science.1058040>
- Watson Robert, T., Furukawa, M., Chiang, S.-H., Boeglin, D., Kanzaki, M., Saltiel Alan, R., & Pessin Jeffrey, E. (2003). The Exocytotic Trafficking of TC10 Occurs through both Classical and Nonclassical Secretory Transport Pathways in 3T3L1 Adipocytes. *Molecular and Cellular Biology*, 23(3), 961-974. <https://doi.org/10.1128/MCB.23.3.961-974.2003>
- Wennerberg, K., Rossman, K. L., & Der, C. J. (2005). The Ras superfamily at a glance. *J Cell Sci*, 118(Pt 5), 843-846. <https://doi.org/10.1242/jcs.01660>
- Whisstock, J. C., & Lesk, A. M. (1999). SH3 domains in prokaryotes. *Trends Biochem Sci*, 24(4), 132-133. [https://doi.org/10.1016/s0968-0004\(99\)01366-3](https://doi.org/10.1016/s0968-0004(99)01366-3)
- Wittinghofer, A., & Vetter, I. R. (2011). Structure-function relationships of the G domain, a canonical switch motif. *Annu Rev Biochem*, 80, 943-971. <https://doi.org/10.1146/annurev-biochem-062708-134043>
- Wittle, A. E., Kamdar, K. P., & Finnerty, V. (1999). The *Drosophila* cinnamon gene is functionally homologous to *Arabidopsis* *cnx1* and has a similar expression pattern to the mammalian gephyrin gene. *Molecular and General Genetics MGG*, 261(4), 672-680. <https://doi.org/10.1007/s004380050010>
- Worthylake, D. K., Rossman, K. L., & Sondek, J. (2000). Crystal structure of Rac1 in complex with the guanine nucleotide exchange region of Tiam1. *Nature*, 408(6813), 682-688. <https://doi.org/10.1038/35047014>
- Xiang, S., Kim, E. Y., Connelly, J. J., Nassar, N., Kirsch, J., Winking, J., Schwarz, G., & Schindelin, H. (2006). The Crystal Structure of Cdc42 in Complex with Collybistin II, a Gephyrin-interacting Guanine Nucleotide Exchange Factor. *Journal of Molecular Biology*, 359(1), 35-46. <https://doi.org/10.1016/j.jmb.2006.03.019>

- Xiang, S., Nichols, J., Rajagopalan, K. V., & Schindelin, H. (2001). The Crystal Structure of Escherichia coli MoeA and Its Relationship to the Multifunctional Protein Gephyrin. *Structure*, 9(4), 299-310. [https://doi.org/10.1016/s0969-2126\(01\)00588-3](https://doi.org/10.1016/s0969-2126(01)00588-3)
- Yoon, H. S., Hajduk, P. J., Petros, A. M., Olejniczak, E. T., Meadows, R. P., & Fesik, S. W. (1994). Solution structure of a pleckstrin-homology domain. *Nature*, 369(6482), 672-675. <https://doi.org/10.1038/369672a0>
- Yu, H., Bai, X. C., & Wang, W. (2021). Characterization of the subunit composition and structure of adult human glycine receptors. *Neuron*, 109(17), 2707-2716.e2706. <https://doi.org/10.1016/j.neuron.2021.08.019>
- Zheng, Y. (2001). Dbl family guanine nucleotide exchange factors. *Trends in Biochemical Sciences*, 26(12), 724-732. [https://doi.org/10.1016/s0968-0004\(01\)01973-9](https://doi.org/10.1016/s0968-0004(01)01973-9)
- Zhou, L., Kiss, E., Demmig, R., Kirsch, J., Nawrotzki, R. A., & Kuhse, J. (2021). Binding of gephyrin to microtubules is regulated by its phosphorylation at Ser270. *Histochemistry and Cell Biology*, 156(1), 5-18. <https://doi.org/10.1007/s00418-021-01973-2>
- Zhu, S., Noviello, C. M., Teng, J., Walsh, R. M., Kim, J. J., & Hibbs, R. E. (2018). Structure of a human synaptic GABAA receptor. *Nature*, 559(7712), 67-72. <https://doi.org/10.1038/s41586-018-0255-3>

7.List of publications

1. **Imam N**^ψ, Choudhury S^ψ, Hemmen K., Katrin G. H.,* Schindelin H.* (2022). Deciphering the conformational dynamics of gephyrin-mediated collybistin activation. *Biophysical Reports*. Volume 2, Issue4. doi: <https://doi.org/10.1016/j.bpr.2022.100079>.

2. **Imam N**, Choudhury S., Katrin G. H.,* Schindelin H.* (2022). Differential modulation of collybistin conformational dynamics by the closely related GTPases Cdc42 and TC10. *Frontiers in Synaptic Neuroscience*. Volume 14. <https://doi.org/10.3389/fnsyn.2022.959875>

^ψ Authors contributed equally to this work.

* Corresponding authors.

8. Abbreviations

Å	Ångström
A280	Absorbance at 280 nm
AFM	Atomic force microscopy
CB	Collybistin
CD	Circular-dichroism
Cdc42	Cell division cycle protein 42
CFP	Cyan Fluorescent Protein
CNS	Central nervous system
KDa	Kilo Dalton
Dbl	Diffuse B-cell lymphoma
DH	Dbl homology
E. coli	Escherichia coli
EDTA	Ethylenediaminetetraacetate
E _{FRET}	FRET Efficiency
GABA	Gamma-aminobutyric acid
GABA _A R	Gamma-aminobutyric acid type-A receptor
GEF	Guanine nucleotide exchange factor
Gly	Glycine
Fig.	Figure
FLAsH-EDT	Fluorescein arsenical hairpin binder-ethanedithiol
FPS	FRET Positioning Software
FRET	Forster Resonance Energy Transfer
tCM	Tetra-Cysteine motif
GDP	Guanosine diphosphate
Geph	Gephyrin
GephE	Gephyrin E domain
GephE _{mm}	Gephyrin E domain monomeric mutant
GephG	Gephyrin G domain
GTP	Guanosine triphosphate

HEPES	4-(2-hydroxyethyl)-1- piperazineethanesulfonic acid
hPEM-2	Human homolog of posterior end mark-2
icd	Intracellular cytosolic domain
IPTG	Isopropyl- β -thiogalactoside
iPSD	Inhibitory Postsynaptic Density
K _D	Dissociation constant
KDa	Kilo Dalton
M	Molarity
MCMC	Markov-chain Monte-Carlo
min	Minute
ml	Milliliter
Moco	Molybdenum Cofactor
NL2	Neuroigin2
NL4	Neuroigin4
nm	Nanometer
nM	Nanomolar
NMDA	N-methyl-D-aspartate
PAGE	Polyacrylamide gel electrophoresis
PBS	Phosphate-buffered saline
PDB	Protein data bank
PH	Pleckstrin homology
PI3P	Phosphatidylinositol 3-phosphate
Rho	RAS-homologue
rmsd	Root mean square deviation
R ₀	Förster distance
RT	Room temperature
SAXS	Small-angle X-ray scattering
SD	Standard deviation
SDS	Sodium dodecyl sulfate
SH3	Src-homology 3
TC10	Tetratocarcinoma10

TCSPC	Time-correlated single photon counting
Tris	Tri(hydroxymethyl)aminomethane
UV	Ultraviolet
WT	Wild-type
β -ME	β -Mercaptoethanol
μ L	Microliter
μ M	Micromolar

9. Plasmid constructs

Insert	Vector/affinity tag/Protease site	Source
CB FRET sensor (F1 _{D0})	pETM-14/ N-term 6xHis/ 3C	Imam, N.
CB FRET sensor (F28 _{D0})	pETM-14/ N-term 6xHis/ 3C	Imam, N.
CB FRET sensor (F73 _{D0})	pETM-14/ N-term 6xHis/ 3C	Imam, N.
CB FRET sensor (F99 _{D0})	pETM-14/ N-term 6xHis/ 3C	Imam, N.
CB-tCM1	pETM-14/ N-term 6xHis/ 3C	Imam, N.
CFP	pETM-14/ N-term 6xHis/ 3C	Imam, N.
Single mutant sensor(F1 _{smD0})	pETM-14/ N-term 6xHis/ 3C	Imam, N.
Double mutant sensor(F1 _{dmD0})	pETM-14/ N-term 6xHis/ 3C	Imam, N.
CB-SH3(10-79)	pETM-14/ N-term 6xHis/ 3C	Imam, N.
Gephyrin Full length P2 (1-750)	pET-28b/ N-term 6xHis/thrombin	Sander, B.
Gephyrin G domain	pET-28b/ N-term 6xHis/thrombin	Sander, B.
Gephyrin Linker-E	pET-28b/ N-term 6xHis/thrombin	Sander, B.
Gephyrin E	pET-28b/ N-term 6xHis/thrombin	Lee, E.Y.
Gephyrin E _{mm}	pTWIN/N-term Intein	Lee, E.Y.
Neuroigin2 (700-836)	pETM11/ N-term 6xHis/TEV	Sander, B.
TC10	pETM-14/ N-term 6xHis/ 3C	Bader, N.
TC10KR/GS	pETM-14/ N-term 6xHis/ 3C	Imam, N.
TC10ΔC	pETM-14/ N-term 6xHis/ 3C	Imam, N.
Cdc42	pET15b/ N-term 6xHis/Thrombin	Xiang, S.

10. Affidavit

I hereby confirm that my thesis entitled "***Molecular basis of Collybistin conformational dynamics***" is the result of my own work. I did not receive any help or support from commercial consultants. All sources and / or materials applied are listed and specified in the thesis.

Furthermore, I confirm that this thesis has not yet been submitted as part of another examination process neither in identical nor in similar form.

Würzburg,
Place, Date

Signature

Eidesstattliche Erklärung

Hiermit erkläre ich an Eides statt, die Dissertation „***Molekulare Prinzipien der konformellen Aktivierung von Collybistin***“ eigenständig, d.h. insbesondere selbständig und ohne Hilfe eines kommerziellen Promotionsberaters, angefertigt und keine anderen als die von mir angegebenen Quellen und Hilfsmittel verwendet zu haben.

Ich erkläre außerdem, dass die Dissertation weder in gleicher noch in ähnlicher Form bereits in einem anderen Prüfungsverfahren vorgelegen hat.

Würzburg,
Ort, Datum

Unterschrift

11. Acknowledgments

The work presented in this dissertation would not have been possible without the incessant support and motivation from the lovely people, whom I would like to pen down in this section.

I would like to thank first and foremost, Prof. Dr. Hermann Schindelin for providing me the opportunity to work on exciting projects and allowing me to pursue my Ph.D. under his invaluable supervision. Thank you for your guidance and for giving me work freedom which helped me develop critical thinking. I express my sincere appreciation to Prof. Dr. Katrin G. Heinze for her unceasing support, guidance, and fantastic collaboration, without which this work would not have been possible. I would also like to thank Prof. Dr. Carmen Villmann and Prof. Dr. Thomas Müller for being members of my thesis advisory committee and for their invaluable suggestions and evaluations during the annual thesis committee meetings. I thank Prof. Dr. Caroline Kisker for straightforward advice and suggestions in the Structural biology seminars.

I am immensely thankful to Dr. Susobhan Choudhury for sharing his wealth of experience in TCSPC and data analysis, for extensive scientific discussions, and for friendship. I am forever grateful to Dr. Katherina Hemmen for her invaluable suggestions, fruitful discussions, and for performing *in silico* studies for me.

I would like to express my gratitude to all the past and present members of the Schindelin lab. I thank Nicole Bader and Dr. Vikram Kasaragod for assisting me during the initial days of my Ph.D. Dr. Truong V. Ngoc and Carolina Galgenmuller, thank you for being cheerful lab mates and fantastic friends. I would like to thank my office-bench neighbors, Pia van gen Hassend, Tamsanqa T. Hove. and Shurong Li for the joyful and cordial ambiance in the office. I thank Monica Kuhn for her excellent technical support.

I express my thankfulness to all the former and current members of lab 206. Thank you, Dr. Florian Sauer, for fruitful discussions and for being a joyful and witty lab-bench neighbor. I express my sincere thanks to Ishu Saini for her help in the lab and for being a wonderful friend.

I wish to express my gratitude to Dr. Rahul Nair and Dr. Barbara Orth, members of Lorenz lab (presently based in Gottingen). Rahul, I am immensely thankful for your friendship, help during critical times in the lab, and motivating words. Barbara, thank you for your

motivating words and for constantly being around the lab during weekends.

I cannot thank enough Teresa Frank, Andrea Heinzmann, and Gabriele Ries for their unceasing administrative support and for taking care of the secretarial work.

I thank Dr. Niklas Trehoeven, Roland Markert, and Dr. Bernhard Froehlich for their excellent IT support and for being steadfast in helping me with any computer and internet-related issues.

To all my lovely friends in Wuerzburg, India, and across the world, whom I could not list here, thank you for the wonderful memories and for making my existence more meaningful.

Finally, I would like to thank my parents, sister, and brother for their care and unconditional support, without whom I could have gotten this far.

12. Curriculum Vitae